PONTIFÍCIA UNIVERSIDADE CATÓLICA DO RIO GRANDE DO SUL
PRÓ-REITORIA DE PESQUISA E PÓS-GRADUAÇÃO
PROGRAMA DE PÓS-GRADUAÇÃO EM ENGENHARIA E TECNOLOGIA DE MATERIAIS
Faculdade de Engenharia
Faculdade de Física
Faculdade de Química

PUCRS

PGETEMA

DEVELOPMENT AND ANALYSIS OF SILICON SOLAR CELLS WITH LASER-FIRED CONTACTS AND SILICON NITRIDE LASER ABLATION

RODRIGO LOPES SAUAIA

Master of Science in Renewable Energy (Loughborough University)

Bachelor of Science in Chemistry with Technological and Biotechnological Attributions (University of São Paulo)

Licentiate in Chemistry (University of São Paulo)

DOCTORAL THESIS IN PARTIAL FULFILMENT OF THE REQUIREMENTS FOR THE DEGREE OF DOCTOR IN MATERIALS ENGINEERING AND TECHNOLOGY

Porto Alegre

July, 2013

PONTIFÍCIA UNIVERSIDADE CATÓLICA DO RIO GRANDE DO SUL
PRÓ-REITORIA DE PESQUISA E PÓS-GRADUAÇÃO
PROGRAMA DE PÓS-GRADUAÇÃO EM ENGENHARIA E TECNOLOGIA DE MATERIAIS
Faculdade de Engenharia
Faculdade de Física
Faculdade de Química

PUCRS

PGETEMA

DEVELOPMENT AND ANALYSIS OF SILICON SOLAR CELLS WITH LASER-FIRED CONTACTS AND SILICON NITRIDE LASER ABLATION

RODRIGO LOPES SAUAIA

Master of Science in Renewable Energy (Loughborough University)

Bachelor of Science in Chemistry with Technological and Biotechnological Attributions (University of São Paulo)

Licentiate in Chemistry (University of São Paulo)

SUPERVISOR: Prof. Dr. Izete Zanesco (PUCRS)

CO-SUPERVISOR: Prof. Dr. Adriano Moehlecke (PUCRS)

CO-SUPERVISOR: Dr. Markus Glatthaar (Fraunhofer ISE)

Doctoral thesis presented to the Postgraduate Program in Materials Engineering and Technology (PGETEMA) of the Pontifical Catholic University of Rio Grande do Sul, in partial fulfilment of the requirements for the Degree of Doctor in Materials Engineering and Technology.

Work linked to research and development project titled "Células Solares de Alta Eficiência com Emissores Seletivos", contract CEEE-D/2009-9942400.

Porto Alegre

July, 2013

Pontifícia Universidade Católica do Rio Grande do Sul
FACULDADE DE ENGENHARIA
PROGRAMA DE PÓS-GRADUAÇÃO EM ENGENHARIA E TECNOLOGIA DE MATERIAIS

DEVELOPMENT AND ANALYSIS OF SILICON SOLAR CELLS WITH LASER-FIRED CONTACTS AND SILICON NITRIDE LASER ABLATION

CANDIDATO: RODRIGO LOPES SAUAIA

Esta Tese de Doutorado foi julgada para obtenção do título de DOUTOR EM ENGENHARIA E TECNOLOGIA DE MATERIAIS e aprovada em sua forma final pelo Programa de Pós-Graduação em Engenharia e Tecnologia de Materiais da Pontifícia Universidade Católica do Rio Grande do Sul.

DRA. IZETE ZANESCO – ORIENTADORA

DR. MARKUS GLATTHAAR - CO-ORIENTADOR

DR. ADRIANO MOEHLECKE - CO-ORIENTADOR

BANCA EXAMINADORA

DR. JOSÉ RUBÉN GUTIÉRREZ SERRANO - DA ESCUELA TÉCNICA SUPERIOR DE INGENIERÍA DE BILBAO – UPV

DR. ROBERTO ZILLES - DO INSTITUTO DE ENERGIA E AMBIENTE – USP

DR. JOÃO BENARDES DA ROCHA FILHO – FACULDADE DE FÍSICA - PUCRS

DRA. ELEANI MARIA DA COSTA - DO PGETEMA/FENG – PUCRS

DR. RICARDO MEURER PAPALEO - DO PGETEMA/FENG – PUCRS

PUCRS
Campus Central
Av. Ipiranga, 6681 - Prédio 30 - Sala 103 - CEP: 90619-900
Telefone: (51) 3353.4059 - Fax: (51) 3320.3625
E-mail: engenharia.pg.materiais@pucrs.br
www.pucrs.br/feng

Pontifícia Universidade Católica do Rio Grande do Sul
FACULDADE DE ENGENHARIA
PROGRAMA DE PÓS-GRADUAÇÃO EM ENGENHARIA E TECNOLOGIA DE MATERIAIS

DEVELOPMENT AND ANALYSIS OF SILICON SOLAR CELLS WITH LASER-FIRED CONTACTS AND SILICON NITRIDE LASER ABLATION

DOCTORAL CANDIDATE: RODRIGO LOPES SAUAIA

This doctoral thesis was evaluated as a requirement to obtain the degree of DOCTOR IN MATERIALS ENGINEERING AND TECHNOLOGY and was approved in its final version by the Postgraduate Program in Materials Engineering and Technology of the Pontifical Catholic University of Rio Grande do Sul.

DR. IZETE ZANESCO - SUPERVISOR

DR. MARKUS GLATTHAAR - CO-SUPERVISOR

DR. ADRIANO MOEHLECKE - CO-SUPERVISOR

DOCTORAL THESIS COMMITTEE

DR. JOSÉ RUBÉN GUTIÉRREZ SERRANO - FACULTY OF ENGINEERING OF BILBAO - UPV

DR. ROBERTO ZILLES - INSTITUTE OF ENERGY AND ENVIRONMENT - USP

DR. JOÃO BENARDES DA ROCHA FILHO - FACULTY OF PHYSICS - PUCRS

DR. ELEANI MARIA DA COSTA - PGETEMA/FENG – PUCRS

DR. RICARDO MEURER PAPALEO - PGETEMA/FENG - PUCRS

PUCRS
Campus Central
Av. Ipiranga, 6681 - Prédio 30 - Sala 103 - CEP: 90619-900
Telefone: (51) 3353.4059 - Fax: (51) 3320.3625
E-mail: engenharia.pg.materiais@pucrs.br
www.pucrs.br/feng

DEDICATION

In general terms, my work is dedicated to all individuals, past, present, and future, who worked, work, or will work in the different fields of science with the shared goal of improving our understanding of reality, refining our knowledge of the universe and consequently improving our standards of living, always bearing in mind the respect for people and nature alike.

Specifically in the field of photovoltaics, I dedicate this work to those who were, are, or will be engaged in developing the technology to its full potential. Each and every contribution given to advance photovoltaics forward brings it, and all its benefits, closer to widespread deployment around the world. With perseverance, we will surely get there.

Let us keep up the good work.

ACKNOWLEDGEMENTS

First and foremost, I thank my supervisor, Prof. Dr. Izete Zanesco, and co-supervisor, Prof. Dr. Adriano Moehlecke, who welcomed me with open arms to their research group, the Solar Energy Technological Nucleus (NT-Solar). Their scientific and technical guidance, ideas and suggestions, as well as their incentive for me to independently develop my own ideas, concepts, and experiments were essential throughout my doctoral work.

Secondly, I share my gratitude to Dr. Stefan Glunz and Dr. Filip Granek, who opened the doors of the *Fraunhofer Institut für Solare Energiesysteme* (ISE) to me and agreed with my joint-research project request. I also thank Dr. Markus Glatthaar and Dr. Sybille Hopman, who co-supervised my work during my stay in Freiburg im Breisgau, Germany, and provided me invaluable technical and scientific support in respect to solar cells, device processing, characterization methods, and laser technologies, during and after my stay at the Fraunhofer ISE.

Thirdly, I am glad to acknowledge the efforts and support of all colleagues, from both NT-Solar and Fraunhofer ISE, who directly or indirectly supported me during the years of my doctoral research. You have been an integral part of this initiative and your support was essential to fulfil the goals of this work.

Next, I thank the financial support received during the course of my doctoral studies, which was fundamental to fund the research activities carried out during this thesis. Many thanks to the Coordination for Improvement of Higher Education Personnel (CAPES), for the scholarships provided through the CAPES-PROSUP Program, in Brazil, as well as through the DAAD-CAPES-CNPq partnership during my activities at the Fraunhofer ISE, in Germany. My gratitude also goes to the *Deutscher Akademischer Austausch Dienst* (DAAD) for providing me with the opportunity to further develop my knowledge of the German language during my stay in Germany, as well as to learn more about the German culture, society, and history. I also thank the *Companhia Estadual de Distribuição de Energia Elétrica* (CEEE-D)

for the financial support provided through the research projects CEEE-D Contract Nº 9942400.

I would also like to acknowledge my friends, from Brazil and abroad, who followed and supported me during the good and harsh moments of these four important years of my life. I will always be there for you guys when you need me.

Last and most importantly, I deeply thank my family, who always provided me with their invaluable attention, conversations, positive criticism, care, and love.

“Ohne Energie geht nichts, das muss man wissen. Wir stehen vor dem größten Strukturwandel der Wirtschaft seit Beginn des Industriezeitalters.”
Dr. Hermann Scheer, 1944 - 2010

LIST OF FIGURES

Figure 2.1. (a): cross-section of a conceptual p-n junction solar cell [54]. (b): respective band diagrams of the metal contacts and different doped semiconductor layers comprising the solar cell presented on the top of the figure [57]. 48

Figure 2.2. Solar cell I-V characteristics in dark and under illumination and relevant electrical parameters obtained from such measurements [62]. 55

Figure 2.3. Standard industrial Al-BSF solar cell. Adapted from [66]. 62

Figure 2.4. Passivated emitter and rear cell [67]. 64

Figure 2.5. Random-pyramid passivated emitter and rear cell. Adapted from [66]. .. 65

Figure 2.6. Passivated emitter rear locally diffused cell [69]. 67

Figure 3.1. The laser buried contact solar cell [72]. 70

Figure 3.2. Description of the LFC processing method. Adapted from [88]..... 72

Figure 3.3. Comparison of the performance of LFC and PERC solar cells on p-type silicon for different base resistivities (left to right: 10 Ω cm to 0.5 Ω cm) [90]. 74

Figure 3.4. Optical microscopy of an LFC-processed region on an aluminium layer over a silicon substrate, with its distinct inner crater, outer crater and external circular ring [97]. 76

Figure 3.5. EBIC image of an LFC-processed region on an n-type silicon substrate, with inner crater, outer crater and external circular ring [96]. 78

Figure 3.6. Schematic representation of the LCP method. Adapted from [125]. 86

Figure 3.7. Two possible LCP applications: (a) front surface opening with selective emitter formation and (b) rear surface opening with local back-surface field formation [129]..... 87

Figure 3.8. Laser ablation mechanisms on dielectric layers used as front side antireflection coating: (a) direct laser ablation mechanism and (b) indirect laser ablation mechanism..... 91

Figure 4.1. Flowchart diagram used for the optimization of laser parameters to develop LFC solar cells without rear oxide passivation layer. 96

Figure 4.2. Schematic structure of LFC solar cells developed in this work. Both surfaces were textured (feature not shown on the rear surface for clarity purposes). Adapted from [109]. 98

Figure 4.3. SEM images (top and cross-section views) of “as-cut” (upper images) and textured (lower images) silicon wafers used in this chapter’s experiments. 104

Figure 4.4. Reflectance curves of silicon wafers: “as-cut”, textured, and textured with TiO_2 ARC. 109

Figure 4.5. Layout of the screen-printing mask used for front surface metallization. 110

Figure 4.6. Schematic representation of the Nd:YAG laser system available at NT-Solar and employed in this chapter. Adapted from [159]. 112

Figure 4.7. Schematics of the laser scribing areas at the front surface (left, red lines) and of the LFC-processing of the rear surface for local contact formation (right, red dots). 112

Figure 4.8. Pictures of the front (a) and rear (b) sides of a finished laboratory-scale crystalline silicon solar cell incorporating laser-fired contacts, produced during this work at NT-Solar. 113

Figure 4.9. J-V curves of LFC solar cells processed with different pumping lamp currents. Fixed laser processing parameters were: 20.0 kHz q-switch frequency and 1.00 mm contact pitch. 116

Figure 4.10. J-V curves of LFC solar cells processed with different q-switch frequencies. Fixed laser processing parameters were: 33.0 A pumping lamp current and 1.00 mm contact pitch. Emitter sheet resistance of samples was (41 ± 6) Ω/sq. 119

Figure 4.11. J-V curves of LFC solar cells processed with different rear contact distances. 121

Figure 4.12. Selected J-V curves of LFC solar cells annealed at different temperatures. Fixed laser processing parameters were: 33.0 A pumping lamp current, 20.0 kHz q-switch frequency, 13.0 W laser power, and 0.50 mm contact pitch. Emitter sheet resistance was (41 ± 6) Ω/sq and conveyor belt speed was 220 cm/min. 123

Figure 4.13. J-V curves of LFC solar cell 05A01A, with SiO_2 rear surface passivation and annealed sequentially at different conveyor belt speeds. Fixed laser processing parameters were: 33.0 A pumping lamp current, 20.0 kHz q-switch frequency, 13.0 W laser power, and 0.50 mm contact pitch. Emitter sheet resistance was (50 ± 4) Ω/sq. 136

Figure 4.14. J-V curves of the best solar cells without Al-BSF, with Al-BSF, and with LFC, fabricated on the same type of CZ-Si substrate, with equivalent screen-printed front metallization, and processed under similar conditions. 144

Figure 4.15. Reflectance and IQE of the best solar cells without Al-BSF, with Al-BSF, and with LFC, fabricated on the same type of CZ-Si substrate, with equivalent screen-printed front metallization, and processed under similar conditions. 146

Figure 4.16. Optical microscopy images of LFC contacts processed by two different laser systems: (a) LFC performed with the laser system with X-Y table employed in this work and (b) LFC using the new scanning head mirror galvanometer laser system recently installed at NT-Solar. 147

Figure 5.1. Flowchart diagram used for the development of solar cells with SiN_X laser ablation and selective Ni/Ag front side metallization. 151

Figure 5.2. Processing method for solar cells with SiN_X laser ablation and Ni/Ag selective electrochemical front grid metallization. Surface texturing not shown for simplicity. 151

Figure 5.3. Schematic structure of a solar cell with SiN_X laser ablation and selective Ni/Ag front surface metallization. Adapted from [66]. 152

Figure 5.4. Picture of a (156 x 156) mm^2 silicon wafer processed with 16 solar cell with different front metal grids (photolithography, LCP-H_2O, SCA) and laser parameters. 153

Figure 5.5. Confocal scanning microscopy of the SiN_X openings corresponding to the busbar and some fingers, performed by photolithography on textured silicon wafers. 155

Figure 5.6. SEM images of: (a) cross-section of a silicon wafer after screen-printing of the rear contacts and (b) detailed image of the rear contact, showing the formation of a homogeneous Al-BSF (dotted white line). 156

Figure 5.7. (a): schematic representation of the LCP system (adapted from [166]) and (b): detail of its optical head and coupling unit [167]: 1. incoming laser opening, 2. CCD camera, 3. guiding mirror unit, 4. focusing unit, 5. beam path, 6. high-pressure connector for the liquid solution, 7. coupling unit. The red arrow represents the laser beam path. 159

Figure 5.8. Configuration of the galvanometer-based laser processing (SCA) system, with a description of its scanning head components [168]. 160

Figure 5.9. (a): schematic representation of the electroless light-supported plating process setup and (b): detail of the distribution of species and chemical reactions usually attributed to this process [141]. 162

Figure 5.10. Schematic representation of the optical setup of the LCP-H_2O system and laser power measurement points for the determination of optical losses. 165

Figure 5.11. Schematic representation of the optical setup of the SCA system and laser power measurement points for the determination of optical losses. 167

Figure 5.12. Confocal microscopy images of single-pulse laser-ablated points processed with different laser pulse energies using the LCP-H_2O technique. Fixed laser processing parameters were: 1 kHz q-switch frequency, 200 mm/s processing speed, 50 ns pulse duration. Scale: 40 µm. 170

Figure 5.13. Confocal microscopy images of laser-ablated lines processed with different laser pulse energies using the LCP-H_2O technique. Fixed laser processing parameters were: 100.0 kHz q-switch frequency, 300 mm/s processing speed, 40 ns pulse duration, 3.0 µm pulse distance. Scale: 40 µm. 171

Figure 5.14. Confocal microscopy images of single-pulse laser-ablated points processed with different laser pulse energies using the SCA technique. Fixed laser processing parameters were: 100.0 kHz q-switch frequency, 10000 mm/s processing speed, 40 ns pulse duration. Scale: 20 µm. .. 173

Figure 5.15. Confocal microscopy images of laser-ablated lines processed with different laser pulse energies using the SCA technique. Fixed laser processing parameters were: 400.0 kHz q-switch frequency, 1000 mm/s processing speed, and 2.5 µm pulse distance, 145 ns pulse duration. Scale: 20 µm. 173

Figure 5.16. Confocal laser scanning microscopy image of laser-ablated lines with melted pyramid tips and corners. Laser processing parameters were: 4 µJ pulse energy, 400 kHz q-switch frequency, 1000 mm/s processing speed, 2.5 µm pulse distance, 145 ns pulse duration. Scale: 4 µm. 175

Figure 5.17. SiN_X laser-ablated line widths processed with different laser pulse energies using the SCA and LCP-H_2O techniques. 175

Figure 5.18. Confocal microscopy images of single-pulse laser-ablated points processed with different q-switch frequencies using the SCA technique. Fixed laser processing parameters were: 6.0 µJ pulse energy, 15000 mm/s processing speed. Scale: 20 µm. 176

Figure 5.19. Confocal microscopy images of laser-ablated lines processed with different q-switch frequencies using the SCA technique. Fixed laser processing parameter was: 6.25 µm pulse distance. Scale: 20 µm. 177

Figure 5.20. Laser-ablated fingers and busbars processed with different laser pulse energies using LCP-H_2O. Fixed laser processing parameters were: 16.0 kHz q-switch frequency, 100 mm/s laser processing speed, and 6.25 µm pulse distance, 50 ns pulse duration, 80 µm nozzle diameter, 70 bar pump pressure. Scale: 40 µm. 179

Figure 5.21. Laser-ablated fingers and busbars processed with different laser pulse energies using SCA. Fixed laser processing parameters were: 130.0 kHz q-switch frequency, 813 mm/s laser processing speed, and 6.25 µm pulse distance, 50 ns pulse duration. Scale 40 µm. 179

Figure 5.22. Solar cell processed with photolithography: (a) finger and busbar openings on the SiN_X layer, (b) homogeneous Ni plating by ELSP on the exposed Si areas, (c) Ag plating by LIEP, showing detachment of the front metal fingers. Please note the different scales of each measurement. 180

Figure 5.23. Solar cell processed with LCP-H_2O: (a) finger and busbar openings on the SiN_X layer, (b) Ni plating by ELSP, (c) Ag plating by LIEP. Fixed laser parameters were: 15.3 µJ laser pulse energy, 16.0 kHz q-switch frequency, 100 mm/s laser processing speed, and 6.25 µm pulse distance, 50 ns pulse duration, 80 µm nozzle diameter, 70 bar pump pressure. Scale: 20 µm. 181

Figure 5.24. Solar cell processed with SCA: (a) finger and busbar openings on the SiN_X layer, (b) Ni plating by ELSP, (c) Ag plating by LIEP. Fixed laser parameters were: 3.0 µJ laser pulse energy, 130.0 kHz q-switch frequency, 813 mm/s laser processing speed, and 6.25 µm pulse distance, 50 ns pulse duration. Scale: 20 µm. 182

Figure 5.25. Best LCP-H_2O and SCA finger cross-section profiles, with height and width values estimated by confocal laser scanning microscopy. 183

Figure 5.26. Suns-Voc results for the pFF of samples processed by different methods after Ag plating. 184

Figure 5.27. Suns-Voc results for the V_{OC} of samples processed by different methods after Ag plating. 185

Figure 5.28. J-V curves of the best solar cells using SiN_X laser ablation, processed with LCP-H_2O and SCA, as well as the best LFC solar cell. 188

LIST OF TABLES

Table 3.1. Laser processing technologies applied to photovoltaic devices. 71

Table 3.2. Internal reflectance and effective rear surface recombination velocities for different solar cell structures. R_{rear} is the internal reflectance at the rear side, J_{SC} is the maximum short-circuit current density for a 250 µm thick solar cell simulated by 3D ray tracing, S_{rear} is the effective rear surface recombination velocity modelled in PC1D, and V_{OC} PC1D is the open-circuit voltage modelled in PC1D. Adapted from [99]. 79

Table 3.3. Performance of LFC solar cells with different passivation layers and deposited by different methods. All solar cells were produced on p-FZ-Si substrates and had areas of 4.0 cm^2 81

Table 3.4. Performance of LFC solar cells with evaporated Ti/Pd/Ag front contacts and rear aluminium deposited by different methods. 82

Table 3.5. Performance of LFC solar cells on very thin silicon substrates. 83

Table 3.6. Performance of record solar cells and module incorporating the LFC technology. The module data is presented in different V_{OC} and J_{SC} units for clarity. 84

Table 3.7. Performance of high-efficiency LCP solar cells incorporating selective emitters or local back-surface fields produced on p-type FZ-Si. 88

Table 3.8. Results of high-efficiency crystalline silicon solar cells incorporating SiN_X laser ablation and alternative front surface metallization processes. 93

Table 4.1. Experimental parameters and results of the texturing optimization procedure. Process temperature was kept at (80 ± 2) ºC in all experiments. Texturing was performed without stirring. 101

Table 4.2. Metalized area and shaded fraction of solar cells developed. 110

Table 4.3. Electrical parameters of solar cells with laser-firing of the rear contacts, processed under different pumping lamp currents. Fixed laser processing parameters were: 20.0 kHz q-switch frequency and 1.00 mm contact pitch. 116

Table 4.4. Electrical parameters of solar cells with laser-firing of the rear contacts, processed under different q-switch laser frequencies. Fixed laser processing parameters were: 24.0 A pumping lamp current, and 1.00

mm contact pitch. Emitter sheet resistance of samples was (26 ± 4) Ω/sq. 117

Table 4.5. Electrical parameters of solar cells with laser-firing of the rear contacts, processed under different q-switch laser frequencies. Fixed laser processing parameters were: 24.0 A pumping lamp current, and 1.00 mm contact pitch. Emitter sheet resistance of samples was (41 ± 6) Ω/sq. 117

Table 4.6. Electrical parameters of solar cells with laser-firing of the rear contacts, processed under different q-switch laser frequencies. Fixed laser processing parameters were: 32.0 A pumping lamp current, and 1.00 mm contact pitch. Emitter sheet resistance of samples was (41 ± 6) Ω/sq. 118

Table 4.7. Electrical parameters of solar cells with laser-firing of the rear contacts, processed under different q-switch laser frequencies. Fixed laser processing parameters were: 33.0 A pumping lamp current and 1.00 mm contact pitch. Emitter sheet resistance of samples was (41 ± 6) Ω/sq. 118

Table 4.8. Electrical parameters of solar cells with laser-firing of the rear contacts, processed under different rear contact distances. Fixed laser processing parameters provided below for each analysis. Emitter sheet resistance of samples was (41 ± 6) Ω/sq. 120

Table 4.9. Electrical parameters of solar cells with laser-firing of the rear contacts, processed sequentially under different annealing temperatures. Fixed laser processing parameters were: 24.0 A pumping lamp current, 20.0 kHz q-switch frequency, 3.6 W laser power, and 1.00 mm contact pitch. Emitter sheet resistance was (26 ± 4) Ω/sq and conveyor belt speed was 33 cm/min. Process 01. 122

Table 4.10. Electrical parameters of solar cells with laser-firing of the rear contacts, processed under different annealing temperatures. Fixed laser processing parameters were: 33.0 A pumping lamp current, 20.0 kHz q-switch frequency, 13.0 W laser power, and 0.50 mm contact pitch. Emitter sheet resistance was (41 ± 6) Ω/sq and conveyor belt speed was 220 cm/min. Process 04e. 123

Table 4.11. Electrical parameters of solar cells with laser-firing of the rear contacts, processed under different annealing temperatures. Fixed laser processing parameters were: 32.0 A pumping lamp current, 17.5 kHz q-switch frequency, 11.4 W laser power, and 0.50 mm contact pitch. Emitter sheet resistance was (41 ± 6) Ω/sq and conveyor belt speed was 220 cm/min. Process 04e. 124

Table 4.12. Electrical parameters of solar cells without laser processing, before and after an annealing step at 650 ºC. Emitter sheet resistance was (41 ± 6) Ω/sq and conveyor belt speed was 220 cm/min. Process 04c. 125

Table 4.13. Electrical parameters of solar cells with laser-firing of the rear contacts, processed under different annealing temperatures. Laser processing parameters are provided in the table, apart from the fixed contact pitch of 1.00 mm. Emitter sheet resistance was (41 ± 6) Ω/sq and conveyor belt speed was 220 cm/min. Process 04b. 126

Table 4.14. Electrical parameters of solar cells with laser-firing of the rear contacts, before annealing. Process 05B07. 128

Table 4.15. Electrical parameters of solar cells with laser-firing of the rear contacts, after annealing at 400 ºC with a conveyor belt speed of 220 cm/min. Process 05B07. 128

Table 4.16. Electrical parameters of solar cells with laser-firing of the rear contacts, after a second annealing at 400 ºC with a conveyor belt speed of 33 cm/min. Process 05B07. 129

Table 4.17. Electrical parameters of solar cells with laser-firing of the rear contacts, before annealing. Process 05B08. 130

Table 4.18. Electrical parameters of solar cells with laser-firing of the rear contacts, after annealing at 400 ºC with different conveyor belt speeds. Process 05B08. 131

Table 4.19. Electrical parameters of solar cells with laser-firing of the rear contacts, before annealing. Process 05A01. 133

Table 4.20. Electrical parameters of solar cells with laser-firing of the rear contacts, after annealing at 400 ºC with a conveyor belt speed of 220 cm/min. Process 05A01. 134

Table 4.21. Electrical parameters of solar cells with laser-firing of the rear contacts, after a second annealing at 400 ºC with a conveyor belt speed of 33 cm/min. Process 05A01. 135

Table 4.22. Summary of the average values and best electrical parameters of solar cells with laser-firing of the rear contacts for Groups B and A, after annealing at 400 ºC with different conveyor belt speeds. 137

Table 4.23. Electrical parameters of solar cells with a 2 µm rear side aluminium layer and laser-firing of the rear contacts, before annealing. Process 05A01. 139

Table 4.24. Electrical parameters of solar cells with a 4 µm rear side aluminium layer and laser-firing of the rear contacts, before annealing. Process 05A02.139

Table 4.25. Electrical parameters of solar cells with a 4 µm rear side aluminium layer and laser-firing of the rear contacts, after annealing at 400 ºC with a conveyor belt speed of 50 cm/min. Process 05A02. 140

Table 4.26. Electrical parameters of industrial p-type screen-printed solar cells without Al-BSF. Emitter sheet resistance was (41 ± 6) Ω/sq. Screen-printed metal pastes were fired at 840 ºC with a conveyor belt speed of 220 cm/min. 142

Table 4.27. Electrical parameters of industrial p-type screen-printed solar cells with a full-area Al-BSF formed by co-diffusion in a quartz tube furnace at 900 ºC. Emitter sheet resistance was (37 ± 3) Ω/sq. Screen-printed metal pastes were fired at 840 ºC. 143

Table 5.1. Front contact grid design and SiN_X opened areas and area fractions for solar cells developed, according to the method employed for the removal of the SiN_X layer. Designs were optimized for similar opened areas and area fractions. 161

Table 5.2. Laser power measurements at different points and calculated average optical losses for the LCP-H_2O system. 166

Table 5.3. Laser power measurements at different points and calculated average optical losses for the SCA system. 168

Table 5.4. Summary of the average values and best electrical parameters of solar cells with SiN_X laser ablation and Ni/Ag electrochemical metallization using LCP-H_2O and SCA techniques. 186

LIST OF ABBREVIATIONS

ALD	Atomic layer deposition
AM1.5G	Air mass 1.5 global standard solar spectrum
ANEEL	*Agência Nacional de Energia Elétrica*
ARC	Antireflection coating
a-Si	Amorphous silicon
BOS	Balance of system
BSF	Back-surface field
CAPES	*Coordenação de Aperfeiçoamento de Pessoal de Nível Superior*
CFL	*Contatos formados por laser*
CIGS	Copper indium gallium selenide
CNC	Computer numerical control
CZ-Si	Czochralski silicon
DAAD	*Deutscher Akademischer Austausch Dienst*
DSC	Dye-sensitized solar cell
EBE	Electron-beam evaporation
EBIC	Electron-beam induced current
ELSP	Electroless light-supported plating
EPE	*Empresa de Pesquisa Energética*
EQE	External quantum efficiency
EWT	Emitter wrap through
FSF	Front-surface field
FZ-Si	Float zone silicon
GHG	Greenhouse gases
IQE	Internal quantum efficiency
ISE	*Fraunhofer Institut für Solare Energiesysteme*
Laser	Light amplification by stimulated emission of radiation
LBC	Laser buried contacts
LBIC	Light beam induced current
LBSF	Local back-surface field
LCP	Laser chemical processing
LED	Light-emitting diode

LFC	Laser-fired contact
LIP	Light-induced plating
LIEP	Light-induced electroless plating
µc-Si	Microcrystalline silicon
mc-Si	Multicrystalline silicon
MPP	Maximum power point
MWT	Metal wrap through
NREL	National Renewable Energy Laboratory
Nd:YAG	Neodymium-doped yttrium aluminium garnet
NT-Solar	Solar Energy Technological Nucleus
OSC	Organic solar cell
PECVD	Plasma-enhanced chemical vapour deposition
PERC	Passivated emitter and rear contacts
PERL	Passivated emitter and rear locally-diffused
PL	Photolithography
PQL	*Processamento químico com laser*
PSG	Phosphorus silicate glass
PV	Photovoltaics
PVD	Physical vapour deposition
PUCRS	*Pontifícia Universidade Católica do Rio Grande do Sul*
QSSPC	Quasi-steady-state photoconductance
RCA	Radio Corporation of America (refers to: RCA cleaning)
R&D	Research and development
SCA	Scanning head mirror galvanometer laser system
SE	Selective emitter
SEM	Scanning electron microscope
SIMS	Secondary ion mass spectrometry
SR	Spectral response
SRH	Schockley-Read Hall
STC	Standard test conditions
TEM_{00}	Transverse electromagnetic mode
UNSW	University of New South Wales

LIST OF SYMBOLS

α	Absorption coefficient	cm^{-1}
ΔFF	Change in fill factor	---
λ	Wavelength	nm
v	Frequency	Hz
η	Efficiency	%
ρ	Reflectance	%
ρ_W	Weighted average reflectance	%
τ	Minority charge carrier lifetime	µs
τ_e	Minority charge carrier lifetime in the emitter region	µs
τ_i	Initial minority charge carrier lifetime	µs
τ_f	Final minority charge carrier lifetime	µs
A	Area	m^2
c	Speed of light in vacuum	$m.s^{-1}$
C_S	Surface doping concentration	cm^{-3}
D	Diffusion coefficient	$cm^2.s^{-1}$
D_P	Distance of the laser-fired rear contacts	mm
E_C	Energy level at the bottom of the conduction band	eV
E_F	Fermi energy level	eV
E_g	Energy bandgap	eV
E_V	Energy level at the top of the valence band	eV
E_t	Energy level of traps (e.g. impurities, defects)	eV
f	Q-switch frequency of the laser system	Hz
FF	Fill Factor	---
G	Light source intensity (i.e. solar irradiance)	$W.cm^{-2}$
h	Planck's constant	eV.s
I	Electric current	A
I_0	Dark saturation current (i.e. diode leakage current)	A
I_L	Photogenerated current (i.e. photocurrent)	A
I_{Lamp}	Pumping lamp current of the laser system	A
I_{MPP}	Current at maximum power point	A
I_{SC}	Short-circuit current	A

J_{MPP}	Current density at maximum power point	$mA.cm^{-2}$
J_{SC}	Short-circuit current density	$mA.cm^{-2}$
k	Boltzmann constant	$eV.K^{-1}$
L	Minority carrier diffusion length	µm
n	Electron concentration	cm^{-3}
n_{ARC}	Refractive index of the antireflection coating	---
n_e	Electron flux	V m
n_p	Photon flux	$m^{-2}.s^{-1}$
N_A	Acceptor impurity density	cm^{-3}
N_D	Donor impurity density	cm^{-3}
p	Hole concentration	cm^{-3}
pFF	Pseudo-fill factor	---
pJ_{SC}	Pseudo-short-circuit current density	$mA.cm^{-2}$
pη	Pseudo-efficiency	%
P_D	Laser pulse duration	ns
P_E	Laser pulse energy	µJ
P_L	Power of the laser system	W
P_{MPP}	Power at maximum power point	W
q	Electronic charge	C
R_S	Series resistance	Ω
R_{SH}	Shunt resistance (i.e. parallel resistance)	Ω
$R_{\square}$	Sheet resistance	Ω/sq
SRV	Surface recombination velocity	$cm.s^{-1}$
S_F	Front surface recombination velocity	$cm.s^{-1}$
S_B	Rear surface recombination velocity	$cm.s^{-1}$
S_{eff}	Effective rear surface recombination velocity	$cm.s^{-1}$
t	Time	s
T	Temperature	K
T_A	Annealing temperature	ºC
x_j	Junction depth	µm
V	Voltage	V
v_{Belt}	Conveyor belt speed	cm/min
V_{bi}	Built-in voltage (i.e. built-in potential)	V
V_{MPP}	Voltage at maximum power point	V

V_{OC}	Open-circuit voltage	V

RESUMO

SAUAIA, Rodrigo Lopes. **Desenvolvimento e análise de células solares de silício com contatos posteriores formados por laser e ablação laser de nitreto de silício.** Porto Alegre. 2013. Tese de doutorado. Programa de Pós-Graduação em Engenharia e Tecnologia de Materiais, Pontifícia Universidade Católica do Rio Grande do Sul.

O objetivo desta tese foi o desenvolvimento e análise de células solares em substrato de silício cristalino com processamento por radiação laser. Células solares com estrutura n^+pp^+ em substrato de CZ-Si tipo p foram fabricadas, analisadas e comparadas, com base em duas técnicas de processamento laser: contatos posteriores formados por laser (CFL) e ablação do filme antirreflexo frontal de nitreto de silício por processamento químico com laser (PQL) ou por processamento com laser guiado por galvanômetro de espelhos (SCA). O método CFL foi utilizado na formação dos contatos posteriores de células solares, após a deposição de uma camada de alumínio. Os métodos PQL e SCA foram usados no desenvolvimento de um processo de ablação a laser do filme frontal de nitreto de silício. Trilhas foram abertas no filme antirreflexo e posteriormente metalizadas seletivamente por deposição química de níquel e prata, para formar a malha de metalização frontal. Os melhores parâmetros de processamento laser encontrados para células solares CFL foram: corrente da lâmpada de bombeamento óptico de 33,0 A, freqüência q-switch de 20,0 kHz e distância entre contatos posteriores de 0,50 mm. Células solares CFL com metalização frontal por serigrafia e passivação posterior com SiO_2 alcançaram uma eficiência média de 14,4 % e melhor valor de 15,3 %, após tratamento térmico a 400 ºC com velocidade de esteira de 50 cm/min. O aumento da espessura da camada de alumínio posterior de 2 µm para 4 µm não resultou em melhora significativa da performance das células solares. Os melhores parâmetros de processamento encontrados para o processo de ablação a laser de nitreto de silício pela técnica PQL foram: energia do pulso laser de 15,3 µJ, freqüência q-switch de 16,0 kHz e velocidade de processamento de 100 mm/s. Os melhores parâmetros de processamento encontrados para o processo de ablação a laser de nitreto de silício pela técnica SCA foram: energia do pulso laser de 5,0 µJ, freqüência q-switch de 130,0 kHz e velocidade de processamento de 813 mm/s. Células solares com

ablação a laser de nitreto de silício, metalização frontal seletiva por deposição química de níquel e prata e metalização posterior por serigrafia atingiram a eficiência média de 16,1 % e o melhor valor de 16,8 % com a técnica PQL e a eficiência média de 16,3 % e melhor valor de 16,6 % com a técnica SCA.

Palavras-Chave: célula solar de silício cristalino, contatos formados por laser, processamento químico com laser.

ABSTRACT

SAUAIA, Rodrigo Lopes. **Development and analysis of silicon solar cells with laser-fired contacts and silicon nitride laser ablation.** Porto Alegre. 2013. Doctoral thesis. Postgraduate Program in Materials Engineering and Technology, Pontifical Catholic University of Rio Grande do Sul.

The goal of this thesis was the development and analysis of crystalline silicon solar cells processed by laser radiation. Solar cells with n^+pp^+ structure on p-type, CZ-Si solar grade substrate were developed, analysed, and evaluated, based on two laser processing techniques: laser-fired rear contacts (LFC) and laser ablation of the front surface silicon nitride by means of laser chemical processing (LPC) or using a mirror galvanometer laser system (SCA). The LFC method was employed to form the rear contacts of crystalline silicon solar cells after the deposition of an aluminium layer. The LCP and SCA methods were used to develop a silicon nitride ablation process. The laser ablation process was employed to open regions of the device's antireflection coating, followed by selective chemical deposition of Ni/Ag to form the front metal grid. The best laser processing parameters found for LFC solar cells were: 33.0 A pumping lamp current, 20.0 kHz q-switch frequency, and 0.50 mm contact distance. LFC solar cells with screen printed front metallization and SiO_2 rear passivation layer achieved an average efficiency of 14.4 % and best value of 15.3 %, after an annealing step at 400 ºC with a belt speed of 50 cm/min. Increasing the rear aluminium layer thickness from 2 μm to 4 μm did not improve the performance of the devices significantly. The best laser processing parameters found for the silicon nitride laser ablation process based on the LCP technique were: 15.3 μJ laser pulse energy, 16.0 kHz q-switch frequency, and 100 mm/s processing speed. The best laser processing parameters found for the silicon nitride laser ablation process based on the SCA technique were: 5.0 μJ laser pulse energy, 130.0 kHz q-switch frequency, and 813 mm/s processing speed. Solar cells with silicon nitride laser ablation, front side metallization by Ni/Ag selective electrochemical deposition, and screen-printed rear side metallization achieved an average efficiency of 16.1 % and best value of 16.8 % for the LCP technique and an average efficiency of 16.3 % and best value of 16.6 % for the SCA technique.

Keywords: crystalline silicon solar cell, laser-fired contacts, laser chemical processing.

TABLE OF CONTENTS

1. INTRODUCTION 30

1.1. Background and Motivation 30

1.1.1. Photovoltaics as a Contributor to Sustainability 31

1.1.2. The Brazilian Potential for Photovoltaics 39

1.2. Thesis Aims and Objectives 41

2. CRYSTALLINE SILICON SOLAR CELLS 45

2.1. Principles of Solar Cells 45

2.1.1. Semiconductors, Doping, and p-n Junction Diodes 46

2.1.2. Efficiency Limits and Loss Mechanisms 48

2.2. Characterization of Samples and Solar Cells 51

2.2.1. Four Point Probe Resistivity 52

2.2.2. Dark and Illuminated Current-Voltage Curves 52

2.2.3. Spectral Response and Quantum Efficiency 56

2.2.4. Suns-Voc 57

2.2.5. Light Beam Induced Current 58

2.3. Solar Cell Concepts and Structures 60

2.3.1. Aluminium Back-Surface Field Solar Cell 61

2.3.2. Passivated Emitter and Rear Cell 63

2.3.3. Passivated Emitter Rear Locally Diffused Cell 66

3. LASER PROCESSING TECHNOLOGIES FOR SILICON SOLAR CELLS 68

3.1. Laser Processing and Photovoltaic Solar Cells 68

3.2. Laser-Fired Contacts 71

3.2.1. Technology Overview 72

3.2.2. Characteristics of the Laser-Fired Point Contact 75

3.2.3. Internal Reflectance and Rear Passivation Quality 78

3.2.4. Types of Rear Passivation Layers and Deposition Methods 80

3.2.5. Rear Aluminium Deposition Methods 81

3.2.6. Thermal Treatment 83

3.2.7. Solar Cells on Very Thin Substrates 83

3.2.8. World Records and Industrial Devices with Laser-Fired Contacts 84

3.3. Laser Chemical Processing 85
3.3.1. Technology Overview 85
3.3.2. Best Solar Cell Results of Laser Chemical Processing on p-Type Silicon Substrates 88
3.4. Laser Ablation of Dielectric Layers 89
3.4.1. Technology Overview 89
3.4.2. High-Efficiency Solar Cells with SiN_X Laser Ablation 93
4. DEVELOPMENT OF SILICON SOLAR CELLS WITH LASER-FIRED CONTACTS 95
4.1. Processing Sequences and Methods for Solar Cells with Laser-Fired Contacts 95
4.1.1. Chemical Processing 98
4.1.1.1. Anisotropic Chemical Etching 98
4.1.1.2. RCA-1 and RCA-2 Cleaning 104
4.1.1.3. Acid Etching of Phosphorus Silicates and Oxides 105
4.1.2. Thermal Oxidation and Passivation 105
4.1.3. Phosphorus Diffusion in Quartz Tube Furnace 107
4.1.4. TiO_2 and Aluminium Deposition by Evaporation 108
4.1.5. Screen-Printing Metallization of the Front Contacts 109
4.1.6. Laser Scribing and Laser Processing of the Rear Contacts 111
4.1.7. Thermal Treatment 113
4.2. Characterization Methods for Samples and Solar Cells with Laser-Fired Contacts 114
4.3. Solar Cells without Rear Side Passivation 114
4.3.1. Influence of the Pumping Lamp Current 115
4.3.2. Influence of the Q-Switch Frequency 117
4.3.3. Influence of the Rear Contact Distance 119
4.3.4. Influence of the Annealing Temperature 121
4.4. Solar Cells with Rear Side Passivation and Phosphorus Silicate Glass .. 126
4.5. Solar Cells with Rear Side Passivation Treated with Chemical Etching ... 132
4.5.1. Influence of the Belt Speed During Annealing 133
4.5.2. Influence of the Rear Aluminium Thickness 138
4.6. Comparison between Laser-Fired Contact and Screen-Printed Solar Cells

5. EVALUATION OF SILICON SOLAR CELLS WITH LASER-ABLATED SILICON NITRIDE LAYERS 149

5.1. Processing Sequences and Methods for Solar Cells with Laser Ablation 150

5.1.1. Processing Sequences 150

5.1.2. SiN_X Openings Defined by Photolithography 154

5.1.3. Screen-Printing Metallization of the Rear Contacts 155

5.1.4. Laser Ablation of the SiN_X Layer 157

5.1.5. Metallization of the Front Contacts using Ni/Ag Plating 161

5.2. Characterization Methods for Samples and Solar Cells with Laser Ablation 163

5.3. Development of SiN_X Ablation using Laser Processing 164

5.3.1. Determination of the Optical Losses of the Laser Systems 164

5.3.1.1. Laser Chemical Processing with Deionised Water 165

5.3.1.2. Scanning Head Mirror Galvanometer Laser System 167

5.3.2. Influence of the Laser Pulse Energy 169

5.3.2.1. Laser Chemical Processing with Deionised Water 170

5.3.2.2. Scanning Head Mirror Galvanometer Laser System 172

5.3.3. Influence of the Laser Pulse Frequency 176

5.4. Solar Cells Based on SiN_X Laser Ablation 178

5.4.1. Selection of Laser Processing Parameters 178

5.4.2. Comparison of the Different SiN_X Removal Methods 180

5.4.2.1. Photolithography 180

5.4.2.2. Laser Chemical Processing with Deionised Water 181

5.4.2.3. Scanning Head Mirror Galvanometer Laser System 182

5.4.3. Electrical Performance of Samples and Finished Solar Cells 183

5.5. Comparison of Solar Cells with Laser-Fired Contacts and SiN_X Laser Ablation 187

6. CONCLUSIONS AND OUTLOOK 190

7. REFERENCES 194

1. INTRODUCTION

1.1. Background and Motivation

According to the Intergovernmental Panel on Climate Change (IPCC) Fourth Assessment Report, warming of the world's climate system is unequivocal. The impacts of such effect should not be underestimated: increases in global average air and ocean temperatures, widespread melting of glacial and permanent ice, and rising global average sea levels pose great threat to the humankind and the world's ecosystems [1].

One of the drivers of this global warming effect is the anthropogenic emission of greenhouse gases (GHG), especially carbon dioxide (CO_2), methane (CH_4), and nitrous oxide (N_2O) [1]. The links between human-emitted GHG and the warming of the planet are becoming increasingly evident as scientific studies confirm that natural processes alone would not account for the extension of the observed phenomena [2], [3].

The anthropogenic emission of GHG continues to rise steeply since pre-industrial times, and has recently reached astonishing levels [4]. One of the crucial contributors to anthropogenic GHG emissions is the energy sector. Driven by global economy, income, and population growths, this sector has accounted for approximately 25.9 % of total anthropogenic GHG emissions in 2004 [1]. Additionally, recent and future improvements on the living standards in developing countries (e.g. life expectancy, economic stability, and income distribution), which account for the majority of the human population, will further increase the world's energy needs for the foreseeable future. Thus, in order to provide society with energy in a sustainable way, it is essential to develop technologies capable of

harnessing the potential of alternative and renewable energy sources. This will indeed be of the utmost importance for mitigation of and adaptation to a warming world.

An in-depth economic analysis of the risks and consequences associated with climate change and global warming, known as the Stern Review on the Economics of Climate Change, concluded that the benefits of strong, early action on climate change vastly outweighs the associated costs. Stern suggested that at least 1 % of the global gross domestic product (GDP) be invested annually in mitigation initiatives, including switching to lower-carbon technologies for electric energy production, in order to avoid the most drastic effects of climate change. If such investment is not made available to minimize the negative impacts of this threat, the future global GDP could be strongly affected by the negative effects of climate change, becoming up to 20 % lower than its corresponding potential [5].

Other important factors also press the international community to adapt its energy consumption patterns and switch to renewable energy technologies, such as: the sustained increase in global energy demand [6], depleting the reserves of exhaustible energy resources available to mankind and making security of supply a relevant concern; the unstable and volatile prices of fossil fuels, especially coal, natural gas, and petroleum, which account for an important part of the current energy sector [6], [7]; and the increase in air pollution levels due to extensive burning of fossil fuels, reducing overall quality of life due to pollution-related environmental damage and health problems, resulting in considerable external costs to fossil fuel-based energy generation [8 - 11]. These and other factors provide a strong drive towards research, development, and implementation of alternative and renewable energy technologies, now considered essential to the sustainable development of societies.

1.1.1. Photovoltaics as a Contributor to Sustainability

Amongst the available alternative energy options one can find different types of renewable energies, such as solar, wind, hydro, and biomass. In a broad sense,

renewable energy can be defined as “energy obtained from natural and persistent flows of energy occurring in the immediate environment” [12]. It has the advantage of relying on inexhaustible sources with low social, health, and environmental impacts during production, installation, operation, and decommissioning. On the one hand, in a long-term analysis, electricity prices from renewable energy technologies tend to decrease due to technological improvements, economies of scale, and experience gains in deployment and use, because there are no fuel expenses during operation, or the fuel can be obtained from natural processes happening in an acceptable timescale. On the other hand, electricity prices from non-renewable (exhaustible) sources have an upward trend, as fuel prospection and extraction costs increase and risk of scarcity pushes market prices to higher levels.

Photovoltaic (PV) solar energy is recognised as a promising renewable energy technology for the development of sustainable societies. PV technology is based on the direct conversion of solar energy into electric energy by means of the photovoltaic effect. The main component of a PV system is the solar cell, a semiconductor device with a p-n junction capable of harnessing the energy of photons. Several solar cells are connected in series or parallel to form a PV module. PV modules are then connected together into strings and arrays of PV systems [13]. PV technology only requires solar energy to produce electricity, a ubiquitous and virtually inexhaustible resource to the human scale. Hence, it qualifies very well as both mitigation and adaptation technology for tackling the threat of climate change, as well as for improving people’s quality of life.

When comparing PV with other electric energy production technologies, an extensive list of advantages and a range of benefits to society can be recognised, most notably, but not limited to:

- Low lifecycle environmental impact.
- No gas, liquid, or solid emissions during operation.
- No noise emission during operation.
- No moving parts, resulting in a very robust system, with low maintenance requirements.

- High durability, with verified system lifetimes exceeding 25 years of use for some technologies, such as crystalline silicon PV.
- Small area footprint, as systems can be integrated into existing buildings, such as on rooftops and façades.
- Modular technology, supporting increases in demand by installing additional PV modules to a system.
- No fuel consumption, therefore, no fuel costs during operation.
- Capable of compensating peak demand in daily peaking electricity grids (i.e. peak shaving), improving electricity demand management and potentially reducing related costs.
- Capable of producing electric energy in a distributed configuration, reducing transmission losses and potentially postponing investments in new transmission lines.
- Capable of increasing electricity diversity and security of supply, since it is based on solar radiation, an unregulated, unrestricted, free, reliable, and widely available resource.
- Versatile electricity source, suitable for remote and mobile applications, such as: rural communities, telecommunication systems, satellites and space vehicles, consumer devices, land, sea and air vehicles, amongst others.

In fact, there are only two appreciable disadvantages in PV electricity production that should be properly acknowledged. The first is inherent to the nature of the solar resource: it depends on the availability of sunlight to work. As such, it is an intermittent electric energy production technology, with an electricity production proportional to the availability of solar radiation. Therefore, the electricity output of a PV system will vary throughout the day, as well as according to the seasons and the local microclimate. Clouds and other natural (e.g. dust, fog) or anthropogenic (e.g. combustion fumes) aerosols also influence the amount of radiation reaching a PV system, but normally to a minor extent. Since major environmental conditions can be predicted and accounted, electric energy production from a PV system can generally be planned upfront. In fact, long-term solar resource availability can be projected with fairly good precision, therefore the long-term electric energy yield of PV systems can

be estimated with uncertainties below 10 % [14]. Additionally, the intermittent nature of the PV output can be mitigated by the employment of energy storage technologies (e.g. batteries, hydrogen, pumped-storage hydroelectricity, supercapacitors, flywheels etc.). Even without energy storage, studies have confirmed that, despite its low dispatchability, penetration levels on the grid above 5 % of PV installed capacity in areas with high daytime electricity demand profiles are not only possible, but can even be favourable to the stabilization of the local electricity grid [15 - 17].

The second disadvantage of PV electricity generation is transient and will eventually be overcome: in many countries, the price of PV electric energy (price/kWh) is still higher than that of current mainstream technologies. Therefore, PV systems are not yet fully competitive when compared to traditional means of electric energy production. Nevertheless, since the price of PV electricity is systematically being decreased, in a few years it will become competitive with, and eventually even cheaper than, mainstream electricity [18 - 20].

In the last decades, the PV sector has experienced the highest average annual growth rates amongst all renewable energy technologies, exceeding 30 % since 1998. Global cumulative installed capacity grew over this period from a few hundred MW to tens of GW, resulting in more than 69 GW by 2011 [21]. PV has become the third most important renewable energy source in the world in terms of installed capacity, behind hydro and wind. Global annual PV installations had a remarkable growth from 16.8 GW in 2010 to 29.7 GW in 2011, an increase of more than 76 % year over year [21]. This is significantly more than the capacity of the biggest hydroelectric power complex in the world, the Three Gorges Dam, with an installed capacity of 18.2 GW. According to NPD Solarbuzz market analysis, business activity in the PV sector resulted in annual revenues of approximately US$ 93 billion in 2011 [22]. In terms of technology market share, crystalline silicon solar cells and modules (both monocrystalline and multicrystalline) are the dominant technology since the beginning of terrestrial applications, with annual market shares of around 80 % to 90 %. For instance, in 2010 more than 85 % of the market was based on crystalline silicon [23]. The other 10 % to 20 % of the market was split amongst different thin film technologies, such as: amorphous silicon (a-Si) and

microcrystalline silicon (µc-Si), cadmium telluride (CdTe), chalcopyrite-based solar cells made of compounds containing Cu, In, Ga, S, and Se (referred to collectively as CIGS for simplicity), organic solar cells (OSC), and dye-sensitised solar cells (DSC).

The most promising thin film PV devices use elements like tellurium (CdTe) and indium (CIGS). Estimations on their availability indicate that tellurium and indium reserves are insufficient for large scale deployment of PV systems, especially when considering scenarios were solar electricity plays a major role in future energy supply [24], [25].

Differently, crystalline silicon PV is based on abundant elements and materials. Silicon represents approximately 27.7 % of the Earth's crust by weight, being the second most abundant element of the crust, surpassed only by oxygen [26]. Historically, silicon PV has also benefited from the scientific and technological knowledge, as well as the infrastructure, developed by the microelectronic industry, which also uses silicon as the prevailing constituent for the fabrication of integrated circuits [27]. Silicon PV technology is already mature both in respect to its scientific and industrial basis. Since several decades, c-Si solar cells and modules have been both evaluated in real working conditions and thoroughly tested for their long-term stability and reliability. Crystalline silicon's price-to-performance ratio, long-term stability, and reliable potential for additional cost reductions indicate that this technology will continue to be a leader in terrestrial PV applications for the foreseeable future. Therefore, in terms of long-term development of the technology, crystalline silicon is expected to dominate the market for the forthcoming decades [28].

The accelerated growth of the PV sector, combined with economies of scale and new technological implementations, is promoting consistent reductions in average selling prices and increasing the competitiveness of the technology on the global electricity market. For decades, the average selling price of PV modules have consistently declined by an average of approximately 18 % for every doubling of cumulative production volumes [18], [29]. This was only possible with strong investments in innovative research and development (R&D) initiatives, creating new

device structures and industrial processes capable of producing higher efficiency solar cells at lower costs.

Historically, the development of the PV sector has been based on three essential and complementary areas, which can be understood as the pillars for it's sustainable long-term growth: technology, supported by R&D at universities, research institutes, and companies; regulations and policies, supported by governments, as well as national and international associations; and access to financial resources, supported by governments, financial institutions, and national and international organizations.

In terms of regulation and policies, the reason for several years of sustained high growth rates and strong cost reductions in the PV sector is strongly related to governments' subsidies. This includes voluntary mechanisms, investment credits, quota systems, and fixed price systems. Amongst fixed price subsidies, feed-in tariffs are considered to be the most effective subsidy policy to date [30], [31]. Additionally, special programs aimed at rural electrification or similar off-grid applications also played an important role in incentivising the use of PV technology, especially in developing countries [32], [33]. These initiatives have promoted the demand and application of PV systems.

Between the four main types of PV applications – grid-connected distributed systems, grid-connected centralized systems, off-grid domestic systems, and off-grid non-domestic systems – the two grid-connected segments are responsible for more than 95 % of global capacity increase and for the accelerated industrial activity reported at present times [34]. However, systems are not evenly distributed around the globe. The remarkable growth of the PV sector is being led mostly by a small group of countries that made clear political commitments to support the technology, such as: Japan, Germany, Spain, the USA, Italy, France, Belgium, and most recently China, Taiwan, Australia, and India. This indicates that the implementation of PV is still somewhat constrained when compared to its overall potential.

In terms of market segmentation, after implementing aggressive legislation to promote the development of renewable energies, especially the Renewable Energy Sources Act (EEG), Germany gradually became the leading PV market globally. As a result of the EEG law, there was a strong demand for PV systems in the country. German companies and entrepreneurs embraced this opportunity, creating new businesses in the sector. During several years, Germany alone accounted for more than 50 % of the global annual PV market [21]. The country became a reference for PV, not only as a market, but especially as an industry, equipment, and technology hub. Many of these companies made strong investments in R&D activities, directly or through partnerships with universities and research institutes. This strategy was essential to assure the country a leading role in the PV sector.

Despite these efforts, the penetration of PV technology in the global electricity matrix is still rather limited. One of the crucial reasons for that is its higher price per kWh when compared to other electric energy production technologies. Although the combination of technology improvements, government subsidies, and strong increase in global PV manufacturing capacities has led to substantial decreases in cost, only in the last decades prices began to reflect this cost reduction.

During the boom period of the technology, PV markets were being partially led by demand rather than supply, meaning that prices were influenced by a strong willingness to buy, rather than by pure competition between industrial manufacturers. In 2005 the PV industry has experienced a shortage in high-purity silicon (polysilicon) stocks, as suppliers were unable to keep up with wafer and cell manufacturers in terms of capacity increase and market demand [35]. As a consequence, monocrystalline and multicrystalline solar cell manufacturers had to struggle over a limited amount of polysilicon material, raising its prices. As prices went up, the financial burden was carried throughout the production chain to the consumers, shadowing the cost reductions obtained by process improvements and economies of scale during production scale-up. In the last decade, however, high-purity silicon stock availability has been reassured after strong production expansions from major suppliers and new entrants, stabilizing polysilicon prices at acceptable levels.

After years of this demand-led market induced by strong government subsidies and incentives, the PV sector started to experience a significant increase in competition, caused by mainly two reasons. First, many governments reviewed and reduced their support policies for the technology due to budget restrictions or political pressure. Second, the PV sector experienced a significant increase in the amount of companies operating throughout the value chain. The combination of these two aspects resulted in a shift of the market condition from a demand-led structure to a supply-led structure. Consequently companies started to compete for a demand that, although growing consistently, did not grew at the same pace as the global production capacity being established. The resulting market imbalance created by this product overcapacity triggered a fierce competition between companies and led to a steep fall in average selling prices of raw materials, production equipments, PV modules, as well as services [18]. Many of these competitors did not resisted such a constrained environment and were acquired by competitors, left the PV sector, or even were forced to end their activities permanently. Nevertheless, such a fierce competitive environment has helped to bring down the prices of PV systems even further, contributing to the overall goal of spreading the use of technology throughout the planet. In fact, crystalline silicon module prices have fallen by approximately 80 % over the past four years. During the same period, high-purity polysilicon prices have fallen at an average annual rate of approximately 38 % [22].

In order to survive this so called “PV sector shakeout”, companies, universities and research institutions, and governments from around the world have turned to technology and R&D for solutions. In terms of its most important strategic goal for technology development and positive, practical impact on society, the overall objective of PV R&D is neither to develop a solar cell or PV system with the highest efficiency possible, nor to obtain the lowest cost solar cell possible. The goal is actually to obtain a PV system which allows for the lowest electric energy generation cost possible for the lifetime of the system (i.e. lowest price/kWh). Two milestones towards this goal would be: first, to reach equal or lower electricity prices than currently paid for by end consumers (i.e. consumer grid parity), and second, to reach equal or lower electricity costs than current mainstream technologies, such as hydro

or coal-fired power plants (i.e. generation grid parity). In order to reach this goal, improvements and innovations must be incorporated in all segments of the PV sector, from quartz mining, silicon extraction and purification, through crystalline silicon growth and wafer production, solar cell and module fabrication, until systems design and installation, maintenance, decommissioning and, finally, reuse, recycling and adequate disposal of exhausted goods.

PV R&D efforts have spurred new equipments, methods, and processes, designed to reduce costs in several segments of the sector's production chain. Considerable effort has been dedicated to the development of innovative solar cell concepts, with the main objectives of increasing solar cell efficiencies and reducing production costs [28], [36], [37].

The highest efficiency crystalline silicon solar cell to date was developed at the University of New South Wales (UNSW) and has 25.0 % efficiency under standard test conditions (STC: air mass 1.5 global solar spectrum (AM1.5G), one-sun irradiance of 1 kW/m^2, solar cell temperature of 25 ^{o}C, four point probe measurement setup to remove the effect of probe-to-cell contact resistance) [38]. This solar cell was developed with a complex and expensive structure, featuring selective emitters, passivated surfaces, and local back-surface fields. Several R&D projects aim to simplify the production processes used in this device, in order to adapt this high efficiency solar cell structure to large-scale production.

1.1.2. The Brazilian Potential for Photovoltaics

Brazil has recently been pointed out as a promising PV market [39 - 41] due to a combination of several favourable factors: excellent solar resource [42]; one of the world's largest high-quality quartz reserves (the raw material for the production of high-purity silicon) [43]; one of the world's most clean electricity matrix, with more than 85 % of its electricity produced by renewable energy technologies [44]; large territorial area, with a relevant part of the population living in remote locations and more than 1.4 million inhabitants still lacking access to electricity [45]; and a booming economy with strong electricity needs [44]. These aspects point out to a unique

opportunity to establish the country not only as a PV market, but also as a producer and developer of PV technology and equipments, with the establishment of local industries capable of fabricating the necessary materials and components for the PV sector.

In terms of the country's regulatory framework, the year of 2012 was a landmark for PV in Brazil. On April 2012, the Brazilian Electricity Regulatory Agency (ANEEL) approved two relevant regulations that promote the PV sector: a country-wide net-metering program, started on December 2012 [46], [47], and an 80 % discount in the transmission (TUST) and distribution (TUSD) networks usage fees for solar power plants of up to 30 MW connected before the end of 2017 [48]. Both initiatives are expected to spur strong and sustained growth of the country's PV cumulative installed capacity for the following years.

Additionally, Brazil has currently a pipeline of more than 2000 MW of grid-connected PV projects requesting or already with permission to be built. However, the majority of this pipeline is waiting for the announcement of solar public tenders by the government. Since no tenders have been confirmed yet, there is no certainty how many of these projects will be developed.

Because of the combination of such favourable characteristics and conditions, Brazil was qualified in 2012 for the first time as a so-called "key emerging market" or "tier 1 emerging market" by different PV market analysts [41], [49]. Therefore, in a moment of tight competition and diminishing incentives for PV markets worldwide, Brazil is standing out as a strategic option for companies of different segments of the PV value chain searching for new opportunities and looking to expand its business into new regions.

To reach its PV potential, Brazil will have to invest intellectual and financial resources in training, technology, R&D activities, and industrial infrastructure to attract national and international companies into strengthening the national PV sector. The government will also have a pivotal role in promoting the establishment of the PV sector by creating or harmonizing policies and regulations, as well as

defining adequate short, medium, and long-term targets for the technology. Without the combined positive impact of such initiatives, both the development of a local PV market and the establishment of PV companies, industries, and investment groups will hardly be possible.

The only Brazilian research group reported in the literature to have employed laser processing technologies for crystalline silicon solar cell fabrication is the Solar Energy Technological Nucleus (NT-Solar), located at the Pontifical Catholic University of Rio Grande do Sul (PUCRS), in Porto Alegre, Brazil. The researchers have studied and developed techniques for the formation of selective emitters by laser processing with phosphorus impurities, yet so far no finished solar cells have been fabricated with this method [50].

Therefore, aligned with international PV R&D goals and considering the specifics of the aforementioned Brazilian scenario, the purpose of this thesis was to develop and implement laser processing methods for crystalline silicon solar cell fabrication. Two approaches were evaluated and discussed, with the general purpose of increasing solar cell efficiencies and promoting solar cell fabrication processes based on laser processing methods transferrable to industrial environments.

1.2. Thesis Aims and Objectives

The general objective of this work was to develop, analyse, and compare crystalline silicon solar cells processed by different laser methods. Two different laser processing techniques were studied, implemented, optimized, and evaluated: the laser-fired contacts (LFC) method, used to produce localized contacts through a passivation layer located at the rear surface of the solar cell, and the laser ablation method, used to locally remove selected areas of a silicon nitride layer located at the front side of the solar cell.

On the laser-fired contact approach, laser processing was performed at the rear surface of the solar cell, keeping the front surface of the device with a standard

industrial design, based on screen-printed metal contacts. The aim of the research was to develop and optimize the laser process in order to produce solar cells with efficiencies comparable or superior to solar cells processed under similar conditions using the standard industrial rear design, based on screen-printed rear metal contacts.

On the silicon nitride laser ablation approach, laser processing was performed at the front surface of the solar cell, keeping the rear surface of the device with a standard industrial design, based on screen-printed metal contacts. The aim of the research was to develop and optimize a laser ablation process to produce solar cells with Ni/Ag front contacts deposited by selective electrochemical deposition. Samples processed by the ablation method were compared with others processed by photolithography, in order to evaluate the influence of the laser step on device performance.

The specific objectives of this work can be summarized as follows:

1. Experimentally optimize laser processing parameters relevant to the LFC laser processing method: pumping lamp current, q-switch frequency, and distance between laser-fired rear contacts.

2. Develop, characterize, and analyse crystalline silicon solar cells with LFC and screen-printed front surface metallization. Evaluate the influence of the rear side evaporated aluminium layer thickness on device performance. Compare devices with and without rear surface passivation by thermally grown silicon oxide. Compare the influence on device performance of two approaches to remove the phosphorus silicate glass on solar cells with SiO_2 rear surface passivation.

3. Compare LFC-processed solar cells with standard industrial screen-printed Al-BSF solar cells produced under similar conditions.

4. Optimize and analyse an annealing process for LFC solar cells. Optimize relevant process parameters, such as: annealing temperature and conveyor belt speed.

5. Develop and implement a SiN_X laser ablation process employing the LCP method using DI H_2O as liquid medium.

6. Develop and implement a SiN_X laser ablation process employing the SCA method.

7. Characterize and compare the influence of LCP and SCA laser ablation processes with reference samples having the SiN_X openings performed by photolithography.

8. Develop, characterize, and analyse crystalline silicon solar cells with front metal contacts incorporating SiN_X laser ablation and Ni/Ag selective electrochemical deposition.

The innovation of this doctoral thesis in regards to the laser-fired contacts method was to obtain a solar cell fabrication process incorporating rear passivation and with less processing steps, adapted to the needs of an industrial environment. This was done by developing a fabrication sequence for solar cells with SiO_2 rear passivation using only one high-temperature thermal oxidation step for the formation of the SiO_2 layer. The SiO_2 layer served simultaneously as rear surface diffusion barrier and passivation. Apart from additional thermal oxidation step, the process developed also eliminates auxiliary steps that would be required in case a second thermal oxidation was employed, such as photoresist deposition, acid etching, and chemical cleaning.

The innovation of this doctoral thesis in regards to the silicon nitride laser ablation method was to develop and optimize the laser processing parameters for a laser ablation method based on two different laser techniques: wet laser processing

with laser chemical processing using deionised water as liquid medium, and dry laser processing with a scanning head mirror galvanometer laser system.

By separating the front and rear laser processes and coupling them with industrial screen-printing solar cell designs, it was possible to independently evaluate the effect of each laser technique on solar cell performance.

This thesis was developed through an international research collaboration with the Laser Chemical Processing Laboratory of the Novel Processes Department of the *Fraunhofer Institut für Solare Energiesysteme*, in Freiburg im Breisgau, Germany.

2. CRYSTALLINE SILICON SOLAR CELLS

This chapter provides a brief description of the working principles of solar cells, taking into account relevant parameters and properties that influence the performance of such devices. Afterwards, the main parameters of the characterization methods employed throughout this work for analysing samples and finished solar cells are presented. In sequence, the current industrial standard PV solar cell structure is described and its main limiting factors are discussed. Lastly, a selection of laboratory-scale solar cell structures designed to overcome the limitations of the industrial standard device is presented. The benefits and challenges of these alternatives are pointed out. Lastly, the case for the implementation of laser technologies to improve the performance and reduce costs of these alternatives is presented.

2.1. Principles of Solar Cells

Solar cells are devices designed to convert solar energy (i.e. electromagnetic radiation) into electric energy by means of the physical process known as the photovoltaic effect. The phenomenon was first elucidated in 1839 by Alexandre-Edmond Becquerel, during experimentation with an electrochemical system exposed to electromagnetic radiation of different wavelengths [51]. The first modern concept of a solar cell, which served as the basis for the development of current PV technology, was devised and fabricated by Chapin, Fuller, and Pearson in 1954 at Bell Telephone Laboratories, New Jersey, USA [52].

2.1.1. Semiconductors, Doping, and p-n Junction Diodes

A modern solar cell can be described as a large-area, semiconductor-based, p-n junction diode optimized to convert solar radiation (i.e. photons) into electric energy. Although it is possible to utilize a series of different materials to fabricate a solar cell, this thesis focuses on crystalline silicon solar cells, because crystalline silicon technology represents the vast majority of the PV market, industry, and R&D efforts worldwide since the beginning of terrestrial PV applications.

Silicon has several of the properties and characteristics that make it a good candidate for photovoltaic applications. It is a stable, abundant, and relatively inexpensive material, making it appropriate for the fabrication of devices with large active areas, such as solar cells and modules. It is a chemical element of the group 14 and a semiconductor, with an intrinsic energy bandgap (E_g) of approximately 1.12 eV at 300 K, which is a good match in terms of photon absorption from the solar spectrum. Additionally, silicon can be easily doped with group 13 (for p-doping) or group 15 (for n-doping) chemical elements, which is essential to tune its electrical properties and behaviour to effectively and efficiently convert photons into electric energy.

The controlled and well-engineered addition of impurities, known as doping agents, is capable of significantly increasing the performance of a solar cell. The presence of doping elements in different layers of the semiconductor alters the electrical properties of the device, by increasing the concentration of free charge carriers in the material: electrons in n-type semiconductors and holes in p-type semiconductors. In silicon solar cell processing, the most common doping elements employed are phosphorus (donor impurity) for n-type doping and boron or aluminium (acceptor impurities) for p-type doping. Generally, intrinsic silicon is initially doped with phosphorus or boron to respectively form an n-type or p-type semiconductor that will serve as substrate or base to the fabrication of a silicon solar cell. Afterwards, a layer with higher doping concentration is created by diffusing phosphorus, boron, or aluminium into the silicon substrate. This compensates the base doping of the substrate and gives rise to a p-n or an n-p junction.

A p-n junction is an asymmetrical electronic structure, which possesses a higher concentration of electrons on one side (n-type) and a higher concentration of holes on the other side (p-type), for example by the incorporation of phosphorus and boron impurities, respectively. This results in the formation of a region depleted of electrons and holes (i.e. depletion region or space charge region), with fixed charges composed of phosphorus cations on the n-type interface and boron anions on the p-type interface. The space charge region gives rise to an internal potential difference between the p and n sides of the structure, resulting in an internal electric field from the n-type (positive fixed charges) to the p-type (negative fixed charges). The electric field in the p-n junction is capable of separating free charge carriers (electrons and holes) by directing those to different regions of the semiconductor. This is also the case for high-low junctions, such as n^+n and p^+p. These properties and behaviours are an essential aspect of the physics of a solar cell.

Figure 2.1(a) illustrates the cross-section of a simple silicon solar cell, highlighting the fixed ionic charges of space charge region of the p-n junction (grey area) and Figure 2.1(b) illustrates the theoretical concepts of the device behaviour in equilibrium conditions. When electrons and holes are generated by the absorption of photons (i.e. photogeneration) in a semiconductor containing a p-n junction, they may be separated by the built-in electric field in the space charge region. Minority charge carriers are effectively separated by the electric field only if they are generated nearby, or if carriers have lifetimes long enough to allow its diffusion to the vicinity of the space charge region prior to recombination. The accumulated charge difference between the two sides of the p-n junction gives rise to a potential difference. By connecting the different sides of the device to an external circuit, this potential difference can be effectively harnessed to produce useful work [53]. A thorough mathematical description of the physics of p-n junctions and solar cells can be found in references [54 - 57].

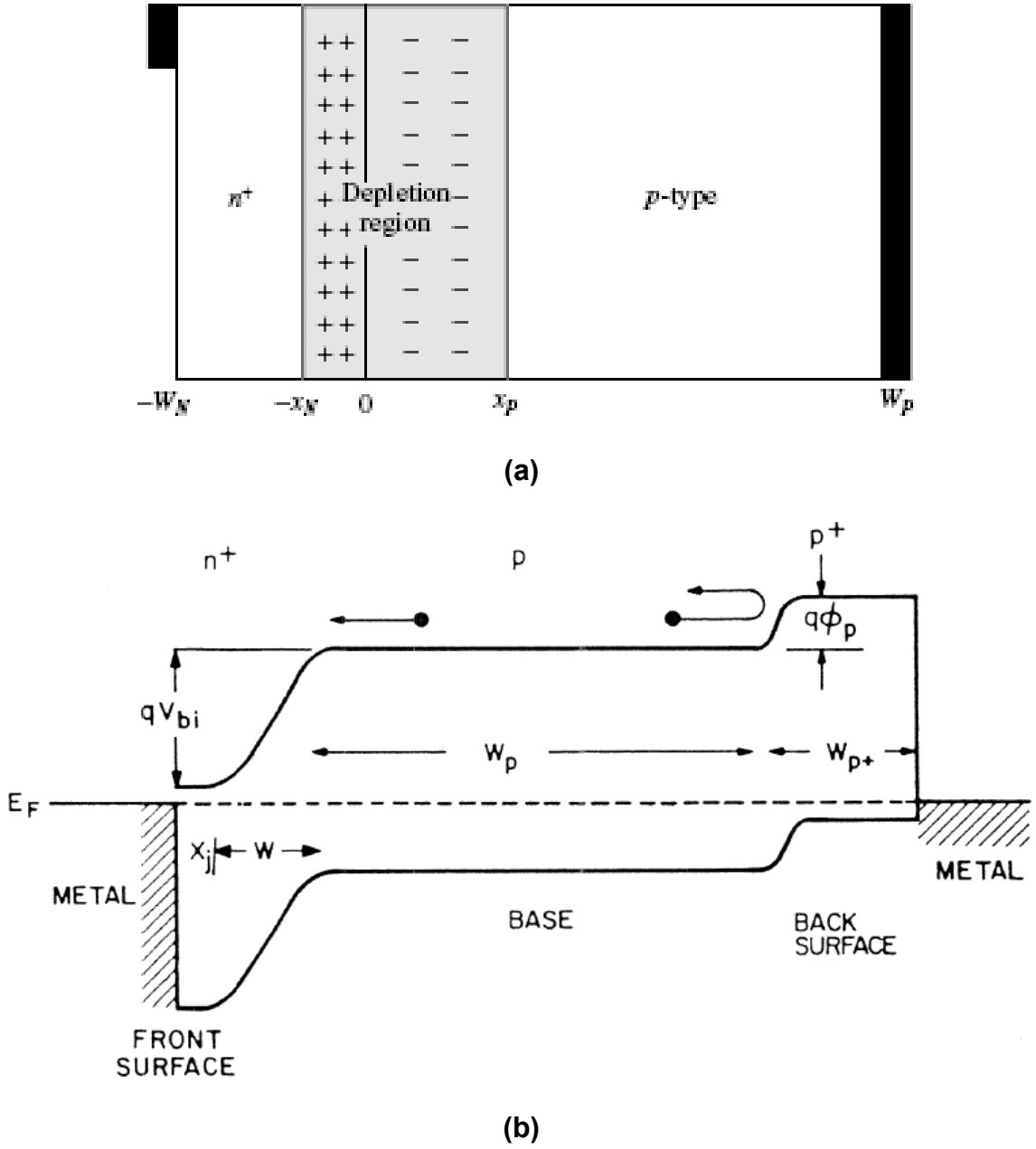

Figure 2.1. (a): cross-section of a conceptual p-n junction solar cell [54]. (b): respective band diagrams of the metal contacts and different doped semiconductor layers comprising the solar cell presented on the top of the figure [57].

2.1.2. Efficiency Limits and Loss Mechanisms

A comprehensive evaluation of the efficiency limits of a single-junction crystalline silicon solar cell was performed and discussed by several researchers. These analyses serve as cornerstones for the design and fabrication of practical devices. Amongst one the most important theoretical calculations is the seminal work

performed by Schockley and Queisser in 1961, which employed the detailed balance limit to derive the maximum thermodynamic efficiency of 30 % for an ideal p-n junction solar cell [58]. An updated calculation using the same method but considering an AM1.5G solar spectrum suggested a maximum thermodynamic efficiency of 33.2 % for a perfect absorber with an E_g of 1.15 eV and 29.8 % for an 80 μm thick finite absorber made of silicon (E_g = 1.12 eV) incorporating losses caused by Auger recombination [59]. A new version of the calculation was performed, once another group of researchers elucidated that the Auger parameterization used at previous recombination calculations was inappropriate for the doping concentrations used in solar cells. After reviewing and updating the parameters of theoretical model, they proposed a more accurate maximum efficiency limit of 29.05 % for a 90 μm thick single-junction silicon solar cell incorporating Auger recombination losses [60].

The performance of a solar cell is never as high as theoretical calculations would predict, because practical (i.e. non-ideal) devices are influenced by a complex sum of losses and imperfections of the materials that compose them. Consequently, the study of loss mechanisms of solar cells is crucial to understanding the differences between the ideal and practical behaviours of PV devices.

There are basically two loss mechanisms influencing solar cell performance. Optical losses result from a combination of reflection, transmission, and shadowing effects. They reduce the amount of solar radiation (i.e. quantity of photons) that reach or may be absorbed at the active area of the solar cell. As such, they strongly influence the electric current that the photovoltaic device can generate. Electrical losses can be further divided into ohmic losses and recombination losses. Ohmic losses refer to the electrical resistance to current flow through regions of the device. These losses occur mainly on regions within the semiconductor material with low electrical conductivity, on regions forming the contacts of the device, such as fingers, busbars, and rear contacts, as well as around imperfect metal-semiconductor contacts. Recombination losses refer to the recombination of electrons and holes before they can have their energy harvested. These losses occur mainly on the front and rear surfaces of the device, on highly doped semiconductor regions (e.g.

emitter), and on internal regions of the semiconductor material possessing unwanted impurities and crystalline defects. Electrical losses have negative effects both on the current and on the voltage of a solar cell [55].

When solar energy reaches a semiconductor material, three basic physical phenomena may occur. First, photons may be reflected at the surface of the device, without penetrating it. Reflected photons cannot have their energy harnessed and, thus, are completely lost. In one common approach to reduce losses from reflection in silicon solar cells, the surface of the semiconductor is textured with microscopic pyramidal structures, increasing the number of reflections at the semiconductor surface and, consequently, the probability of absorption. Another common technique is to deposit an antireflection layer onto the surface of the device to better match the refractive indexes of air and the silicon substrate, drastically reducing reflection at its surface. The antireflection coating (ARC) is usually made of a single or double-layer of TiO_2, SiO_2, SiO_X (i.e. non-stoichiometric silicon oxide), SiN_X (i.e. non-stoichiometric silicon nitride), MgF_2/ZnS, or other similar material systems, with an adequate refractive index, density and thickness to reduce reflection on the region of interest of the solar spectrum.

Second, photons reaching the solar cell may be transmitted through the device, without interaction. This occurs when the energy of incoming photons is smaller than the E_g of the semiconductor and, thus, photons are unable to excite electrons of the device from the valence band to the conduction band. These photons are commonly not converted to electric energy by a solar cell. They are usually absorbed in other regions of the device, such as the rear side metal layer, being converted into thermal energy and increasing the operating temperature of the solar cell. Transmission losses may also happen for photons with energies higher than the semiconductor E_g, if the absorption coefficient ($\alpha(\lambda)$) of the semiconductor is low and there is only a thin layer of material available to absorb incoming photons. To reduce such losses, radiation trapping mechanisms are usually employed to increase the number of passes of the light rays inside the material. This increases the optical path length of the radiation in the active layer of the solar cell. Examples of radiation trapping concepts usually applied in solar cell design include front

surface texturing and rear surface reflectors. Such mechanisms improve the probability of effective photon absorption and simultaneously reduce transmission losses significantly.

Third, photons with energy equal or higher than the E_g of the semiconductor material may be absorbed by it. The energy transferred during absorption of a photon promotes one electron from the valence band to the conduction band of the semiconductor, leaving behind a vacant space on the valence band, denominated “hole”. This phenomenon gives rise to an electron-hole pair, and is commonly referred to as photogenation of charge carriers. Both the excited electron occupying an electronic orbital in the conduction band and the hole left on the electronic orbital of the valance band contribute to increase the conduction of the semiconductor and play a major role in the extraction of electric power from the solar cell.

In summary, for an efficient photovoltaic energy conversion, three important requisites must be fulfilled: first, there must be an adequate absorption of the incoming radiation, generating a considerable quantity of electron-hole pairs; second, the mechanism of charge separation must be fast and effective, in order to avoid recombination of electron-hole pairs before they are collected; third, the separated charge carriers must be transported to an external circuit with minimal losses, so that their energy can be effectively transformed into useful work.

2.2. Characterization of Samples and Solar Cells

The application of characterization techniques on samples and finished solar cells is essential to the development and optimization of processing methods employed throughout this work. The characterization procedures used in this thesis were selected according to availability at the research facilities where work was performed, as well as the type, quality, and reliability of the data that could be obtained from them. A short description of the most important characterization methods employed throughout this work, alongside with their main working principles, is provided below.

2.2.1. Four Point Probe Resistivity

Four point probe resistivity measurements were performed to evaluate the sheet resistance ($R_{\square}$) of silicon wafers after $POCl_3$ phosphorus diffusion in a quartz tube furnace. This is an indirect approach to control the homogeneity of the diffusion process, as well as to estimate the phosphorus doping level incorporated onto the silicon substrates. The method uses a set of four metallic probes evenly spaced, which are positioned onto the region of interest of the silicon surface. An electric current is passed through the two outer probes and the potential difference (i.e. voltage) is measured through the two inner probes. The applied current (I) and resulting voltage (V) are then used to determine the sample's $R_{\square}$ according to Equation 2.1 [61]:

$$R_{\square} = \frac{\pi}{\ln(2)} \frac{V}{I} = 4.53 \frac{V}{I} \tag{2.1}$$

In order to increase reliability on the results, the $R_{\square}$ of each processed silicon wafer was determined by calculating the average of a minimum of 13 four point probe measurements performed in different positions evenly spaced throughout the surface of the substrate. By comparing the results at different points of the wafer surface, it was also possible to evaluate the homogeneity of the phosphorus diffusion process over the silicon wafer surface.

2.2.2. Dark and Illuminated Current-Voltage Curves

The electrical parameters measured under STC define the overall performance of solar cells. Consequently, all solar cells produced in this work had their electric current and voltage (I-V) curves measured. By measuring the I-V curve of a solar cell while applying an external bias voltage to it (from reverse to forward bias), it is possible to obtain valuable information regarding its electrical behaviour. If the solar cell is kept in the dark, the resulting curve will be the typical diode I-V curve, referred to as dark I-V curve. The behaviour is mathematically described by Equation 2.2 [13]:

$$I = I_0\left[\exp\left(\frac{qV}{kT}\right)-1\right] \tag{2.2}$$

where I is the electric current measured in dark, I_0 is the dark saturation current (the diode leakage current in the dark, measured under reverse bias), q is the electron charge, V is the applied voltage, k is Boltzmann's constant and T is the temperature in kelvin.

When the cell is illuminated, the I-V curve is shifted due to the photogenerated current, or photocurrent (I_L). A new term is included in the equation to account for the observed phenomenon, as follows [13]:

$$I = I_0\left[\exp\left(\frac{qV}{kT}\right)-1\right]-I_L \tag{2.3}$$

From Equation 2.3, it is possible to obtain the main electrical parameters of a solar cell. A list of such parameters, as well as their definition and mathematical description, is presented below:

1. **Short-circuit current (I_{SC}):** the current measured under illumination when no load is present (at, ideally, zero series resistance and infinite shunt resistance). From Equation 2.3 and considering these ideal conditions one arrives at:

$$I_{SC} = I_L \tag{2.4}$$

When I_{SC} is divided by the solar cell area, the short-circuit current density (J_{SC}) is obtained, a necessary parameter for comparison of the performance of different solar cells. The resulting curves are then called J-V curves.

2. **Open-circuit voltage (V_{OC}):** the voltage obtained under illumination when a load of infinite resistance (or very high resistance in practical terms) is connected to the photovoltaic device. Under such conditions no current is measured between the terminals of the solar cell (I = 0). Based on Equation 2.3, the following equation is obtained:

$$V_{OC} = \frac{kT}{q} \ln\left[\left(\frac{I_L}{I_0}\right) + 1\right] \tag{2.5}$$

3. **Maximum power point (MPP):** the point on the I-V curve where the product of the voltage and current values is its maximum. This corresponds to the optimal operating point of the device and is the maximum electric power (P_{MMP}):

$$P_{MMP} = I_{MMP} V_{MMP} \tag{2.6}$$

4. **Fill factor (FF):** the ratio of the maximum electric power to the maximum theoretical electric power of the photovoltaic cell. The FF can be defined mathematically as:

$$FF = \frac{I_{MMP} V_{MMP}}{I_{SC} V_{OC}} \tag{2.7}$$

5. **Photovoltaic conversion efficiency (η):** is the ratio between the maximum electric power and the total incident solar irradiance (G) reaching the device area (A). It indicates the effectiveness of the device in terms of converting the incoming solar energy into electric energy and can be defined mathematically as:

$$\eta(\%) = \frac{I_{MMP} V_{MMP}}{AG} 100\% = \frac{I_{SC} V_{OC} FF}{AG} 100\% \tag{2.8}$$

6. **Series resistance (R_S):** represents the sum of series resistances of the photovoltaic device. These include: the resistance of the semiconductor substrate; the resistance at the highly doped semiconductor regions, such as emitter and back-surface field; the contact resistance at the metal-semiconductor junctions on the front and rear of the solar cell; the resistance of the metallic fingers, busbars, and metal layers used as front and rear electrodes to collect the electric current; and the spreading resistance arising from lateral current flows due to the spacing of metallic electrodes. Since high resistance values mainly result in current losses, solar cells with high performance have considerably low R_S values.

7. **Shunt or parallel resistance (R_{SH}):** defined as the resistance resulting from current leakages through the device. It represents crystal defects, non-uniform doping of the emitter, grain boundary effects, and pinholes which result in current loss through shunts in the p-n junction. Since low shunt resistance values result in current leakage and voltage losses, solar cells with high performance have considerably high R_{SH} values.

A schematic representation of a typical I-V characteristic, in dark and under illumination, is presented in Figure 2.2, showing each of the parameters described above. The FF is calculated from the two dashed rectangles in the fourth-quadrant.

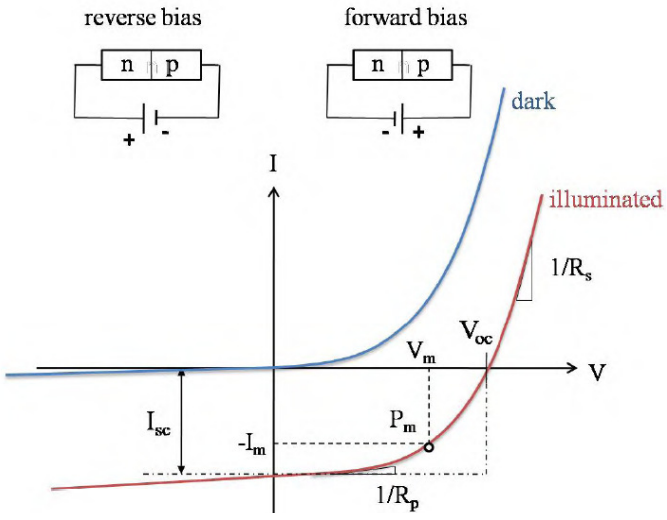

Figure 2.2. Solar cell I-V characteristics in dark and under illumination and relevant electrical parameters obtained from such measurements [62].

2.2.3. Spectral Response and Quantum Efficiency

The spectral response of a solar cell provides information on how photons of different wavelengths (i.e. energies) contribute to the short-circuit current of the device. It is the ratio of the current generated by the solar cell (i.e. measured by an external circuit) compared to the power incident on the device (known from the spectral composition and irradiance of the source used to illuminate the sample). Photons with higher energies (i.e. shorter wavelengths) have a higher probability of being absorbed near the front surface of the solar cell, whereas photons with lower energies (i.e. longer wavelengths) have a higher probability of being absorbed near the rear surface of the solar cell. Therefore, analysing the spectral response provides indirect information on which region of the device is responsible for current gains or losses when compared with other device structures or designs. This allows researchers to evaluate and compare the benefits or drawbacks of different solar cell design parameters, such as: p-n junction depth, front and rear side passivation, antireflection coatings, texturing methods, rear surface reflectors, amongst others.

Spectral response is usually converted to quantum efficiency data in solar cell characterization. External quantum efficiency is similar to spectral response, but evaluates the number of charge carriers collected from the solar cell compared to the number of photons incident on the device. Results are usually normalized to a 0 to 1 or 0 % to 100 % scale, with the lower end indicating poor collection of electrons on the external circuit for photons of a given wavelength and the upper end indicating that each photon incident on the device resulted in the collection of one electron on the external circuit. The conversion of spectral response to external quantum efficiency can be performed as described in Equation 2.9 [13]:

$$SR(\lambda) = \frac{I_{SC}}{G(\lambda)} = \frac{qn_e}{\frac{hc}{\lambda} n_{ph}} = \frac{q\lambda}{hc} EQE(\lambda) \tag{2.9}$$

where SR(λ) is the wavelength-dependent spectral response, G(λ) is the incident irradiance of each wavelength, n_e is the electron flux, h is Planck's constant, n_{ph} is

the wavelength-dependent photon flux, and EQE(λ) is the wavelength-dependent external quantum efficiency.

External quantum efficiency can also be differentiated from internal quantum efficiency (IQE). On the one hand, EQE measurements consider the collection of electrons compared to the total amount of incident photons, thus including in the calculation reflected photons (i.e. without discounting solar cell reflection losses). On the other hand, IQE measurements compare the collection of electrons only to the amount of photons that can be effectively absorbed by the solar cell, thus excluding the losses of photons reflected by the device (i.e. discounting solar cell reflection losses). Therefore, it follows logically that, for any given wavelength, the EQE of a solar cell will be always smaller than, or in the best case (i.e. no reflection losses) equal to, its respective IQE. Mathematically, the relation between EQE and IQE is described in Equation 2.10:

$$EQE(\lambda) = (1 - F_S)(1 - \rho)IQE(\lambda) \tag{2.10}$$

where F_S is the shadowing factor (i.e. shadow caused by the solar cell front metal grid).

2.2.4. Suns-Voc

Suns-Voc is an electrical characterization method which employs variable irradiance on the sample to measure the voltage output of the device under open-circuit conditions [63]. The irradiance is monitored by using a calibrated reference solar cell and correlating its generated current to the amount of radiation reaching the sample. The method uses a stroboscopic flash lamp with a slow decay, resulting in a quick, simple, and non-destructive characterization procedure. It is usually performed under a controlled temperature of around 25 ºC, to avoid temperature-related uncertainties.

Since the focus of Suns-Voc is to measure the performance of the sample under open-circuit conditions, this technique avoids the effects of series resistances

from both the front and rear contacts of the device. This means that characterization can be performed on any silicon wafer incorporating a p-n junction, even if the device does not have metal contacts on the front side. Nevertheless, since it is necessary to properly contact the sample with the measurement stand, rear contacts are generally required to avoid inconsistencies during measurements.

As the current generated by a silicon solar cell is proportional to the light intensity reaching the device, Suns-Voc measurement data can be transformed into a pseudo J-V curve. This is done by using the sample's measured voltage and including a pseudo short-circuit current density (pJ_{SC}) defined as a fixed parameter. In this work, pJ_{SC} was set to 35.0 mA/cm^2.

In summary, the useful parameters that can be directly obtained or indirectly derived from Suns-Voc measurement include: open-circuit voltage, pseudo current density-voltage curve (pJ-V), pseudo fill factor (pFF), pseudo efficiency ($p\eta$), and estimated shunt resistance.

Throughout this work, the Suns-Voc technique was employed on the evaluation and comparison of samples incorporating SiN_X laser ablation, as well as reference samples with the front SiN_X opened by photolithography (PL) followed by chemical etching. Samples were measured before and after laser ablation or photolithography, as well as before and after the electrochemical deposition of the front surface contacts made of Ni and Ag.

2.2.5. Light Beam Induced Current

In the light beam induced current (LBIC) technique a beam of quasi-monochromatic light, produced by a laser source, is scanned over a sample placed under short-circuit configuration. By measuring the short-circuit currents induced by the localized radiation source, maps of minority carrier lifetime (τ), EQE, and reflectance (ρ) of the whole active area of the device under investigation can be determined. By combining both data it is possible to calculate the respective IQE map of the sample. Thus, when applied to the study of solar cells and photovoltaic

devices, the light beam induced current technique provides two-dimensional images representing the different degrees of quantum efficiency observed on samples. The LBIC technique can also be employed to determine the minority carrier diffusion length (L), a parameter which depends on factors such as impurity content and crystalline defects of the substrate, and which is directly related to the minority carrier lifetime and the minority carrier diffusivity (D).

A solar cell is a large area device, prone to localized variations both in composition and in structure. Consequently, the electrical performance of a solar cell will vary according to the position where measurements are made. A region of poor performance will have a disproportionate negative effect on the performance of the whole solar cell, leading to a strong reduction in overall efficiency. LBIC information can be used to identify and locate shunts and other defect centres that are responsible for degradation of solar cell efficiencies and minority carrier lifetimes. This information can be used to further improve fabrication methods and solar cell designs, in an attempt to reduce shunts and localized defect centres.

The LBIC method is not only used to map the homogeneity and quality of the active area of the fabricated solar cell in two dimensions. Since it is possible to perform quantum efficiency measurements using different wavelengths with the LBIC method, one can map samples also by considering different radiation penetration depths. When using shorter wavelengths, regions closer to the front side of the device can be mapped and when longer wavelengths are employed, regions closer to the rear side of the sample are highlighted.

Throughout this work, the LBIC technique was used in the characterization and analysis of laser-fired contact and screen-printed solar cells processed at NT-Solar. Measurements were performed in selected samples and results were later compared and correlated to solar cell performance.

2.3. Solar Cell Concepts and Structures

Solar cell fabrication represents a relevant fraction of the total cost of a photovoltaic module, corresponding to approximately 25 % of the cost of a finished crystalline silicon module produced in 2010 [64]. It has a considerable impact on the overall cost of PV electricity, since solar cell fabrication strongly influences the efficiencies of both photovoltaic cells and modules. Historical data shows that, between 1980 and 2001, improvements in solar cell and module efficiencies were responsible for approximately 30 % of the cost reduction of terrestrial PV devices [65]. This indicates the relevance of solar cell R&D in reducing costs and advancing the widespread adoption of PV technology.

Solar cell and module efficiencies will depend on the quality of the materials used for their production (e.g. type of silicon substrate, purity of chemicals etc.). Yet, they are also significantly determined by the processes and technologies employed during fabrication [54]. Processes, methods and technologies are chosen according to the structure of the solar cell to be produced. In this respect, expensive processing methods will only be considered for industrial implementation if they can produce high-efficiency devices, thus compensating for the added manufacturing costs.

The main goal of silicon solar cell R&D is to reduce the price of PV electricity. To reach this goal different approaches have been followed, three of them being of particular importance: (i) improving the efficiency of industrial solar cells by applying high-efficiency concepts to the devices, such as improved radiation trapping, selective emitters, surface passivation, fine-line printing, amongst others, but avoiding significant increases in fabrication costs; (ii) using thinner silicon wafers (thickness fairly below 200 μm), minimizing the amount of high-purity silicon required to fabricate each solar cell and, therefore, reducing material costs; (iii) increasing the nominal production capacity of existing facilities by implementing high-yield, high-throughput processes, combined with automation, allowing processing rates of more than 1000 wafers per hour, hence better utilizing fixed costs through economies of scale [65].

One of the technical challenges of employing thinner silicon wafers is that thinner substrates are more fragile and prone to breakage during processing and handling. This translates into a reduction in production yield, with negative impacts on overall cost per unit. Additionally, below 200 μm, the thickness of typical CZ-Si or mc-Si substrates may become smaller than the minority carrier diffusion length (L). Hence, more minority carriers are able to reach the surfaces of the wafer, where recombination probability is high. Thus, although shifting to thinner wafers would imply in less silicon utilization, if no other aspects of the device are changed, this would also result in lower efficiencies due to increased surface recombination losses. To overcome this problem, industrial efforts have turned to the implementation of passivation methods capable of reducing minority carrier recombination at the surfaces of solar cells.

Another idea under investigation is the use of automatic and low-stress handling methods. This concept dramatically reduces solar cell fabrication breakage rates and has the potential to increase both the overall yield and the throughput of thinner solar cells. Laser processing methods applied to crystalline silicon solar cells are compatible with both the shift to thinner substrates and the increase of manufacturing automation.

In the following subsections, a selection of solar cell structures relevant to this work is described, including a brief comparison of their advantages and limitations, the potential of large-scale industrial implementation, as well as technical aspects regarding their performances.

2.3.1. Aluminium Back-Surface Field Solar Cell

The standard method for reducing the rear surface recombination rate is to fire on a conveyor belt furnace an aluminium screen-printed paste, approximately 20 μm thick, deposited on the rear of the device. This technique is widely used by the PV industry in the fabrication of solar cells. It is the most common approach for the formation of the rear surface contacts, when associated with screen-printed Ag rear contact strips that allow easy soldering and interconnecting of solar cells. The high-

temperature process (T > 600 ºC) allows the diffusion of aluminium atoms into the silicon substrate's rear surface, giving rise to a high-low junction (p^+p), frequently referred to as back-surface field (BSF). Since the doping atoms forming the BSF are of aluminium, the abbreviation Al-BSF is commonly employed. The electric field observed in its space charge region is responsible for repelling electrons close to the rear of the device, reducing the rate of recombination at the rear surface, where otherwise high recombination would prevail. Consequently, more charge carriers can be collected at the device's terminals, directly improving its electrical performance. A schematic representation of a standard industrial Al-BSF solar cell is shown in Figure 2.3.

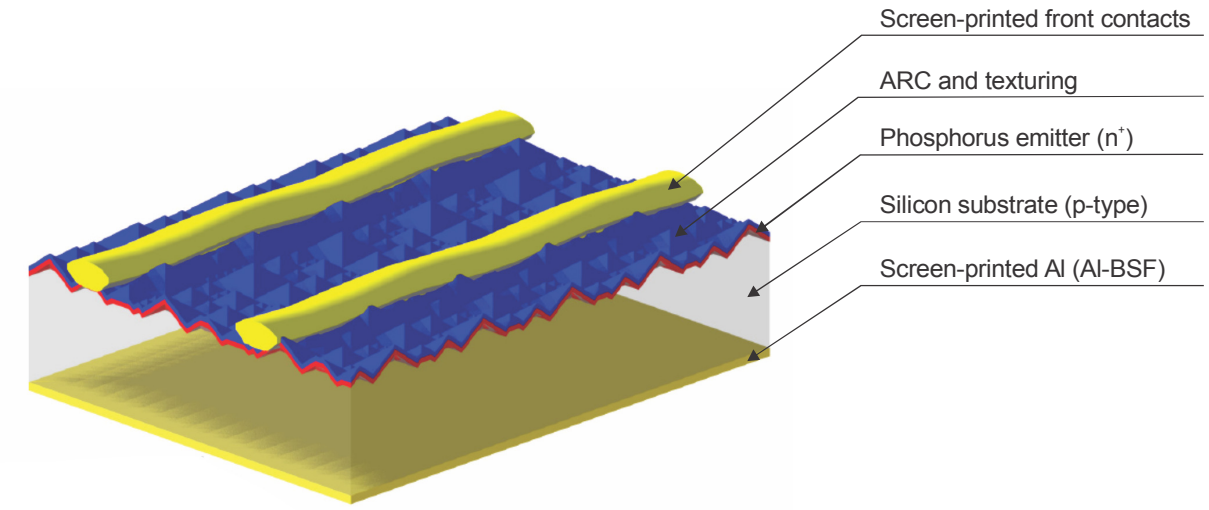

Figure 2.3. Standard industrial Al-BSF solar cell. Adapted from [66].

Unfortunately, there are a number of drawbacks and limitations to this approach. First, conveyor belt furnace firing is a high-temperature process, which may reduce minority charge carrier lifetimes, degrading the electrical properties of the solar cell. Second, the fired aluminium paste has a relatively low internal reflectance of approximately 70 %, which results in less electron-hole pair generation, since a fraction of the radiation will be transmitted thought the device. Consequently, Al-BSF solar cells have limited performances, reaching efficiencies below 20 % in large-scale production. Third, this method is incompatible with the aim of reducing wafer thicknesses: when applied to substrates with thicknesses lower than about 200 µm, the wafers may suffer from bowing during the cooling interval of the metallization firing step. This bowing is caused mainly by the different thermal

expansion coefficients of silicon and aluminium. This aspect becomes increasingly relevant when thinner silicon substrates are used. Solar cells that suffer from bowing are structurally fragile and have an increased probability of breaking during mechanically-demanding processing steps (e.g. solar cell soldering, module lamination), which would lead to lower production yields and thus increased production costs. Consequently, alternative approaches to the traditional Al-BSF process are under investigation by both the industrial and academic community.

2.3.2. Passivated Emitter and Rear Cell

One promising alternative to the Al-BSF structure is the passivated emitter and rear cell (PERC), initially developed in 1989 and reaching record efficiencies of 22.8 % at that time [67]. The PERC solar cell has a lightly doped emitter with heavier diffusions under the front metal contacts (i.e. selective emitter - SE). A dielectric passivation layer of SiO_2 is grown on the surfaces of the solar cell. Not only does the SiO_2 passivate the surfaces, but it also acts as an antireflection coating on the front surface, further reducing reflection and thus increasing the amount of radiation absorbed. In sequence, openings are performed on the passivation layer followed by the deposition of the rear metal contacts. This is generally done through square or circular openings, usually referred to as “point contacts”. The result is a small, well defined contact area between metal and semiconductor, covering only approximately 1 % of the rear surface, allowing a considerable part of the rear surface to be kept at low recombination rates by the passivation layer. To obtain devices with high efficiencies using this rear contact approach, the silicon substrate has to be sufficiently heavily doped (below approximately 0.5 Ω cm for p-type substrates) to assure that contact resistance between the metal and the semiconductor is sufficiently low. This resulted in significant increases in both voltage and current density when compared to standard Al-BSF structures, leading to higher efficiencies. Figure 2.4 shows the basic structure of the PERC solar cell.

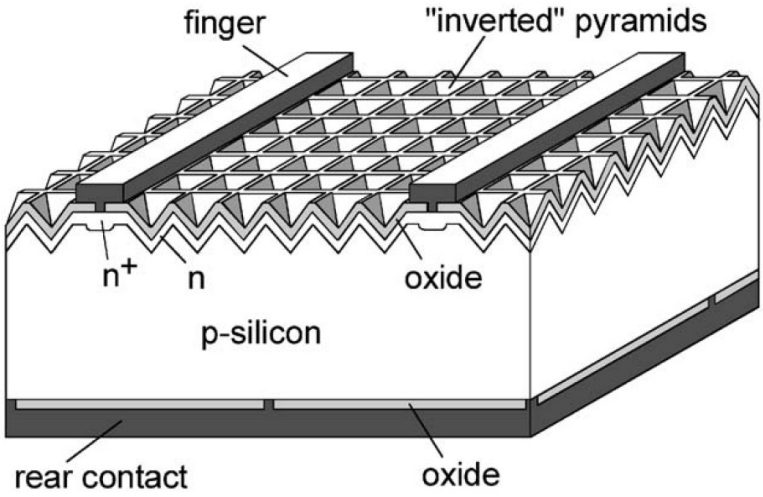

Figure 2.4. Passivated emitter and rear cell [67].

In laboratory-scale devices, the openings for point contacts can be produced by photolithographic methods, which are complex, multi-step processes, inappropriate for industrial implementation due to cost and time limitations. The first PERC devices had inverted pyramids on its front surface, which significantly reduce the reflectance of the device. Unfortunately, the fabrication techniques used to produce inverted pyramids are relatively expensive, laborious and time-consuming. Therefore, the fabrication sequence was adapted, replacing the inverted pyramids by random pyramids, produced by anisotropic etching. Further adaptations and simplifications of the PERC structure have resulted in efficiencies higher than 20 % with simpler and cheaper fabrication methods [68].

On the one hand, devices produced using the PERC structure have reached efficiencies considerably higher than those based on the standard Al-BSF approach. Some of the relevant advantages of the PERC structure are: considerably lower surface recombination rates due to SiO_2 passivation on the front and rear surfaces; increased optical reflectance of the rear side, resulting in better radiation trapping; using thinner wafers does not result in wafer bowing, since no firing of the deposited aluminium is required; significant reduction in material utilization, since the aluminium layer (approximately 2 μm of high-purity aluminium) used as rear contact in PERC cells is considerably thinner than the aluminium paste (approximately 20 μm of paste) used in screen-printed Al-BSF cells.

On the other hand, there are some drawbacks to the PERC structure. One problem is that no diffusion at the rear metal contacts is performed. This has to be avoided because the high-temperature step required would degrade the quality of the passivation layer. This may result in higher contact resistance. The absence of a rear BSF also results in higher recombination losses at unpassivated areas of the rear surface. Additionally, PERC devices require more processing steps to open the rear passivation layer for rear contacts, which are usually expensive and inadequate for industrial production.

Despite its limitations, several research groups have developed and studied adaptations of the PERC structure to bring the technology to industrial implementation. The main focus of these adaptations is to replace the use of expensive and time-consuming photolithography by industrial processes compatible with the large-scale production of solar cells, for example, chemical etching and laser ablation. Additionally, replacing the thermal silicon oxide, which is a slow and energy intensive process, by other passivation layers (e.g. non-stoichiometric silicon nitride, aluminium oxide etc.) may also collaborate to the plans of industrial production of PERC devices. Figure 2.5 shows an adapted PERC design aimed at industrial production.

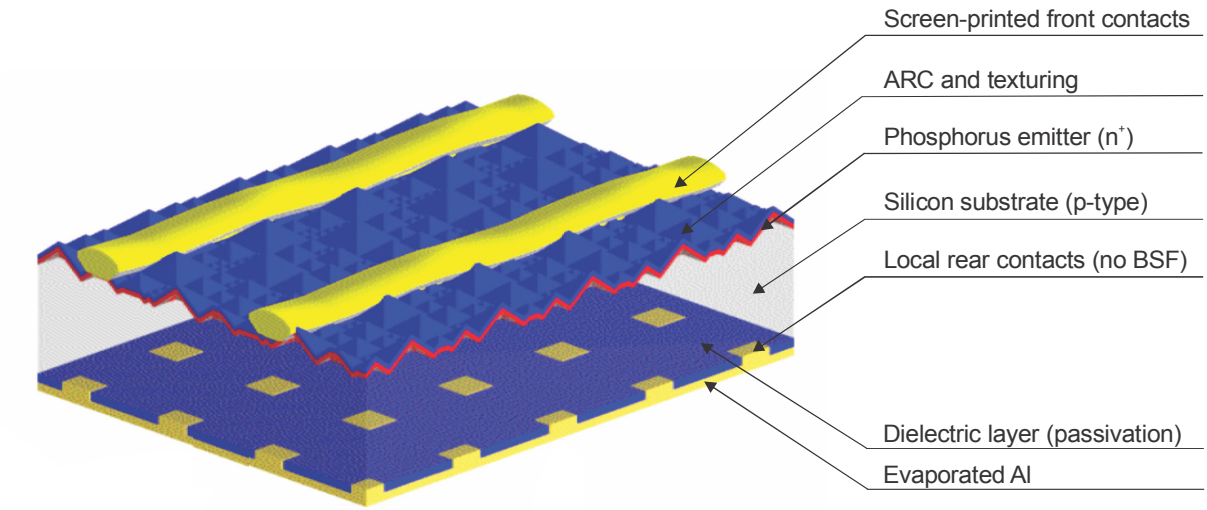

Figure 2.5. Random-pyramid passivated emitter and rear cell. Adapted from [66].

In general terms, fabrication methods applied to the industrial production of crystalline silicon solar cells are simplifications of the technologies developed in R&D laboratories. Such simplifications are necessary during the stage of scaling-up production. This adaptation frequently results in some losses in device efficiency, since one has to refrain from using complex processes or expensive materials in order to make the devices economically competitive.

2.3.3. Passivated Emitter Rear Locally Diffused Cell

As an evolution of the PERC structure, the passivated emitter rear locally diffused cell (PERL) incorporates a combination of benefits of BSF and PERC devices. While PERC solar cells have improved passivation, they don't have the BSF effect observed at the rear contacts of Al-BSF devices. Additionally to the features of the PERC structure, PERL combines both SiO_2 surface passivation and BSF by incorporating localized p^+ boron (instead of aluminium) doping in the rear of the device, in the opened areas (about 100 μm^2 per contact) of the dielectric layer where rear contacts will be deposited. This results in local back-surface fields (LBSF), which reduces minority carrier recombination at the rear metal-semiconductor interface and also reduces rear contact resistance.

The addition of the LBSF was very effective in improving device performance when compared to the PERC structure. PERL solar cells achieved the highest efficiency amongst crystalline silicon solar cell structures to date, reaching an efficiency of 25.0 % [38]. A schematic representation of the PERL structure is shown in Figure 2.6.

Despite its outstanding performance, PERL solar cells are inappropriate for large-scale production, because of the complex and expensive processing sequence, including steps such as: photolithography, to perform steps like selective emitter formation and LBSF; long dry thermal oxidation, to grow high-quality SiO_2 passivation layers; "alneal" processing under forming gas, to improve passivation quality and reduce surface recombination [69]; front surface structure with inverted pyramids, to reduce front surface reflection and improve radiation trapping; and

deposition of a double layer ARC, to further reduce front surface reflection. Many of these methods are only used to produce laboratory-scale solar cells and would be too slow, expensive or complex for manufacturing plants.

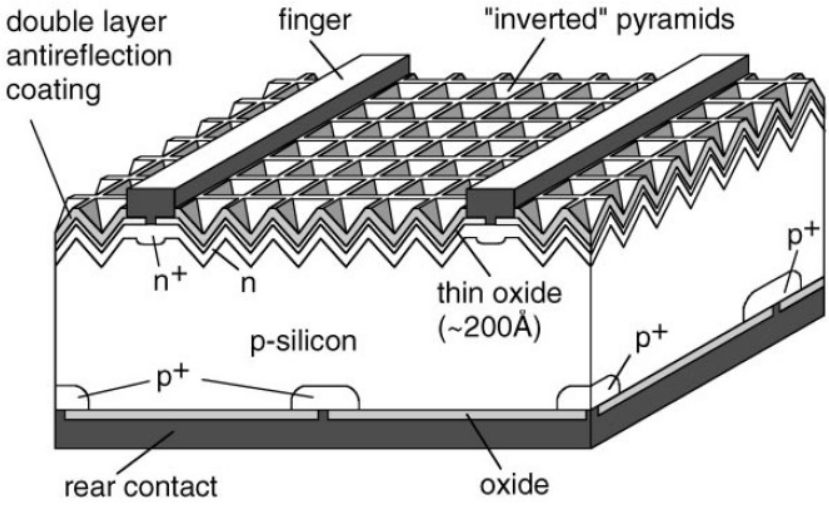

Figure 2.6. Passivated emitter rear locally diffused cell [69].

Nevertheless, the experience gained with the PERL structure served as basis for the development of new processing technologies and methods. As it will be argued in the following chapter, laser processing methods are a promising approach towards implementation of some of the advanced features used in PERC and PERL structures into industrial solar cells. This can significantly contribute to the improvement of solar cell performances while simultaneously keeping production costs at acceptable levels.

3. LASER PROCESSING TECHNOLOGIES FOR SILICON SOLAR CELLS

This chapter starts with a brief review of laser methods for processing silicon solar cells, focusing on the approaches that serve as basis for the experimental research of this work: laser-fired contacts (LFC), laser chemical processing (LCP), and silicon nitride laser ablation. The advantages, drawbacks, and challenges of these three methods are analysed and relevant results available in the literature are presented and discussed.

3.1. Laser Processing and Photovoltaic Solar Cells

Simply stated, a laser (acronym for **L**ight **A**mplification by **S**timulated **E**mission of **R**adiation) is a photonic device that converts energy into electromagnetic radiation with certain specific characteristics. In general terms, lasers are composed of electromagnetic radiation with high degrees of spatial and temporal coherence. This results in a narrow, well-defined radiation beam, capable of achieving high levels of irradiation (i.e. high energy) in a remarkably small area. The radiation emitted by laser systems is generally pseudo-monochromatic, with a narrow emission wavelength band. Such systems are very precise high-energy tools, frequently used for cutting, scribing, micromachining, and heating or melting materials in specific regions. Laser processing is considered an accurate, fast, and versatile method and is widely employed in several industrial applications. Laser tools can be used to perform a wide range of processes under different conditions. Another important use of the technology is in metrology, where lasers serve as inspection or measurement tools both in research and industrial environments. A comprehensive description of the physical principles of lasers is available in references [70], [71].

In the field of PV, laser processing methods can provide two important benefits to device fabrication: reduction of production costs and improvement of solar cell efficiencies. Laser processing has already been applied to solar cell fabrication for several years, with many examples of positive results. The technology has been used for a wide range of applications both in crystalline silicon and thin film solar cells. Another main advantage of laser processing is that it allows localized heating of specific regions, without affecting the bulk of the device. This minimizes negative effects commonly experienced when devices are fully submitted to high-temperature thermal processes (i.e. thermal stress, structural defects, reduction of minority carrier lifetimes, incorporation of unwanted impurities etc.). Additionally, lasers permit thermal processes to be carried out on small areas with complex geometries, such as forming selective emitters below the front metal contacts or LBSF below the rear metal contacts.

One of the historical landmarks in using laser methods for solar cell processing was developed during the 1980's, at the University of New South Wales (UNSW), Australia. Researchers at UNSW developed the laser buried contacts (LBC) solar cell, which was later patented and transferred to industrial production through licensing by BP Solar (BP Solarex at that time). The approach was a simplification of microelectronics processing methods, adapted to produce high-efficiency solar cells using low cost technologies. It avoided photolithographic steps and expensive metallization methods, replacing them by a laser-processed groove and electrochemical deposition of the front metal contacts, respectively. The electrochemical metallization of the front metal fingers inside the laser-grooved lines improved the ratio of the finger depth to width, reducing shading losses without impairing current collection at the front contacts. The laboratory version of the LBC solar cell was complemented with the diffusion of a selective emitter (n^{++}) on the laser grooves, before metallization, in order to improve the metal-semiconductor contact and reduce contact resistance. This resulted in the production and commercialization of the so called "Saturn" PV modules, which demonstrated the highest module efficiencies at that time [36]. A schematic description of the LBC structure is presented in Figure 3.1.

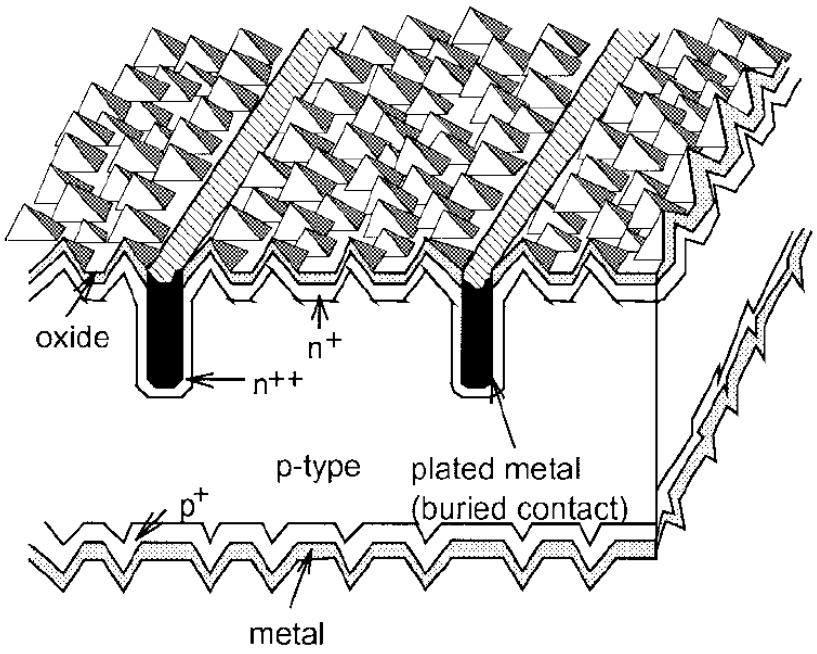

Figure 3.1. The laser buried contact solar cell [72].

Laser processes have also been widely used, both in R&D and in industrial manufacturing, for isolation of the edges and other shunted areas of photovoltaic devices, both in crystalline silicon and thin-film technologies. Other uses of laser processing for solar cells include: to ablate dielectric layers, exposing areas of the device for further processing steps (e.g. selective emitter formation, metallization, local back-surface field etc.); to texture surfaces for reduced reflection and improved radiation trapping; to create specific microstructures on the silicon substrate; to drill holes in silicon for emitter wrap through (EWT) and metal wrap through (MWT) solar cell designs; amongst others. A list of the main R&D topics and industry uses of laser processing in photovoltaics, supported by a selection of literature references on each topic, is presented in Table 3.1.

Because of its versatility, robustness, precision, and throughput, laser technologies are considered a strategic approach for reducing the price of PV electricity by increasing the efficiency of solar cells and reducing processing costs. There are several research initiatives focusing on laser processing technologies for photovoltaics. One example that was funded as part of the European Seventh Framework Programme in 2008 by the European Union is the demonstration project entitled “Next Generation Solar Cell and Module Laser Processing Systems” [73],

[74]. The project goal was to lower the manufacturing costs of crystalline silicon solar cells and modules and simultaneously increase solar cell and module efficiencies. This could be achieved by improving and optimizing a set of different laser processes to facilitate their integration in different steps of the industrial PV manufacturing chain. Similar work based on laser processing for PV has been developed by numerous other initiatives, such as research or demonstration projects supported by the European Union [75]. Moreover, new projects continue to be implemented, indicating that there are still several opportunities for research in this field.

Table 3.1. Laser processing technologies applied to photovoltaic devices.

Laser Process	PV Application	Reference
Scribing	Edge Isolation; Thin Film PV	[76]
LFC	Rear Contact; LBSF	[77]
LCP	Dielectric Layer Ablation; Selective Emitter; LBSF; Rear Contact Formation	[78]
p^+ Doping	LBSF	[79]
n^+ Doping	Selective Emitter; Full Area Doping	[80]
Dielectric Layer Ablation	SE; Metallization; LBSF	[81]
Silicon Drilling	EWT; MWT	[82]
Layer Deposition	ARC (i.e. TiO_2)	[83]
Laser Marking	Wafer Identification	[84]
Micromachining	LBC; Surface Texturing	[85]
Soldering	Solar Cell Interconnection	[86]

In recent years, the *Fraunhofer Institut für Solare Energiesysteme* (ISE) has proposed, developed, and patented two promising laser processing technologies, namely laser-fired contacts [77] and laser chemical processing [78], both of which will be studied in this work.

3.2. Laser-Fired Contacts

The first results of the LFC approach were published in 2001 [87] and, since then, the technology has been thoroughly investigated at the Fraunhofer ISE. In recent years, it became a new standard method for rear processing of solar cells produced at the referred research institute.

The following topics provide a detailed description of the technology, a discussion of its advantages and limitations, a selection of some of the most promising R&D results available in the literature, and examples of industrial transfer of the technology into large-scale production.

3.2.1. Technology Overview

The LFC technology allows the formation of rear contacts using a laser approach, reducing breakage and avoiding bowing of thin silicon substrates. In this process, local back-surface fields are formed using a dielectric layer (rear surface passivation), an aluminium layer (rear contact), deposited on the silicon substrate, and applying a laser process technique, as shown in Figure 3.2.

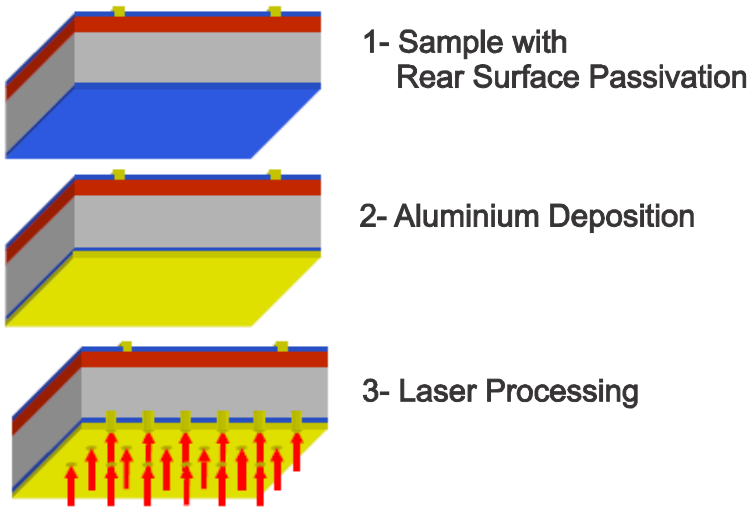

Figure 3.2. Description of the LFC processing method. Adapted from [88].

After the formation of the rear passivation layer, an aluminium metal layer is deposited over the passivating dielectric. The rear contacts are subsequently formed using laser radiation, by locally alloying the aluminium into the silicon substrate, perforating small fractions of the passivation layer.

There are a number of advantages of LFC solar cells when compared to standard industrial Al-BSF devices, the most relevant being [87]:

- Improved rear surface passivation due to the incorporation of a dielectric layer, resulting in lower surface recombination rates and, thus, in higher V_{OC} values (details in section 3.2.3).

- Since the aluminium layer deposited on the rear surface is not contacted to the silicon substrate over the whole rear surface area, as in the screen-printing method, the internal reflectance at this region is superior to that of Al-BSF solar cells. This results in better internal radiation trapping and improves electric current densities of the device (details in section 3.2.3). This can be verified by a superior spectral response of the device and improved radiation absorption close to the rear surface (i.e. wavelengths between 800-1200 nm).

- By avoiding the high temperature firing step of the screen-printed rear aluminium layer, commonly applied to Al-BSF devices, unwanted bowing of the substrate is prevented. Therefore, the processing sequence of LFC solar cells can be compatible with the industrial aim of using very thin silicon substrates to reduce material-related production costs. LFC solar cells with thicknesses below 50 µm have already been successfully demonstrated, showing excellent performance and low breakage rates (details in section 3.2.7).

- Reduction of material consumption by replacing the relatively thick screen-printed rear aluminium layer (20 µm) by a much thinner high-purity aluminium layer (~ 2 µm).

- In the LFC process, the rear contact can be formed without severely damaging the rear passivation layer or the silicon substrate itself. This is important to avoid degradation of minority carrier lifetimes, which would negatively impact the electrical parameters of solar cells [89].

LFC solar cells have also demonstrated a number of advantages in comparison to the PERC and PERL structures. The method is simpler and less

expensive than traditional photolithography approaches, and results in devices with equivalent performances. The steps of opening regions of the passivation layer and of metal-semiconductor contact formation at the rear side are replaced by a single laser-firing step [77]. Additionally, there is the formation of p^+ local back-surface fields in the laser-processed regions. This is one of the main advantages of the LFC structure over the PERC approach. Additionally, it allows the use of higher resistivity wafers in the fabrication of high-efficiency solar cells, a feature that is limited for PERC devices due to its higher rear contact resistance. The lower base doping concentration of higher resistivity wafers allows for higher minority carrier lifetimes. This also means that substrates with a wider variation of base resistivity can produce high-efficiency solar cells and, thus, gives the method more flexibility to deal with different types of substrates. Figure 3.3 compares the performance of LFC and PERC solar cells in respect to base resistivity.

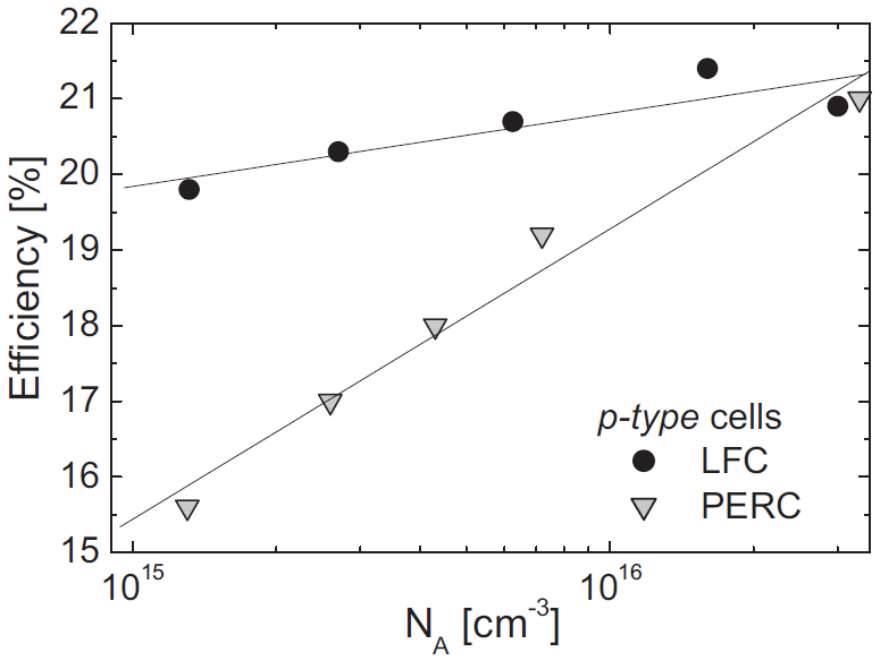

Figure 3.3. Comparison of the performance of LFC and PERC solar cells on p-type silicon for different base resistivities (left to right: 10 Ω cm to 0.5 Ω cm) [90].

Another benefit of the LFC technology is that the LFC method has a low processing cost (i.e. very low consumables, operation, and maintenance costs) and short processing time. By using a set of galvanometer-driven laser scanning mirrors to control and position the laser beam of the equipment, it is possible to apply the

LFC process on a large area industrial solar cell in just a few seconds. The method is compatible with industrial throughput of more than 1000 wafers per hour and could be easily adapted to a manufacturing environment using equipments that are readily available to the industry. Additionally, laser-firing can be performed with automatic wafer handling equipments and in a continuous flow process, which would allow for additional cost-reductions in manufacturing.

In terms of the limitations of the LFC design, two difficulties have been identified. First, both spreading resistance and contact resistance at the rear surface need to be adequately accounted for, due to the discrete structure of the contacts (local points instead of full area contact). Otherwise resistance-related losses could significantly impact the fill factor of the solar cells and, consequently, decrease efficiency. Second, for good and reliable interconnection of solar cells into strings, soldering of metal interconnectors is necessary. Obtaining good soldering properties directly over the thin rear evaporated aluminium layer can be quite difficult, thus an additional processing step prior to soldering may be required. Two options to overcome this limitation would be to deposit a thin layer of silver over the aluminium or to use a low temperature soldering paste prior to solar cell interconnection [91]. Therefore, this interconnection issue is not considered as a long term obstacle for the technology and should be overcome with incremental improvements on the technique. Proof of this is found in the fact that there are already products available on the market successfully employing LFC-based solar cells (details in section 3.2.8).

3.2.2. Characteristics of the Laser-Fired Point Contact

Researchers at the Fraunhofer ISE have examined in detail the morphology, depth profile and chemical composition of rear contacts processed by the LFC method on flat silicon substrates [92 - 96]. The point contacts were already investigated by several characterization techniques and may be divided into three distinct parts, with different characteristics. They are described below with the aid of Figure 3.4.

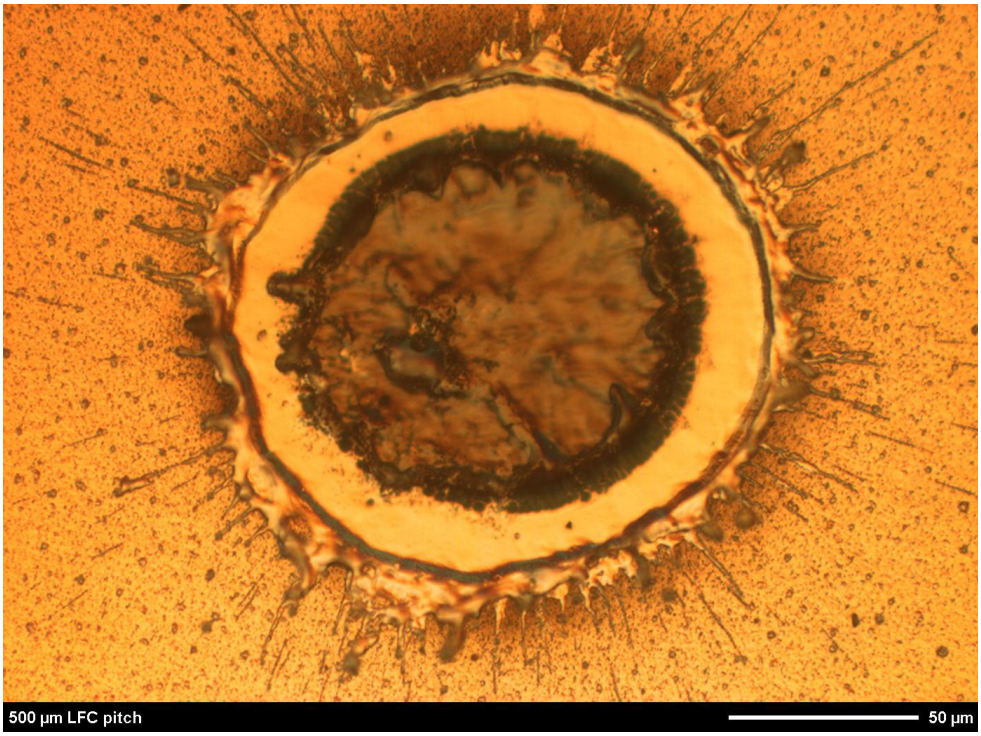

Figure 3.4. Optical microscopy of an LFC-processed region on an aluminium layer over a silicon substrate, with its distinct inner crater, outer crater and external circular ring [97].

The first part of the contact is an inner crater, smaller in size than the laser beam focus diameter used for the LFC processing and with a depth of between 4-10 µm according to laser parameters. This inner crater is composed of a mixture of silicon and aluminium, with aluminium atoms diffused into the silicon substrate due to the high laser energy during LFC processing. The aluminium doping produces a beneficial LBSF in this region of the contact. Secondary ion mass spectrometry (SIMS) analysis of the inner crater indicates that this aluminium doping reaches a depth of approximately 1.5 µm into the silicon substrate [92], [111]. If adequately processed, this inner crater perforates the dielectric passivation layer and forms an ohmic contact between the substrate and the rear metal layer, exhibiting a low contact resistance. This part of the point contact is responsible for the formation of a good electric contact on the rear, thus it is crucial for a good performance of an LFC solar. When calculating the total rear contact area, only the area of the inner craters of the point contacts should be considered as making direct electric contact with the silicon substrate. In terms of morphology, the surface of the inner crater region was found to be relatively rough due to the high energy laser processing.

The second part of the contact is an outer crater, which is affected by the laser radiation but does not receive enough energy to perforate the passivation layer. This part of the crater is formed mainly by melted and subsequently resolidified aluminium, with no significant change in the dielectric passivation layer below it. There is no direct contact between the silicon substrate and this part of the metal layer, therefore it does not contribute to the active rear contact area of the device. The outer crater remains covered by a slightly thinner aluminium layer than the rear areas unaffected by laser processing.

The third part of the contact is seen at the external edges of the outer crater. During laser processing, some of the melted aluminium is expelled from the crater region by the impact of the laser. This material then quickly resolidifies over the deposited aluminium, producing an external circular ring of aluminium surrounding the point contact. This ring is approximately 5 μm high in relation to the initial aluminium layer. The aluminium ring does not contact the underlying silicon substrate.

To confirm the diffusion of aluminium atoms into the silicon substrate and the formation of a LBSF by the LFC method, researchers prepared and analysed n^+np^+ test structures [98]. The advantage of using an n-type substrate for the test structure is that there will only be the formation of a p-n junction if the laser processing on the rear side is able to diffuse aluminium atoms into the silicon substrate, thus resulting in local p-n junctions in each laser-processed zone. These junctions can then be analysed by electron-beam induced current (EBIC), as seen in Figure 3.5. The bright region of the EBIC image, on the inner LFC crater, indicates the formation of a p-n junction after laser processing. Therefore, aluminium atoms must have been diffused into the silicon substrate during laser processing, since aluminium is the only source of acceptor atoms (p doping impurities).

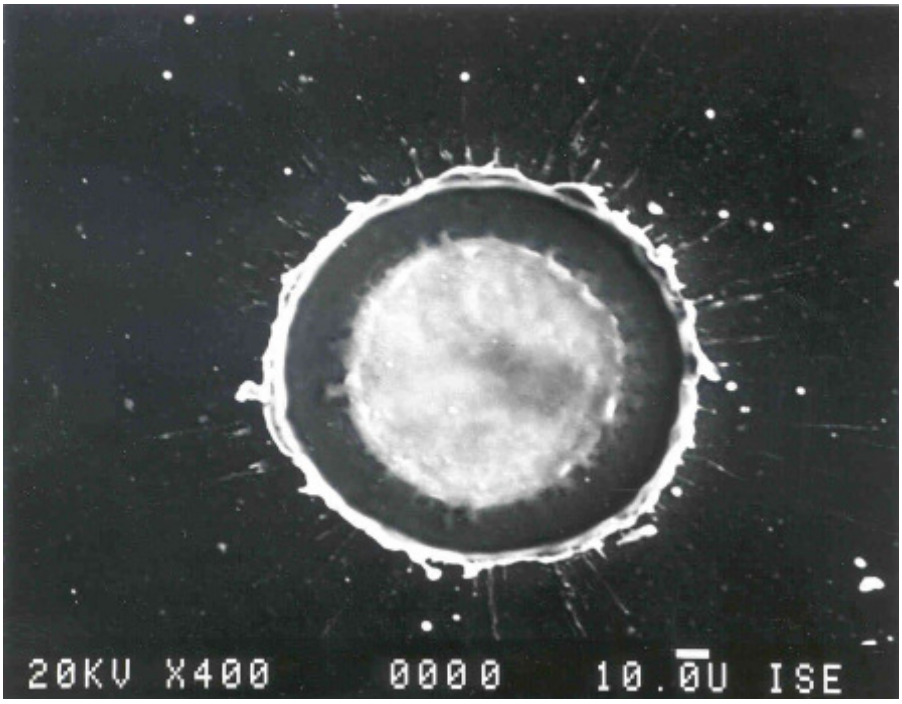

Figure 3.5. EBIC image of an LFC-processed region on an n-type silicon substrate, with inner crater, outer crater and external circular ring [96].

Other electrical characterization methods can also be employed to the n^+np^+ samples. For example, by measuring the electrical characteristics of the samples with J-V curves, one can demonstrate the formation of such p-n junctions. This was carried out on 1 Ω cm n-type FZ-Si substrates, with inverted pyramids on the front surface, evaporated front metal contacts, a front-surface field (FSF) obtained by phosphorus diffusion ($R_{\square}$ = 120 Ω/sq), and passivated by thermal silicon oxide (~ 105 nm) on both front and rear surfaces. A thin aluminium layer (~ 2 μm) was deposited on the rear side, followed by laser-firing. The results confirmed the formation of local p-n junctions, with the diffusion of aluminium atoms into the silicon substrate [98].

3.2.3. Internal Reflectance and Rear Passivation Quality

Researchers at the Fraunhofer ISE performed a comparison between different rear solar cell structures in terms of their internal reflectance, passivation quality, and effective rear surface recombination velocities, when processed by the LFC approach. To facilitate the evaluation, the front surface structures of the samples were fabricated by an identical high-efficiency processing sequence: inverted pyramids, evaporated front contacts, homogeneous phosphorus diffusion ($R_{\square}$ ~ 120

Ω/sq), and 105 nm thermal silicon oxide passivation. The analysis was based on reflectance measurements and internal quantum efficiency (IQE), and was modelled with the aid of Phong exponents, 3D ray tracing, and PC1D simulations [99]. The results are summarized in Table 3.2.

Table 3.2. Internal reflectance and effective rear surface recombination velocities for different solar cell structures. R_{rear} is the internal reflectance at the rear side, J_{SC} is the maximum short-circuit current density for a 250 μm thick solar cell simulated by 3D ray tracing, S_{rear} is the effective rear surface recombination velocity modelled in PC1D, and V_{OC} PC1D is the open-circuit voltage modelled in PC1D. Adapted from [99].

Solar Cell Structure	R_{rear} [%]	J_{SC} [mA/cm^2]	S_{rear} [cm/s]	V_{OC} PC1D [mV]
LFC (105 nm SiO_2)	95.5	42.23	110	680
PERC (105 nm SiO_2)	95.0	42.18	200	676
PERL (105 nm SiO_2)	94.5	42.16	60	685
Evaporated Al Ohmic Contact	83	41.61	10^7	626
Diffused B-BSF	71	41.14	430	657
Screen-printed Al-BSF	65	41.08	750	650

From the presented values, one can notice the higher internal reflectance of the three oxide-passivated structures when compared to structures without rear passivation. The main reason for that difference is that the pattern of reflection in the first three structures is specular, whereas for the latter three the pattern of reflection is diffuse. Specular reflection results in improved radiation trapping in the device, consequently increasing its current density. Regarding the effective rear surface recombination velocities, again the three oxide-passivated designs prove its superiority, with considerably lower recombination than the latter three. This is the result of a better rear passivation quality of the 105 nm thermal silicon oxide layer and lower recombination of the small localized point contacts, compared to the full area BSF and full area contact of the Al-BSF or B-BSF structures. Finally, the sample with a full area evaporated Al ohmic contact has its performance strongly influenced by considerably high rear recombination losses, as there is no rear passivation incorporated in the device. Additionally, due to the rear passivation layer and rear contacts with LBSF, the LFC structure has the second best passivation quality, also being simpler and more industrially feasible than the PERL design.

When the combined effects of internal reflectance and effective surface recombination are taken into account to simulate the electrical characteristics of the devices using the PC1D software, a very good performance of the LFC design was predicted. This structure presents the highest predicted short-circuit current density and second highest open-circuit voltage. Therefore, the advantages of the LFC structure compared to alternative structures are quite clear, especially when compared to the standard screen-printed Al-BSF structure currently used in industrial production. Additionally, when considering recent industrial efforts to reduce silicon wafer thickness, both the importance of internal reflectance and surface recombination velocities increase the comparative advantage of the LFC structure, as these parameters have an even greater role for thinner crystalline silicon solar cells.

3.2.4. Types of Rear Passivation Layers and Deposition Methods

The LFC method has been evaluated with different materials as rear passivation layer, as well as different deposition methods. Single layers of SiO_2, SiN_X, SiC_X, as well as multi-layers of SiO_2/SiO_2, SiN_X/SiO_2, $SiO_2/SiN_X/SiO_2$, SiC_X/SiC_X, a-Si:H/a-SiN_X:H, a-Si:H/SiO_X, SiO_XN_Y/SiN_X, SiN_X/SiO_X, Al_2O_3/SiN_X and A_2O_3/SiO_X where tested as passivation. Deposition methods investigated include dry and wet oxidation, plasma-enhanced chemical vapour deposition (PECVD), radiofrequency-sputtering, and atomic layer deposition (ALD). The deposition methods have passed through initial optimization and the solar cells fabricated used high-efficiency front surface structures, typical of laboratory experiments. Table 3.3 shows a selection of the main results obtained with LFC solar cells using different passivation layers and deposition methods.

All solar cells reached efficiencies over 20 % on p-type FZ-Si, even when considerably different passivation layers are compared. This indicates the flexibility of the technology in terms of both the composition of the passivation layer and the deposition method employed. Besides the excellent performance of samples passivated by thermal silicon oxide, with efficiencies as high as 22.0 %, two other passivation layers have also reached outstanding performances: a double layer of a-

Si:H (~ 70 nm) and SiO_X (~ 100 nm) deposited by PECVD in a single step, reaching an efficiency of 21.7 %, and a single layer of AlO_X (~ 100 nm) deposited by PECVD, reaching an efficiency of 21.5 %. Other interesting LFC studies not included in Table 3.3 reached similar conclusions and performances, with different rear passivation layers, and are available in references [100 - 102].

Table 3.3. Performance of LFC solar cells with different passivation layers and deposited by different methods. All solar cells were produced on p-FZ-Si substrates and had areas of 4.0 cm^2.

Passivation Layer(s)	Deposition Method	Resistivity [Ω cm]	V_{OC} [mV]	J_{SC} [mA/cm^2]	FF	η [%]	Reference
SiO_2	Thermal Oxidation (Dry)	0.5	685	39.7	0.809	22.0	[103]
a-Si:H/SiO_X	PECVD	0.5	677	39.5	0.811	21.7	[104]
SiC_X	PECVD	0.5	665	37.5	0.803	20.2	[105]
SiN_X/SiO_X	Sputtering/PECVD	0.5	669	38.6	0.797	20.6	[103]
SiN_X/SiO_X	PECVD	0.5	670	38.5	0.798	20.6	[103]
$SiO_X/SiN_X/SiO_X$	PECVD	1.0	664	38.2	0.787	20.0	[103]
Al_2O_3/SiO_X	ALD/PECVD	0.5	681	39.3	0.796	21.3	[106]
Al_2O_3/SiO_X	PECVD	0.5	678	39.7	0.794	21.3	[106]
AlO_X	PECVD	0.5	684	39.4	0.798	21.5	[106]

3.2.5. Rear Aluminium Deposition Methods

There are several different approaches to deposit a metal layer on the rear side of the silicon substrate to produce LFC devices. The most frequently used method for depositing aluminium in laboratory-scale LFC solar cells is electron-beam physical vapour deposition, frequently referred to as electron-beam evaporation (EBE). Researchers at the Fraunhofer ISE have investigated different processes and equipments for the deposition of the aluminium metal layer, such as: electron-beam evaporation, industrial (high-throughput) physical vapour deposition (PVD) metallization, sputtering, screen-printing, and also using a simple commercial aluminium metal foil. Table 3.4 shows a selection of the main results obtained for LFC solar cells using different aluminium deposition methods.

Results clearly indicate that the LFC method is compatible with a variety of metal deposition methods. Solar cells with comparable efficiencies were produced by

EBE, PVD, sputtering, and even screen-printing methods. Replacing the costly high-purity aluminium (99.999 %) by cheaper lower-purity aluminium (99.98 %) did not reduce the efficiency of the solar cells [108]. The only method that resulted in some loss of solar cell performance was the use of a commercial aluminium foil as rear contact, yet even in this case the efficiency loss was limited to approximately 1 % absolute [107]. These results further confirm the flexibility of the method.

Table 3.4. Performance of LFC solar cells with evaporated Ti/Pd/Ag front contacts and rear aluminium deposited by different methods.

Al Deposition Method	Resistivity [Ω cm]	Substrate	Area [cm^2]	V_{OC} [mV]	J_{SC} [mA/cm^2]	FF	η [%]	Reference
EBE Best	1.0	p-FZ-Si	4.0	666	39.1	0.805	21.0	[107]
EBE Al 99.999%	1.0	p-FZ-Si	4.0	660	39.1	0.775	20.0	[108]
EBE Al 99.98%	1.0	p-FZ-Si	4.0	661	39.0	0.778	20.1	[108]
PVD	1.0	p-FZ-Si	4.0	677	39.4	0.784	20.9	[108]
Industrial PVD	1.0	p-FZ-Si	4.0	665	39.1	0.805	21.0	[109]
Sputtering	1.0	p-FZ-Si	4.0	669	39.0	0.788	20.6	[108]
Screen-printing	1.0	p-FZ-Si	4.0	655	39.3	0.796	20.5	[110]
Aluminium Foil	1.0	p-FZ-Si	4.0	653	38.0	0.798	19.8	[107]

Additionally to the results presented above, a metallization approach using a double layer of Al-Ag was also investigated [111]. The technique was devised to improve the soldering properties of the rear metal layer and to overcome the challenge of interconnecting LFC solar cells into strings. A 2 µm Ag layer was deposited over Al layers with thicknesses of 5 µm, 10 µm or 15 µm, followed by laser-firing. The results indicate that no limitation to the maximum efficiency due to the deposition of an additional Ag layer over the Al is observed. There were also no efficiency losses when using a thick layer of up to 15 µm of evaporated aluminium as the rear contact. In both cases, LFC solar cells with efficiencies as high as 21 % using FZ-Si substrates with high-efficiency front surface structures were obtained.

Other complementary studies which investigated the influence of rear aluminium deposition methods with LFC solar cells are available in references [112 - 114]. Their conclusions were aligned with the results presented above.

3.2.6. Thermal Treatment

One of the important processing steps to improve the quality of LFC solar cells is a thermal treatment (annealing) step, performed after laser processing [111], [115]. Annealing is usually carried out at relatively low temperatures of between 300-400 ºC, with the objective of improving the metal-semiconductor contact quality, as well as reducing some of the structural stress caused by the high-energy laser processing [111]. The efficiency gain after this step is considerable, with absolute efficiencies increasing from approximately 16 % prior to annealing to 20 % after annealing. It has been shown that performing the process under forming gas, nitrogen gas, or compressed air flow yields similar benefits. A comparison between performing the annealing in a quartz tube furnace (very clean environment) and in an industrial conveyor belt furnace indicates that there is no disadvantage in performing the process in industrial equipment, with less stringent cleanliness control. This suggests that the annealing benefits are a result of transformations occurring within the sample, with little dependence on the external medium.

3.2.7. Solar Cells on Very Thin Substrates

The LFC method was demonstrated to be appropriate to fabricate high-efficiency solar cells also on very thin silicon substrates. One of the landmarks of this technology was reached when solar cells with thicknesses below 40 µm and efficiencies above 20 % for FZ-Si and CZ-Si were fabricated. Table 3.5 presents a selection of the thinnest LFC solar cells produced to date.

Table 3.5. Performance of LFC solar cells on very thin silicon substrates.

Thickness [µm]	Resistivity [Ω cm]	Substrate	Area [cm^2]	V_{OC} [mV]	J_{SC} [mA/cm^2]	FF	η [%]	Reference
36	0.8	p-CZ-Si	4.0	667	37.5	0.799	20.3	[116]
36	0.5	p-FZ-Si	4.0	679	37.5	0.795	20.2	[116]
37	0.25	p-FZ-Si	4.0	677	37.5	0.816	20.7	[116]
37	0.25	p-FZ-Si	4.0	677	36.9	0.804	20.1	[117]
37	0.25	p-FZ-Si	4.0	671	36.8	0.816	20.2	[118]

The very thin substrates used to fabricate the above devices were especially prepared to reach such thicknesses through mechanical grinding of thick wafers, as there is still no industrial process capable of producing such thin wafers in large scale. This process is clearly inadequate for industrial application and serves only for the purpose of R&D activities. Therefore, it must be highlighted that, at the current technological level, very thin silicon wafers are still unavailable to the PV industry, because there is no specific large-scale fabrication process to manufacture them in an economical way.

3.2.8. World Records and Industrial Devices with Laser-Fired Contacts

In 2004, researchers from the Fraunhofer ISE set a new world efficiency record for multicrystalline silicon solar cells of 20.4 % with a 1 cm^2 LFC-processed laboratory-scale solar cell. This device has surpassed the previous record of 19.8 %, dating from 1998, by a considerable margin. Additionally, the LFC technology has been successfully applied by a PV company to produce a record-setting high-efficiency industrial multicrystalline silicon solar cell. Such industrial LFC devices have also been used to fabricate a record-setting multicrystalline silicon solar module, with 17.8 % efficiency. Table 3.6 shows the electrical parameters of these outstanding devices based on the LFC approach:

Table 3.6. Performance of record solar cells and module incorporating the LFC technology. The module data is presented in different V_{OC} and J_{SC} units for clarity.

Thickness [µm]	Resistivity [Ω cm]	Substrate	Area [cm^2]	V_{OC} [mV]	J_{SC} [mA/cm^2]	FF	η [%]	Reference
99	0.6	p-mc-Si	1.002	664	38.0	0.809	20.4	[119], [120]
–	–	p-mc-Si	242.7	652	39.0	0.767	19.5	[120]
–	–	Module-mc	14920	38.86 V	9.04 A	0.757	17.8	[120]

After successful implementation in the R&D environment, the LFC method has been transferred to a high-volume production facility at the Fraunhofer ISE. A Nd:YAG laser system with galvanometer-driven scanning mirrors was employed and submitted to extensive testing. Results show that the technology is compatible with industrial processing methods and could be used in a continuous flow process [121].

Recently, the LFC technology has been successfully incorporated by the PV industry. Some companies already employ the technology on laser processing equipments [122] and PV products [123].

3.3. Laser Chemical Processing

3.3.1. Technology Overview

Laser-assisted doping processes, also called laser-induced diffusion, have been recently investigated by the PV scientific community for solar cell applications. In this method, impurities are kept in contact with the substrate surface and diffused into the material with the aid of laser radiation. The laser energy is absorbed by the silicon substrate and very locally heats up and melts regions of its surface, allowing impurities to penetrate into the material, which re-crystallises epitaxially once the laser radiation is halted. There are several approaches to laser-assisted doping and impurity sources can be gaseous (e.g. $POCl_3$, PH_3, BBr_3), liquid (usually chemical solutions containing phosphorus, boron etc.) or solid (oxides, spin-on films, ion-implanted elements etc.) [124].

The laser chemical processing method, developed by the Fraunhofer ISE [125], employs a liquid jet-guided laser beam capable of performing localised diffusions without the need of masking or high-temperature thermal processes on the whole device. It allows the ablation of the dielectric passivation layer and subsequent melting of the silicon surface underneath it, forming highly doped regions on the substrate. Both processes are performed in one single step. The method is applicable in high-efficiency silicon solar cell designs including features such as selective emitters and local back-surface fields, with the distinct advantage of a reduced number of processing steps required for device fabrication. Additionally, the technology can be combined with different metallization schemes, such as screen-printing [126], plating methods for the front contacts (i.e. light-induced plating) [127], and aerosol jet printing [128]. The working principle behind the LCP method is illustrated in Figure 3.6 and described below.

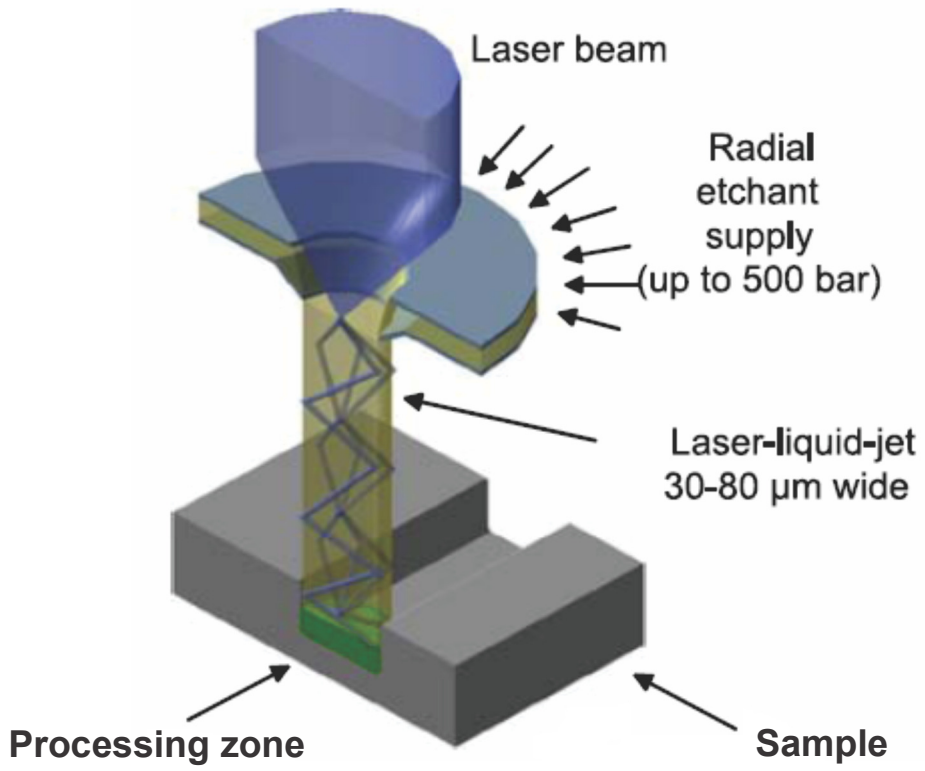

Figure 3.6. Schematic representation of the LCP method. Adapted from [125].

In the LCP method, a liquid solution is injected radial-symmetrically into a small nozzle, creating a thin liquid jet with laminar flow. A laser beam is focused into this jet and is guided through the nozzle by means of total internal reflection, until it reaches the sample surface. At that point, the laser locally heats the substrate and promotes physical and chemical changes in the affected area. Depending on the process parameters, the technique can result in material etching, ablation, doping or deposition. The main process parameters that can be adjusted are the following: chemical composition of the liquid medium, nozzle diameter, liquid flow speed (by controlling its injection pressure), laser radiation wavelength, laser system power, laser mode (continuous wave, q-switched etc.), laser pulse duration, and scanning speed.

When performing a doping process, the liquid solution used to guide the laser contains impurity atoms of interest, such as phosphorus or boron atoms. Hence, for

solar cell applications, the method is a fast and practical approach to create elaborate structures that incorporate selective emitters and local back-surface fields, in combination with surface passivation by dielectric layers and low temperature metallization methods (e.g. electroless deposition), amongst other concepts used in high-efficiency solar cells. Two examples of applications of the LCP method in solar cell processing are shown in Figure 3.7.

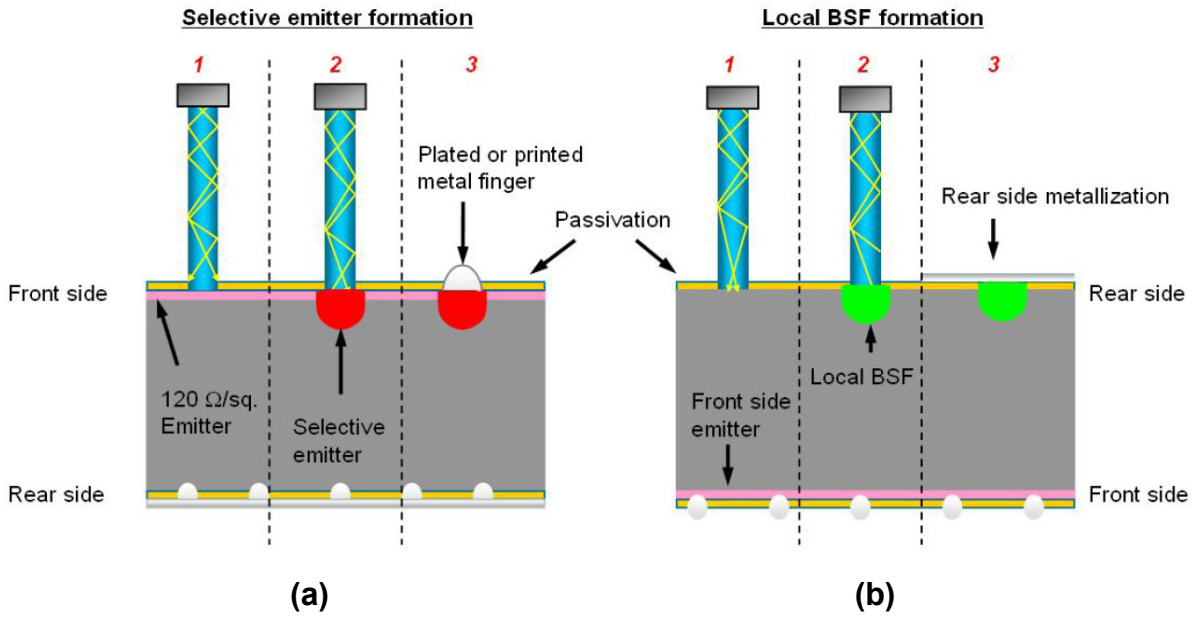

Figure 3.7. Two possible LCP applications: (a) front surface opening with selective emitter formation and (b) rear surface opening with local back-surface field formation [129].

For the selective emitter formation on p-type silicon, the jet-guided solution contains phosphorus atoms and LCP is used to open the ARC layer and generate highly-doped n^{++} regions on the front surface, as shown in Figure 3.7(a). A metal seed layer is deposited and subsequently grown over the n^{++} regions, whereas the rest of the device is kept protected from deposition. The main advantage of using a selective emitter concept is that it allows reducing the doping concentration in the homogeneous n-type emitter layer, hence minimizing recombination losses, especially Auger and Shockley-Read-Hall (SRH) recombination. The highly doped n^{++} regions below the metal grid guarantee an adequate metal-semiconductor interface, as well as low contact resistance.

Alternatively, for the LBSF formation on p-type silicon, the jet-guided solution contains boron atoms instead of phosphorus. LCP is used to open the passivation layer and generate highly-doped p^{++} regions on the rear surface, as shown in Figure 3.7(b). Finally, the rear metallization is performed, contacting the silicon only on the open highly-doped areas. This leaves the rest of the rear side passivated, reducing rear surface recombination and increasing cell performance, similarly to the PERL solar cell design.

3.3.2. Best Solar Cell Results of Laser Chemical Processing on p-Type Silicon Substrates

Promising results have been achieved by LCP-processed solar cells incorporating selective emitters or LBSFs. In both cases, solar cells with efficiencies above 20 % have been obtained for devices fabricated on p-type FZ-Si using high-efficiency front surface structures. A selection of the best results is presented in Table 3.7.

Table 3.7. Performance of high-efficiency LCP solar cells incorporating selective emitters or local back-surface fields produced on p-type FZ-Si.

Solar Cell Structure	Thickness [µm]	Resistivity [Ω cm]	Area [cm^2]	V_{OC} [mV]	J_{SC} [mA/cm^2]	FF	η [%]	Reference
SE	250	0.5	4.0	665	38.7	0.792	20.4	[78]
LBSF	250	0.5	4.0	675	38.7	0.800	20.9	[130]

To date, the LCP method has been optimized mainly for the two processes previously described: n^+ for selective emitters and p^+ doping for LBSF of n^+pp^+ solar cells produced on p-type silicon substrates.

Therefore, there are still opportunities for the development and implementation of the LCP technology for doping crystalline silicon solar cells produced on n-type silicon substrates. In this respect, p^+ doping could be used to form selective emitters and n^+ doping could be used to form LBSF of p^+nn^+ solar cells. Additionally, the basic physical and chemical mechanisms governing the laser chemical processing method are not yet fully understood. Therefore, there are also

opportunities to evaluate and compare the differences between the LCP method and other laser processing methods, such as a scanning head mirror galvanometer laser system (SCA). This work evaluates and compares the characteristics of samples processed by the LCP and SCA methods under similar conditions.

3.4. Laser Ablation of Dielectric Layers

3.4.1. Technology Overview

One of the promising applications of laser processing technologies to PV is the ablation of specific regions of thin dielectric layers, such as the front surface ARC or the rear surface passivation layer [131 - 133]. This procedure is normally employed to selectively expose areas of the silicon substrate that will be subject to subsequent processing steps, without having to expose the whole surface area of the device to the same processing conditions. When compared to alternative methods of selective removal of dielectric layers, such as chemical etching based on liquid solutions or mechanical micromachining, laser ablation is considered a contactless, high-throughput, precise, and cheap way of performing the task.

One of the challenges of laser ablation on crystalline silicon solar cells is that the front surface of the device is usually rough, due to random pyramid texturing. The roughness height between tips and valleys of the textured surfaces is of the order of micrometers or a few tens of micrometers. Additionally, the structured morphological profile of the random texture gives rise to interference effects of different magnitudes, depending on whether the laser beam is reaching tops, corners, side faces, or valleys of the random pyramids. This effect was evaluated in detail in reference [81], where researchers concluded that interference effects may concentrate the laser beam on pyramid tops and corners by a factor of up to 10. This indicates that homogeneous laser ablation of a dielectric layer deposited on top of random pyramids would not be possible, since lower laser beam intensities would be needed at the tops and corners compared to faces and valleys of the pyramids.

The dielectric layers used on the front surface of solar cells usually have a lower absorption coefficient than the underlying silicon, to avoid significant solar radiation absorption losses at the dielectric layer. As a result, selective processing of such layers avoiding that the laser beam energy reaches the underlying silicon is very difficult. Consequently, laser processes usually have some degree of penetration on the silicon substrate. This may lead to unwanted laser-induced damage on electrically active regions of the device, such as the space charge region, if the penetration is too deep. This laser induced damage is particularly strong if the device is subjected to additional high temperature processing steps [134]. One way to reduce this effect is by controlling the laser beam energy employed during laser ablation, so that the laser induced damage caused by the radiation is maintained at acceptable levels, even at the event of reaching the space charge region. Another option would be to design the photovoltaic device in such a way that the regions subjected to laser processing are able to cope with the resulting laser damage. Yet this is not always possible and may constitute a complicated task.

The most common dielectric layer industrially employed in crystalline silicon solar cells is by far silicon nitride, usually deposited by industrial PECVD machinery [135]. The density, refractive index, and thickness of the material are chosen so that it may serve simultaneously as antireflection coating and passivation layer. This results in an optimized refractive index (n_{ARC}) of approximately 2.1 and a layer thickness of approximately 70-75 nm [54]. The composition of the PECVD silicon nitride layer is non-stoichiometric, therefore it is commonly referred to as non-stoichiometric silicon nitride (SiN_X).

The mechanisms of laser ablation of a dielectric layer have been proposed by different researchers with similar descriptions [136], [137]. They can be divided into mainly two limiting cases: direct laser ablation and indirect laser ablation. An illustration of the two mechanisms is provided in Figure 3.8.

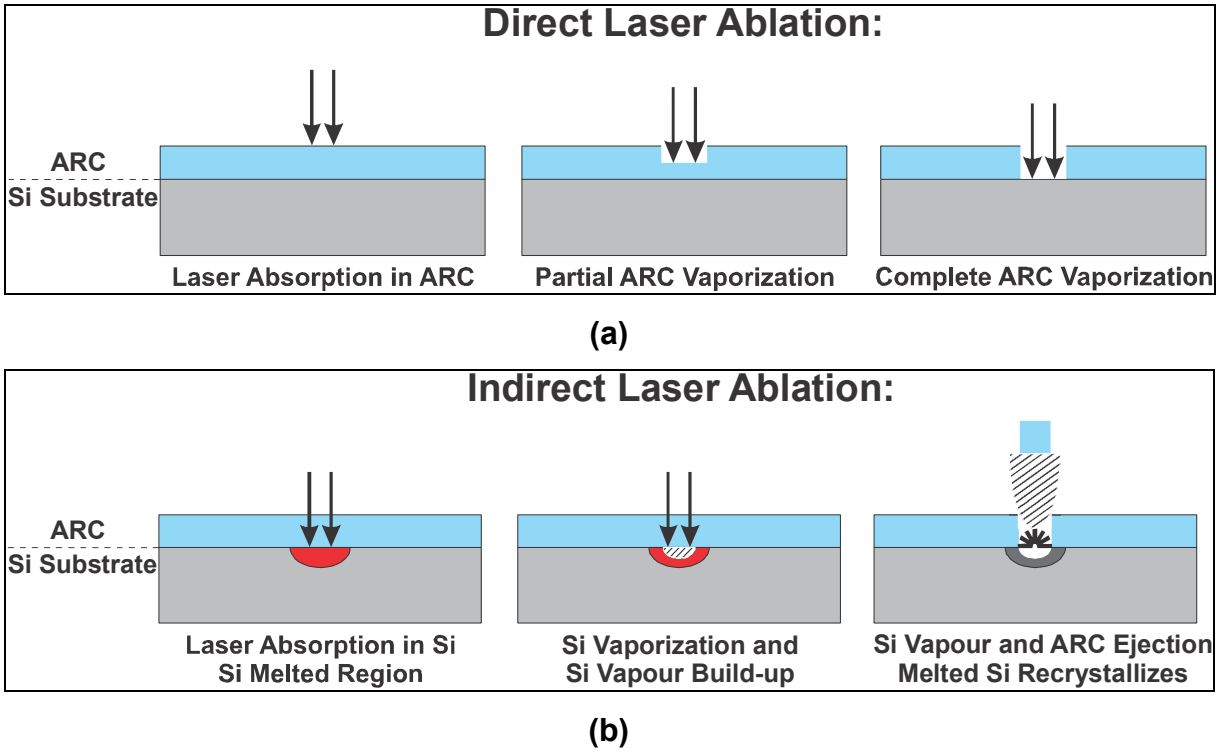

Figure 3.8. Laser ablation mechanisms on dielectric layers used as front side antireflection coating: (a) direct laser ablation mechanism and (b) indirect laser ablation mechanism.

In the direct laser ablation, the energy of incoming photons of the laser beam is above the E_g of the dielectric layer. Consequently, photons are absorbed directly in the dielectric layer, which is then locally heated and vaporized until its complete removal. In the indirect laser ablation, the energy of incoming photons of the laser beam is below the E_g of the dielectric layer, but above the E_g of the silicon substrate. Consequently, photons are transmitted through the dielectric layer and absorbed in the underlying silicon substrate. The silicon is locally melted, vaporized, and the pressure build-up created by this vapour plume is capable of ejecting (i.e. blowing out) a fraction of the material above it, therefore indirectly lifting-off the dielectric layer. These two limiting cases, however, are not necessarily exclusive. Depending on the wavelength of the laser beam employed and on the absorption coefficient (α) of the dielectric layer, a combination of the two cases may occur: part of the energy may be absorbed by the dielectric layer, causing a certain degree of direct ablation, whereas the other part of the energy may reach the silicon substrate, causing some degree of indirect ablation.

One of the major applications of laser ablation of SiN_X layers is on the selective deposition of front metal contacts by means of electrochemical reactions. Initially, specific regions of the front surface SiN_X layer are removed by means of laser ablation, locally exposing the underlying silicon substrate. Afterwards, the front surface metal contacts are selectively deposited only on the exposed regions by means of electrochemical deposition [138 - 140].

Some of the important advantages of switching from the industrially-established screen-printing technology, currently used in front contact formation, to an electrochemical deposition method include, amongst others [141]:

- Replacing expensive silver used in screen-printing pastes by affordable metals, such as nickel, copper, and tin.
- Avoiding the use of lead, an essential component of traditional industrial screen-printing pastes, necessary to allow the pastes to react with the silicon nitride antireflection coating and reach the underlying silicon emitter. Lead is a toxic heavy metal, which already had its use in electric and electronic products banned by several countries. It is therefore crucial that the PV industry plan the elimination of lead use in solar cell processing in the long-term, especially if it expects to keep its reputation as an environmentally-friendly and sustainable technology.
- Improving the aspect ratio of the front contacts, since the electrochemical deposition allows an improved control over the height, width, and morphology of the metal fingers. This reduces reflection losses and increases the J_{SC} of resulting solar cells.
- Switching from a contact-based metallization method (screen-printing) to a contactless metallization method (electrochemical deposition), which reduces the chances of solar cell breakage during processing, especially when considering current industrial efforts of using thinner silicon wafers.
- Switching from an alignment-dependent approach (screen-printing) to a self-aligned or selective metallization approach (electrochemical deposition), where there is no need to specifically align the silicon wafers during the metallization step.

- Switching from a batch industrial process to a continuous industrial process, with the corresponding benefit of higher processing speeds and increased throughput.

3.4.2. High-Efficiency Solar Cells with SiN_X Laser Ablation

Promising solar cell results on crystalline silicon have been achieved by means of SiN_X laser ablation in combination with alternative metallization methods for the formation of the front contacts, such as evaporation of metal seed layers, evaporation of complete metal stacks, and selective electrochemical deposition of metal contacts. Table 3.8 presents a list of notable photovoltaic devices that employed SiN_X laser ablation during its fabrication process.

Table 3.8. Results of high-efficiency crystalline silicon solar cells incorporating SiN_X laser ablation and alternative front surface metallization processes.

Thickness [µm]	Resistivity [Ω cm]	Substrate	Area [cm^2]	V_{OC} [mV]	J_{SC} [mA/cm^2]	FF	η [%]	Reference
200	–	p-CZ-Si	–	637	37.3	0.779	18.5	[142]
200	–	p-CZ-Si	148.6	639	38.4	0.791	19.4	[143]
250	1.0	p-FZ-Si	4.0	639	38.0	0.786	19.1	[81]
250	1.0	p-FZ-Si	4.0	651	39.4	0.807	20.7	[144]

The first and second results presented above were obtained on industrial p-type Czochralski-grown crystalline silicon substrates. The solar cells were large area devices, with similar size to those produced in industrial factories. In the first case, researchers compared the performance of laser ablated front contacts with line and point opening designs. Best results were obtained with line openings, but point openings also presented quite similar performances to the former. In the second case, researchers evaluated a variety of different metal combinations to form the front surface contacts, such as titanium, tantalum, and nickel, amongst others. Best results were obtained with evaporated titanium as a seed layer, which was subsequently electrochemically plated with copper. Nevertheless, titanium might not be the best choice when considering economical aspects, since it cannot be selectively plated onto the silicon surface. Additionally, the vacuum evaporation

method employed to deposit titanium on the samples is normally avoided in industrial production of solar cells, due to complexity and cost issues.

The two last results presented in Table 3.8 were obtained on high quality p-type float zone silicon substrates, using a relatively thicker substrate, with 250 μm thickness. The solar cells were laboratory-scale devices, with considerably smaller areas than those used on industrial processes. Differently from the samples discussed in the previous paragraph, the metallization process employed was light-induced plating (LIP), a selective electrochemical deposition method. The devices were capable of reaching very good efficiencies, with a remarkably high short-circuit current density for the last device presented on the table. These results indicate the promising potential of SiN_X laser ablation combined with alternative metallization methods, especially self-aligned approaches.

4. DEVELOPMENT OF SILICON SOLAR CELLS WITH LASER-FIRED CONTACTS

In this chapter the methods, experiments, and results of the work that was done at NT-Solar R&D facilities, in PUCRS, Brazil are presented and analysed. Work was focused on the development of p-type crystalline silicon solar cells processed with a laser firing method for the formation of the rear contacts, as well as the optimization of a conveyor belt furnace annealing step for the thermal treatment of samples after laser processing. The front surface metallization was performed using screen-printing technology, similar to the one applied in industrial processes.

Solar cells were developed using p-type (boron doped) solar-grade CZ-Si wafers, with <100> crystallographic orientation, (100 ± 0.5) mm diameter, (200 ± 30) μm thickness, and base resistivity range of 1-20 Ω cm. For this resistivity range, the base boron doping is between 1.5 x 10^{16} cm^{-3} and 6.7 x 10^{14} cm^{-3}, respectively [57]. From each monocrystalline silicon wafer, nine square n^+pp^+ solar cells with 2.04 cm side (total area of 4.16 cm^2) were fabricated.

4.1. Processing Sequences and Methods for Solar Cells with Laser-Fired Contacts

Solar cells were produced by two distinct process sequences. The first process, summarized in the flowchart diagram of Figure 4.1, was used for the experimental evaluation of different laser processing parameters for the formation of the rear contacts of the solar cells.

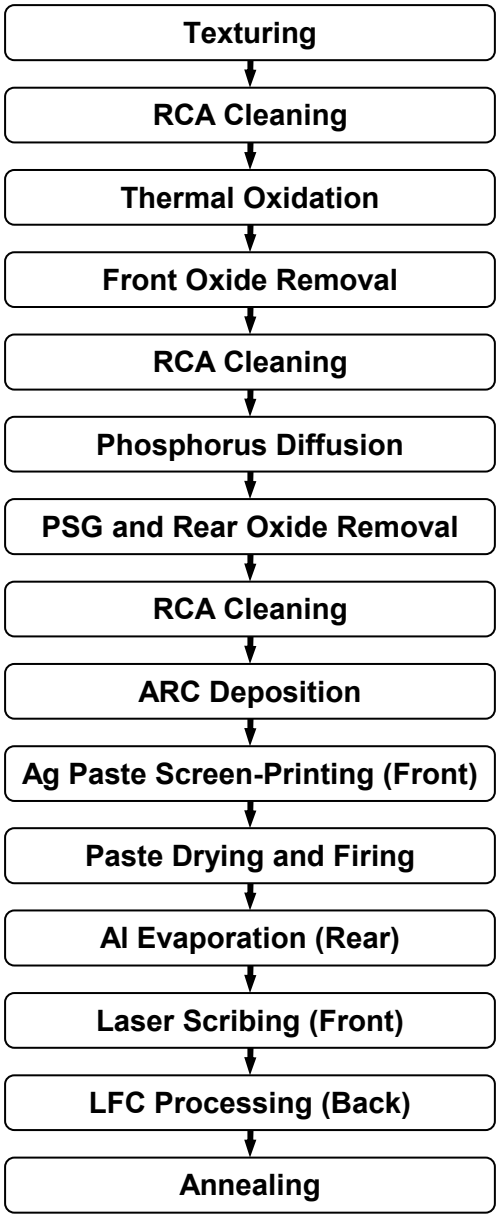

Figure 4.1. Flowchart diagram used for the optimization of laser parameters to develop LFC solar cells without rear oxide passivation layer.

The processing steps outlined in Figure 4.1 are described throughout this chapter. The LFC process developed for the formation of the rear contact was initially evaluated without the implementation of rear surface passivation. The aim of this preliminary analysis was to evaluate and optimize the laser processing parameters, in order to obtain an adequate contact between the aluminium metal layer and the silicon substrate. Additionally, the annealing conditions (temperature and speed of the conveyor belt furnace) after LFC processing were investigated and optimized.

After the determination of the initial conditions for the production of laser-processed rear contacts for solar cells, the best process parameters were used on a new processing sequence. The sequence was further divided into two groups (Groups B and A), according to the method employed for the removal of the phosphorus silicate glass (PSG), a phosphorus-rich layer formed during the quartz tube furnace phosphorus diffusion step.

The removal of the PSG layer on samples from Group B was performed by initially protecting the rear surface of wafers with a photoresist layer before the removal of the PSG in a buffered HF/F^- aqueous solution, composed of ammonium fluoride and hydrofluoric acid (details in section 4.1.1.3). Consequently, Group B samples had a thicker rear oxide, which still contained phosphorus atoms in the silicon oxide passivation layer. Differently, the PSG removal of samples from Group A was performed by submerging wafers in the buffered HF/F^- solution without protecting the rear surface silicon oxide. This resulted in a thinner rear oxide, which may contain less phosphorus atoms. The objective of this procedure was to evaluate the effect that the reduction of phosphorus atoms might have on solar cell performance.

The structure of the LFC solar cells developed throughout this chapter is described in Figure 4.2.

The solar cell design included random pyramid texturing on the front and rear surfaces, a homogeneous phosphorus emitter on the front surface, a TiO_2 ARC with approximately 68 nm, screen-printed front surface metallization similar to the process used in industrial production, a rear surface dielectric passivation layer of thermally-grown silicon dioxide, covered with an evaporated aluminium layer, and laser-fired rear contacts.

Batches of 5 CZ-Si wafers were used in each fabrication process. Samples from the same batches were used for comparative studies, such as: different laser processing parameters (i.e. pumping lamp current, q-switch frequency, rear contact distance); thermal treatment conditions (i.e. conveyor belt furnace annealing speed,

annealing temperature); and the influence of the rear surface aluminium layer thickness (i.e. 2 μm or 4 μm). A description of each processing step presented on the flowchart diagram of Figure 4.1 is provided in the following subsections.

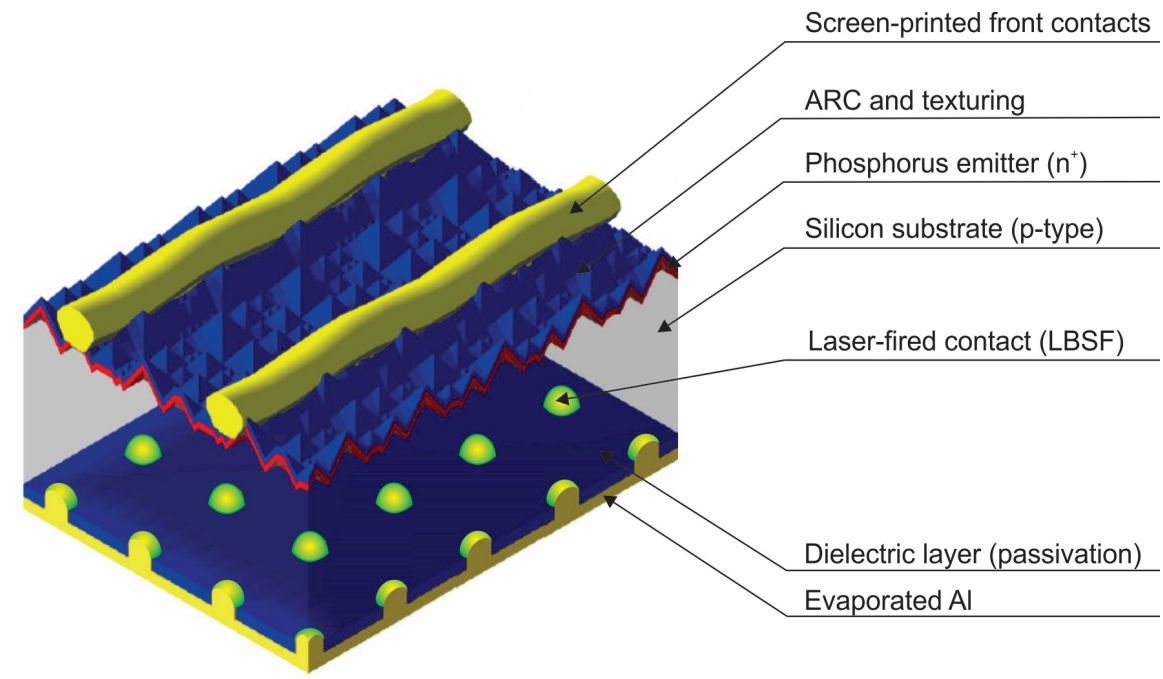

Figure 4.2. Schematic structure of LFC solar cells developed in this work. Both surfaces were textured (feature not shown on the rear surface for clarity purposes). Adapted from [109].

4.1.1. Chemical Processing

Several different chemical processes based on aqueous solutions are employed during the fabrication of crystalline silicon solar cells. Each of these steps has its own function and specific characteristics. The chemical processing steps employed in this work included: anisotropic chemical etching, RCA-1 and RCA-2 cleaning, and diluted HF oxide etching. All aqueous solutions were based on high-resistivity deionised water (DI H_2O) of more than 18 MΩ cm.

4.1.1.1. Anisotropic Chemical Etching

Anisotropic chemical etching (texturing) is a processing technique employed in the fabrication of silicon-based semiconductor devices since the 1960's [145]. It is based on the different etching rates of crystallographic planes of <100>-oriented

silicon wafers. When using the adequate solution compositions, the etching rates of the {100} and {110} planes are higher than that of the {111} planes due to the considerably higher atomic packing density of the latter. Consequently, the {111} planes are exposed, giving rise to randomly-distributed, square-based microscopic pyramids covering the wafer surface [146].

The solution used to texture silicon wafers was composed of a mixture of deionised water, potassium hydroxide, and isopropyl alcohol (IPA). The main chemical reaction of the texturing process can be described by Equation 4.1 [139]:

$$2KOH_{(aq)} + Si_{(s)} + H_2O_{(l)} \rightarrow K_2SiO_{3\,(aq)} + 2H_{2\,(g)} \quad (4.1)$$

Texturing is important in solar cell applications for two main reasons. First, the process etches off a few micrometers of the surface of the wafer, eliminating unwanted impurities and some of the structural damage caused by the process of sawing silicon ingots into wafers. Second, the random pyramid surface structure reduces the reflectance of the wafer, allowing more photons to penetrate the device and also improving radiation trapping, hence increasing radiation absorption and electron-hole pair generation. The combination of these positive effects results in solar cells with considerably higher electric current densities [147].

The main process parameters in texturing are the chemical composition of the etching solution, the process temperature, and the process time. By fine-tuning these parameters, one can obtain quite distinct results in regards to both the size of the pyramids and the distribution of such structures throughout the silicon wafer surfaces. In order to guarantee an adequate reproducibility of the texturing process, the technique was first optimized for the silicon wafers employed in this work.

The optimization was carried out experimentally, fixing the processing temperature at (80 ± 2) ºC and varying the other relevant parameters in separate processes: the chemical composition of the texturing solution (while fixing the processing time), or the processing time (while fixing the chemical composition of the texturing solution). No active stirring method was employed in the process. Batches of 5 to 18 wafers were prepared for each processing condition. After texturing, the

silicon wafers were analysed in respect to the homogeneity of the micropyramids and reflectance. The surface analysis was performed with a XL30 Philips scanning electron microscope (SEM). It focused on two aspects: a qualitative evaluation of the homogeneity of the micropyramids on the surface, and cross-section measurements of the height of selected pyramids that were representative to the sample. Reflectance analysis was performed with a Lambda 950 PerkinElmer UV-VIS-NIR spectrophotometer. The analysis was done by calculating and evaluating the average weighted reflectance (ρ_W) of the textured wafers. The ρ_W values take into account the influence of both the solar spectrum and the solar cell spectral response. A detailed definition and mathematical description of ρ_W can be found in references [148], [149]. Usually, such analysis is performed between 350 nm and 1200 nm, which correspond to the spectral region of interest for solar cells. Unfortunately, at the time of research, the equipment was being repaired and the spectral region that could be evaluated was limited to between 400 nm and 850 nm. Nevertheless, this range provides enough information for a comparative experimental optimization of the texturing process. An overview of the experimental results is described in Table 4.1.

The experiment groups of Table 4.1 are separated by thicker horizontal lines. The first seven processes were based on an earlier texturing solution composition that was developed at NT-Solar for a different p-type CZ-Si substrate. Some processes are shown more than once, in different experiment groups. This was done to increase clarity in analysing different parameters of the experimental optimization, such as: IPA concentration (processes 1, 2, 3, 4), KOH concentration (processes 2, 5, 6), and texturing time (processes 2, 7). Process 8 was performed using an etching solution composition similar to that employed at Fraunhofer ISE in pilot plant scale [150]. Unfortunately, this process proved to be incompatible with the setup, reactants, experimental conditions, and silicon substrates used at NT-Solar, resulting in wafers with insufficient pyramid surface coverage and high average weighted reflectance values. In an attempt to adapt the Fraunhofer ISE conditions to NT-Solar, the remaining processes, RLS01 to RLS10, were developed with the intention of reaching low average weighted reflectance values and, simultaneously, pyramid heights of up to approximately 10 µm.

Table 4.1. Experimental parameters and results of the texturing optimization procedure. Process temperature was kept at (80 ± 2) ºC in all experiments. Texturing was performed without stirring.

Process	Chemical Composition of the Texturing Solution	Processing Time [min]	Micropyramid Height [µm] [1]	ρ_W [%] [2]
0	("as-cut" silicon wafer, before texturing)	–	–	26.4
1	80.0 g KOH + 100 ml IPA + 1600 ml H_2O	60	26	12.2
2	80.0 g KOH + 146 ml IPA + 1600 ml H_2O	60	29	11.6
3	80.0 g KOH + 180 ml IPA + 1600 ml H_2O	60	23	11.4
4	80.0 g KOH + 200 ml IPA + 1600 ml H_2O	60	19	11.6
5	70.0 g KOH + 146 ml IPA + 1600 ml H_2O	60	25	11.6
2	80.0 g KOH + 146 ml IPA + 1600 ml H_2O	60	29	11.6
6	90.0 g KOH + 146 ml IPA + 1600 ml H_2O	60	28	12.2
7	80.0 g KOH + 146 ml IPA + 1600 ml H_2O	40	26	11.9
2	80.0 g KOH + 146 ml IPA + 1600 ml H_2O	60	29	11.6
8	16.1 g KOH + 112 ml IPA + 1500 ml H_2O	40	6	12.9
RLS01	17.2 g KOH + 120 ml IPA + 1600 ml H_2O	40	5	13.3
RLS02	25.0 g KOH + 120 ml IPA + 1600 ml H_2O	40	9	11.9
RLS03	35.0 g KOH + 122 ml IPA + 1600 ml H_2O	40	11	11.8
RLS04	17.2 g KOH + 70 ml IPA + 1600 ml H_2O	40	9	12.7
RLS05	17.2 g KOH + 90 ml IPA + 1600 ml H_2O	40	8	13.5
RLS01	17.2 g KOH + 120 ml IPA + 1600 ml H_2O	40	5	13.3
RLS06	25.0 g KOH + 90 ml IPA + 1600 ml H_2O	40	10	11.8
RLS07	25.0 g KOH + 105 ml IPA + 1600 ml H_2O	40	9	12.1
RLS02	25.0 g KOH + 120 ml IPA + 1600 ml H_2O	40	9	11.9
RLS08	25.0 g KOH + 150 ml IPA + 1600 ml H_2O	40	9	12.8
RLS09	35.0 g KOH + 105 ml IPA + 1600 ml H_2O	40	13	11.9
RLS03	35.0 g KOH + 122 ml IPA + 1600 ml H_2O	40	11	11.8
RLS10	35.0 g KOH + 150 ml IPA + 1600 ml H_2O	40	11	12.6

[1] Pyramid height values were obtained by cross-section SEM measurements of textured wafers.

[2] Average weighted reflectance values calculated in the range 400-850 nm.

From the above results, it is possible to notice some important trends. In respect to the volume of IPA used, the reaction etch rate is inversely proportional to the concentration of IPA in the initial solution [151]. This results in lower pyramid heights and lower pyramid surface coverage for higher volumes of IPA, considering similar processing times. Therefore, it is possible to control, to some extent, the texturing rate through the concentration of IPA. This behaviour can be clearly

observed in the following experimental groups: processes 2, 3, and 4; processes RLS04, RLS05, and RLS01; processes RLS06, RLS07, and RLS01; and processes RLS09 and RLS03. Although the same trend would be expected in process 1, the solution had a significantly lower concentration of IPA then other 60 minutes processes and measurement uncertainty was relatively high. This led to an inhomogeneous surface morphology of the textured wafers. This was caused by excessive accumulation of hydrogen gas on the surfaces of the wafers and influenced the pyramid height and pyramid surface coverage of these samples [152]. For processes RLS08 and RLS10 the pyramid surface coverage was significantly lower than their corresponding counterparts, confirming a lower etch rate and efficacy with the increased concentration of IPA in the initial solution composition.

Regarding the mass of KOH, the reaction etch rate is directly proportional to the concentration of KOH in the initial solution. This results in increasing pyramid heights for higher masses of KOH, as can be observed in processes 5, 2, and 6. This behaviour can be also clearly observed in processes RLS01, RLS02, and RLS03.

When considering the processing time, the silicon etching is directly proportional to the duration of the reaction, as would be expected in this case. This is confirmed in processes 7 and 2, with higher pyramid heights for the 60 minutes process in comparison to the 40 minutes process.

Processes RLS03 and RLS06, had micropyramid heights of approximately 10 μm, high pyramid surface coverage, and lower average weighted reflectance values. Nevertheless, the homogeneity of samples produced with process RLS03 was higher than those of samples produced with process RLS06. Additionally, process RLS03 showed the lowest average weighted reflectance when compared to other RLS texturing processes with micropyramid heights in the 10 μm range, with a ρ_W value of only 11.8 %.

Although IPA does not participate directly on the chemical reaction governing texturing, it is an important additive, used to improve the control over the KOH etch rate of silicon. If the etch rate of silicon is not kept at a controlled level, the silicon wafer will be etched too fast and become polished instead of textured. Additionally,

since the reaction is performed without stirring, IPA is also essential to improve the wettability of the rough silicon surface [153]. This helps the removal of hydrogen gas bubbles formed during the etching reaction. When attached to the silicon surface, these hydrogen bubbles create a gap between the silicon surface and the etching solution, preventing the chemical reaction in the region to proceed as expected. This results in inhomogeneous etching on the regions of the wafer surface with attached hydrogen bubbles. Since the reaction takes place at a temperature very close to the boiling point of IPA (approximately 82.5 ºC), this reactant is continuously evaporating during the reaction [152].

Therefore, after a comprehensive development and optimization of the texturing process, process RLS03 was defined as the standard procedure for samples produced in this chapter. The texturing step was performed as follows: the “as-cut” silicon wafers were submerged for 40 minutes in a texturing solution composed of KOH : isopropyl alcohol (IPA) : DI H_2O (35.0 g : 122 ml : 1600 ml) and kept at a temperature of (80 ± 2) ºC with the aid of a water thermostatic bath, without active stirring. The textured structures featured pyramid heights between 5-11 µm and a high pyramid surface coverage. After applying the optimized texturing step, the average weighted reflectance of wafers was significantly reduced from 26.4 % down to 11.8 % for the interval between 400-850 nm.

Figure 4.3 presents a comparison of SEM images of silicon wafers before and after the optimized texturing process. The “as-cut” silicon substrate presents an irregular but essentially flat surface, with small roughness (difference between peaks and valleys below 5 µm) caused by sawing damage during fabrication of individual silicon wafers from the Czochralski-grown silicon ingots. This flat surface is responsible for the considerably high reflectance of “as-cut” wafers. Differently, the textured substrate features random pyramids of heights between 5-11 µm, covering the whole surface of the wafer. A comparison of the reflectance curves of “as-cut” and textured wafers for the active spectral range of a solar cell is available in section 4.1.4.

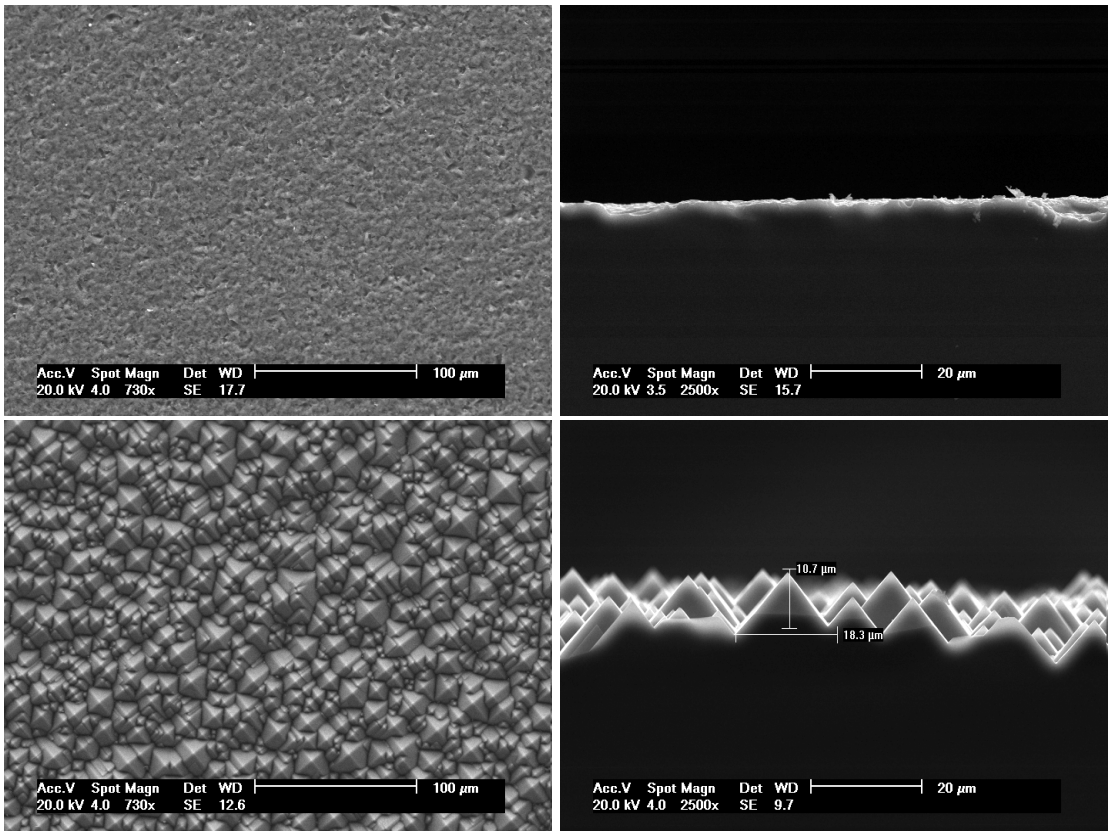

Figure 4.3. SEM images (top and cross-section views) of “as-cut” (upper images) and textured (lower images) silicon wafers used in this chapter’s experiments.

4.1.1.2. RCA-1 and RCA-2 Cleaning

Adequate cleaning processes are essential for the fabrication of high-efficiency crystalline silicon solar cells, especially before high-temperature thermal processes, when unwanted impurities could diffuse into the semiconductor material. Contaminants can cause degradation of electrical properties, formation or nucleation of crystal defects, as well as decrease minority carrier lifetime. Metallic contaminants are especially critical to silicon solar cell performance, as they may diffuse into the substrate during high-temperature processing and introduce energy levels (traps) in the forbidden region of the energy bandgap [154].

In this work, an adapted version of the standard and widely employed RCA (Radio Corporation of America) cleaning procedure, initially developed by Werner Kern in the 1960’s, was be employed [155]. In this method, wafers were first submerged for approximately 10 minutes in a RCA-1 solution, composed of NH_4OH :

H_2O_2 : DI H_2O (ratio 1 : 1 : 5 in volume) and kept at 70-80 ºC. This step oxidizes and solubilises light organic substances, small particles, and some of the metallic impurities at the wafer surfaces. The reaction was halted by cleaning wafers with deionised water. Afterwards, wafers were submerged for approximately 10 minutes in a RCA-2 solution, composed of HCl : H_2O_2 : DI H_2O (ratio 1 : 1 : 5 in volume) and kept at 70-80 ºC. This step removes heavy metal contaminants, alkalis and metal hydroxides from the wafer surface. The reaction was halted by cleaning wafers with deionised water. Additionally to cleaning the wafers, this procedure forms a thin protective oxide on the silicon surface.

4.1.1.3. Acid Etching of Phosphorus Silicates and Oxides

Removal of native or grown oxides and silicates (i.e. phosphorus silicate glass) from the silicon surface was performed by chemical etching, submerging the wafers in a diluted acidic solution composed of HF : DI H_2O (ratio 1 : 30 in volume). The procedure was completed by cleaning wafers with deionised water.

For single-side removal of silicon oxide, wafers with silicon dioxide on both surfaces had one surface protected by a photoresist layer. Afterwards, the wafers were submerged in a buffered acidic solution composed of HF : NH_4F : DI H_2O. In sequence, wafers were cleaned with deionised water. Later, the photoresist protecting was removed by submerging the wafers first in acetone, and then into isopropyl alcohol (IPA). Following the latter step, wafers were cleaned with deionised water. Lastly, wafers were cleaned using the adapted RCA-1 and RCA-2 sequences previously described.

A similar procedure was performed to remove the phosphorus silicate layer of LFC samples from Groups B and A, studied in detail in sections 4.4 and 4.5, respectively.

4.1.2. Thermal Oxidation and Passivation

Surface passivation is considered an important step for the fabrication of high-efficiency solar cells. The overall aim of passivation methods is to reduce as much as

possible losses caused by minority carrier recombination in the wafer surface, which impact the devices mostly on its electrical properties (mainly voltage and current density). This is important because, in high quality or very thin silicon substrates, the diffusion length of minority charge carriers exceeds the thickness of the bulk of the device. Consequently, both the bulk and the surfaces of the solar cell are electronically active and susceptible to recombination of photogenerated electron-hole pairs.

At any bare silicon surface, there are several energy states that could act as recombination centres. These arise from the surface structure of the material, where atoms with incomplete (or dangling) bonds are responsible for additional surface states within the energy bandgap of the material. In order to reduce surface recombination losses, two different types of strategies are generally employed [156]: reduction of the concentration of minority charge carriers at the surface, as elucidated for the Al-BSF and LBSF concepts described in Chapter 2, and reduction of the density of surface states, also called passivation methods.

The standard and most investigated passivation method for silicon devices is thermal oxidation in a conventional quartz tube furnace. The process is performed at elevated temperatures of around 1000 ºC using high-purity oxygen and nitrogen gas flows. It is referred to as “dry oxidation” (as opposed to “wet oxidation”, which uses high-purity water vapour as a reactant) and is based on the straightforward chemical reaction described in Equation 4.2 [156]:

$$Si_{(s)} + O_{2\,(g)} \rightarrow SiO_{2\,(s)} \qquad (4.2)$$

At high temperatures, oxygen reacts with silicon atoms at the wafer surface and produces an amorphous layer of silicon dioxide. In sequence, other oxygen molecules diffuse through this oxide layer and, upon reaching the now underlying silicon surface, react with other silicon atoms, thickening the oxide layer. The reaction displaces the Si-SiO_2 interface to deeper regions of the wafer, increasing the interface quality and improving passivation properties. Since oxygen diffusion through the silicon oxide layer is a slow process, the thicker the layer becomes, the slower the reaction rate progresses. This turns out to be an obstacle when growing

thick silicon oxide layers, as the long oxidation times needed would reduce throughput and indirectly increase fabrication costs. It is the standard passivation method employed by the microelectronic industry because of its relatively simple processing, reasonable costs and excellent properties [156].

In this work, thermal oxidation of silicon wafers was carried out in a conventional quartz tube furnace, with high-purity nitrogen and oxygen gas flows. Oxidation was performed at 1000 ºC for 120 minutes under a high-purity oxygen flow, resulting in a silicon dioxide layer approximately 100 nm thick.

Another application of the thermal silicon oxide was as diffusion mask, to avoid the diffusion of elements into specific regions of the wafer. This was used to avoid the diffusion of phosphorus into the rear surface of solar cells from Groups B and A. The procedure for removing this masking oxide and cleaning the samples thereafter is described in more detail in sections 4.1.1.3, 4.4, and 4.5.

4.1.3. Phosphorus Diffusion in Quartz Tube Furnace

The diffusion of phosphorus into the silicon substrates for the formation of the homogeneous n^+ emitter layer (i.e. the p-n junction on p-type wafers) was performed in a conventional quartz tube furnace. The emitter was formed by one-step diffusion at a diffusion temperature of 875 ºC, using high-purity nitrogen as carrier gas for a $POCl_3$ liquid dopant source. A high-purity oxygen flow was also used, which reacts with $POCl_3$ resulting in the deposition of P_2O_5 on the wafer surfaces, as described in Equation 4.3 [139]:

$$4POCl_{3\,(g)} + 3O_{2\,(g)} \rightarrow 2P_2O_{5\,(s)} + 6Cl_{2\,(g)} \qquad (4.3)$$

The Cl_2 gas liberated in the reaction serves as a cleansing agent and helps to keep the furnace free of contaminants, by forming volatile compounds with metallic impurities. Phosphorus atoms are introduced into the silicon through the reaction of P_2O_5 and O_2 at the wafer surfaces, forming phosphorus-doped SiO_2, commonly referred to as phosphorus silicate glass. The PSG then behaves as a solid

phosphorus source during the diffusion process. The chemical reaction that describes the PSG formation is presented below in Equation 4.4 [139]:

$$2P_2O_{5\,(s)} + 5Si_{\,(s)} \rightarrow 5SiO_{2\,(s)} + 4P_{\,(s)} \quad (4.4)$$

After each phosphorus diffusion step, the sheet resistance of wafers was analysed by four point probe resistivity measurements, as described in section 2.2.1.

4.1.4. TiO_2 and Aluminium Deposition by Evaporation

Antireflection coating composed of TiO_2 was deposited by the electron-beam evaporation technique. ARC film thickness was kept at approximately 68 nm in order to maximize the benefits of the ARC film for the solar spectrum considering a maximum photon flux around 560 nm [55]. The main purpose of the ARC film is to reduce the reflection of incoming radiation. Additionally, when adequately chosen, the ARC can also serve as of front surface passivation. In this respect, TiO_2 has been shown to be ineffective for surface passivation of p-type boron-doped silicon wafers featuring a phosphorus-diffused emitter, despite having higher refractive indexes and lower absorption in the visible spectral range than SiN_X [157]. Therefore, the main role of TiO_2 in this work is as ARC.

The average weighted reflectance of textured samples after ARC deposition was further reduced from the initial “as-cut” value of around 26.4 % to 11.8 % after texturing and, finally, to less than 2.0 % for the range between 350-1200 nm, which comprises the spectral range of interest for crystalline silicon solar cells. This ensures a low front surface reflectance and improves the current density of solar cells. A comparison of the reflectance of initial, textured, and textured with ARC wafers is provided in Figure 4.4. The dislocation of the minimum reflectance wavelength from approximately 850 nm for the “as-cut” wafer, down to approximately 560 nm after texturing and ARC deposition can be noticed.

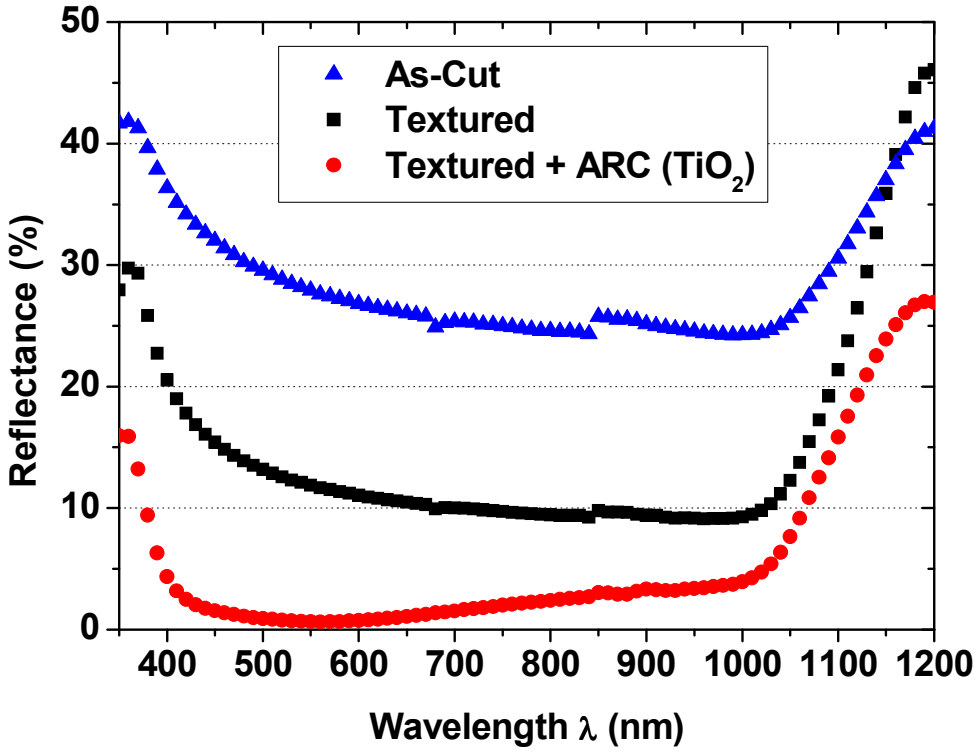

Figure 4.4. Reflectance curves of silicon wafers: "as-cut", textured, and textured with TiO_2 ARC.

Aluminium layers for the rear contact formation of solar cells were deposited by electron-beam evaporation under high-vacuum conditions. For the majority of LFC experiments, the aluminium layer thickness was maintained at approximately 2 µm. One specific experiment compared the influence of the aluminium layer thickness in solar cell performance by employing a layer thickness of approximately 4 µm.

4.1.5. Screen-Printing Metallization of the Front Contacts

Front surface metal contacts were screen-printed on the silicon wafers using a semi-automated industrial screen-printer and silver metallization paste DuPont Solamet® PV159. The paste was dried and subsequently fired at 870 ºC in an infrared lamp-heated three-zone conveyor belt furnace [158]. Both processes were performed under a controlled atmosphere using a filtered dry air flow for cooling.

The front surface mask was the standard screen-printing mask for R&D purposes developed at NT-Solar. It includes nine independent laboratory-scale 2.04 cm x 2.04 cm (4.16 cm^2) solar cells. Figure 4.5 illustrates the layout of the screen-printing mask.

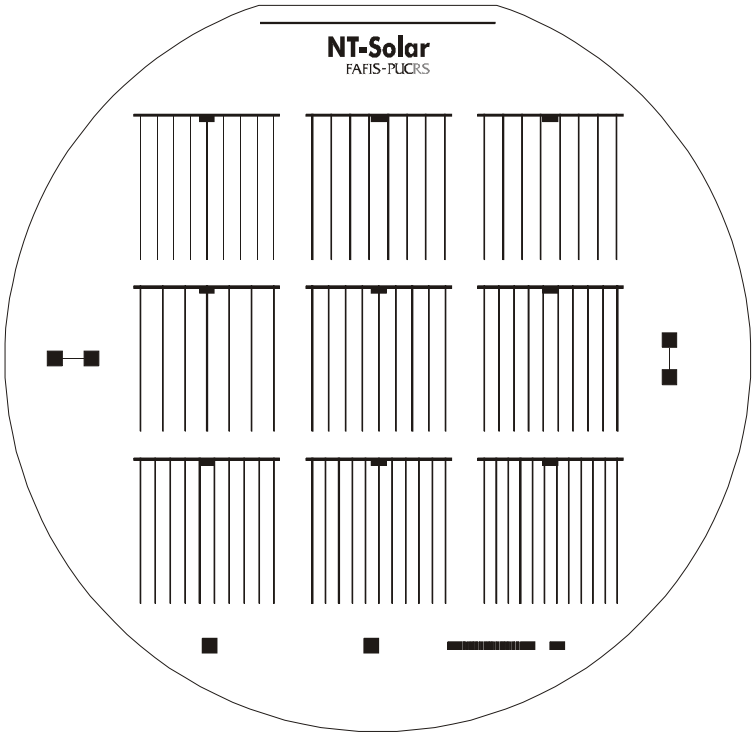

Figure 4.5. Layout of the screen-printing mask used for front surface metallization.

The front metal grid design includes metal fingers of 100 μm width and one busbar with a larger region in the centre for easier electrical characterization. The number of metal fingers of each solar cell varies between 7 and 12, resulting in front contact coverage areas of between 5.2 % and 7.6 %, respectively, as described in Table 4.2.

Table 4.2. Metalized area and shaded fraction of solar cells developed.

Metal Fingers	Samples per Wafer	Metalized Area [cm^2]	Shaded Fraction [%]
7	1	0.22	5.2
8	2	0.24	5.7
9	2	0.26	6.1
10	2	0.27	6.6
11	1	0.29	7.1
12	1	0.31	7.6

4.1.6. Laser Scribing and Laser Processing of the Rear Contacts

The equipment used for laser processes at NT-Solar was a Nd:YAG 4000 lamp-pumped laser system, with a high-precision X-Y table. A schematic representation of the laser system is shown in Figure 4.6. The laser beam emission occurs in the cavity resonator (or optical resonator cavity), composed of a rear mirror, an intracavity, the q-switch controller, the laser source (laser head), and blocking and frontal mirrors. After the resonator, the laser beam is shaped in a secondary optical setup, through beam expander and collimator lenses, and finally guided through the focal system to the sample surface. Since the optical setup has no moving parts, the X-Y table is used to scan the whole surface area of samples with the laser beam. The X-Y table is composed of direct current motors, controlled by a computer numerical control (CNC) device, a microcomputer, and a charge-coupled device (CCD) camera. It is a precise position control device, with a precision and repeatability of approximately ± 2 μm, a movement speed of up to 200 mm/s, and a maximum processing area of 225 cm^2 (150 mm x 150 mm).

The equipment operates in TEM_{00} (transverse electromagnetic mode), emitting a laser beam with pseudo-monochromatic wavelength centred at 1064 nm (fundamental harmonic). The system maximum average power is approximately 17 W. The system is controlled by a q-switch and has a frequency range of 1-33 kHz and a pumping lamp current range of 1-33 A, when operating under this mode. An automatic shutter controls the exposure time, as well as the number of laser pulses. Processing can be monitored with the aid of the CCD camera.

The laser system was used mainly for two processes: initially, for laser scribing of the solar cells, to define the total area (4.16 cm^2) of each solar cell. After laser scribing and prior to LFC processing, samples were mechanically cleaved. Schematics of the laser processed areas on the front side of the wafers and on the rear side of the solar cells is presented in Figure 4.7.

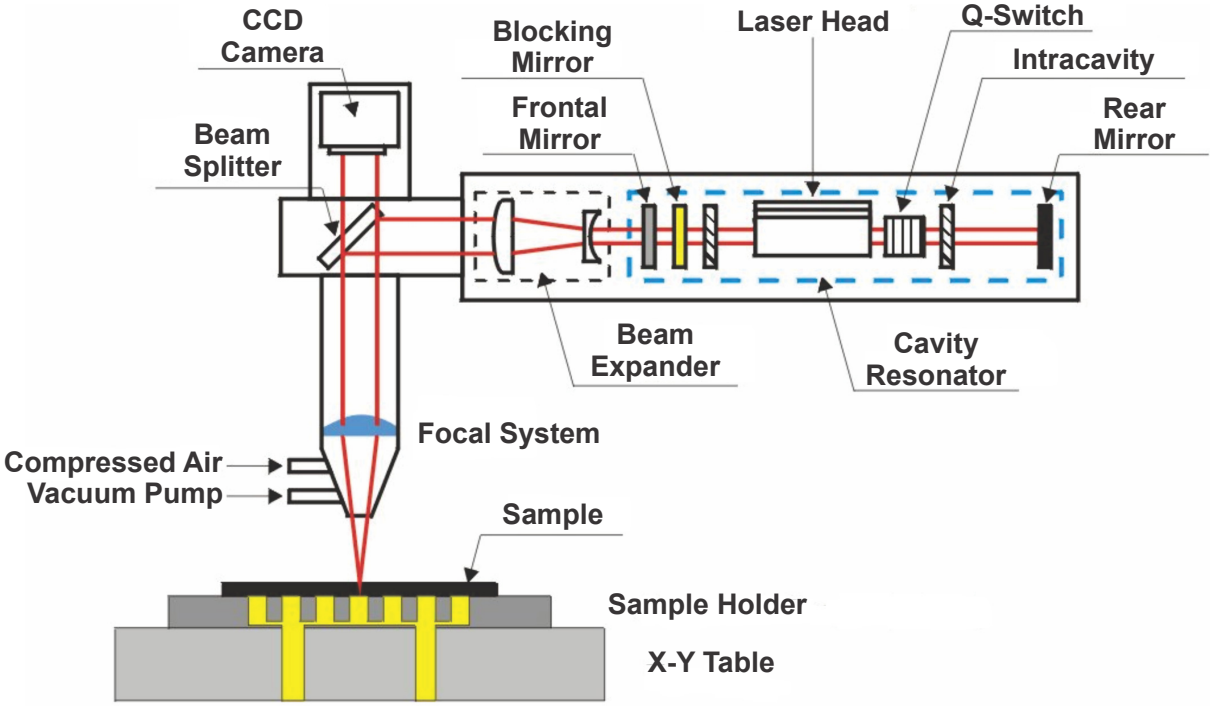

Figure 4.6. Schematic representation of the Nd:YAG laser system available at NT-Solar and employed in this chapter. Adapted from [159].

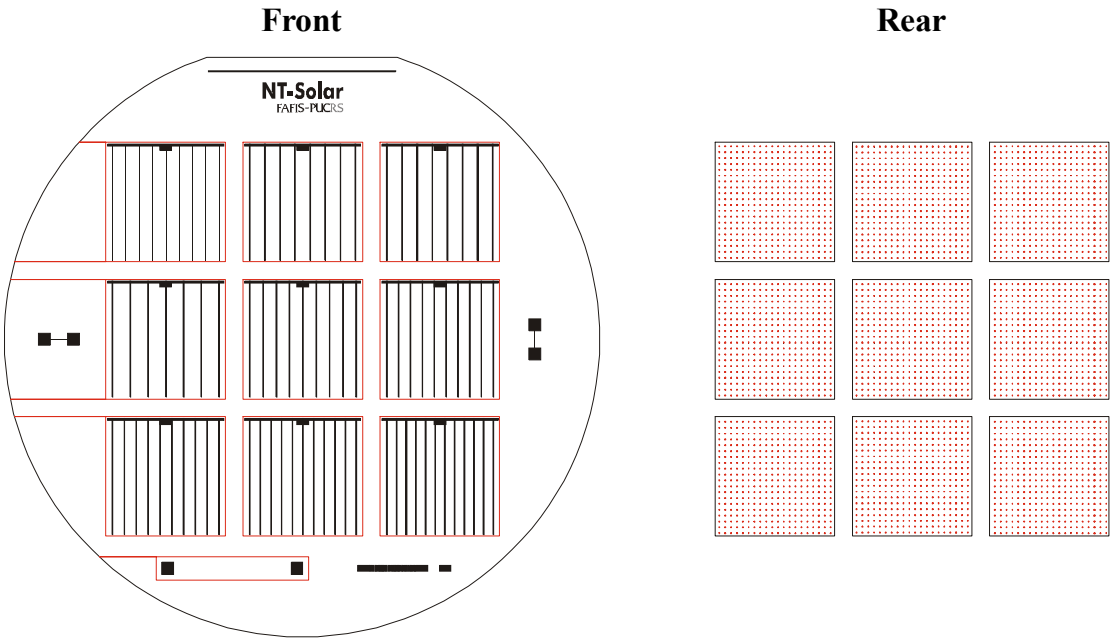

Figure 4.7. Schematics of the laser scribing areas at the front surface (left, red lines) and of the LFC-processing of the rear surface for local contact formation (right, red dots).

The laser parameters studied and optimized in this work were the following: pumping lamp current (range from 22.0 A to 33.0 A), frequency of the q-switch

(range from 1.0 kHz to 30.0 kHz), and distance between the rear contacts (range from 0.25 mm to 1.50 mm).

4.1.7. Thermal Treatment

As discussed in section 3.2.6, a crucial step to improve the performance of LFC solar cells is a thermal treatment (annealing) after laser processing. This was performed on the same conveyor belt furnace to be used during screen-printing metallization. The process was optimized by empirical experimentation, with a group of solar cells processed on the same wafer substrate. This permits a reliable evaluation of annealing parameters, excluding the influence of other processing steps. The parameters that were analysed are annealing temperature (range from 300 ºC to 650 ºC) and conveyor belt speed (range from 33 cm/min to 220 cm/min).

An example of the front and rear structures of a finished solar cell incorporating the processing steps described in this chapter is provided in Figure 4.8.

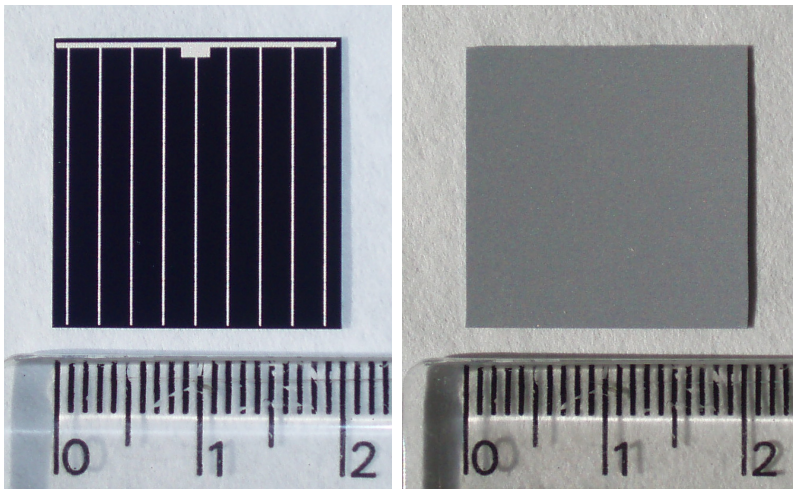

(a) **(b)**

Figure 4.8. Pictures of the front (a) and rear (b) sides of a finished laboratory-scale crystalline silicon solar cell incorporating laser-fired contacts, produced during this work at NT-Solar.

4.2. Characterization Methods for Samples and Solar Cells with Laser-Fired Contacts

A group of characterization techniques was employed as tools during sample and solar cell fabrication. Additionally, other characterization methods were applied to finished samples in order to verify their electrical properties. The methods and techniques performed during the development of solar cells with LFC were the following:

1. Electrical parameters (efficiency, fill factor, short-circuit current, open-circuit voltage), extracted from illuminated current density-voltage curves. The curves were obtained with the aid of solar simulator built in-house, under standard test conditions (STC – AM1.5G solar spectrum, irradiance of 1000 W/m^2, sample temperature of 25 ºC) [160].

2. External quantum efficiency (EQE) and internal quantum efficiency (IQE), calculated from spectral response and reflectance measurements.

3. Semiconductor sheet resistance obtained by four point probe resistivity measurements.

4. Scanning electron microscopy for topographical evaluation of samples.

5. Optical microscopy for topographical evaluation of samples.

4.3. Solar Cells without Rear Side Passivation

As described earlier, the LFC process was initially optimized without the implementation of SiO_2 rear surface passivation. In this preliminary analysis, samples were fabricated according to the flowchart shown in Figure 4.1. The aim was to evaluate and optimize the laser processing parameters, in order to obtain an adequate contact between the aluminium metal layer and the silicon substrate.

Additionally, the annealing conditions (temperature and speed of the conveyor belt furnace) after LFC processing were optimized.

4.3.1. Influence of the Pumping Lamp Current

The first laser parameter to be evaluated in this step was the pumping lamp current (I_{Lamp}) of the laser system, which is related to the average output power of the laser system (P_L) and the amount of energy reaching the sample during processing. The lamp current was evaluated between 22.0 A and 33.0 A, the latter being the equipment's upper limit for this parameter. For samples processed below 22.0 A, the laser energy was too low and no noticeable effect of the laser process on the aluminium layer was verified. To allow reliable comparison between samples, experiments were performed using a fixed laser frequency of 20.0 kHz and contact pitch (distance between laser-fired point contacts) of 1.00 mm. The sheet resistances of the two processes used in this evaluation were: (26 ± 4) Ω/sq for process 01, equivalent to a phosphorus surface concentration (C_S) of approximately 1.8 x 10^{20} cm^{-3}, and (41 ± 6) Ω/sq for process 04, equivalent to a C_S of approximately 1.0 x 10^{20} cm^{-3}, respectively. Results are presented in Table 4.3 and a selection of representative J-V curves are shown in Figure 4.9.

For the lamp current range evaluated in this experiment, a clear trend of increasing electrical performance of the solar cells with increasing lamp current was verified. This is mainly caused by a consistent increase in V_{OC}, as a consequence of an improved rear contact formation and higher diffusion of aluminium into the silicon substrate, which improves the LBSF. The sum of these effects is responsible for higher solar cell efficiencies. Although the FF of samples also shows an increasing trend for increasing lamp current, the overall low FF of samples indicates that solar cells are strongly influenced by series resistance, resulting in a limiting efficiency of 11.3 % for the highest lamp current of 33.0 A.

From the J-V curves presented in Figure 4.9, an increase in V_{OC} values with an increase in pumping lamp current can be clearly noticed when comparing the curves of solar cells processed with 24.0 A and 28.0 A pumping lamp current.

Table 4.3. Electrical parameters of solar cells with laser-firing of the rear contacts, processed under different pumping lamp currents. Fixed laser processing parameters were: 20.0 kHz q-switch frequency and 1.00 mm contact pitch.

Process	Solar Cell	I_{Lamp} [A]	P_L [W]	V_{OC} [mV]	J_{SC} [mA/cm^2]	FF	η [%]
01	01N	22.0	2.1	520.7	19.7	0.295	3.0
	01O	23.0	2.9	555.0	27.7	0.584	9.0
04	04A	24.0	3.6	482.5	30.7	0.619	9.2
	04E	25.0	4.6	498.5	31.0	0.654	10.1
	04F	26.0	5.5	501.1	31.1	0.679	10.6
	04I	27.0	6.6	510.4	30.3	0.691	10.7
04b	04bA	28.0	7.7	524.4	30.5	0.658	10.5
	04bE	29.0	8.6	518.7	30.7	0.682	10.8
	04bI	30.0	9.5	525.8	29.5	0.697	10.8
04c	04cA	31.0	10.5	533.9	30.1	0.640	10.3
	04cB	32.0	11.5	527.6	31.2	0.669	11.0
	04cE	33.0	13.0	532.2	30.9	0.686	11.3

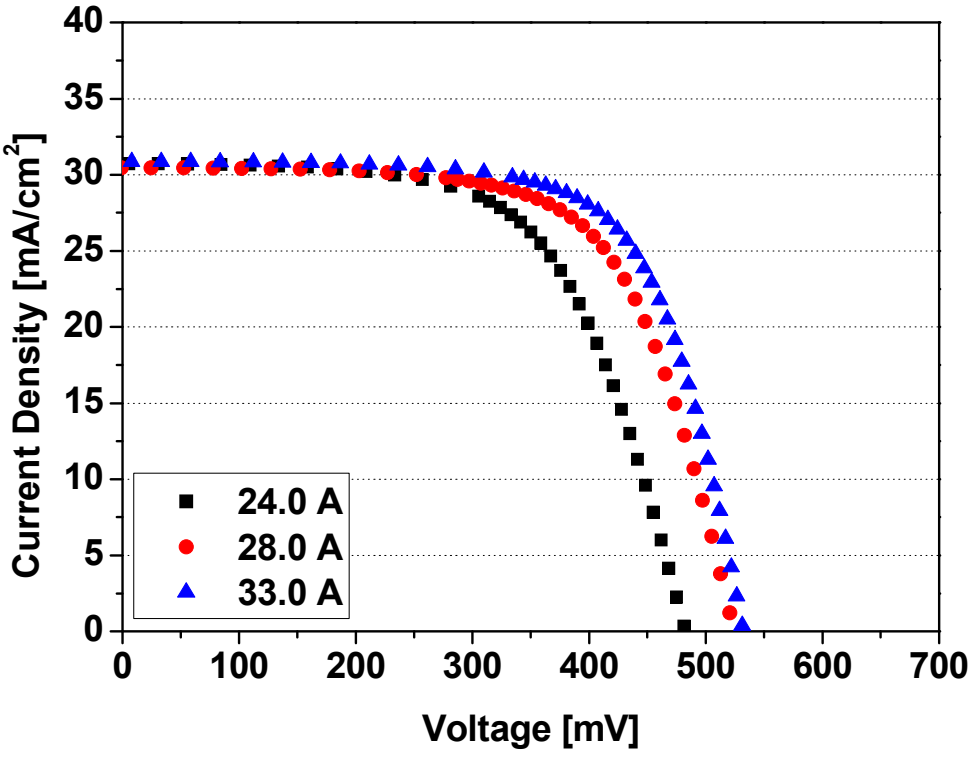

Figure 4.9. J-V curves of LFC solar cells processed with different pumping lamp currents. Fixed laser processing parameters were: 20.0 kHz q-switch frequency and 1.00 mm contact pitch.

4.3.2. Influence of the Q-Switch Frequency

When operating in q-switched mode, the q-switch frequency also influences the average output power of the laser system. Consequently, the energy reaching the sample during the formation of both the rear contacts and the LBSF on the rear surface of the device is influenced by the q-switch frequency employed. The q-switch frequency of the laser system was evaluated between 1.0 kHz and 30.0 kHz, which comprises the whole frequency range of the equipment available at NT-Solar. Results are presented for solar cells with emitter sheet resistances of (26 ± 4) Ω/sq and (41 ± 6) Ω/sq in Table 4.4 and Table 4.5, respectively.

Table 4.4. Electrical parameters of solar cells with laser-firing of the rear contacts, processed under different q-switch laser frequencies. Fixed laser processing parameters were: 24.0 A pumping lamp current, and 1.00 mm contact pitch. Emitter sheet resistance of samples was (26 ± 4) Ω/sq.

Process	Solar Cell	f [kHz]	P_L [W]	V_{OC} [mV]	J_{SC} [mA/cm^2]	FF	η [%]
02	02Q	30.0	3.7	525.7	26.5	0.436	6.1
	02P	25.0	3.7	541.1	26.4	0.450	6.4
01	01P	20.0	3.6	562.3	27.8	0.598	9.4

Table 4.5. Electrical parameters of solar cells with laser-firing of the rear contacts, processed under different q-switch laser frequencies. Fixed laser processing parameters were: 24.0 A pumping lamp current, and 1.00 mm contact pitch. Emitter sheet resistance of samples was (41 ± 6) Ω/sq.

Process	Solar Cell	f [kHz]	P_L [W]	V_{OC} [mV]	J_{SC} [mA/cm^2]	FF	η [%]
04	04A	20.0	3.6	482.5	30.7	0.619	9.2
	04C	15.0	3.6	479.6	31.5	0.649	9.8
	04B	10.0	3.6	478.0	31.6	0.634	9.6
	04D	5.0	3.3	480.8	31.3	0.591	8.9
04c	04cC	1.0	1.4	425.7	28.2	0.501	6.0

When comparing the results from Tables 4.4 and 4.5, the significant difference in J_{SC} between the two groups of samples can be attributed to the emitter sheet resistance. J_{SC} increases with increasing emitter sheet resistance due to a reduction in minority charge carrier recombination in the emitter region caused by the lower concentration of phosphorus atoms. Consequently, the response of solar cells to shorter wavelengths between 350 nm and 450 nm (blue response) is improved.

From the results presented in both tables, the same trend for q-switch frequency parameters was found: best results were obtained for frequencies between 10.0 kHz and 20.0 kHz, with which solar cells having superior FF values were fabricated.

To confirm these results, a new batch of solar cells was fabricated with a homogeneous emitter of sheet resistance (41 ± 6) Ω/sq, employing q-switch frequencies between 10.0 kHz and 25.0 kHz and using the best parameters for the pumping lamp current (I_{Lamp}). The results of are shown in Table 4.6, for I_{Lamp} of 32.0 A, and Table 4.7, for I_{Lamp} of 33.0 A.

Table 4.6. Electrical parameters of solar cells with laser-firing of the rear contacts, processed under different q-switch laser frequencies. Fixed laser processing parameters were: 32.0 A pumping lamp current, and 1.00 mm contact pitch. Emitter sheet resistance of samples was (41 ± 6) Ω/sq.

Process	Solar Cell	f [kHz]	P_L [W]	V_{OC} [mV]	J_{SC} [mA/cm^2]	FF	η [%]
04c	04cB	20.0	11.5	527.6	31.2	0.669	11.0
04d	04dC	17.5	11.4	532.4	30.9	0.687	11.3
	04dA	15.0	11.3	539.7	30.2	0.659	10.7
	04dB	10.0	11.0	506.5	28.8	0.432	6.3

Table 4.7. Electrical parameters of solar cells with laser-firing of the rear contacts, processed under different q-switch laser frequencies. Fixed laser processing parameters were: 33.0 A pumping lamp current and 1.00 mm contact pitch. Emitter sheet resistance of samples was (41 ± 6) Ω/sq.

Process	Solar Cell	f [kHz]	P_L [W]	V_{OC} [mV]	J_{SC} [mA/cm^2]	FF	η [%]
04c	04cH	25.0	16.7	535.1	30.2	0.699	11.3
	04cE	20.0	13.0	532.2	30.9	0.686	11.3
	04cF	15.0	12.8	528.5	29.9	0.613	9.7
	04cG	10.0	12.5	522.4	29.0	0.537	8.1

In comparison to results from Tables 4.4 and 4.5, data summarized in Tables 4.6 and 4.7 confirm that, by performing the laser-firing step with the optimized pumping lamp current, it is possible to improve the electrical characteristics of solar cells, especially in regards to the FF values. On the one hand, the variation in q-switch frequency did not influenced V_{OC} values significantly. On the other hand, the J_{SC} and FF show an increase with increasing q-switch frequency. For higher q-switch

frequency values, an improvement in the shunt resistance of the solar cells was observed, as can be seen from Figure 4.10.

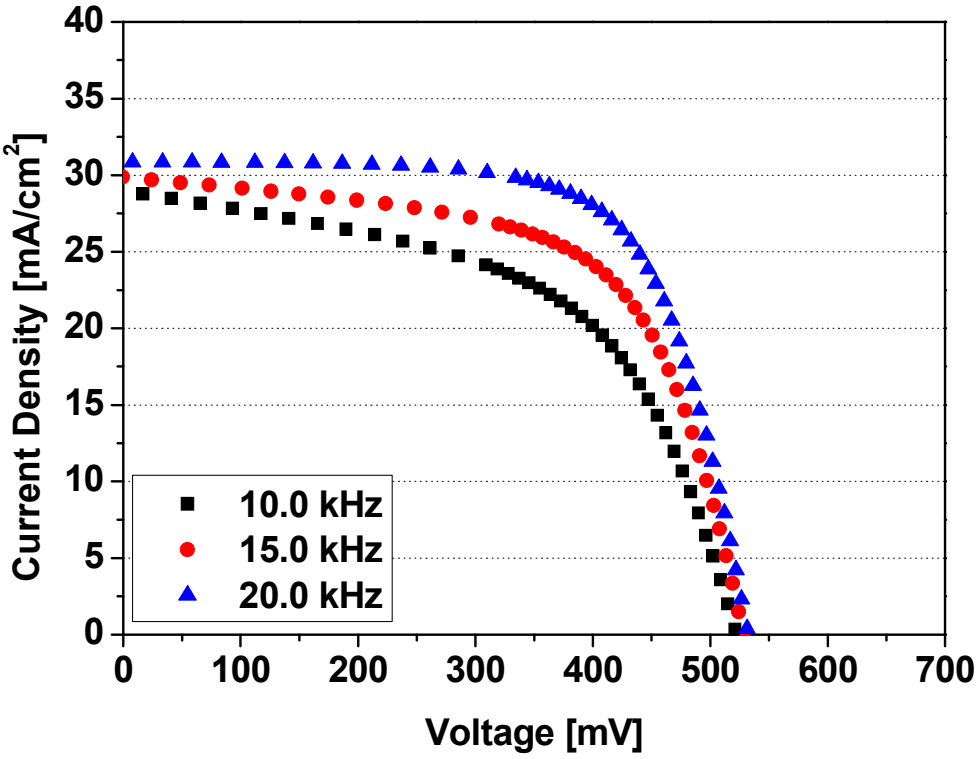

Figure 4.10. J-V curves of LFC solar cells processed with different q-switch frequencies. Fixed laser processing parameters were: 33.0 A pumping lamp current and 1.00 mm contact pitch. Emitter sheet resistance of samples was (41 ± 6) Ω/sq.

Despite the improvements observed in J_{SC} and FF, devices were still limited by a low FF value, reaching maximum efficiencies of up to 11.3 %, when processed with q-switch frequencies between 17.5 kHz and 25 kHz. For such q-switch frequency range, the FF losses observed in this case can be attributed to high series resistances on the devices.

4.3.3. Influence of the Rear Contact Distance

The distance between the laser-fired rear point contacts of a solar cell (D_P), commonly referred to as the contact pitch, is another parameter that can influence the electrical performance of the devices under development. The distance between rear contacts was evaluated between 0.25 mm and 1.50 mm. First, a preliminary analysis was performed using the following laser processing parameters: 24.0 A

pumping lamp current, 20.0 kHz q-switch frequency, and 3.6 W laser power. After the optimization of the pumping lamp current and frequency values, a second evaluation of D_P was performed using the following optimized laser processing parameters: 33.0 A pumping lamp current, 20.0 kHz q-switch frequency, and 13.0 W laser power. Results are summarised in Table 4.8 and a selection of representative J-V curves are shown in Figure 4.11.

Table 4.8. Electrical parameters of solar cells with laser-firing of the rear contacts, processed under different rear contact distances. Fixed laser processing parameters provided below for each analysis. Emitter sheet resistance of samples was (41 ± 6) Ω/sq.

First Analysis: I_{Lamp} = 24.0 A, f = 20.0 kHz, P_L = 3.6 W

Process	Solar Cell	D_P [mm]	V_{OC} [mV]	J_{SC} [mA/cm^2]	FF	η [%]
04	04G	1.50	339.9	29.6	0.428	4.3
	04H	1.50	338.1	29.6	0.452	4.5
	04A	1.00	482.5	30.7	0.619	9.2
04b	04bG	0.75	532.3	30.0	0.697	11.1
	04bF	0.50	557.3	30.0	0.731	12.2
	04bH	0.25	572.7	29.8	0.683	11.7

Second Analysis: I_{Lamp} = 33.0 A, f = 20.0 kHz, P_L = 13.0 W

Process	Solar Cell	D_P [mm]	V_{OC} [mV]	J_{SC} [mA/cm^2]	FF	η [%]
04c	04cE	1.00	532.2	30.9	0.686	11.3
04d	04dG	0.75	556.2	29.9	0.658	10.9
	04dF	0.50	568.0	30.1	0.733	12.6
	04dH	0.25	572.0	29.5	0.509	8.6

The influence of the rear contact distance is found to be similar in both cases evaluated. The FF of solar cells is influenced by the distance between rear contacts, increasing significantly when it is increased from 0.25 mm to 0.50 mm. The best results were obtained with a contact pitch of 0.50 mm, as evidenced in Figure 4.11 and on Table 4.8 by samples 04bF and 04dF, resulting in a FF of up to 0.733 and an efficiency of up to 12.6 % for the latter sample, which was processed with improved laser processing parameters. When D_P is increased from 0.50 mm until 1.50 mm, the FF trend is inversely proportional, with values decreasing until reaching their lower limit for the investigated range at a value of 1.50 mm between the rear contacts,

resulting in a low FF of 0.428 and a corresponding efficiency of only 4.3 %. This trend is also clearly noticed in Figure 4.11. Additionally, a reduction on the distance between rear contacts resulted in a direct increase in V_{OC} values in the whole investigated range. This would be expected, as the device is unpassivated and, therefore, an increase in the laser-fired area results directly in an increase in the effect of the LBSFs, formed at the laser-processed zones.

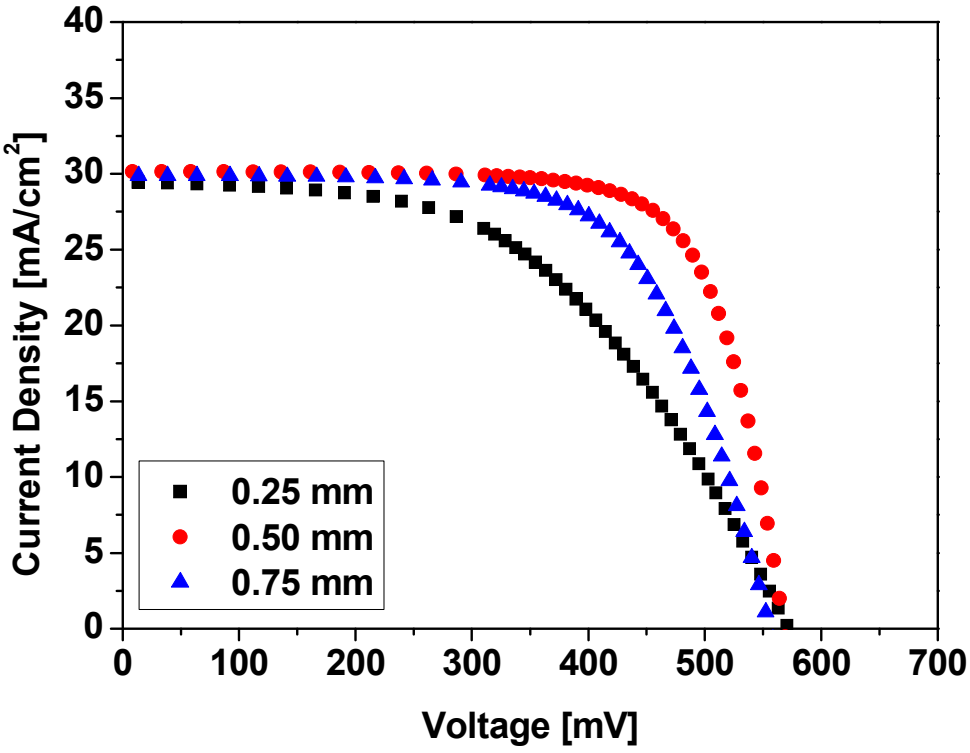

Figure 4.11. J-V curves of LFC solar cells processed with different rear contact distances.

4.3.4. Influence of the Annealing Temperature

As described in section 3.2.6, an annealing process after the laser-firing step is usually necessary to improve the quality of the metal-semiconductor contacts formed at the laser-processed regions, as well as possibly reducing part of the structural stress caused to the crystalline structure of the substrate by the laser radiation.

Initially, the process was evaluated at annealing temperatures (T_A) between 300 ºC and 450 ºC for a fixed conveyor belt speed of 33 cm/min. This was initially

performed as sequential annealing steps using the same solar cell. Electrical characteristics the device subjected to annealing is shown in Table 4.9.

Table 4.9. Electrical parameters of solar cells with laser-firing of the rear contacts, processed sequentially under different annealing temperatures. Fixed laser processing parameters were: 24.0 A pumping lamp current, 20.0 kHz q-switch frequency, 3.6 W laser power, and 1.00 mm contact pitch. Emitter sheet resistance was (26 ± 4) Ω/sq and conveyor belt speed was 33 cm/min. Process 01.

Solar Cell	T_A [ºC]	V_{OC} [mV]	J_{SC} [mA/cm^2]	FF	ΔFF	η [%]
01P	–	562.3	27.8	0.598	–	9.4
	300	568.4	28.0	0.613	+0.015	9.8
	350	574.1	28.8	0.615	+0.017	10.2
	400	572.8	29.0	0.613	+0.015	10.2
	450	555.2	28.6	0.594	-0.004	9.4

Results from this initial experiment indicate that the performance of the laser-processed devices is positively influenced by the annealing process, with improvements in V_{OC}, J_{SC}, and FF values. Best performances were obtained for annealing temperatures of 350 ºC and 400 ºC. The average change in FF (ΔFF = FF after annealing – FF before annealing) was similar for these two temperatures. When annealing was performed at 450 ºC, the solar cell electrical performance was reduced. This suggests that excessive thermal budget during the annealing step can negatively impact the solar cell.

The process was also investigated for a conveyor belt speed of 220 cm/min, a value usually employed when firing screen-printed metal pastes in industrial production. Different solar cells were employed for each annealing temperature. Additionally, laser parameters were based on optimized values from previous studies: 33.0 A pumping lamp current, 20.0 kHz q-switch frequency, 13.0 W laser power, and 0.50 mm contact pitch. The annealing temperature was investigated between 350 ºC and 650 ºC. Results are presented in Table 4.10 and a selection of representative J-V curves is shown in Figure 4.12.

Table 4.10. Electrical parameters of solar cells with laser-firing of the rear contacts, processed under different annealing temperatures. Fixed laser processing parameters were: 33.0 A pumping lamp current, 20.0 kHz q-switch frequency, 13.0 W laser power, and 0.50 mm contact pitch. Emitter sheet resistance was (41 ± 6) Ω/sq and conveyor belt speed was 220 cm/min. Process 04e.

Solar Cell	T_A [ºC]	V_{OC} [mV]	J_{SC} [mA/cm^2]	FF	ΔFF	η [%]
04eA	–	567.7	30.2	0.706	–	12.1
	350	567.2	30.3	0.726	+0.020	12.5
04eB	–	568.0	30.9	0.689	–	12.1
	400	567.4	30.8	0.728	+0.039	12.7
04eD	–	560.0	30.8	0.606	–	10.5
	450	562.9	30.6	0.663	+0.057	11.4
04eG	–	565.7	30.1	0.701	–	11.9
	550	566.5	30.2	0.709	+0.008	12.1
04eH	–	565.5	30.2	0.649	–	11.1
	600	565.9	30.1	0.705	+0.056	12.0
04eI	–	565.7	29.9	0.720	–	12.2
	650	575.8	29.9	0.746	+0.026	12.9

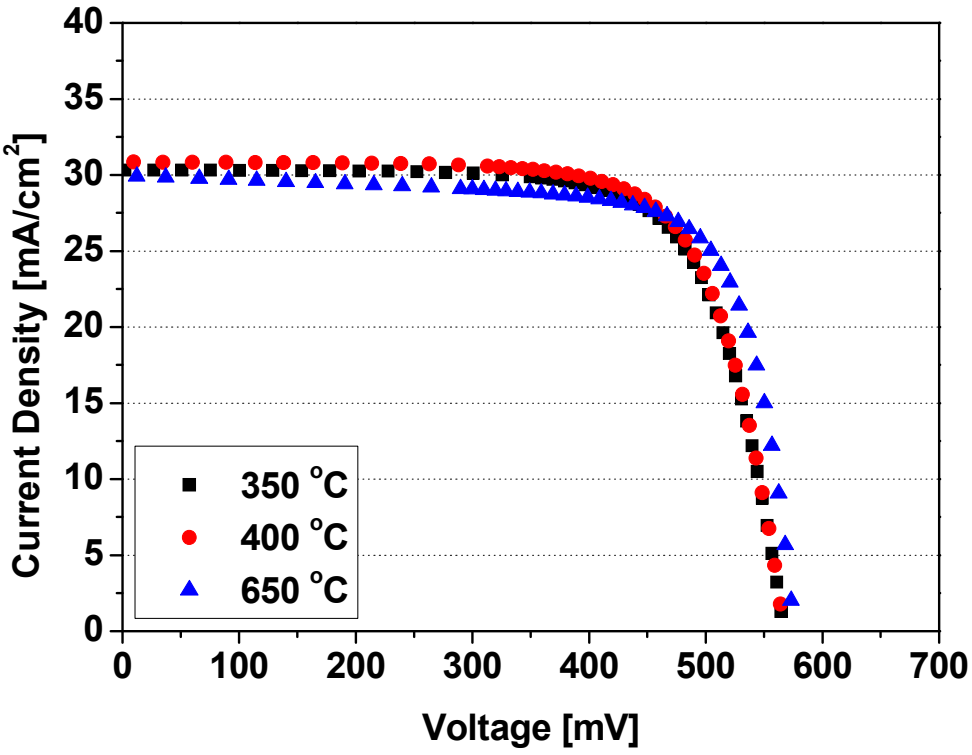

Figure 4.12. Selected J-V curves of LFC solar cells annealed at different temperatures. Fixed laser processing parameters were: 33.0 A pumping lamp current, 20.0 kHz q-switch frequency, 13.0 W laser power, and 0.50 mm contact pitch. Emitter sheet resistance was (41 ± 6) Ω/sq and conveyor belt speed was 220 cm/min.

Once again, the results have confirmed the benefit of performing the annealing step with temperatures of 350 ºC and 400 ºC. Between these two values, a slightly improved performance for an annealing temperature of 400 ºC can be identified, as also noticeable in Figure 4.12. The annealing step resulted in an increase mainly in the FF of samples. At the temperature of 650 ºC, in addition to the FF, the V_{OC} also had noticeable increases. The increase in V_{OC} indicates that at this temperature the aluminium layer deposited over the whole rear surface starts to diffuse into the silicon substrate, instead of only in the region formed by the local contact points. Since the device is not yet passivated at the rear, this forms the BSF on the whole rear side of the solar cell, reducing recombination losses at the rear surface and thus increasing V_{OC}. To confirm and better evaluate this phenomenon the effect was further investigated in another experiment, described below in this section.

The same methodology described above was implemented to evaluate solar cells incorporating a different set of optimized laser parameters: 32.0 A pumping lamp current, 17.5 kHz q-switch frequency, and 11.4 W laser power. Contact pitch (0.50 mm), emitter sheet resistance ((41± 6) Ω/sq), and conveyor belt speed (220 cm/min) were kept unaltered. Results are presented in Table 4.11.

Table 4.11. Electrical parameters of solar cells with laser-firing of the rear contacts, processed under different annealing temperatures. Fixed laser processing parameters were: 32.0 A pumping lamp current, 17.5 kHz q-switch frequency, 11.4 W laser power, and 0.50 mm contact pitch. Emitter sheet resistance was (41 ± 6) Ω/sq and conveyor belt speed was 220 cm/min. Process 04e.

Solar Cell	T_A [ºC]	V_{OC} [mV]	J_{SC} [mA/cm^2]	FF	ΔFF	η [%]
04eC	–	563.5	30.6	0.631	–	10.9
	400	563.7	30.5	0.648	+0.017	11.1
04eE	–	567.7	30.9	0.699	–	12.3
	450	567.0	30.6	0.712	+0.013	12.4
04eF	–	566.4	30.3	0.706	–	12.1
	500	566.7	30.4	0.737	+0.031	12.7

For this set of optimized laser parameters, the effect of the annealing process was similar to that observed in Table 4.10: the main parameter that was improved by

annealing was the FF. Nevertheless, the best results in this case were obtained with higher annealing temperatures, which conflicts with findings from the previous experiment.

Therefore, in order to better understand the influence of the annealing temperature and verify at which temperature the aluminium layer starts diffusing into the whole rear surface of the silicon substrate, a new investigation was carried out. Solar cells with the rear surface covered by a layer of evaporated aluminium were produced, but this time no laser processing was performed. Samples were characterized before and after annealing at 650 ºC with a conveyor belt speed of 220 cm/min. Results are presented in Table 4.12.

Table 4.12. Electrical parameters of solar cells without laser processing, before and after an annealing step at 650 ºC. Emitter sheet resistance was (41 ± 6) Ω/sq and conveyor belt speed was 220 cm/min. Process 04c.

Solar Cell	T_A [ºC]	V_{OC} [mV]	J_{SC} [mA/cm^2]	FF	ΔFF	η [%]
04cD	–	61.5	2.3	0.214	–	0.0
	650	578.9	31.4	0.738	+0.524	13.4
04cI	–	69.4	12.0	0.232	–	0.2
	650	578.8	30.3	0.768	+0.536	13.5

As expected, before the annealing process, the electrical performance of the device was very poor, since an effective metal-semiconductor contact structure cannot be easily achieved by only depositing a layer of metal on a semiconductor material. After the annealing process at 650 ºC, the metal-semiconductor contact of both solar cells was properly formed, resulting in FF of 0.738 and 0.768 and solar cell efficiencies of 13.4 % and 13.5 %, respectively. These results are typical for solar cells with full-area aluminium contacts that do not incorporate an Al-BSF, such as the solar cells presented in Table 4.12. Therefore, it is clear that when the annealing process is performed at 650 ºC, a good quality metal-semiconductor contact between the silicon and the aluminium layer was formed.

Additionally, a second batch of solar cells was selected, this time incorporating the laser-firing step, in order to compare the above results with those for solar cells

annealed at higher temperatures after laser processing. The solar cells were subjected to annealing at different temperatures between 550 ºC and 650 ºC, to confirm if and at which temperature a full-area aluminium contact would be formed. Results are presented in Table 4.13.

Table 4.13. Electrical parameters of solar cells with laser-firing of the rear contacts, processed under different annealing temperatures. Laser processing parameters are provided in the table, apart from the fixed contact pitch of 1.00 mm. Emitter sheet resistance was (41 ± 6) Ω/sq and conveyor belt speed was 220 cm/min. Process 04b.

Solar Cell	T_A [ºC]	I_{Lamp} [A]	f [kHz]	P_L [W]	V_{OC} [mV]	J_{SC} [mA/cm^2]	FF	ΔFF	η [%]
04bD	–	29.0	15.0	8.4	517.3	30.9	0.650	–	10.4
	550	29.0	15.0	8.4	515.4	31.8	0.634	-0.016	10.4
04bE	–	29.0	20.0	8.6	518.7	30.7	0.682	–	10.8
	600	29.0	20.0	8.6	517.0	31.5	0.664	-0.018	10.8
04bI	–	30.0	20.0	9.5	525.8	29.5	0.697	–	10.8
	650	30.0	20.0	9.5	578.8	30.3	0.768	+0.071	13.5

Similarly to results observed previously, a full-area contact is formed at 650 ºC also in solar cells incorporating laser processing. Comparing Table 4.13 with Table 4.12, it is possible to notice that the electrical parameters of devices with and without laser processing annealed at 650 ºC were remarkably similar, both resulting in efficiencies of 13.5 %. This indicates that the annealing process was similar in both cases, and that such high temperature will actually cause the formation of a complete aluminium rear contact, with the formation of an Al-BSF instead of the laser-based LBSFs.

4.4. Solar Cells with Rear Side Passivation and Phosphorus Silicate Glass

After the development of an optimized set of parameters for the fabrication of solar cells with laser-processed rear contacts, the best process parameters were used on a new processing sequence. The developed solar cells incorporate a thermally-grown SiO_2 on the rear side as passivation layer. The processing sequence was divided into two groups (Groups B and A), according to the method employed for the removal of the phosphorus silicate glass. Processes or samples belonging to a specific group are identified by the letter of the third character position used for

coding process and sample names. For instance, for Group B identification was: XXBXX for a process or XXBXXZ for a sample, where X and Z represent numbers and letters, respectively. This section will focus on the analysis of experiments performed with solar cells from Group B.

For Group B solar cells, the removal of the PSG layer was performed by initially protecting the rear surface of wafers with a photoresist layer before the removal of the PSG in a buffered HF/F^- solution. Consequently, Group B samples had a thicker rear oxide, which still contained phosphorus atoms. The thickness of the rear passivation layer of samples was estimated at approximately 50 nm by means of reflectance measurements.

The complete LFC solar cell design included random pyramid texturing on the front and rear surfaces, a homogeneous phosphorus emitter on the front surface with a sheet resistance of (50 ± 4) Ω/sq, equivalent to a C_S of approximately 8.0×10^{19} cm^{-3}, a TiO_2 ARC with approximately 68 nm, screen-printed front surface metallization, a rear surface dielectric passivation layer of thermally-grown SiO_2, covered with a 2 μm thick evaporated aluminium layer, and laser-fired rear contacts.

The conveyor belt speed of the annealing process was investigated at a temperature of 400 ºC. First, a batch of solar cells was fabricated using the following laser-firing parameters: 33.0 A pumping lamp current, 20 kHz q-switch frequency, 13.0 W laser power, and 0.50 mm contact pitch. Samples were characterized by I-V measurements before and after annealing at 400 ºC for a conveyor belt speed of 220 cm/min.

Results are presented in Tables 4.14 and 4.15 for initial and annealed samples, respectively.

When comparing results between Tables 4.14 and 4.15, no improvement from the annealing step performed at a conveyor belt speed of 220 cm/min could be confirmed. In fact, the average electrical performance of the solar cells before and after annealing was similar.

Table 4.14. Electrical parameters of solar cells with laser-firing of the rear contacts, before annealing. Process 05B07.

Solar Cell	V_{OC} [mV]	J_{SC} [mA/cm^2]	FF	η [%]
05B07A	575.8	32.3	0.711	13.2
05B07B	573.5	32.7	0.638	12.0
05B07C	574.9	33.0	0.714	13.5
05B07D	574.8	32.9	0.691	13.1
05B07E	572.9	32.4	0.591	11.0
05B07F	573.5	32.1	0.716	13.2
05B07G	572.9	32.2	0.704	13.0
05B07H	573.2	32.1	0.682	12.5
05B07I	572.9	31.9	0.724	13.3
Average	573.8 ± 1.1	32.4 ± 0.4	0.69 ± 0.04	12.8 ± 0.8

Table 4.15. Electrical parameters of solar cells with laser-firing of the rear contacts, after annealing at 400 ºC with a conveyor belt speed of 220 cm/min. Process 05B07.

Solar Cell	V_{OC} [mV]	J_{SC} [mA/cm^2]	FF	η [%]
05B07A	574.8	32.6	0.692	13.0
05B07B	572.4	33.1	0.629	11.9
05B07C	573.9	33.2	0.711	13.5
05B07D	573.4	33.3	0.694	13.3
05B07E	571.5	32.7	0.587	11.0
05B07F [1]	600.8	34.9	0.707	14.8
05B07G	572.0	32.4	0.706	13.1
05B07H	573.8	32.2	0.693	12.8
05B07I	573.3	31.9	0.725	13.3
Average [2]	573.1 ± 1.1	32.7 ± 0.5	0.68 ± 0.05	12.7 ± 0.9

[1] Sample 05B07F was annealed at 400 ºC and conveyor belt speed of 33 cm/min.

[2] Sample 05B07F's displayed data was not included in the calculation of average and standard deviation values.

Differently from the rest of the 05B07 process batch, sample 05B07F was annealed at 400 ºC and a conveyor belt speed of 33 cm/min as a preliminary test. The change in annealing speed had a considerable impact on the effect of the annealing process, as can be seen in Table 4.15. The sample presented noticeable improvements in V_{OC} (from 573.5 mV to 600.8 mV) and J_{SC} (from 32.1 mA/cm^2 to 34.9 mA/cm^2), resulting in an efficiency gain of 1.6 % absolute, from 13.2 % to 14.8

%. This improvement can be attributed to two aspects: the formation of better metal-semiconductor contact between the silicon substrate and the aluminium laser-fired point contacts, and mainly the formation of LBSFs at the laser-processed contact zones. From the above results, it is possible to conclude that not only the annealing temperature, but also the duration of the annealing process, controlled by the conveyor belt speed, have to be optimized for the LFC method.

After the positive results obtained with sample 05B07F, the remaining solar cells from process 05B07 were annealed again using a conveyor belt speed of 33 cm/min. Results are presented in Table 4.16.

Table 4.16. Electrical parameters of solar cells with laser-firing of the rear contacts, after a second annealing at 400 ºC with a conveyor belt speed of 33 cm/min. Process 05B07.

Solar Cell	V_{OC} [mV]	J_{SC} [mA/cm^2]	FF	η [%]
05B07A	602.0	34.9	0.699	14.7
05B07B	598.2	34.8	0.558	11.6
05B07C	599.5	35.0	0.668	14.0
05B07D	599.6	35.0	0.640	13.4
05B07E	588.6	34.2	0.494	10.0
05B07F [1]	596.7	34.1	0.676	13.8
05B07G	589.0	33.0	0.679	13.2
05B07H	589.3	32.6	0.567	10.9
05B07I	590.9	32.5	0.700	13.5
Average [2]	595.3 ± 5.7	34.1 ± 1.1	0.635 ± 0.077	12.9 ± 1.7

[1] Sample 05B07F was annealed for a second time at 400 ºC and conveyor belt speed of 33 cm/min.

[2] Sample 05B07F's performance data from Table 4.15 was used in the calculation of average and standard deviation values presented above.

The results indicate that performing the annealing step at 33 cm/min has a more pronounced effect on the electrical performance of the solar cells. The V_{OC} and J_{SC} of samples were noticeably improved. Nevertheless, the FF values of all devices were slightly negatively impacted by the annealing process, when compared to values before the second annealing. The V_{OC}, J_{SC}, and FF trends were also clearly noticeable on the average values. As a result, the average efficiency of process 05B07 was only slightly increased in comparison to samples without annealing and

with annealing at 220 cm/min conveyor belt speed. Additionally, the standard deviation values of all electrical parameters increased, indicating that the homogeneity and reproducibility between samples has also deteriorated. It is possible that the excessive thermal treatment of two annealing steps may have contributed to the degradation of the metal grid of samples. In relation to sample 05B07F, it suffered a reduction in all of its electrical parameters after the second annealing step, indicating that excessive thermal treatment may indeed lead to a degradation of the device.

Therefore, based on the results obtained from process 05B07 and sample 05B07F, solar cells were processed with different conveyor belt speeds to evaluate the effect on the benefit of the annealing process. The conveyor belt speeds (v_{Belt}) selected for the new experiment were 33 cm/min, 50 cm/min, and 70 cm/min. The 33 cm/min speed had to be investigated again, since previous samples were submitted to two consecutive annealing processes, a condition that is not directly comparable to a single annealing process at the same speed. The electrical characterization of solar cells before and after the annealing step is presented in Tables 4.17 and 4.18, respectively.

Table 4.17. Electrical parameters of solar cells with laser-firing of the rear contacts, before annealing. Process 05B08.

Solar Cell	V_{OC} [mV]	J_{SC} [mA/cm^2]	FF	η [%]
05B08C	576.4	33.1	0.706	13.5
05B08D	573.5	33.0	0.700	13.2
05B08I	575.4	32.2	0.718	13.3
Average	575.1 ± 1.5	32.8 ± 0.5	0.708 ± 0.009	13.3 ± 0.2
05B08A	574.8	32.4	0.706	13.1
05B08B	573.0	32.8	0.637	12.0
05B08F	575.2	32.6	0.712	13.3
Average	574.3 ± 1.2	32.6 ± 0.2	0.685 ± 0.042	12.8 ± 0.7
05B08E	572.6	32.4	0.648	12.0
05B08G	572.2	32.3	0.712	13.2
05B08H	573.1	32.3	0.697	12.9
Average	572.6 ± 0.5	32.3 ± 0.1	0.686 ± 0.033	12.7 ± 0.6

Table 4.18. Electrical parameters of solar cells with laser-firing of the rear contacts, after annealing at 400 ºC with different conveyor belt speeds. Process 05B08.

Solar Cell	V_{Belt} [cm/min]	V_{OC} [mV]	J_{SC} [mA/cm^2]	FF	ΔFF	η [%]
05B08C	33.0	604.9	36.1	0.687	-0.019	15.0
05B08D	33.0	603.7	35.9	0.656	-0.044	14.2
05B08I	33.0	598.3	33.3	0.701	-0.017	14.0
Average	–	602.3 ± 3.5	35.1 ± 1.6	0.681 ± 0.023	-0.027 ± 0.015	14.4 ± 0.5
05B08A	50.0	604.4	36.0	0.703	-0.003	15.3
05B08B	50.0	601.1	36.0	0.620	-0.017	13.4
05B08F	50.0	603.4	34.7	0.695	-0.017	14.5
Average	–	603.0 ± 1.7	35.6 ± 0.8	0.673 ± 0.046	-0.012 ± 0.008	14.4 ±1.0
05B08E	70.0	594.1	34.9	0.642	-0.006	13.3
05B08G	70.0	592.5	34.6	0.700	-0.012	14.4
05B08H	70.0	595.5	34.2	0.689	-0.008	14.0
Average	–	594.0 ± 1.5	34.6 ± 0.4	0.677 ± 0.031	-0.009 ± 0.003	13.9 ± 0.6

Comparing the results of Tables 4.17 and 4.18, some noteworthy aspects may be highlighted. Before annealing, the efficiency distribution of samples was between 12.0 % and 13.5 %. After annealing at 400 ºC, the efficiency distribution was sensibly increased to between 13.3 % and 15.3 %. As observed in previous experiments, improvements in efficiency values were a result of higher V_{OC} and J_{SC} values compared to samples prior to annealing. Comparing the three different conveyor belt speeds, the best average performances were obtained for solar cells annealed at 33 cm/min and 50 cm/min. In both cases, an average efficiency of 14.4 % was obtained, whereas at 70 cm/min the average efficiency was of 13.9 %. Between 33 cm/min and 50 cm/min, the ΔFF was higher for samples processed at 33 cm/min. ΔFF was 2.3 times higher for 33 cm/min than the value obtained with a conveyor belt speed of 50 cm/min: -0.027 at 33 cm/min versus -0.012 at 50 cm/min. The best solar cell was annealed using a conveyor belt speed of 50 cm/min, reaching a V_{OC} of 604.4 mV, a J_{SC} of 36.0 mA/cm^2, a FF of 0.703, and an efficiency of 15.3 %. Because of its good average efficiency, higher maximum efficiency, and lower average losses in FF, the conveyor belt speed of 50 cm/min has been selected as the best option for the annealing process at 400 ºC.

All solar cells continued to present efficiencies limited by relatively low FF values. This indicates that rear contact resistance was higher than expected, even after the development and optimization of an annealing process for the laser-processed solar cells.

4.5. Solar Cells with Rear Side Passivation Treated with Chemical Etching

Another method for the removal of the phosphorus silicate glass, formed during the quartz tube furnace phosphorus diffusion step, was developed. The PSG removal on samples from Group A was performed by submerging wafers in a 1.2 % HF solution without protecting the rear surface silicon oxide. Wafers were kept submerged until the front surface was hydrophobic, which indicates the complete removal of the PSG at this surface. The reaction was halted by cleaning wafers with DI H_2O. This reduced the SiO_2 oxide thickness on the rear side, but simultaneously eliminated phosphorus atoms and other residues, as well as the PSG layer grown during homogeneous emitter formation by phosphorus diffusion on the front side.

The complete solar cell design included random pyramid texturing on the front and rear surfaces, a homogeneous phosphorus emitter on the front surface with a sheet resistance of (50 ± 4) Ω/sq, a TiO_2 ARC with approximately 68 nm, screen-printed front surface metallization similar to the process used in industrial production, a rear surface dielectric passivation layer of thermally-grown SiO_2, slightly etched, covered with a 2 µm thick evaporated aluminium layer (or 4 µm in a process batch of section 4.5.2), and laser-fired rear contacts.

Additionally, a comparison between the performance of samples fabricated with SiO_2 layer, with and without chemical etching, allows an evaluation of the effect that phosphorus atoms in the SiO_2 layer might have on solar cell performance, and whether an additional processing step for the removal of the rear surface PSG layer is necessary during solar cell fabrication.

4.5.1. Influence of the Belt Speed During Annealing

Due to the exposure of the rear surface to HF during removal of the PSG layer, the annealing process of Group A samples was independently optimized. Therefore, experiments were carried out to investigate the conveyor belt speed during the annealing process at 400 ºC.

For that purpose, solar cells were fabricated using the laser-firing parameters optimized previously: 33.0 A pumping lamp current, 20 kHz q-switch frequency, 13.0 W laser power, and 0.50 mm contact pitch. Samples were characterized by I-V measurements before and after annealing at 400 ºC with conveyor belt speeds of 220 cm/min and 33 cm/min. Characterization data before annealing is presented in Table 4.19.

Table 4.19. Electrical parameters of solar cells with laser-firing of the rear contacts, before annealing. Process 05A01.

Solar Cell	V_{OC} [mV]	J_{SC} [mA/cm^2]	FF	η [%]
05A01A	576.9	33.2	0.693	13.3
05A01B	576.1	33.2	0.646	12.4
05A01C	575.2	33.6	0.636	12.3
05A01D	575.1	33.7	0.685	13.3
05A01E	574.6	33.3	0.642	12.3
05A01F	576.5	33.1	0.693	13.2
05A01G	577.0	32.9	0.704	13.4
05A01H	575.9	32.9	0.672	12.7
05A01I	574.9	32.8	0.717	13.5
Average	575.8 ± 0.9	33.2 ± 0.3	0.677 ± 0.029	12.9 ± 0.5

Comparing results from Tables 4.14 (Group B before annealing) and 4.19 (Group A before annealing), the average electrical parameters of the fabricated solar cells were quite similar. This result indicates that, before annealing, there is only a small impact on the electrical parameters of solar cells processed under the two different SiO_2 rear passivation layers. After the characterization before annealing, solar cells from process 05A01 were annealed at 400 ºC with a conveyor belt speed of 220 cm/min. Results are shown in Table 4.20.

Table 4.20. Electrical parameters of solar cells with laser-firing of the rear contacts, after annealing at 400 ºC with a conveyor belt speed of 220 cm/min. Process 05A01.

Solar Cell	V_{OC} [mV]	J_{SC} [mA/cm^2]	FF	η [%]
05A01A	574.5	33.2	0.711	13.6
05A01B	574.0	33.6	0.628	12.1
05A01C	573.5	33.6	0.634	12.2
05A01D	574.0	33.5	0.680	13.1
05A01E	573.3	33.1	0.650	12.3
05A01F [1]	601.8	35.4	0.703	15.0
05A01G	575.7	33.0	0.715	13.6
05A01H	575.1	33.0	0.679	12.9
05A01I	573.5	32.8	0.721	13.6
Average [2]	574.2 ± 0.8	33.2 ± 0.3	0.677 ± 0.037	12.9 ± 0.6

[1] Sample 05A01F was annealed at 400 ºC and conveyor belt speed of 33 cm/min.

[2] Sample 05A01F's displayed data was not included in the calculation of average and standard deviation values.

No consistent improvement from the annealing step performed at a conveyor belt speed of 220 cm/min can be verified. The average electrical parameters were very similar, with the same average efficiency of 12.9 % before and after annealing. This is in line with results obtained for samples from Group B, analysed in section 4.4, indicating that for both cases the conveyor belt speed of 220 cm/min is inappropriate for an effective annealing step of laser-processed solar cells produced in this work. Differently from other samples of the 05A01 process batch, sample 05A01F was annealed at 400 ºC and a conveyor belt speed of 33 cm/min as a preliminary test. As observed in section 4.4, the reduction of the annealing speed had a significant positive impact on the annealing step. This resulted in a solar cell with improved V_{OC} (from 576.5 mV to 601.8 mV) and J_{SC} (from 33.1 mA/cm^2 to 35.4 mA/cm^2) values, resulting in a total efficiency gain of 1.8 % absolute, from 13.2 % to 15.0 %. The improvement is attributable to the same effects mentioned earlier: the formation of a better metal-semiconductor contact between the silicon substrate and the aluminium laser-fired point contacts, and mainly the improvement of the quality of the LBSFs at the laser-processed contact zones.

After the positive results displayed by sample 05A01F, the remaining solar cells from process batch 05A01 were annealed again using a conveyor belt speed of 33 cm/min. Results are presented in Table 4.21. Additionally, a comparison of the J-V curves of solar cell 05A01A before annealing, after annealing at 220 cm/min and after annealing at 33 cm/min is shown in Figure 4.13.

Table 4.21. Electrical parameters of solar cells with laser-firing of the rear contacts, after a second annealing at 400 ºC with a conveyor belt speed of 33 cm/min. Process 05A01.

Solar Cell	V_{OC} [mV]	J_{SC} [mA/cm^2]	FF	η [%]
05A01A	601.5	35.7	0.698	15.0
05A01B	600.5	36.2	0.620	13.5
05A01C	599.3	35.9	0.584	12.6
05A01D	600.5	36.3	0.664	14.5
05A01E	600.2	35.9	0.607	13.1
05A01F [1]	599.7	35.4	0.655	13.9
05A01G	596.7	34.4	0.684	14.0
05A01H	598.2	34.3	0.612	12.6
05A01I	591.1	33.6	0.698	13.8
Average [2]	598.9 ± 3.3	35.3 ± 1.0	0.652 ± 0.046	13.8 ± 0.9

[1] Sample 05A01F was annealed for a second time at 400 ºC and conveyor belt speed of 33 cm/min.

[2] Sample 05A01F's performance data from Table 4.20 was used in the calculation of average and standard deviation values presented above.

As observed in section 4.4, results confirm that the annealing step at 33 cm/min has a stronger effect on the electrical performance of the solar cells than the annealing step at 220 cm/min. In general, when annealing at 33 cm/min, both the V_{OC} and J_{SC} of samples were improved, with average values increasing from 574.2 mV to 598.9 mV and from 33.2 mA/cm^2 to 35.3 mA/cm^2, respectively. This effect can be clearly observed in Figure 4.13, where the J-V curve of solar cell 05A01A after annealing at 33 cm/min had a better electrical performance than both the device before annealing and after annealing at 220 cm/min. On the other hand, annealing the sample at 220 cm/min caused no consistent improvement in solar cell performance, and resulted in a J-V curve very similar to the device before annealing. Nevertheless, the FF values of samples annealed at 33 cm/min were slightly negatively impacted by the annealing process, when compared to values before

annealing, decreasing from an average value of 0.677 to 0.652. This indicates that series resistance (including contact resistance) on the rear side of the solar cells is playing an important role in limiting device performance.

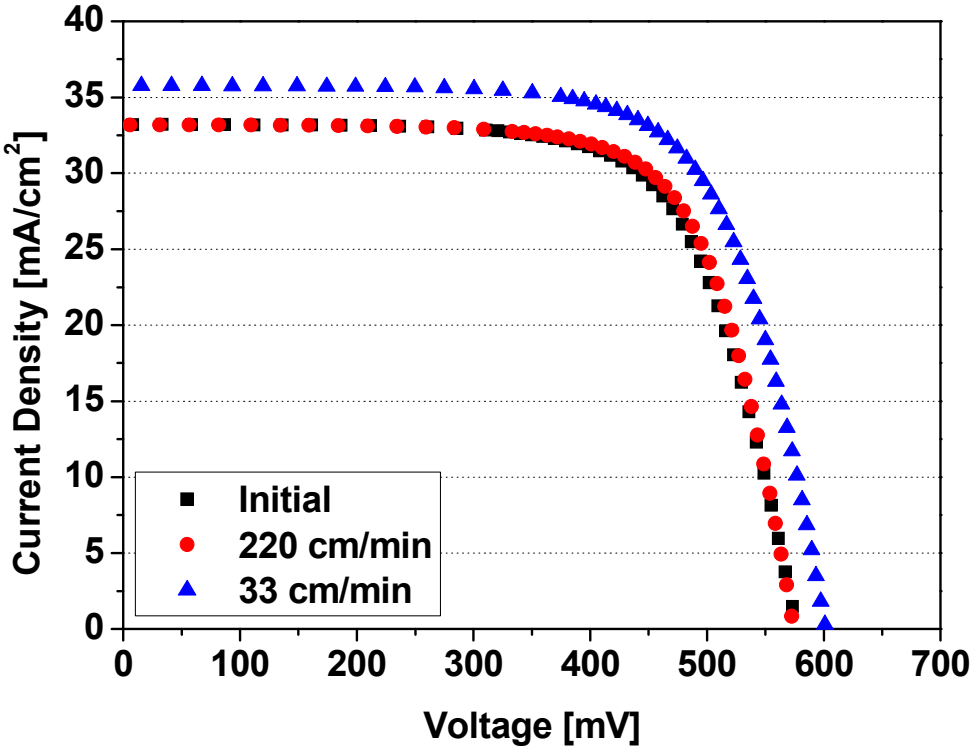

Figure 4.13. J-V curves of LFC solar cell 05A01A, with SiO_2 rear surface passivation and annealed sequentially at different conveyor belt speeds. Fixed laser processing parameters were: 33.0 A pumping lamp current, 20.0 kHz q-switch frequency, 13.0 W laser power, and 0.50 mm contact pitch. Emitter sheet resistance was (50 ± 4) Ω/sq.

As a result, the average efficiency of process 05A01 was 13.8 %, higher than both samples without and with annealing at 220 cm/min conveyor belt speed, with an average efficiency of 12.9 % in both cases. The standard deviation values of all electrical parameters increased, indicating that the homogeneity and reproducibility between samples has also deteriorated with two annealing steps. When analysing sample 05A01F, which was subjected to two thermal treatments at 33 cm/min, it suffered a reduction in V_{OC}, FF, and efficiency values after the second annealing step, indicating that excessive thermal treatment may indeed lead to a degradation of the device.

By analysing Tables 4.15 and 4.20 and Tables 4.16 and 4.21, it is possible to compare the impact of the different SiO_2 rear passivation layers of Groups B and A after samples were annealed at 220 cm/min and subsequently at 33 cm/min, respectively. In order to facilitate this comparison, the average values and best electrical parameters of solar cells from each group are summarised in Table 4.22.

Table 4.22. Summary of the average values and best electrical parameters of solar cells with laser-firing of the rear contacts for Groups B and A, after annealing at 400 ºC with different conveyor belt speeds.

Process	v_{Belt} [cm/min]	Solar Cell	V_{OC} [mV]	J_{SC} [mA/cm^2]	FF	η [%]
05B07	220.0	Best	573.9	33.2	0.711	13.5
		Average	573.1 ± 1.1	32.7 ± 0.5	0.679 ± 0.047	12.7 ± 0.9
05A01	220.0	Best	573.5	32.8	0.721	13.6
		Average	574.2 ± 0.8	33.2 ± 0.3	0.677 ± 0.037	12.9 ± 0.6
05B07	33.0	Best	600.8	34.9	0.707	14.8
		Average	595.3 ± 5.7	34.1 ± 1.1	0.635 ± 0.077	12.9 ± 1.7
05A01	33.0	Best	601.8	35.4	0.703	15.0
		Average	598.9 ± 3.3	35.3 ± 1.0	0.652 ± 0.046	13.8 ± 0.9

Analysis of Table 4.22 shows no clear distinction between the average performance of samples from Groups B and A for a conveyor belt speed of 220 cm/min. Nevertheless, it is important to remind that a conveyor belt speed of 220 cm/min was already identified as an inappropriate annealing speed for the solar cells developed. More information can be obtained by a comparison between solar cells which were subjected to two annealing steps, one at 220 cm/min and another at 33 cm/min. All average electrical parameters of Group B samples were lower than those of Group A samples, with this difference being higher for J_{SC} (34.1 mA/cm^2 against 35.3 mA/cm^2) and FF (0.635 against 0.652). As a result, the average efficiency of Group B samples was 12.9 %, lower than the value obtained from Group A samples of 13.8 %. Additionally, the standard deviation values of solar cells of Group B annealed at 33 cm/min was almost two times higher than those of Group A devices, indicating that employing the same process to Group A samples resulted in more homogeneous solar cells, with less performance spreading between devices.

Therefore, it is possible to conclude that the removal of the phosphorus-rich layer of the SiO_2 rear passivation layer, as done in samples from Group A, was beneficial to device performance and also reduced the variability of results between samples. In terms of the process sequence, performing the simultaneous removal of the front and rear surface PSG layer by an HF etch of the unprotected rear surface simplifies the fabrication sequence by eliminating unnecessary processing steps with photoresist and, thus reducing processing costs. Additionally, it was demonstrated that the HF etch performed on Group A samples did not compromise the performance of the SiO_2 rear surface passivation layer. Since the HF etch was relatively fast (approximately 2 minutes), only a small fraction of the SiO_2 layer was removed during this step. Therefore, solar cells from Group A presented V_{OC} and J_{SC} compatible to those of rear passivated devices.

4.5.2. Influence of the Rear Aluminium Thickness

The influence of the thickness of the rear surface aluminium layer on LFC device performance was also evaluated. For the comparison, two batches of Group A solar cells were fabricated, each with a different rear aluminium layer thickness: 2 µm and 4 µm. Samples were laser-fired using the parameters previously optimized: 33.0 A pumping lamp current, 20 kHz q-switch frequency, 13.0 W laser power, and 0.50 mm contact pitch. The resulting solar cells were characterized by I-V measurements before and after annealing at 400 ºC with a conveyor belt speed of 50 cm/min. Results before annealing are reported in Tables 4.23 and 4.24.

The results before annealing indicate that samples with a 4 µm rear side aluminium layer presented a slight improvement in FF average values in comparison to samples with only 2 µm of aluminium, with one sample reaching a FF of 0.738. Nevertheless, this improvement was followed by a small decrease in the average value of J_{SC} for the thicker aluminium layer. The overall result was a slight increase in average efficiency from 12.9 % for 2 µm thick aluminium layer, to 13.1 % for 4 µm thick aluminium layer, mainly caused by the gain in FF.

Table 4.23. Electrical parameters of solar cells with a 2 µm rear side aluminium layer and laser-firing of the rear contacts, before annealing. Process 05A01.

Solar Cell	V_{OC} [mV]	J_{SC} [mA/cm^2]	FF	η [%]
05A01A	576.9	33.2	0.693	13.3
05A01B	576.1	33.2	0.646	12.4
05A01C	575.2	33.6	0.636	12.3
05A01D	575.1	33.7	0.685	13.3
05A01E	574.6	33.3	0.642	12.3
05A01F	576.5	33.1	0.693	13.2
05A01G	577.0	32.9	0.704	13.4
05A01H	575.9	32.9	0.672	12.7
05A01I	574.9	32.8	0.717	13.5
Average	575.8 ± 0.9	33.2 ± 0.3	0.677 ± 0.029	12.9 ± 0.5

Table 4.24. Electrical parameters of solar cells with a 4 µm rear side aluminium layer and laser-firing of the rear contacts, before annealing. Process 05A02.

Solar Cell	V_{OC} [mV]	J_{SC} [mA/cm^2]	FF	η [%]
05A02A	575.2	32.8	0.701	13.2
05A02B	574.1	32.9	0.674	12.7
05A02C	574.5	33.0	0.700	13.3
05A02D	573.5	33.2	0.687	13.1
05A02E	572.3	32.5	0.690	12.8
05A02F	572.8	32.2	0.738	13.6
05A02G	573.7	32.6	0.712	13.3
05A02H	573.4	32.4	0.684	12.7
05A02I	572.8	32.1	0.714	13.1
Average	573.6 ± 0.9	32.6 ± 0.4	0.700 ± 0.019	13.1 ± 0.3

In sequence, samples with 4 µm thick aluminium layer were annealed at 400 ºC with a conveyor belt speed of 50 cm/min. Results after annealing are presented in Tables 4.25.

Comparing Table 4.24 with Table 4.25, both V_{OC} and J_{SC} increased with the annealing process, as would be expected from previous results. The average efficiency of samples after annealing was 13.6 %.

Table 4.25. Electrical parameters of solar cells with a 4 µm rear side aluminium layer and laser-firing of the rear contacts, after annealing at 400 ºC with a conveyor belt speed of 50 cm/min. Process 05A02.

Solar Cell	V_{OC} [mV]	J_{SC} [mA/cm^2]	FF	η [%]
05A02A	600.2	35.5	0.705	15.0
05A02B	601.1	36.2	0.660	14.4
05A02C	602.0	36.1	0.667	14.5
05A02D	600.9	36.3	0.586	12.8
05A02E	585.1	34.0	0.569	11.3
05A02F	585.3	33.7	0.717	14.2
05A02G	592.4	34.1	0.662	13.4
05A02H	591.0	34.4	0.664	13.5
05A02I	590.2	33.3	0.688	13.5
Average	594.2 ± 6.9	34.9 ± 1.2	0.657 ± 0.050	13.6 ± 1.1

The influence of the aluminium layer thickness can be evaluated by analysing and comparing Tables 4.25 and 4.21. The average efficiency of 13.6 % achieved with a 4 µm aluminium layer is lower than the average efficiency of 13.8 % obtained with a 2 µm aluminium layer. In the latter case, average V_{OC} and J_{SC} values are slightly higher than those measured for solar cells with 4 µm aluminium layer. The highest efficiency device of each process was 15.0 % for both 2 µm and 4 µm aluminium layer thicknesses, with very similar FF values of 0.698 and 0.705, respectively.

The conclusion of this evaluation was that no clear benefit of increasing the thickness of the rear side aluminium layer could be confirmed for solar cells processed with LFC and annealed under optimized conditions. Therefore, it is recommended that solar cells be fabricated with a 2 µm rear side aluminium layer, as usual. Increasing the thickness to 4 µm would lead to unnecessary material consumption and additional process-related costs, without bringing any significant value to the resulting device.

4.6. Comparison between Laser-Fired Contact and Screen-Printed Solar Cells

In order to compare the characteristics of laser-processed solar cells developed at NT-Solar with traditional solar cells, batches of devices produced in a

standard industrial processing sequence used at NT-Solar were fabricated. These samples had screen-printed rear metallization instead of the evaporated aluminium layer and laser-fired local contacts used in LFC solar cells. They also did not incorporate a rear surface SiO_2 passivation layer. They can be further divided in two groups: industrial solar cells with and without a full-area rear Al-BSF. For a reliable comparison, solar cells were produced using the same p-type silicon substrate and similar processing sequences than those used for LFC devices.

The general solar cell design included random pyramid texturing on the front and rear surfaces, a homogeneous phosphorus emitter on the front surface, a TiO_2 ARC with approximately 68 nm, and screen-printed front and rear metallization. This is comparable to a fabrication sequence that is usually employed in industrial mass-production of silicon solar cells. Similarly to the front surface screen-printing metallization, rear surface metal contacts were screen-printed onto the silicon wafers using a screen-printer and aluminium metallization paste DuPont Solamet® PV202. The rear metal grid mask layout had a surface coverage area of more than 53 %. The front and rear pastes were sequentially dried and simultaneously fired in an infrared lamp-heated three-zone conveyor belt furnace, using a conveyor belt speed of 220 cm/min. Processes at the conveyor belt furnace were performed under a controlled atmosphere using a filtered dry air flow for cooling. Finally, wafers containing the samples were laser scribed and manually cleaved into individual samples. These solar cells had no significant Al-BSF formation at the rear surface. Results of the screen-printed solar cells without Al-BSF are presented in Table 4.26.

The industrial p-type screen-printed solar cells without Al-BSF had an average V_{OC} of 575.2 mV, J_{SC} of 30.5 mA/cm^2, and FF of 0.762, with a resulting average efficiency of 13.3 %. These performance values are very similar to those described in section 4.3.4, in Tables 4.12 and 4.13, when solar cells with and without the incorporation of laser-firing were annealed at 650 ºC. In that case, the rear surface had no passivation and was covered by an evaporated 2 µm aluminium layer. Results show that the influence on electrical performance of the rear surfaces of both screen-printed and evaporated devices are quite similar when the evaporated aluminium layer is subjected to high-temperature processing. In both processes a good-quality contact between the metal and the semiconductor materials was

formed, as indicated by the FF values of 0.768 and 0.762. Nevertheless, both processes presented relatively low V_{OC} and J_{SC} values, indicating that the formation of a good-quality BSF was not achieved.

Table 4.26. Electrical parameters of industrial p-type screen-printed solar cells without Al-BSF. Emitter sheet resistance was (41 ± 6) Ω/sq. Screen-printed metal pastes were fired at 840 ºC with a conveyor belt speed of 220 cm/min.

Solar Cell	V_{OC} [mV]	J_{SC} [mA/cm^2]	FF	η [%]
0301A	574.0	29.8	0.763	13.1
0301C	575.8	31.0	0.766	13.7
0301D	575.6	30.8	0.762	13.5
0301F	577.1	30.3	0.764	13.3
0301G	574.0	29.8	0.763	13.1
0301I	575.5	30.1	0.771	13.3
0302A	573.1	30.2	0.772	13.4
0302C	576.2	31.5	0.768	13.9
0302D	574.3	31.1	0.710	12.7
0302F	577.8	30.8	0.767	13.6
0302G	572.9	30.0	0.762	13.1
0302I	576.3	30.2	0.772	13.4
Average	575.2 ± 1.6	30.5 ± 0.5	0.762 ± 0.017	13.3 ± 0.3

Comparing the average results of Tables 4.18 and 4.26, it is clear that the LFC devices had a considerably higher V_{OC} and J_{SC}. This is a result of the benefits originated from the SiO_2 rear passivation layer, the LBSFs formed during laser-firing of the rear contacts, and an increased internal reflection at the rear surface. Therefore, the performance of LFC devices was superior in terms of V_{OC} and J_{SC} due to a decreased rear surface recombination rate and an increased photogeneration of charge carriers in the NIR. Nevertheless, the average FF of LFC solar cells of only 0.673 was significantly lower than that of industrial screen-printed devices, with an average of 0.762. Since both solar cells had similar front surface designs, the problem can be traced to the rear side structure and processing of the LFC devices. The poor FF of LFC samples can be related to high series resistances (mainly contact and metal resistances) at the rear surface. Overall, the average efficiency of industrial solar cells without Al-BSF was 13.3 %, whereas that of LFC devices

reached 14.4 %, showing the benefits of the laser-processed devices in comparison to the screen-printing approach.

Solar cells incorporating a full-area Al-BSF at the rear surface were produced under a similar processing sequence, but with the following difference: the rear surface Al-BSF and front surface homogeneous phosphorus emitter layer were simultaneously formed by a high-temperature co-diffusion process in a quartz tube furnace. The processing details, parameters, and conditions, such as temperature ramps, processing time, and gas flows, were developed at NT-Solar previously and are described in reference [161]. Afterwards, front and rear metal contacts were screen-printed, dried, and fired in an infrared lamp-heated three-zone conveyor belt furnace. Finally, wafers containing the samples were laser scribed and manually cleaved into individual samples. Results for screen-printed solar cells incorporating a full-area Al-BSF at the rear surface are presented in Table 4.27.

Table 4.27. Electrical parameters of industrial p-type screen-printed solar cells with a full-area Al-BSF formed by co-diffusion in a quartz tube furnace at 900 ºC. Emitter sheet resistance was (37 ± 3) Ω/sq. Screen-printed metal pastes were fired at 840 ºC.

Solar Cell	V_{OC} [mV]	J_{SC} [mA/cm^2]	FF	η [%]
0801A	591.1	33.1	0.765	15.0
0801D	593.9	33.7	0.762	15.3
0801F	589.9	33.3	0.739	14.5
0801G	583.2	32.7	0.718	13.7
0801I	579.3	33.1	0.704	13.5
0802A	591.3	33.0	0.755	14.7
0802C	590.2	33.6	0.715	14.2
0802D	590.0	33.5	0.751	14.8
0802F	587.7	33.2	0.719	14.0
0802G	584.4	32.9	0.760	14.6
0802I	584.7	32.6	0.773	14.7
Average	587.8 ± 4.4	33.2 ± 0.4	0.742 ± 0.024	14.5 ± 0.6

Industrial solar cells incorporating a full-area Al-BSF showed an average V_{OC} of 587.8 mV, J_{SC} of 33.2 mA/cm^2, and FF of 0.742, with a resulting average

efficiency of 14.5 %. The best solar cell had a V_{OC} of 593.9 mV, J_{SC} of 33.7 mA/cm^2, and FF of 0.762, with a resulting efficiency of 15.3 %.

Comparing these results to Table 4.26, the benefit of the Al-BSF is clearly noticeable: the devices present higher average V_{OC}, J_{SC}, and efficiency values, as can be observed in Figure 4.14. The characteristic p^+p high-low junction formed at the rear of the Al-BSF solar cells repels electrons from the region, reducing recombination at the rear surface and improving both V_{OC} and J_{SC}. Nevertheless, the average FF values show a different behaviour: there was a reduction from 0.762 to 0.742. This result indicates that, with the formation of the Al-BSF, additional electrical losses, such as series resistance on the rear side was introduced.

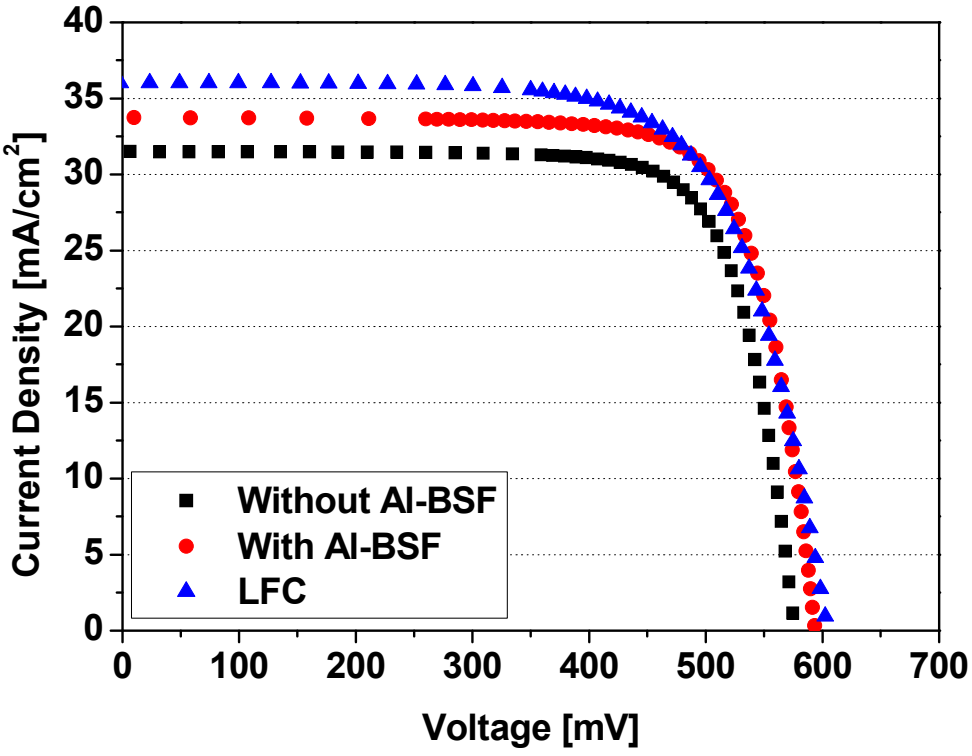

Figure 4.14. J-V curves of the best solar cells without Al-BSF, with Al-BSF, and with LFC, fabricated on the same type of CZ-Si substrate, with equivalent screen-printed front metallization, and processed under similar conditions.

Comparing the performance of LFC solar cells from Table 4.18 with Al-BSF solar cells described in Table 4.27, the LFC devices show higher average V_{OC} and J_{SC} values, due to the presence of the SiO_2 rear side passivation layer. This can be clearly noted in Figure 4.14, where both the J_{SC} and V_{OC} of LFC solar cells stand out

to both screen-printed approaches. Even though the solar cell design was distinct, average efficiencies achieved in both cases were comparable: 14.4 % for LFC solar cells and 14.5 % for Al-BSF solar cells. The best LFC device had a V_{OC} of 604.4 mV, J_{SC} of 36.0 mA/cm^2, FF of 0.703, with a resulting efficiency of 15.3 %, whereas the best Al-BSF had a V_{OC} of 593.9 mV, J_{SC} of 33.7 mA/cm^2, and FF of 0.762, with a resulting efficiency of 15.3 %. The lower FF of LFC solar cells indicate that devices were affected by additional electrical losses related to the rear side processing, such as series and contact resistances. This can also be noted in Figure 4.14, where the slope of the LFC curve near the V_{OC} region indicates a higher series resistance. One possible cause for this phenomenon is the formation of a Schottky barrier at the laser-fired regions, with rectifying characteristics, instead of an ohmic metal-semiconductor contact. The formation of a Schottky barrier at the rear local contacts depends on factors, such as: the metal work function, the E_g of the semiconductor, the type and concentration of dopants at the interface between the silicon substrate and the laser-fired zone of the aluminium layer, amongst others.

A deeper understanding of the causes of the different behaviours of solar cells without Al-BSF, with Al-BSF, and with LFC can be obtained by evaluating the reflectance and IQE curves of these devices, shown in Figure 4.15. For the wavelength range between 350-750 nm, the IQE and reflectance curves of the three devices are equivalent and no significant differences between the behaviour of the devices can be identified. This is in agreement to what would be expected, as the front surface structure of the three designs is equivalent, employing similar a texturing procedure, cleaning steps, homogeneous emitter, TiO_2 ARC, and screen-printed front contacts. Differently, for the wavelength range between 750-1200 nm, the IQE and reflectance curves of the three devices show distinct behaviours. The lowest IQE curve was obtained for the device without Al-BSF. This is expected, since the device has an unpassivated rear surface, with high recombination losses, and does not incorporate the benefits of a rear BSF. Even though the device with Al-BSF had a lower reflectance than the solar cell without Al-BSF, its IQE is higher than the latter. This can be explained by the presence of the Al-BSF, formed by co-diffusion in a quartz tube furnace. The Si-Al alloy exhibits a lower reflectance than both the screen-printed Al paste used for metallization of the device without Al-BSF and the evaporated Al layer employed in the LFC device. Nevertheless, this loss in minority

charge carrier generation due to less rear reflection is more than compensated by the formation of the Al-BSF, which reduces rear surface recombination losses when compared to the device without Al-BSF. Consequently, despite its lower reflectance, the IQE of the solar cell with Al-BSF is higher for the range between 750-1200 nm. The LFC solar cell exhibits a considerably higher reflectance at wavelengths higher than 1050 nm than both screen-printed solar cells. This is a consequence of the combination of a SiO_2 rear passivation layer and an evaporated Al layer, both contributing to an increase in the rear reflection. Additionally, the SiO_2 passivation combined with the LBSFs of the LFC design further reduce rear surface recombination losses, increasing the IQE of the LFC solar cell for higher wavelengths. The combined effect results in an IQE very similar to that of the device with Al-BSF, but with an additional gain between 1050-1200 nm, where the reflectance of the LFC device is superior.

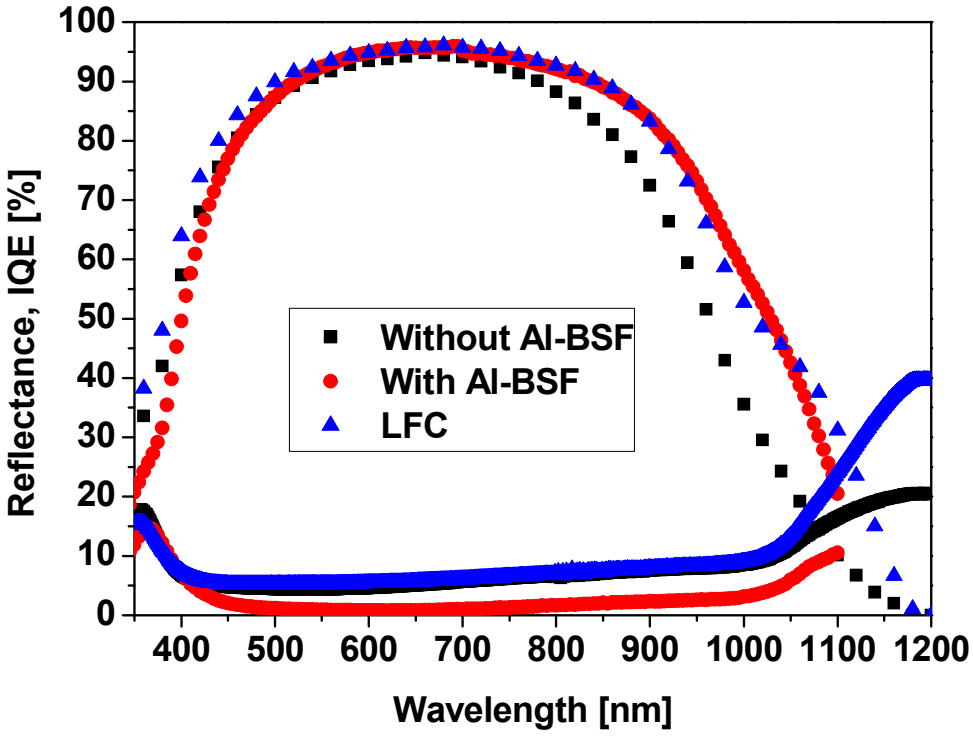

Figure 4.15. Reflectance and IQE of the best solar cells without Al-BSF, with Al-BSF, and with LFC, fabricated on the same type of CZ-Si substrate, with equivalent screen-printed front metallization, and processed under similar conditions.

Therefore, even though the LFC solar cells already reached efficiencies similar to those of Al-BSF solar cells, the electrical losses identified in low FF values

are a strong indication that the LFC processing sequence can be further improved. Such improvements may be implemented by changing processing parameters during fabrication steps, changing the characteristics of the silicon substrate (such as substrate quality and base doping), and employing a new laser system more suitable for LFC processing.

In respect to the use of a laser system better adapted to the LFC processing step, a new equipment was recently installed at NT-Solar to evaluate this possibility. It consists of a scanning head mirror galvanometer laser system, similar to the one that was employed in experiments with the SCA technique, in Chapter 5 of this thesis. Although experimenting with and evaluating this laser system is out of the scope of this work, preliminary tests performed during system setup indicate that the laser-affected zone and the interaction of the laser beam with the substrate is different for each system, as can be seen in Figure 4.16.

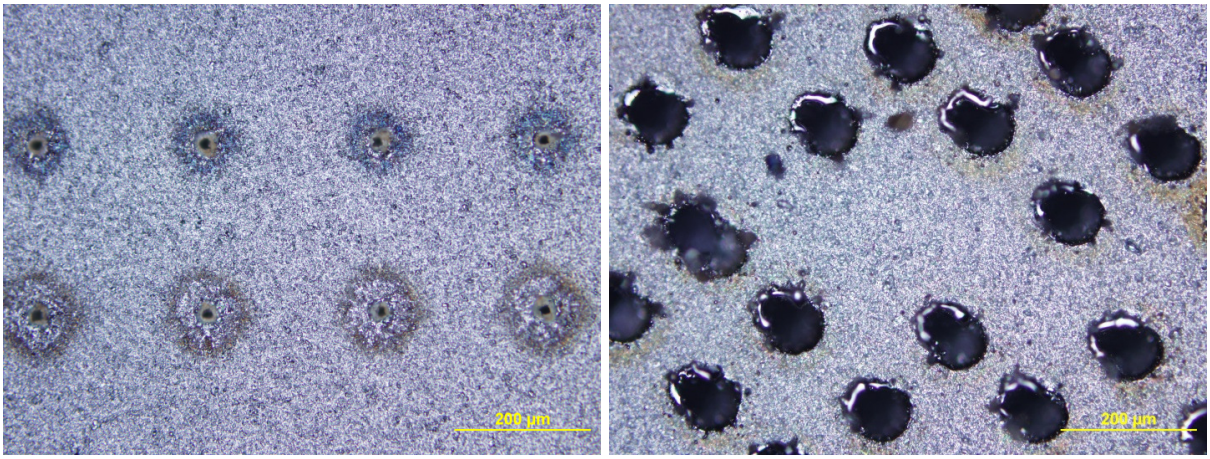

(a) **(b)**

Figure 4.16. Optical microscopy images of LFC contacts processed by two different laser systems: (a) LFC performed with the laser system with X-Y table employed in this work and (b) LFC using the new scanning head mirror galvanometer laser system recently installed at NT-Solar.

On the one hand, when performing the LFC process with the best laser parameters and with the laser system used in this work, the effect of the laser on the processed area leaves a wide ring of inhomogeneous laser-affected area, as shown in Figure 4.16(a). This may be a source of the increased series resistance for the rear contacts of the LFC solar cells produced in this work. On the other hand, the first

tests employing the new laser system available at NT-Solar produced a significantly larger but much more homogeneous laser-affected area after LFC processing, as shown in Figure 4.16(b). This may result in better quality contacts, assuming the other relevant aspects of laser processing are kept constant.

5. EVALUATION OF SILICON SOLAR CELLS WITH LASER-ABLATED SILICON NITRIDE LAYERS

The work of this chapter was focused on the development, analysis, and comparison of two different laser methods for the ablation of localized regions of the silicon nitride antireflection coating layer: laser chemical processing (LCP) and a scanning head mirror galvanometer laser system (SCA). The research activities were performed at the Fraunhofer ISE, in Freiburg im Breisgau, Germany. LCP was used to ablate regions of the SiN_X ARC for subsequent metallization, using deionised water (LCP-H_2O) as liquid medium, thus, without the direct incorporation of doping impurities during laser processing. The SCA system was also used to ablate the SiN_X ARC layer, but in a dry environment, without employing any liquid medium. Both laser processes were performed with the same 532 nm diode-pumped solid-state laser source, coupled to both laser systems with the aid of guiding mirrors.

Initial experiments were aimed at defining and optimizing the laser process of the LCP and SCA laser techniques by evaluating parameters, such as: laser pulse energy and laser pulse frequency. Based on these outcomes, p-type crystalline silicon solar cells with laser-ablated SiN_X front surface openings and selective deposition of Ni/Ag front metal contacts were fabricated using LCP and SCA processes. Next, device performances were characterized and evaluated.

The development and optimization of a silicon nitride ablation method using the LCP and SCA laser systems is presented and discussed. Laser ablation was then applied to fabricate p-type crystalline silicon solar cells incorporating Ni/Ag selectively deposited over the ablated regions by means of electrochemical deposition. Lastly, solar cells produced with LFC, LCP, and SCA laser techniques were compared.

5.1. Processing Sequences and Methods for Solar Cells with Laser Ablation

Since this research is focused on the development of laser processes, other processing steps followed Fraunhofer ISE's standards and were kept constant throughout the work. These standard processes are based on mature technologies applied to solar cell production and have already been studied and improved by previous research at the Fraunhofer ISE, such as [162]. This methodology allowed a proper comparison between samples processed with different laser parameters, with only one parameter being varied at a time.

5.1.1. Processing Sequences

Solar cells produced were based on the process sequence summarized in the flowchart diagram of Figure 5.1. Many of the processing steps employed at the Fraunhofer ISE were similar to those already described in Chapter 4. These were not extensively described in this chapter, unless noteworthy aspects have to be clarified. Photolithography was performed only in selected regions of the silicon wafers, to fabricate reference solar cells. Therefore, photolithography-based solar cells did not include the SiN_X laser ablation step described in the flowchart.

Before the fabrication of solar cells, the laser ablation method and its respective process parameters were developed and optimized. Once homogeneous and controllable processing conditions, with good SiN_X ablation results, were achieved, the best process parameters were employed to fabricate of solar cells by using both the LCP-H_2O and SCA approaches. The main front surface processing steps used in fabricating solar cells developed in this chapter are shown in Figure 5.2. The steps include SiN_X selective removal by photolithography or laser ablation, and Ni/Ag selective electrochemical deposition of the front metal contacts.

The structure of solar cells developed with SiN_X laser ablation and Ni/Ag front contacts, is shown in Figure 5.3.

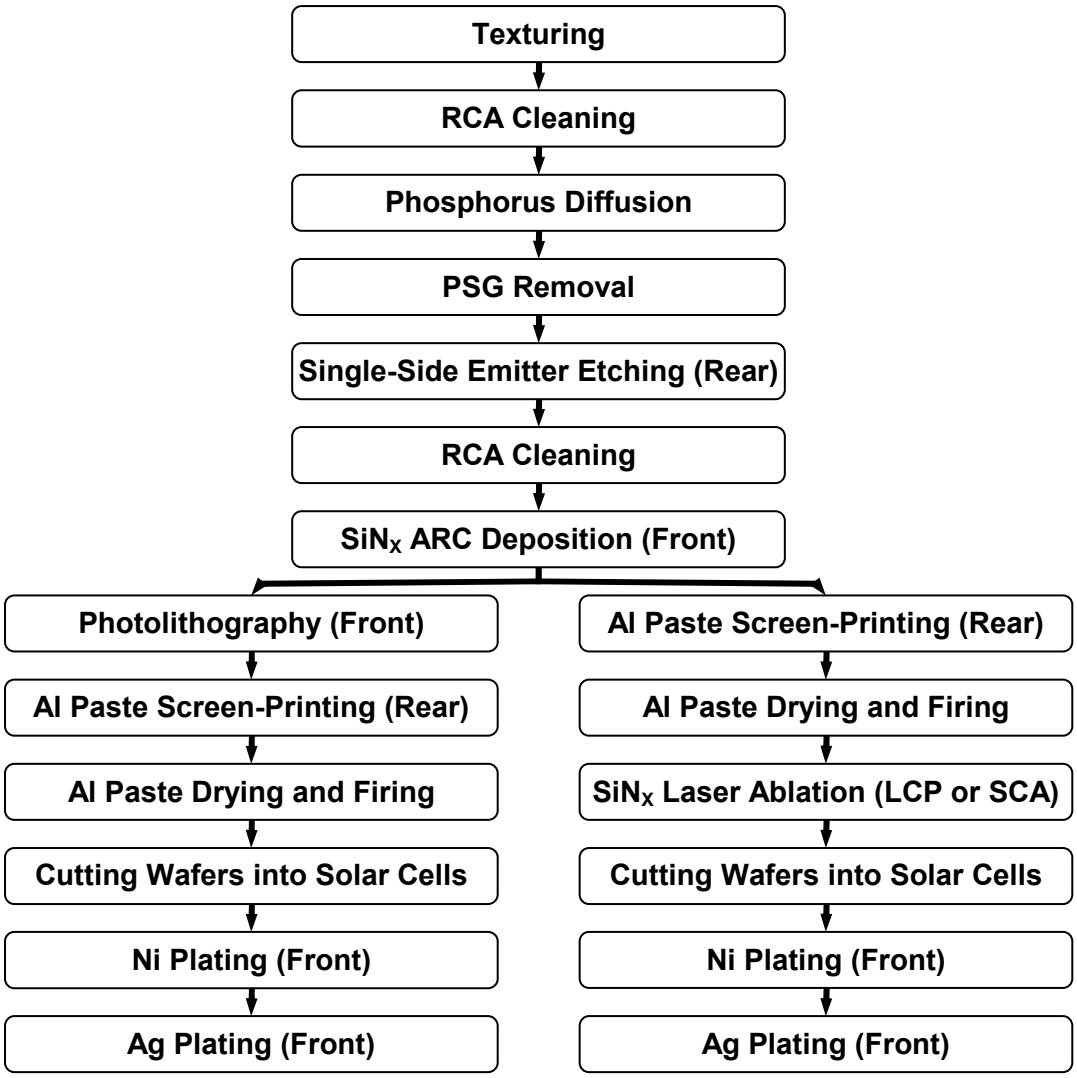

Figure 5.1. Flowchart diagram used for the development of solar cells with SiN_X laser ablation and selective Ni/Ag front side metallization.

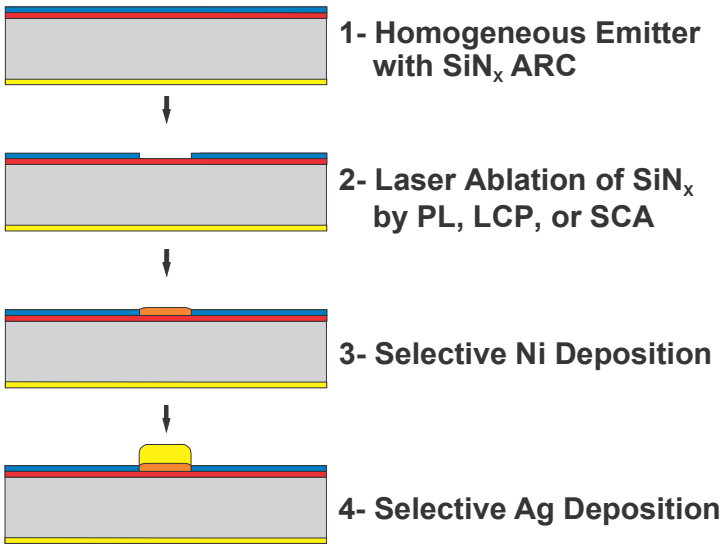

Figure 5.2. Processing method for solar cells with SiN_X laser ablation and Ni/Ag selective electrochemical front grid metallization. Surface texturing not shown for simplicity.

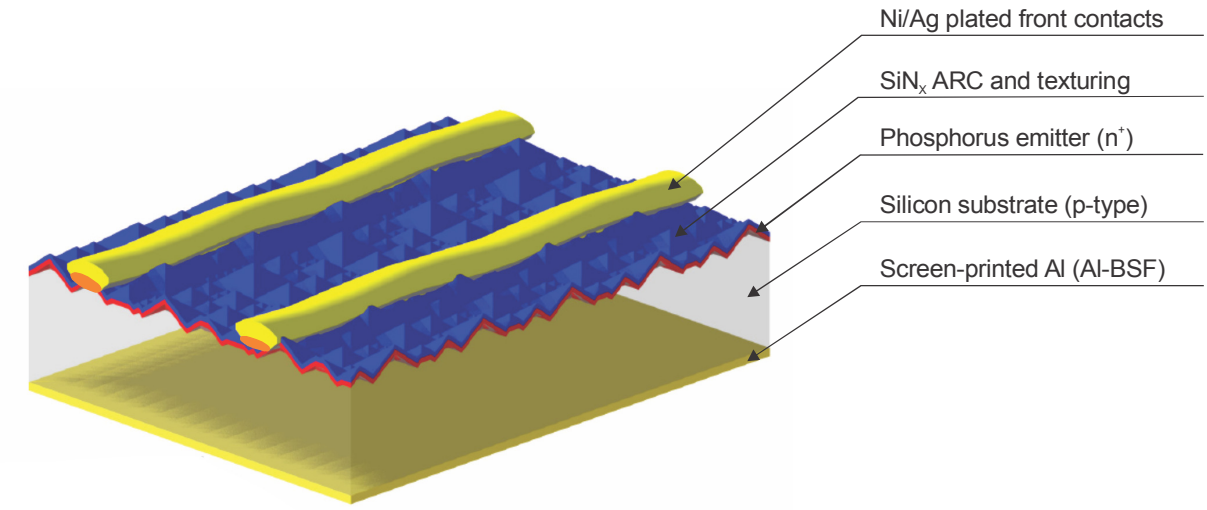

Figure 5.3. Schematic structure of a solar cell with SiN_X laser ablation and selective Ni/Ag front surface metallization. Adapted from [66].

The solar cell design included random pyramid texturing on the front surface, a chemically-etched rear surface, a homogeneous phosphorus emitter on the front surface, a SiN_X ARC with approximately (62 ± 2) nm, screen-printed rear surface metallization similar to the process used in industrial production, and Ni/Ag deposition for front surface metallization, selectively deposited on the SiN_X laser-ablated openings.

To allow the comparison between the different SiN_X removal processes, as well as specific laser parameters, groups of samples with the same parameters or processing conditions were fabricated. Additionally, devices processed with different parameters were produced on the same silicon wafers and used for comparative studies, such as: different laser processing parameters (i.e. laser ablation technique, laser pulse energy). An example of a silicon wafer processed in this way, with a total of 16 different solar cell structures, is shown in Figure 5.4.

Samples used for process optimization and finished solar cells were fabricated on “as-cut”, Czochralski grown, p-type (boron doped), crystalline silicon wafers, with <100> crystallographic orientation, pseudo-square format with 156 mm x 156 mm sides and 190 mm diagonals, 190-200 µm thickness, and base resistivity range of 1-3 Ω cm. For this resistivity range, the base boron doping is between 1.5×10^{16} cm^{-3}

and 4.7 x 10^{15} cm^{-3}, respectively [57]. From each monocrystalline silicon wafer subjected to the process sequence 16 square n^+pp^+ solar cells with 2.00 cm side (total area of 4.00 cm^2) were fabricated with different laser parameters.

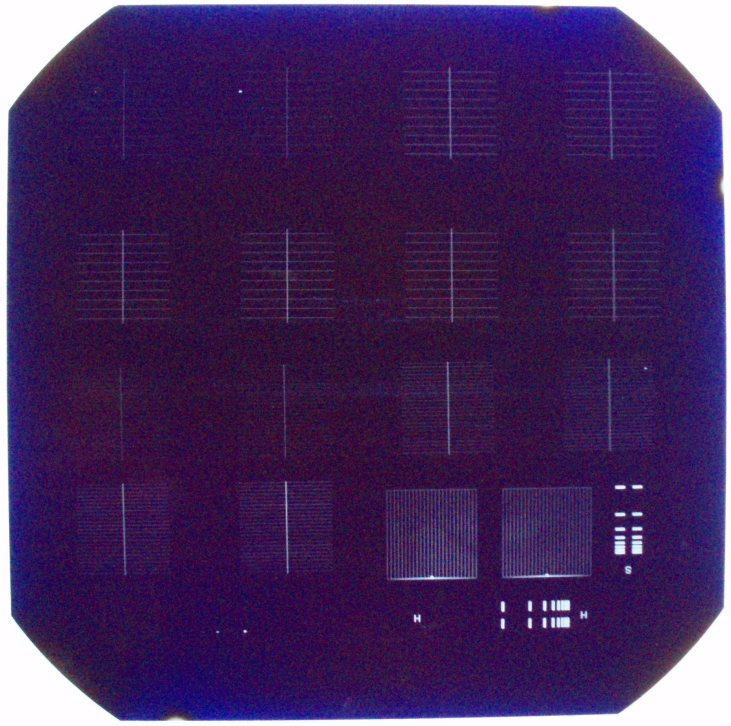

Figure 5.4. Picture of a (156 x 156) mm^2 silicon wafer processed with 16 solar cell with different front metal grids (photolithography, LCP-H_2O, SCA) and laser parameters.

All CZ-Si substrates were submitted to the following standard processing steps: random pyramid texturing with KOH and IPA, resulting in pyramid structures with an average height of approximately 5 µm; homogeneous $POCl_3$ phosphorus emitter diffusion in a quartz tube furnace, resulting in an emitter sheet resistance of 90-95 Ω cm, equivalent to a phosphorus surface concentration of approximately 3.7 x 10^{19} cm^{-3}; SiN_X deposition on the front surface with an industrial plasma-enhanced chemical vapour deposition equipment; single-side chemical etching to remove the homogeneous emitter from the rear surface and simultaneously convert the texture of the rear side into a smoother surface. Since some of these steps were performed in collaboration between the Fraunhofer ISE and an industry partner, details of the aforementioned processing steps cannot be made available in this work.

5.1.2. SiN_X Openings Defined by Photolithography

For the selective removal of SiN_X from reference samples, photolithography was employed. Although this method is very precise and free from crystalline damage to the silicon substrate during removal of the SiN_X layer, it is too expensive and slow for any practical industrial application in solar cell fabrication. Therefore, the process was used as a reference to the SiN_X industrially-feasible laser ablation process developed.

The photolithography processing steps were performed at the photolithography laboratory of the Franhofer ISE clean room, according to the following sequence. First, 6 ml of the AZ 9260 high-resolution thick photoresist was deposited over the SiN_X layer of the silicon wafer, spun-on at 500 rpm and 3000 rpm with a Dominus Coater, and dried at 110 ºC. Second, selected wafer regions were illuminated with ultraviolet radiation through a photomask with the front surface metal grid design of a 2.00 cm x 2.00 cm solar cell, with 25 fingers with 10 µm width and 1.93 cm wide, one finger at the bottom connecting the 25 fingers previously described, and one larger busbar at the top, with a larger region at its centre, also connecting the 25 fingers. Third, samples were immersed in AZ 400K developer diluted in DI H_2O (1 : 3) for 3 minutes. Fourth, samples were etched in buffered HF solution for approximately 24 minutes, removing the SiN_X of the area exposed to ultraviolet radiation. Finally, the remaining photoresist was removed from samples, which were subsequently cleaned with RCA-1 and RCA-2.

An image of a sample after the photolithography step, showing the central SiN_X etched regions of the busbar and its intersection with some grid fingers is shown in Figure 5.5. The dark regions correspond to the surface area covered by SiN_X, whereas the bright regions correspond to the exposed silicon substrate.

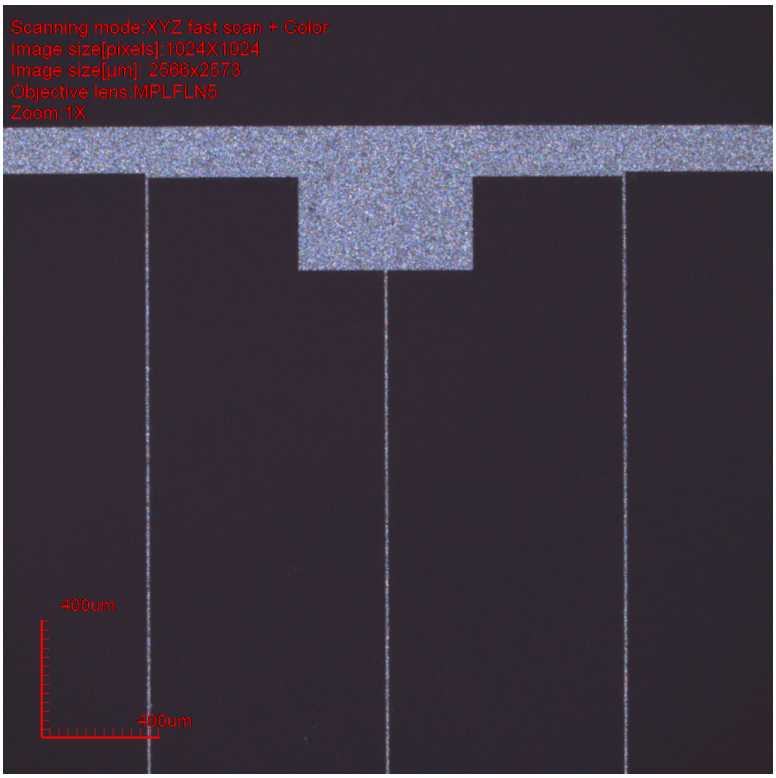

Figure 5.5. Confocal scanning microscopy of the SiN_X openings corresponding to the busbar and some fingers, performed by photolithography on textured silicon wafers.

5.1.3. Screen-Printing Metallization of the Rear Contacts

The rear surface metal contacts of solar cells were screen-printed on the silicon wafers using a semi-automatic precision screen-printer and an industrial aluminium rear side metallization paste. Each 156 mm x 156 mm silicon wafer was printed with a full-area mask layout, resulting in approximately 1.55 grams of wet paste per wafer. The paste was dried and subsequently fired at 900 ºC in an infrared lamp-heated three-zone conveyor belt furnace at a speed of 6200 mm/min. Both processes were performed under a controlled atmosphere using a filtered dry air flow for cooling.

An SEM image of the cross-section of a silicon wafer after screen-printing metallization of the rear contacts is shown in Figure 5.6. A cross-section, comprising the whole wafer thickness is shown in Figure 5.6(a), indicating that for the evaluated area the screen-printing step resulted in a homogeneous rear contact formation. The magnified SEM image shown in Figure 5.6(b) provides more details on the rear BSF

region. The formation of a Si-Al alloy is observed, giving rise to a full-area Al-BSF, approximately 4 µm thick.

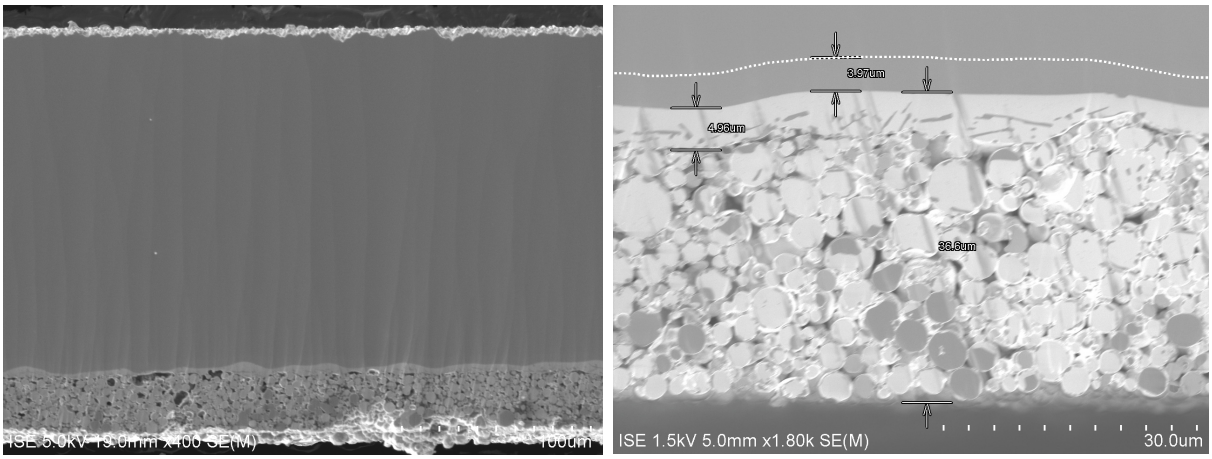

(a) **(b)**

Figure 5.6. SEM images of: (a) cross-section of a silicon wafer after screen-printing of the rear contacts and (b) detailed image of the rear contact, showing the formation of a homogeneous Al-BSF (dotted white line).

After firing, wafers presented a noticeable bow, with an average maximum deviation from the plane of approximately (1.6 ± 0.1) mm at the centre of the wafer. This phenomenon is known to be linked to the different thermal expansion coefficients of the silicon substrate and the aluminium paste during the firing step. Wafer bow may happen under a combination of the following aspects [163 - 165]: processing of very thin silicon wafers, usually with thicknesses below 200 µm; composition and presence of additives on the screen-printing aluminium rear side metallization paste; amount of aluminium metallization paste used during rear surface screen-printing; coverage area of the front metal grid and the amount of silver metallization paste used during front surface screen-printing, which may partially counter the stress between silicon and aluminium at the rear surface.

When applying laser processes to solar cells, surface non-uniformities, such as bowing, can be a considerable challenge to overcome. When scanning a laser beam over the surface of a bowed wafer, the laser beam will be in focus and out of focus in different regions of the wafer. This will result in different energy densities reaching the substrate, making the development of a homogeneous process very

difficult. In order to overcome the bowing condition observed in silicon wafers, the substrates were flattened using a flat silicon base with 0.5 mm thickness as a support for samples during laser processing. Therefore, it was possible to keep silicon wafers flat and in the same focal plane during laser processing.

5.1.4. Laser Ablation of the SiN_X Layer

The ablation processes developed were performed with two different laser system setups: a laser chemical processing and a scanning head mirror galvanometer laser system. Both systems were coupled with the aid of guiding mirrors to the same laser source, a NANIO 532 nm diode-pumped solid-state laser. The optical losses of each system setup were determined and taken into account when evaluating the laser processing parameters, in order to reduce uncertainties during processing. This methodology allowed a reliable comparison between the results obtained with the LCP and SCA methods.

The laser source operates in TEM_{00} (transverse electromagnetic mode), emitting a Gaussian-profile laser beam with pseudo-monochromatic wavelength centred at 532 nm. The system is controlled by a q-switch and has a frequency range of single pulse to 500 kHz. The system has a pulse generator that can operate in both normal or complement configuration. Operation in complement configuration allows the elimination of the high-energy first pulse usually present in pumped laser sources, at the cost of having a low-level background radiation emission during operation. System setup was adjusted so that this background radiation was kept below 3 W of continuous wave emission, corresponding to very low energy intensity. This resulted in a negligible impact of the background radiation on the SiN_X layer or silicon substrate under the processing conditions employed for both LCP and SCA methods.

The laser source setup is similar to that presented in section 4.1.6, but with the difference that the laser system is pumped by light from a diode instead of a lamp. After leaving the laser source enclosure, the laser beam passes through a variable attenuator, where laser power can be verified with the aid of a laser power meter and adjusted to the required value. After leaving the attenuator, the laser

beam is guided with the aid of 532 nm laser mirrors to the LCP or SCA system setup, as appropriate. In sequence, the laser beam is shaped in a secondary optical setup, through beam expander and collimator lenses, and finally guided by mirrors through the focal system to the sample surface.

Since the optical setup of the LCP system has no moving parts, an X-Y table is used to scan the whole surface area of samples with the laser beam coupled into the DI H_2O liquid jet. After preliminary tests with different liquid jet nozzles, the best results were obtained with an 80 μm brass nozzle diameter, under a liquid jet injection pressure of 70 bar, and with a constant N_2 gas flow to stabilize the laminarity of the liquid jet during processing. The X-Y table is composed of direct current motors, controlled by a CNC device, a microcomputer, and a CCD camera. It is a precise position control device, with a precision and repeatability of approximately ± 1 μm, a movement speed of up to 300 mm/s, and a processing area bigger than 243 cm^2 (156 mm x 156 mm). Processing at the LCP system can be monitored with the aid of the CCD camera. A schematic representation of the LCP laser system and a detailed description of its optical head and coupling unit are shown in Figure 5.7.

The LCP system was built over a granite base, for increased stability during laser processing, and includes the following components: 532 nm laser source; variable laser beam attenuator; beam expander and collimator lenses; guiding mirrors; CCD camera; focusing unit; high-pressure liquid jet pump; coupling unit, with liquid jet nozzle and sapphire window, where the laser beam is coupled into the liquid jet by total internal reflection; and X-Y table with a vacuum chuck sample holder. The LCP method was used to ablate regions of the antireflection coating for subsequent Ni/Ag metallization using DI H_2O as liquid medium, therefore without the incorporation of doping impurities.

The SCA system was also used to ablate the SiN_X antireflection layer, but in a dry environment, without the presence of liquids. It was built over the same granite base as the LCP setup, and includes the following components: 532 nm laser source; variable laser beam attenuator; beam expander and collimator lenses; scanning head, composed of two galvanometer-driven mirrors and F-theta focal lens;

and a fix sample holder with a flat silicon base. A schematic representation of the SCA laser system, including beam expander lenses and scanning head, and a description of its components are shown in Figure 5.8.

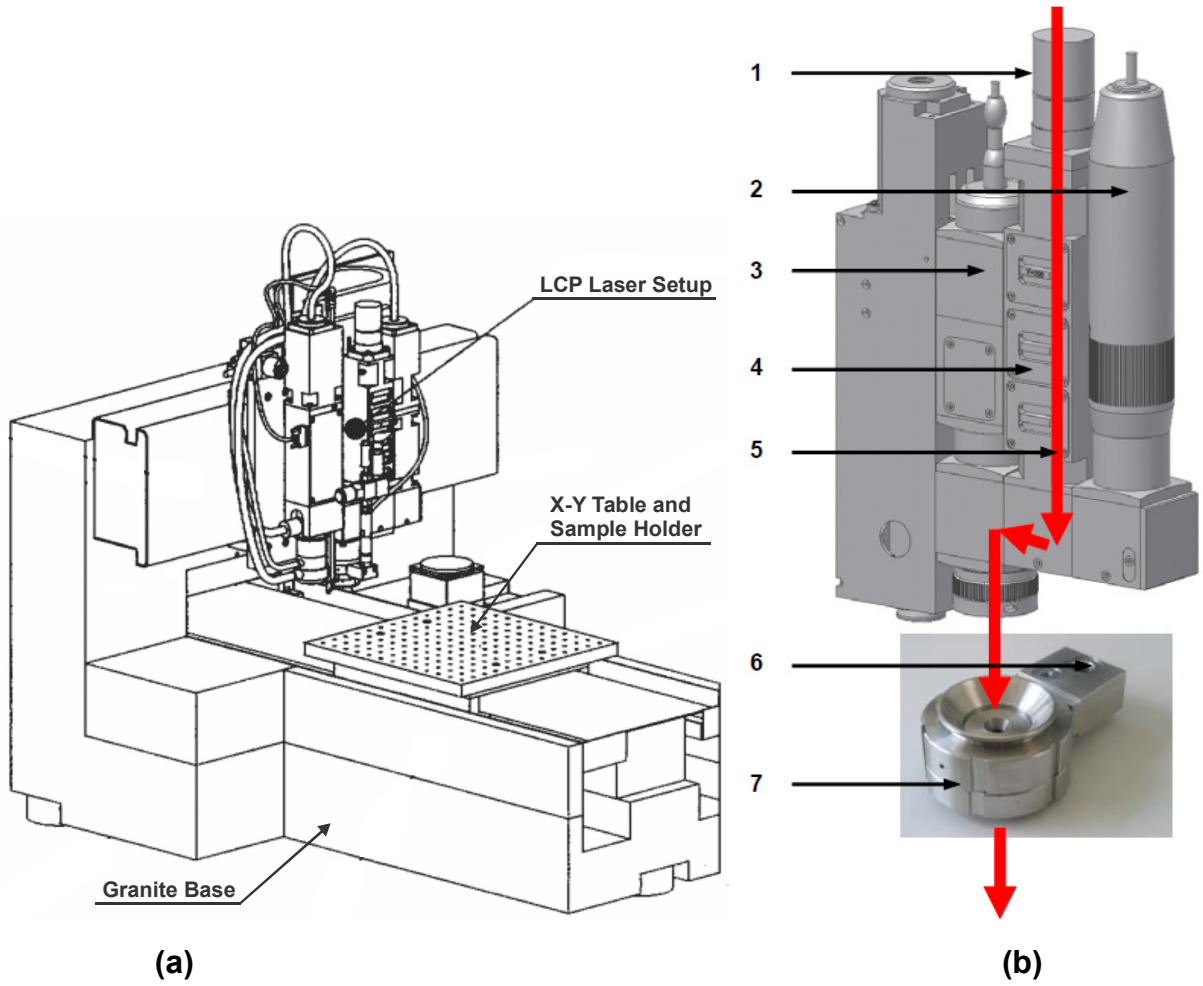

Figure 5.7. (a): schematic representation of the LCP system (adapted from [166]) and (b): detail of its optical head and coupling unit [167]: 1. incoming laser opening, 2. CCD camera, 3. guiding mirror unit, 4. focusing unit, 5. beam path, 6. high-pressure connector for the liquid solution, 7. coupling unit. The red arrow represents the laser beam path.

The laser parameters that were studied and optimized in this work include: laser pulse energy, ranging from 15.3 µJ to 27.5 µJ for the LCP system and from 3.0 µJ to 7.0 µJ for the SCA system; laser pulse frequency, ranging from 1.0 kHz to 500.0 kHz; and laser processing speed and pulse overlap, ranging from 100 mm/s to 300 mm/s for the LCP system and from 500 mm/s to 8000 mm/s for the SCA system.

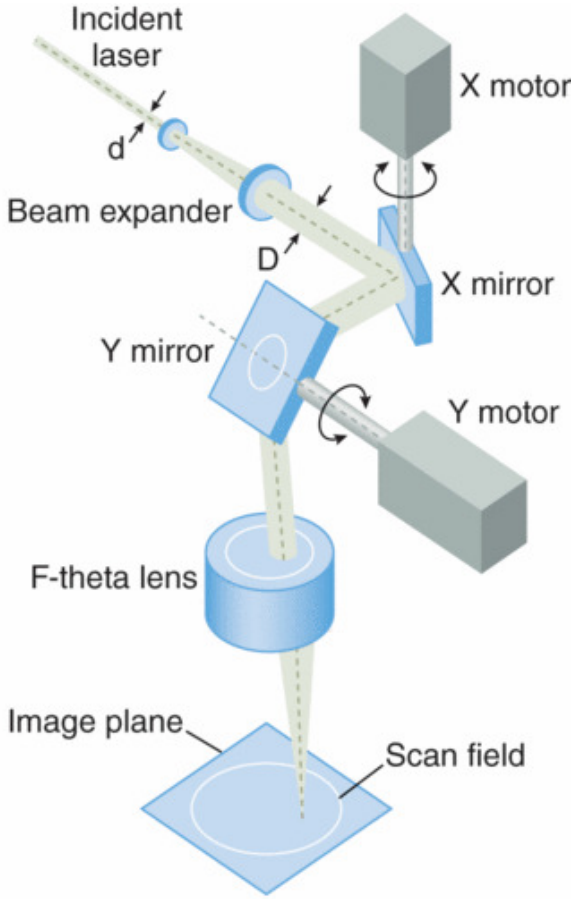

Figure 5.8. Configuration of the galvanometer-based laser processing (SCA) system, with a description of its scanning head components [168].

The SiN_X removal was based on different front grid designs for each of the three methods employed: photolithography, LCP-H_2O, and SCA. The design was defined by limiting factors, such as the smaller homogeneous ablation area with each laser system, and was optimized for similar opened areas and opened area fractions between different grid designs. The choice of a similar SiN_X opened area allowed direct comparison between samples, as the passivated area remained proportional for the different methods under investigation. The solar cell grid design included one larger busbar, to facilitate electrical characterization of devices, and a different number of metal fingers, according to the laser process employed. For laser-ablated solar cells, the busbar structure was obtained with a number of parallel fingers processed side by side. Details are provided in Table 5.1.

After laser processing, silicon wafers were cut into individual samples or solar cells with a diamond dicing saw. Each solar cell was cut into a 3.00 cm x 3.00 cm

sample, leaving 0.50 mm on each side of the device to facilitate sample handling and holding during electrochemical processes. The active area of solar cells was defined by using a 2.00 cm x 2.00 cm mask on the solar cells during measurements under illumination.

Table 5.1. Front contact grid design and SiN_X opened areas and area fractions for solar cells developed, according to the method employed for the removal of the SiN_X layer. Designs were optimized for similar opened areas and area fractions.

Method	Metal Fingers	Finger Width [µm]	Busbar Width [µm]	Opened Area [cm^2]	Opened Area Fraction [%]
Photolithography	25	10	10 to 580[1]	0.06877	1.72
LCP-H_2O	10	25	100 (4 fingers)	0.06975	1.74
SCA	25	10	100 (10 fingers)	0.06975	1.74

[1] The busbars of solar cells incorporating photolithography had a varying shape, thinner at the edges and thicker at the centre, with a rectangular contacting tab in the middle (see Figure 5.5).

5.1.5. Metallization of the Front Contacts using Ni/Ag Plating

After opening specific regions of the front surface SiN_X layer, the exposed silicon substrate was metalized by a two-step deposition of Ni and Ag. Due to its chemical properties, it is possible to selectively deposit nickel over silicon surfaces by means of electrochemical deposition methods. In this approach, the chemical reaction takes place at the interface between the silicon substrate and the electrochemical solution. Therefore, the SiN_X ARC layer covering the majority of the front surface of the silicon wafer acts as a barrier to the reaction, protecting these regions from the direct deposition of nickel. In this work, selective nickel deposition was performed by electroless light-supported plating (ELSP). A schematic representation of the ELSP method is shown in Figure 5.9.

In the ELSP process, samples were initially cleaned with DI H_2O and than submerged in a diluted HF (1 %) solution for 30 seconds, in order to remove any native oxide covering the exposed silicon surface regions, where nickel should be deposited. This activation step was halted by cleaning samples with DI H_2O. In sequence, samples were fixed in the sample holder (up to four simultaneous samples) and submerged in an aqueous solution containing the electrolyte NIPOSIT

PM-988 (Dow Chemical Company), mainly composed of nickel (93-96 %) and phosphorus (4-7 %). The solution was kept at a stable temperature of (30.0 ± 2.0) ºC, a pH of approximately 9.0, and homogenized with a mixing pump during the deposition process. Under these conditions, nickel plating was performed using a green light-emitting diode (LED) array for a fixed time of 90 seconds. After the plating process, samples were cleaned with DI H_2O and dried with nitrogen.

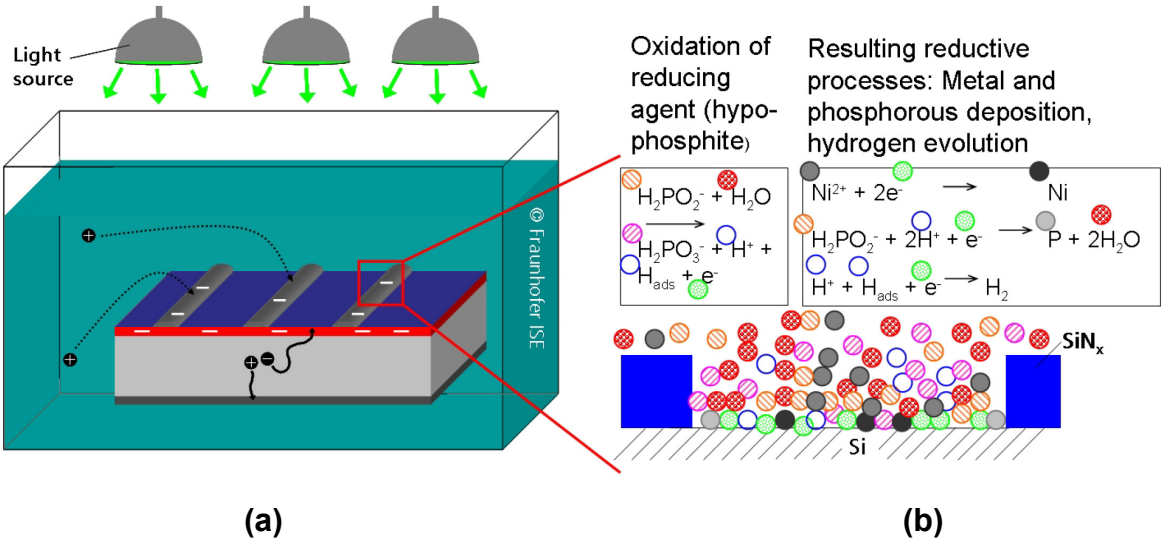

Figure 5.9. (a): schematic representation of the electroless light-supported plating process setup and (b): detail of the distribution of species and chemical reactions usually attributed to this process [141].

The ELSP deposition produced a nickel layer of approximately 0.5-1.5 µm thickness. Obviously, this is not enough metal to make front contacts with low resistive losses, therefore front surface contacts were thickened by means of silver deposition. Silver was chosen for simplicity reasons, since the parameters for a stable deposition process were already established at the Fraunhofer ISE and metal deposition optimization is not part of the focus of this thesis. Nevertheless, silver could be replaced by copper and tin once reproducible, homogeneous, and stable parameters for the deposition of both metals are found [169].

The presence of a nickel layer on the front surface of the solar cell greatly facilitates the selective deposition of silver. This process can be selectively performed by electrochemical deposition, whereby only those areas covered with nickel will participate in the electrochemical reactions and, therefore, be covered with

silver. Silver deposition was performed by light-induced electroless plating (LIEP). In the LIEP method, the system setup is very similar to the one described in Figure 5.9 for ELSP. Samples require no external electrical current applied and no direct electrical contact with the front metal grid during LIEP deposition. Additional advantages of the LIEP method are that deposition rates are normally faster than conventional electroless plating methods and the electrolyte solution does not contain cyanide or ammonia.

In the LIEP technique, solar cells are immersed in a plating solution and irradiated with light, resulting in the deposition of silver on the negatively charged (cathodic) front side of the solar cell. This is accompanied by the dissolution of Al ions from the rear side paste, located on the positively charged (anodic) rear side of the solar cell [170].

Samples were fixed onto the sample holder (up to two simultaneous samples) and submerged in an aqueous solution containing the following electrolyte system: Helios Silver LIEP 840 (silver source), Helios Silver LIEP 841 (reducer), and Helios Silver LIEP 842 (replenisher). The solution was kept at a stable temperature of (50.0 ± 2.0) ºC, a pH of approximately 8.8, and homogenized with a magnetic stirrer during the deposition process. Under these conditions, nickel plating was performed using a white light-emitting diode array. Different plating times of 10, 15, and 30 minutes were tested with the best results observed for 30 minutes of LIEP. After the plating process, samples were cleaned with DI H_2O and dried with nitrogen.

More details about the electrochemical metallization processes employed in this work can be obtained in reference [141].

5.2. Characterization Methods for Samples and Solar Cells with Laser Ablation

A selection of characterization methods was employed to monitor the development and optimization of laser ablation processes, as well as to compare the performance of finished solar cells. Characterization techniques employed during the development of solar cells with SiN_X laser ablation and Ni/Ag metallization were the following:

1. Electrical parameters of finished solar cells (efficiency, fill factor, short-circuit current, open-circuit voltage), extracted from illuminated current density-voltage curves, obtained with the aid of a calibrated solar simulator operating under standard test conditions (AM1.5G solar spectrum, irradiance of 1000 W/m^2, sample temperature of 25 ºC).

2. SiN_X film thickness, estimated by ellipsometry.

3. Suns-Voc characterization, to monitor and evaluate Ni/Ag front contact metallization.

4. Semiconductor sheet resistance estimated from four point probe resistivity measurements.

5. Confocal scanning microscopy with an Olympus LEXT OLS4000 microscope for topographical evaluation of samples.

6. Scanning electron microscopy for topographical evaluation of samples.

5.3. Development of SiN_X Ablation using Laser Processing

The first experimental part of this chapter was focused on determining the optical losses of the LCP and SCA laser system setups. In sequence, a SiN_X laser ablation process was developed and optimized with each of the two laser processing techniques.

5.3.1. Determination of the Optical Losses of the Laser Systems

In order to adequately compare laser processing parameters between the LCP and SCA laser systems, it is important to evaluate and understand the laser beam power, the laser pulse energy, and the laser pulse energy density reaching samples during processing. These parameters depend mainly on the optical setups

of the laser systems and the corresponding optical losses, identified between the laser source and the sample under laser processing.

Therefore, by determining the optical losses of the LCP and SCA laser system under usual operating conditions, it is possible to correlate and compare the laser power values employed in each laser system, as well as better assess the influence this parameter has on the SiN_X laser ablation process.

5.3.1.1. Laser Chemical Processing with Deionised Water

A detailed description of the LCP-H_2O system was already provided in section 5.1.4. A schematic representation of the optical setup of the LCP-H_2O laser system is shown in Figure 5.10, highlighting the measurement points (A, B, and C) where laser power was evaluated to determine the optical losses of the system.

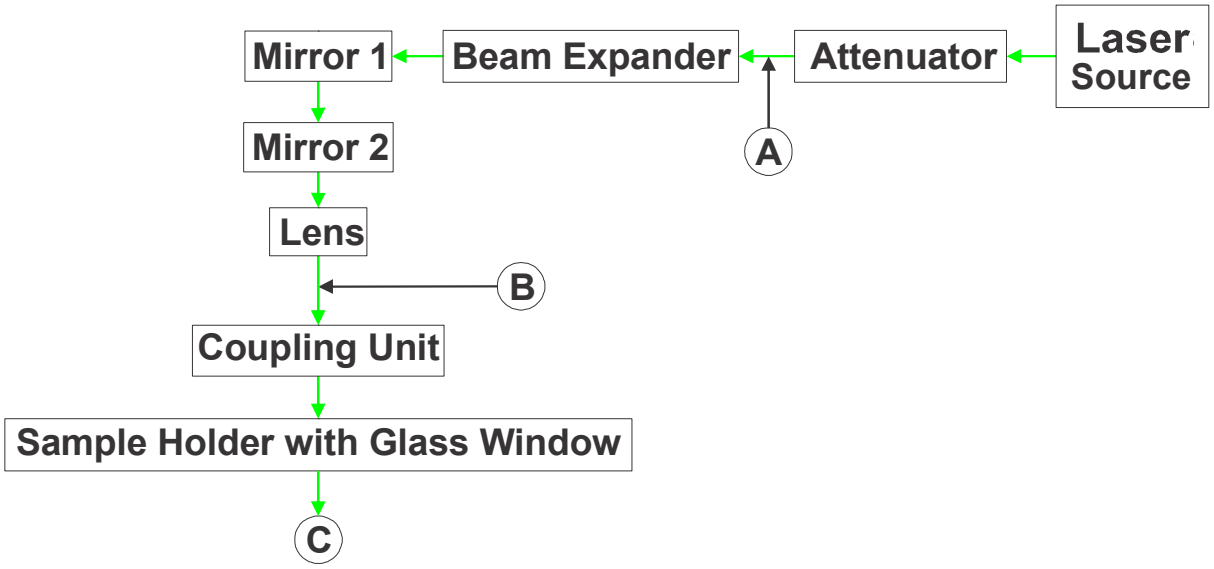

Figure 5.10. Schematic representation of the optical setup of the LCP-H_2O system and laser power measurement points for the determination of optical losses.

The optical setup includes a 532 nm laser source, a variable attenuator with which the laser power intensity can be adjusted, a beam expander, followed by a pair of guiding mirrors and one lens, guiding the laser beam into the coupling unit, where the laser beam is coupled into the pressurized DI H_2O liquid jet, and finally arrives at the sample holder. To allow the determination of the laser power at the sample

position, an adapted sample holder with a glass window was employed in this work, so that the laser power could be measured after the glass window. Losses from the glass window itself were properly accounted for in the calculations and corresponded to (6.9 ± 0.4) %.

The determination of optical losses was performed by measuring and comparing the laser beam power in three different positions: between the variable attenuator and the beam expander (point A), where power measurements are usually performed during experiments; between the lens and the coupling unit (point B); and after the sample holder with a glass window (point C), on top of which the sample would normally be located during laser processing. The total losses of the LCP-H_2O system were obtained by calculating the laser power differences at points A and C, since power measurements during experimentation are usually performed at point A and the laser beam reaches the sample at the sample holder, close to point C. Measurements were performed in conditions similar to those of actual laser processing (i.e. laser beam wavelength, liquid medium, nozzle diameter, N_2 gas flow etc.), such as described in section 5.1.4. Results are summarised in Table 5.2.

Table 5.2. Laser power measurements at different points and calculated average optical losses for the LCP-H_2O system.

A [W]	B [W]	C [W]	Optical Losses [%]
0.200	0.144	-	28.0
0.505	0.379	-	25.0
0.701	0.533	-	24.0
1.000	0.775	-	22.5
0.204	0.144	-	29.4
0.504	0.382	-	24.2
0.703	0.545	-	22.5
1.000	0.792	-	20.8
Average (A to B)			24.6 ± 2.9
0.200	-	0.112	39.8
0.497	-	0.285	38.3
Average (A to C)			39.1 ± 1.1

As can be seen from Table 5.2, the LCP-H_2O laser system has considerable optical losses both before and after the coupling unit. Approximately 60 % of the optical losses are occurring before the coupling unit, between points A and B, thus before the laser beam gets coupled into the DI H_2O liquid jet. This is considerably higher than would be expected, since up to this point the system is mainly composed of special mirrors and lenses, with supposedly low optical losses, that guide and shape the laser beam. The other 40 % of the optical losses are occurring after the coupling unit. Overall, average total optical losses amount to as much as 39.1 % between points A and C, indicating that for this particular optical setup, a significant fraction of the laser beam power is lost before it reaches the sample. This has to be taken into consideration when calculating the threshold laser beam power and energy values during processing conditions.

5.3.1.2. Scanning Head Mirror Galvanometer Laser System

A detailed description of the SCA laser system was already provided in section 5.1.4. A schematic representation of the optical setup of the SCA system is shown in Figure 5.11, highlighting the measurement points (A, B, C, and D) where laser power was evaluated to determine the optical losses of the system.

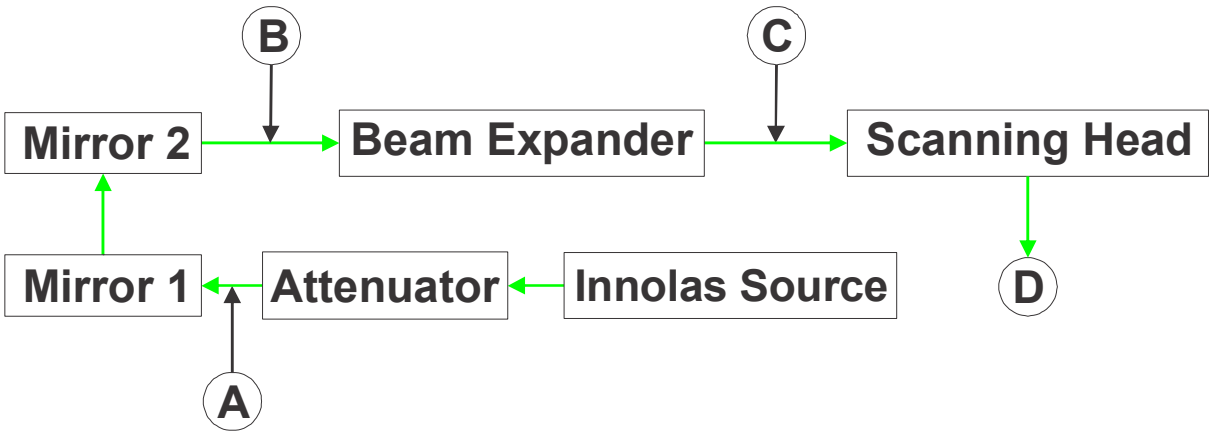

Figure 5.11. Schematic representation of the optical setup of the SCA system and laser power measurement points for the determination of optical losses.

The optical setup includes a 532 nm laser source, a variable attenuator with which the laser power intensity can be adjusted, followed by a pair of mirrors, which guide the laser beam through the beam expander and into the scanning head,

composed of two galvanometer-controlled mirrors and an F-theta lens, as displayed in Figure 5.8. This setup uses the same laser source and attenuator than the LCP-H_2O system, but a different set of mirrors, and beam expander. All mirrors employed in the SCA setup were appropriate for the laser source emission wavelength of 532 nm.

The determination of optical losses was performed by measuring and comparing the laser beam power in four different positions: after the variable attenuator (point A), where power measurements are usually performed during experiments; before the beam expander (point B), to evaluate losses with the first two guiding mirrors; after the beam expander, to evaluate losses at this optical part of the system (point C); and after the scanning head (point D), at the sample holder where samples were processed during experiments, but with defocused measurements to avoid damaging the power meter. Measurements were performed in the same conditions employed during actual processing of samples. Results are summarised in Table 5.3.

Table 5.3. Laser power measurements at different points and calculated average optical losses for the SCA system.

A [W]	B [W]	C [W]	D [W]	Total Optical Losses [%]
1.08	1.07	1.06	1.00	7.4
2.14	2.13	2.11	2.00	6.5
3.20	3.17	3.14	3.00	6.3
4.18	4.17	4.16	4.00	4.3
5.32	5.28	5.26	5.00	6.0
1.06	-	-	1.00	4.8
2.13	-	-	2.00	6.1
3.19	-	-	3.00	6.0
4.26	-	-	4.00	6.1
5.34	-	-	5.00	6.4
Average (A to D)				6.0 ± 0.9

Differently from what was observed with the LCP-H_2O system, the optical setup of the SCA system has considerably lower optical losses. Losses measured at the two guiding mirrors (between points A and B) and at the beam expander

(between points B and C) are only marginal, representing approximately 1 % absolute each. This is significantly lower than losses at the scanning head (between points C and D), which represent about 3-5 % absolute and represent the main source of optical losses of the system. Overall, the average optical losses were of 6.0 %, therefore more than six times lower than losses measured in the LCP-H_2O system. In summary, it is clear that optical losses play an important role when performing power, energy, and energy density analyses with laser systems and that the significant differences between the optical setups of the LCP-H_2O and SCA systems has to be taken into account during experimental work.

A direct comparison of the laser intensity of the LCP-H_2O and SCA laser systems by performing power measurements after the attenuator (point A, where measurements are usually performed) would lead to inconsistent and imprecise conclusions in respect to power and energy values reaching samples during laser processing. In this regards, measuring the laser beam power at the sample processing position avoids this difficulty and can be easily performed with the SCA system. The situation is more complex for the LCP-H_2O system, as in this case the laser beam is coupled into a liquid jet and therefore measurements performed at this position could damage the power meter, since the laser beam is highly focused. Additionally, the DI H_2O liquid jet would influence the measurement. The situation would be even more complex when employing different liquid jet media, such as phosphoric acid or solutions containing highly reactive or toxic components.

Therefore, in order to avoid additional complexities, laser power measurements with the LCP-H_2O system carried out in this work were performed after the attenuator, as usually done at Fraunhofer ISE, and later corrected to account for the optical losses determined in section 5.3.1.1. For the SCA system, laser power measurements were carried out directly at the sample holder stand, after the laser beam has passes through all the optical parts of the system.

5.3.2. Influence of the Laser Pulse Energy

In order to evaluate and compare the influence of the laser pulse energy on the SiN_X laser ablation process, laser ablation thresholds for the LCP-H_2O and SCA

systems were determined. The laser ablation threshold was defined in this work as the laser pulse energy at which laser ablation of the SiN_X layer starts to occur. Two different laser ablation conditions were evaluated. Initially, laser ablation was performed with single laser pulses, resulting in the formation of ablated points on the samples. These results served as a preliminary basis to determining the laser pulse energy range at which laser ablation starts. Since laser ablation based on single pulses does not have any influence from overlapping pulses or multiple irradiations, this greatly simplifies the analysis of the results. Afterwards, laser ablation with multiple laser pulses was performed and analysed. Results served as a basis to the selection of laser processing parameters used in SiN_X laser ablation of front contact fingers and busbars regions of solar cells.

5.3.2.1. Laser Chemical Processing with Deionised Water

Initial laser ablation experiments with the LCP-H_2O system were performed with single laser pulses on random-pyramid textured CZ-Si samples, covered with a SiN_X ARC with estimated thickness of 70 nm. The aim was to determine the minimum laser pulse energy needed to open the SiN_X layer and expose the underlying silicon substrate. A selection of representative results is provided in Figure 5.12.

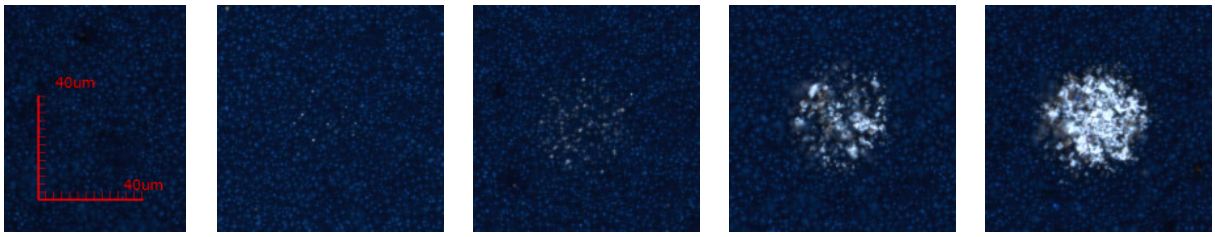

Figure 5.12. Confocal microscopy images of single-pulse laser-ablated points processed with different laser pulse energies using the LCP-H_2O technique. Fixed laser processing parameters were: 1 kHz q-switch frequency, 200 mm/s processing speed, 50 ns pulse duration. Scale: 40 µm.

Results indicate that single-pulse laser ablation using the LCP-H_2O technique starts at laser pulse energy values of approximately 12.2 µJ. As would be expected, there is a direct correlation between laser pulse energy and laser-ablated area, with

an increase of the ablated area for higher energy values. The ablated zone is nonetheless not completely homogeneous, with specific regions of the silicon nitride film being removed prior to others on the same irradiated area. This is an effect mainly caused by a combination of the complex surface roughness of the random pyramids texturing and the inhomogeneous laser energy distribution on the irradiated area. The latter phenomenon is caused by the multimode waveguide properties of the liquid jet into which the laser beam is coupled by total internal reflection, as discussed in reference [171].

After the preliminary analysis with single laser pulses, laser ablation was employed to open lines on the SiN_X ARC. The aim was to determine the laser pulse energy needed to open homogeneous lines on the silicon nitride and expose the underlying silicon substrate. A selection of representative results is shown in Figure 5.13.

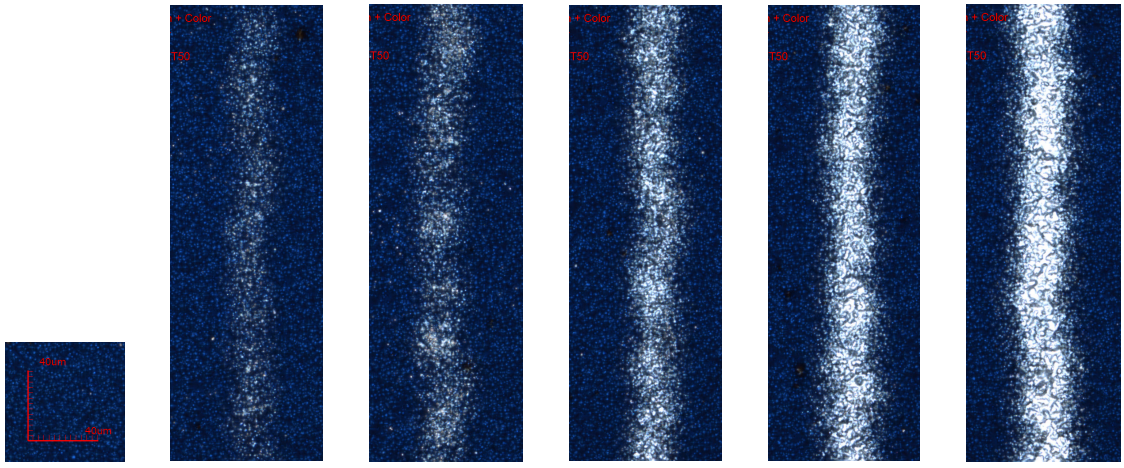

Figure 5.13. Confocal microscopy images of laser-ablated lines processed with different laser pulse energies using the LCP-H_2O technique. Fixed laser processing parameters were: 100.0 kHz q-switch frequency, 300 mm/s processing speed, 40 ns pulse duration, 3.0 µm pulse distance. Scale: 40 µm.

Results indicate that laser-ablated lines can be formed when employing laser pulse energies of 15.3 µJ or more. For 15.3 µJ laser pulse energy, ablated line width was approximately 25 µm, which was the smallest line width for a homogeneous laser-ablated line obtained with the LCP-H_2O technique in this work. Increasing the laser pulse energy produces wider and more homogeneous openings, but also

causes increased melting of the silicon substrate, which may lead to unwanted damaging of the silicon substrate crystalline structure or even the p-n junction itself. For 21.4 µJ laser pulse energy, line width was approximately 30 µm and melting of the underlying silicon substrate became clearer. For 27.5 µJ laser pulse energy, considerable topographical change of the silicon substrate was visible, including molten pyramid structures and reduced surface roughness at the laser-ablated regions. The line width in this case was of approximately 35 µm.

5.3.2.2. Scanning Head Mirror Galvanometer Laser System

Initial laser ablation experiments with the SCA system were performed with single laser pulses on random-pyramid textured CZ-Si samples, covered with a SiN_X ARC with estimated thickness of 70 nm. The aim was to determine the minimum laser pulse energy needed to open the SiN_X layer and expose the underlying silicon substrate. A selection of representative results is provided in Figure 5.14.

Results indicate that single-pulse laser ablation using the SCA technique starts at laser pulse energy values of approximately 3.0 µJ, significantly lower than the values observed for the LCP-H_2O technique. One cause for this is that the laser pulse spot size (i.e. laser beam diameter reaching the sample surface) is different for each system, with a smaller spot size for the SCA system in comparison to LCP-H_2O. As in the previous case, employing higher laser pulse energies resulted in an increase of the SiN_X opened area. Similarly to what was observed with the LCP-H_2O process, the opened area was inhomogeneous, with specific regions of the silicon nitride film being removed prior to others. This effect was clearer for lower laser pulse energy values, such as between 3.0-4.0 µJ, whereby laser ablation resulted in a small opened area fraction, with limited melting of the silicon substrate. When higher energy values were employed, melting of the silicon below the SiN_X layer was increased, as seen for 5.0 µJ, whereby the random pyramid structure was already strongly affected by the ablation process. For 6.0 µJ and 7.0 µJ laser pulse energies, considerable melting and subsequent solidification of the silicon substrate was observed, significantly altering the topography of the laser-ablated region.

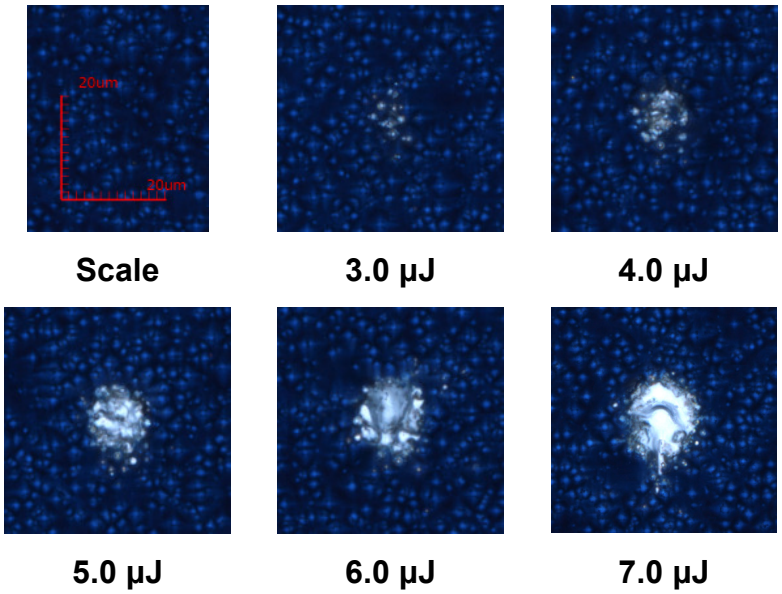

Figure 5.14. Confocal microscopy images of single-pulse laser-ablated points processed with different laser pulse energies using the SCA technique. Fixed laser processing parameters were: 100.0 kHz q-switch frequency, 10000 mm/s processing speed, 40 ns pulse duration. Scale: 20 µm.

After the preliminary analysis with single laser pulses, laser ablation was employed to open lines on the SiN_X ARC. The aim was to determine the laser pulse energy needed to open homogeneous lines on the silicon nitride and expose the underlying silicon substrate. A selection of representative results is shown in Figure 5.15.

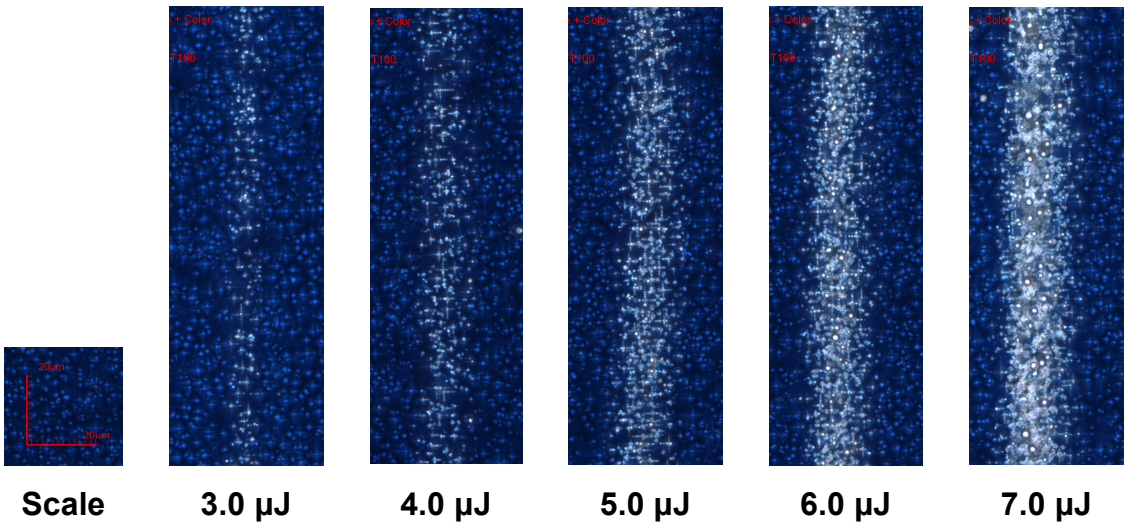

Figure 5.15. Confocal microscopy images of laser-ablated lines processed with different laser pulse energies using the SCA technique. Fixed laser processing parameters were: 400.0 kHz q-switch frequency, 1000 mm/s processing speed, and 2.5 µm pulse distance, 145 ns pulse duration. Scale: 20 µm.

Results indicate that laser-ablated lines can be formed when employing laser pulse energies of 3.0 µJ or more. For 3.0 µJ laser pulse energy, ablated line width was approximately 10 µm, which was the smallest value for a homogeneous laser-ablated line obtained with the SCA technique in this work. As for the LCP-H_2O technique, increasing the laser pulse energy produces wider and more homogeneous openings. For 5.0 µJ laser pulse energy, line width was approximately 13 µm and melting of the silicon substrate could be observed. For 7.0 µJ laser pulse energy, considerable topographical change of the silicon substrate was visible, including molten pyramid structures and reduced surface roughness at the laser-ablated regions. The line width in this case was of approximately 16 µm.

A closer look at the laser-ablated lines at lower laser pulse energy values, between 3.0-5.0 µJ, provided additional information about the process. When laser ablation is performed at energies close to the SiN_X ablation threshold, melting of specific regions of the silicon substrate was observed, as shown in Figure 5.16.

The tips and corners of the random pyramid structures were the first parts of the substrate to be molten during laser ablation. This phenomenon may be attributed to a concentration of the laser beam on the tips and corners of the pyramids, caused by constructive interference patterns of the laser radiation reaching the pyramidal structure [172]. The results shown in Figure 5.16 are an indication of these constructive interference patterns and, therefore, support this explanation. Consequently, it can be stated that, in general terms, when performing laser processes on solar cells with a complex topography, such as texturing, the energy distribution throughout the substrate will be inhomogeneous. In the case of SiN_X laser ablation, this means that it is possible to partially ablate the pyramids of textured silicon wafers, removing the ARC layer from the tips and corners of the pyramids and leaving its sides covered.

A summary of the different line widths obtained during SiN_X laser ablation with the LCP-H_2O and SCA techniques is shown in Figure 5.17.

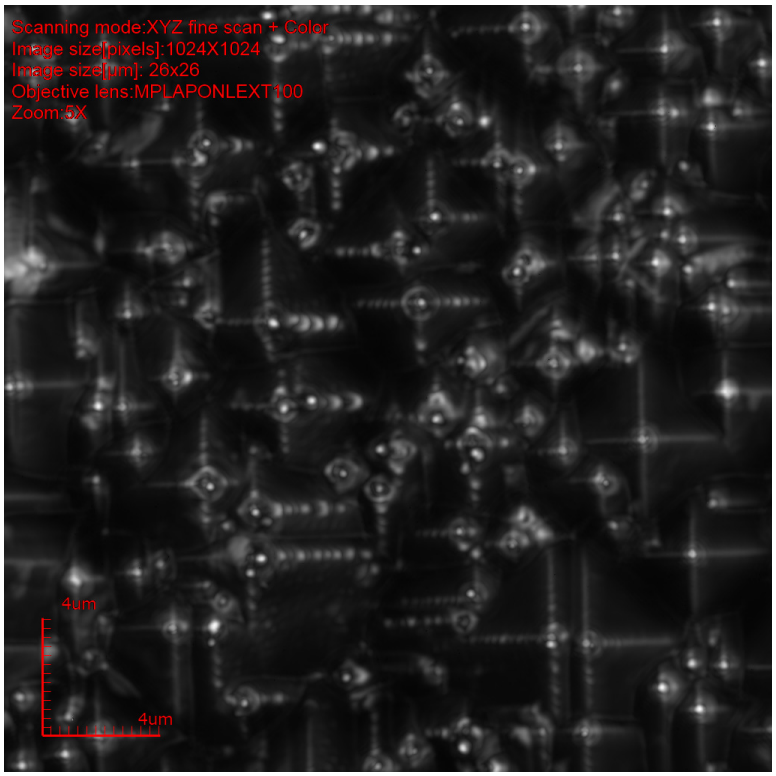

Figure 5.16. Confocal laser scanning microscopy image of laser-ablated lines with melted pyramid tips and corners. Laser processing parameters were: 4 µJ pulse energy, 400 kHz q-switch frequency, 1000 mm/s processing speed, 2.5 µm pulse distance, 145 ns pulse duration. Scale: 4 µm.

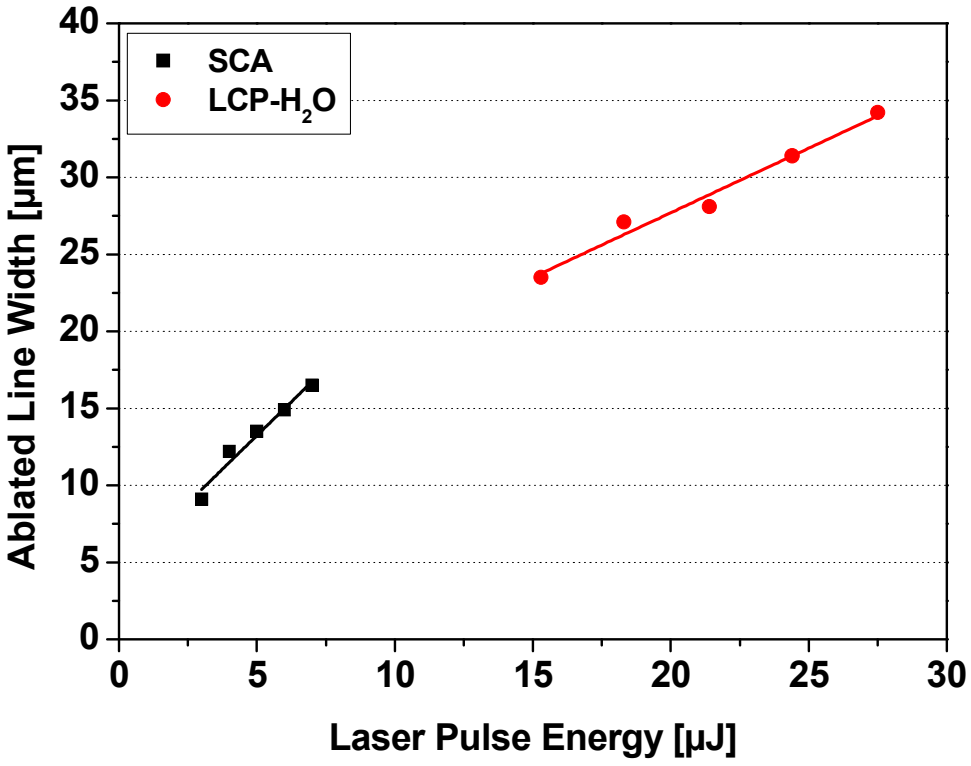

Figure 5.17. SiN_X laser-ablated line widths processed with different laser pulse energies using the SCA and LCP-H_2O techniques.

Laser processing with the SCA technique resulted in significantly smaller laser-ablated line widths than the LCP-H_2O process. This indicates that, for solar cell processing under the conditions investigated in this work, it may be possible to produce smaller finger and busbar openings with the first technique than with the latter. Such differences have to be accounted for in solar cell design, as they change aspects such as the shadowing factor, series resistance, and the fraction of the front surface that remains covered by the SiN_X passivation layer after laser processing.

5.3.3. Influence of the Laser Pulse Frequency

Another relevant parameter for the SiN_X laser ablation process is the frequency of the q-switch used during processing. This section evaluates the influence of this parameter on the ablation process. The analysis performed below is described mainly with results obtained using the SCA technique. Since the laser source is the same for both laser systems, similar experiments performed with the LCP-H_2O technique reached equivalent results. A selection of representative cases is shown in Figure 5.18 and Figure 5.19, for single-pulse laser-ablated points and laser-ablated lines, respectively.

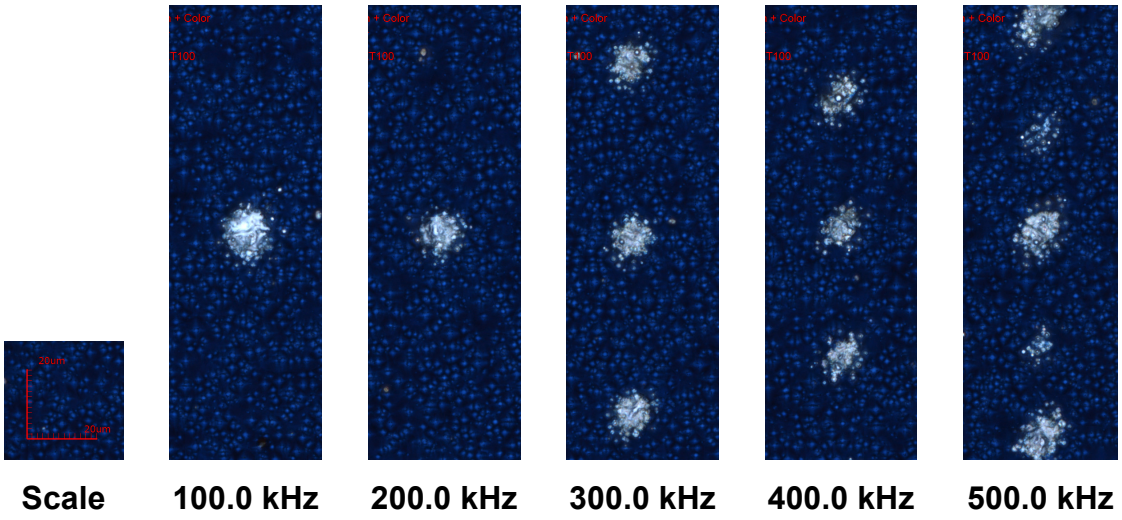

Figure 5.18. Confocal microscopy images of single-pulse laser-ablated points processed with different q-switch frequencies using the SCA technique. Fixed laser processing parameters were: 6.0 µJ pulse energy, 15000 mm/s processing speed. Scale: 20 µm.

From Figure 5.18 a variation in the homogeneity of the laser pulses can be noticed in one case. Laser pulses were relatively homogeneous for the interval between 100.0-400.0 kHz. However, for 500.0 kHz q-switch frequency, two different groups of laser-ablated points were obtained: points with higher ablated areas intercalated by points with lower ablated areas. This indicates that the excitation of the gain medium (i.e. laser pumping) was inhomogeneous due to the very fast q-switch frequency employed, with less energy being released each second pulse. Such non-linear behaviour would be undesired for homogeneous SiN_X laser ablation, therefore processing at 500.0 kHz with this laser source should be avoided.

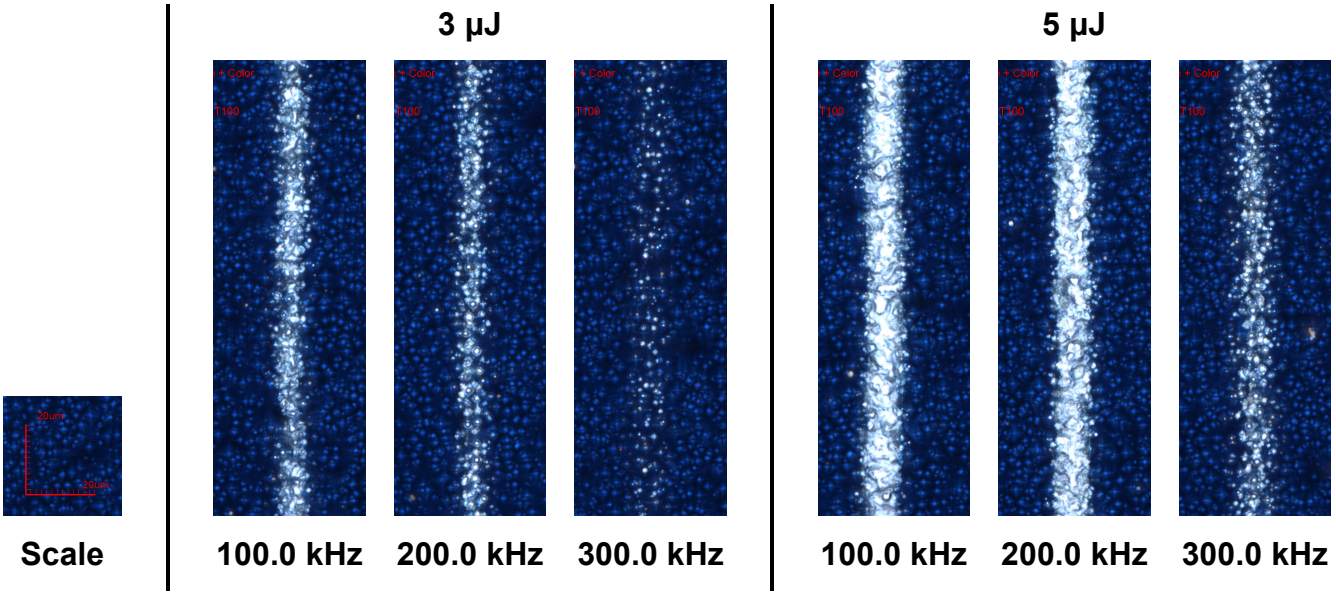

Figure 5.19. Confocal microscopy images of laser-ablated lines processed with different q-switch frequencies using the SCA technique. Fixed laser processing parameter was: 6.25 µm pulse distance. Scale: 20 µm.

The second aspect is clearer in Figure 5.19, where a reduction of the extent of laser ablation for higher q-switch frequencies can be clearly observed. Lines processed with higher q-switch frequencies, such as 300.0 kHz, show significantly less SiN_X ablation than those processed at lower q-switch frequencies, such as 100.0 kHz. This was observed for both laser pulse energies showed in Figure 5.19 and the effect is also apparent in Figure 5.18 for single-pulse ablated points, although harder to identify in the latter case. A similar effect was observed in section 4.3.2 with the laser system used for LFC processing. When the frequency of the q-switch is increased, the interval between laser pulses is reduced. This reduces the temporal

spacing of laser pulses, resulting in single-pulses with lower peak energy values and, therefore, reducing the extent of laser ablation when comparing lower frequency with higher frequency values.

5.4. Solar Cells Based on SiN_X Laser Ablation

After the development and experimental evaluation of the SiN_X laser ablation process, the LCP and SCA techniques were applied to fabricate solar cells on 156 mm x 156 mm industrial CZ-Si wafers from the same process batch. Different laser pulse energies were employed, in order to evaluate the impact of this parameter on the electrical properties of the devices.

The processing sequences and methods employed in solar cell fabrication were already described in detail in section 5.1. Therefore, this section was focused on the analysis and discussion of the results obtained with different laser processing parameters.

5.4.1. Selection of Laser Processing Parameters

Three different laser pulse energies for each of the two SiN_X laser ablation techniques were chosen and evaluated: the first energy value was very close to the ablation threshold of each technique, resulting in a smaller ablated area of the SiN_X layer, with less melting of the silicon substrate; the second energy value was intermediate, resulting in a higher ablated area than the previous case, but also causing more melting of the silicon substrate; the third and final value was a higher energy value, resulting in the largest ablated area and causing significant melting of the silicon substrate on the laser-processed region. Results after laser processing are shown in Figure 5.20 and Figure 5.21 for the LCP-H_2O and SCA techniques, respectively. The images show the intersection of a laser-ablated finger (horizontal line) with the laser-ablated busbar (vertical lines).

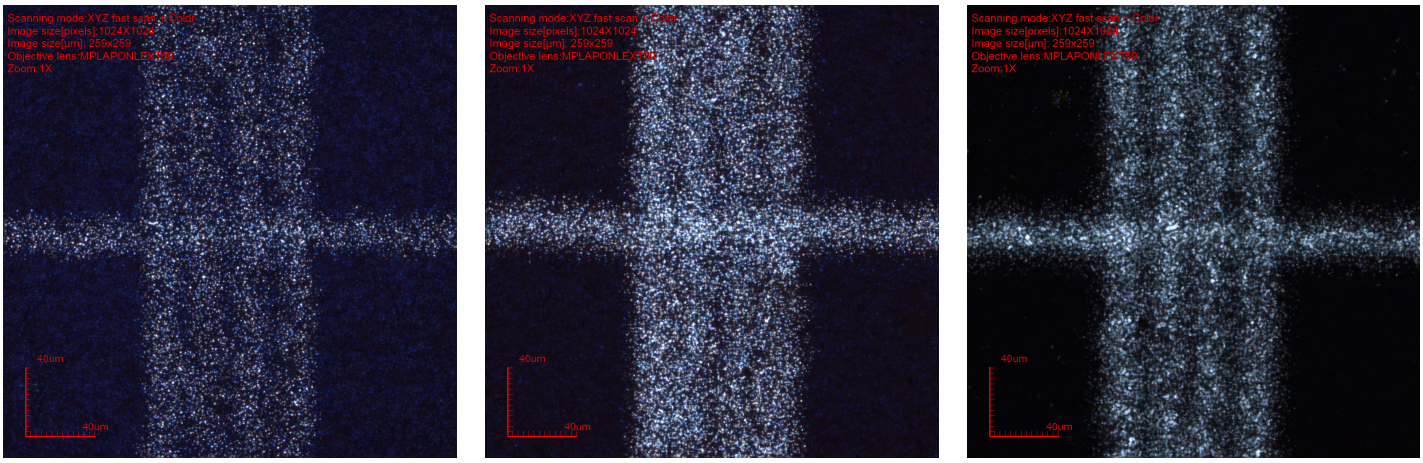

15.3 µJ **21.4 µJ** **27.5 µJ**

Figure 5.20. Laser-ablated fingers and busbars processed with different laser pulse energies using LCP-H_2O. Fixed laser processing parameters were: 16.0 kHz q-switch frequency, 100 mm/s laser processing speed, and 6.25 µm pulse distance, 50 ns pulse duration, 80 µm nozzle diameter, 70 bar pump pressure. Scale: 40 µm.

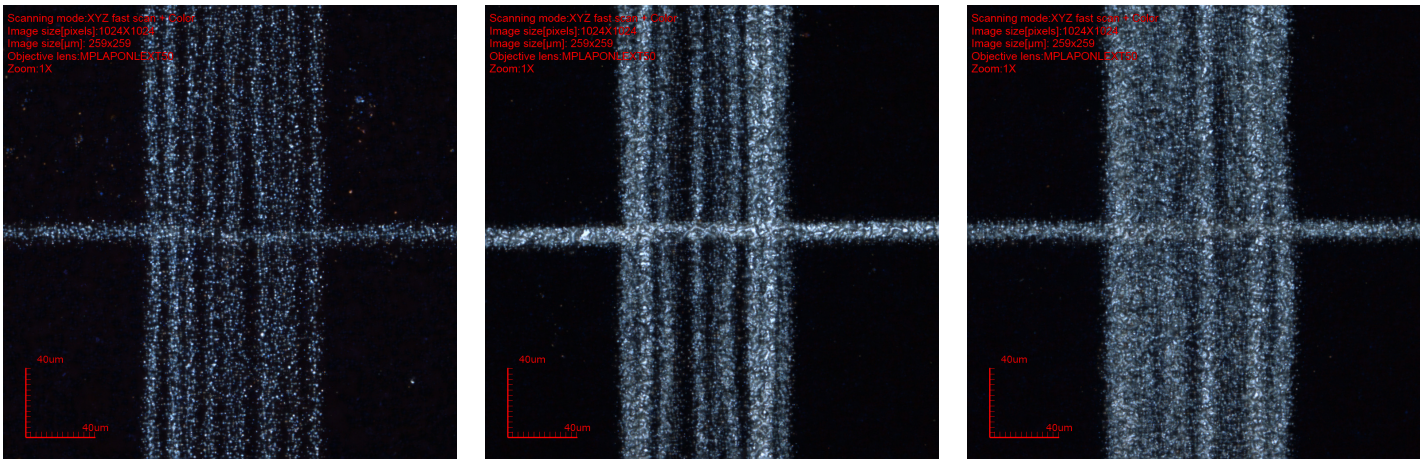

3.0 µJ **4.0 µJ** **5.0 µJ**

Figure 5.21. Laser-ablated fingers and busbars processed with different laser pulse energies using SCA. Fixed laser processing parameters were: 130.0 kHz q-switch frequency, 813 mm/s laser processing speed, and 6.25 µm pulse distance, 50 ns pulse duration. Scale 40 µm.

In both cases, the busbar had approximately 100 µm, being composed of 4 or 10 parallel laser-ablated lines for the LCP-H_2O and SCA techniques, respectively. Results are visually more homogeneous for the LCP-H_2O samples, with straighter ablated lines, whereas for the SCA system lines were slightly curved. The phenomenon was caused by vibration of the scanning head of the system during processing.

5.4.2. Comparison of the Different SiN_X Removal Methods

5.4.2.1. Photolithography

Images of a sample processed with photolithography before and after Ni and Ag plating are shown in Figure 5.22.

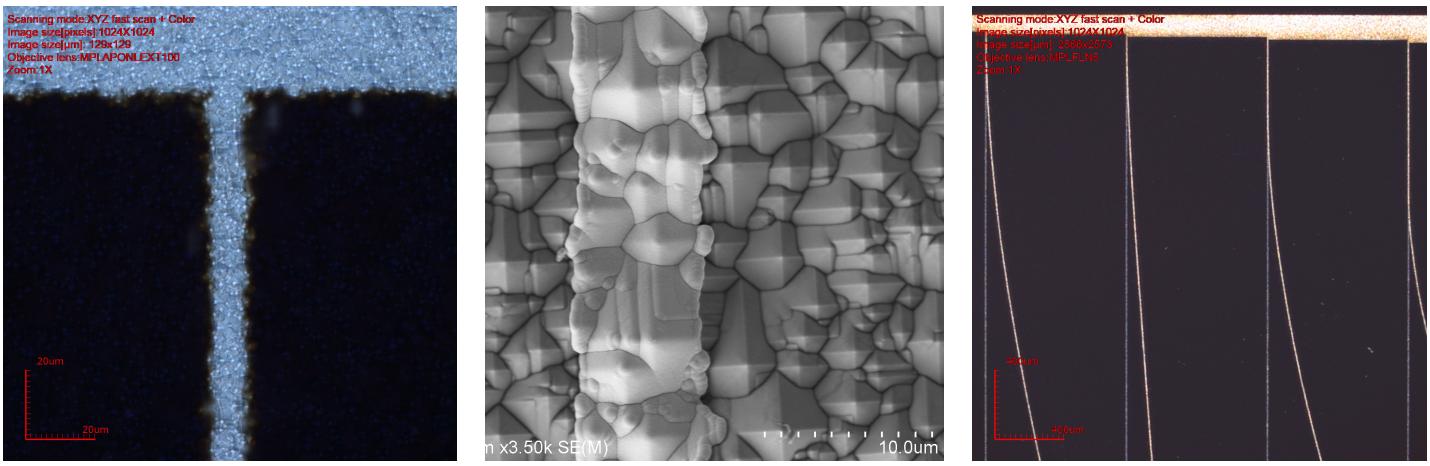

(a) SiN_X Removal by PL **(b) Ni Plating** **(c) Ag Plating**

Figure 5.22. Solar cell processed with photolithography: (a) finger and busbar openings on the SiN_X layer, (b) homogeneous Ni plating by ELSP on the exposed Si areas, (c) Ag plating by LIEP, showing detachment of the front metal fingers. Please note the different scales of each measurement.

Selective SiN_X removal by chemical etching resulted in clean openings that preserved the random pyramid structures of the silicon substrate. The Ni plating step was successful, resulting in the deposition of a homogeneous and continuous metal layer over the exposed silicon surface. The random pyramid topography was still identifiable after Ni deposition, indicating that layer growth rate was homogeneous throughout the exposed area. Differently, all attempts at Ag plating were unsuccessful: during the Ag plating process, metal fingers pealed off from the front surface of photolithography processed solar cells, indicating that Ni adhesion to the silicon substrate was very poor. Because of the problems with Ag plating, it was not possible to measure the electrical performance of photolithography solar cells fabricated in this work. Additionally, results of photolithography samples obtained for Suns-Voc measurements after Ag plating should be analysed with the remark that

only a small fraction of the sample had metal fingers contacting the silicon substrate adequately.

5.4.2.2. Laser Chemical Processing with Deionised Water

Images of a sample incorporating SiN_X laser ablation processed by the LCP-H_2O technique before and after Ni and Ag plating are shown in Figure 5.23.

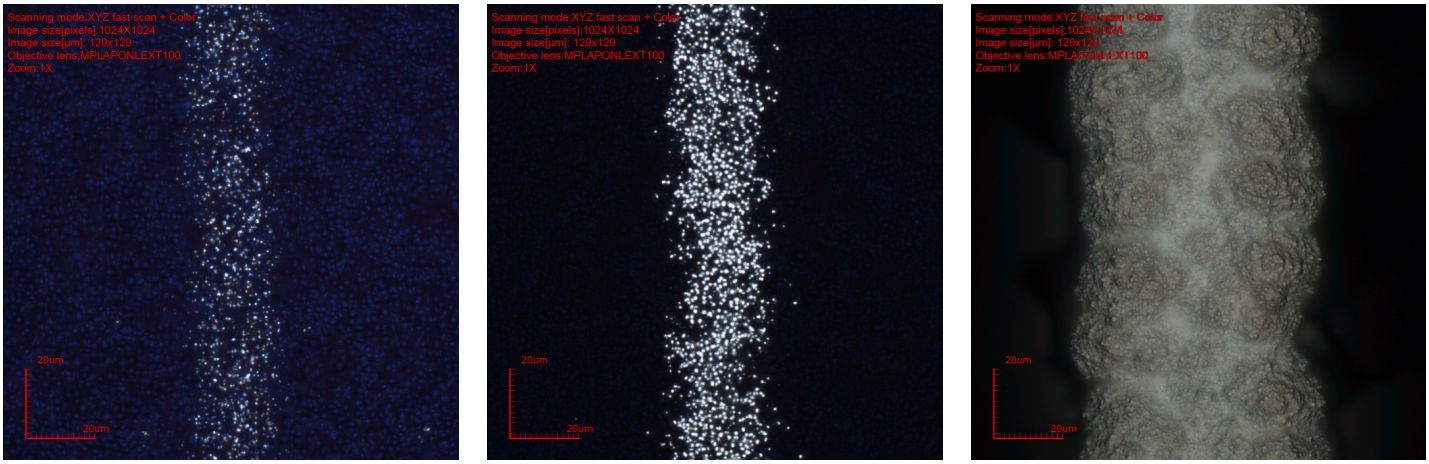

(a) LCP-H_2O Laser Ablation **(b) Ni Plating** **(c) Ag Plating**

Figure 5.23. Solar cell processed with LCP-H_2O: (a) finger and busbar openings on the SiN_X layer, (b) Ni plating by ELSP, (c) Ag plating by LIEP. Fixed laser parameters were: 15.3 μJ laser pulse energy, 16.0 kHz q-switch frequency, 100 mm/s laser processing speed, and 6.25 μm pulse distance, 50 ns pulse duration, 80 μm nozzle diameter, 70 bar pump pressure. Scale: 20 μm.

The laser ablation process resulted in localized opening of the SiN_X layer and exposure of the silicon substrate. The Ni plating step was successful, resulting in the deposition of localized metal agglomerates covering the exposed silicon surface, especially pyramid tips and corners. The Ag plating step also had a positive outcome, resulting in the formation of continuous Ag plated lines, with a relatively rough surface. In this process, the Ni agglomerates served as seed points for Ag growth. Consequently, Ag growth started in several different points for each ablated line and the Ag layer had a multicrystalline structure. Differently from what happened with photolithography solar cells, the plated metal grid was more firmly attached to the silicon substrate and no pealing of the contacts occurred.

5.4.2.3. Scanning Head Mirror Galvanometer Laser System

Images of a sample incorporating SiN_X laser ablation processed by the SCA technique before and after Ni and Ag plating are shown in Figure 5.24.

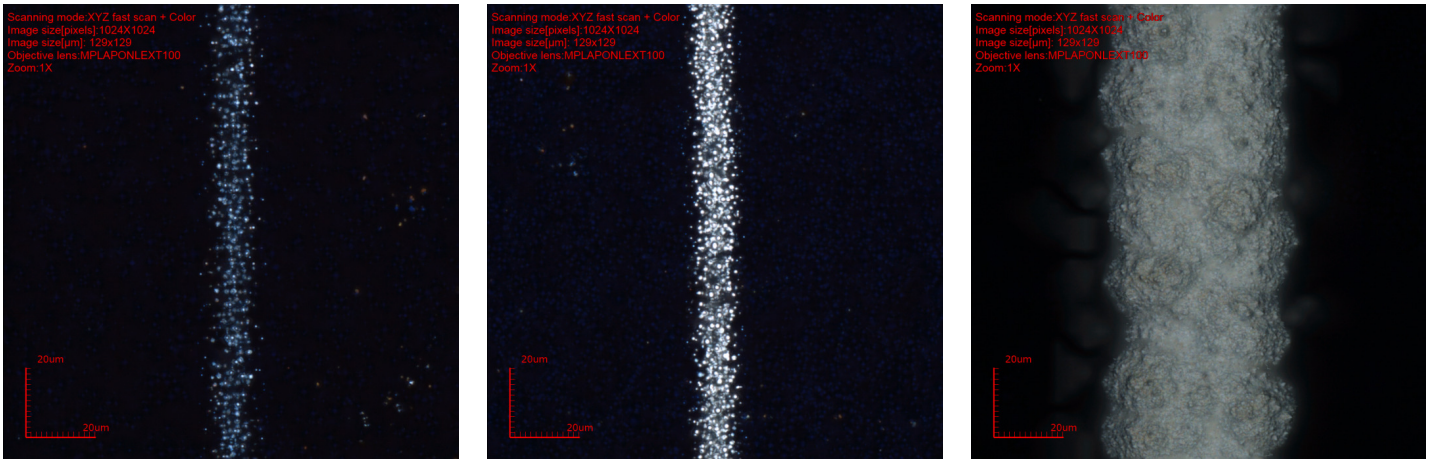

(a) SCA Laser Ablation **(b) Ni Plating** **(c) Ag Plating**

Figure 5.24. Solar cell processed with SCA: (a) finger and busbar openings on the SiN_X layer, (b) Ni plating by ELSP, (c) Ag plating by LIEP. Fixed laser parameters were: 3.0 µJ laser pulse energy, 130.0 kHz q-switch frequency, 813 mm/s laser processing speed, and 6.25 µm pulse distance, 50 ns pulse duration. Scale: 20 µm.

Similar to what was observed for the LCP-H_2O technique, the laser ablation process resulted in localized opening of the SiN_X layer and exposure of the silicon substrate. The Ni plating step was successful, resulting in the deposition of localized metal agglomerates covering the exposed silicon surface, especially pyramid tips and corners. The extent of the Ni coverage was directly proportional to the laser pulse energy employed, as would be expected. The Ag plating step also had a positive outcome, resulting in the formation of continuous multicrystalline Ag plated lines, with a relatively rough surface. The plated metal grid was more firmly attached to the silicon substrate and no pealing of the contacts occurred, as seen for the LCP-H_2O case.

A comparison of the morphology of the metal grid fingers of solar cells processed by LCP-H_2O and SCA techniques is shown in Figure 5.25.

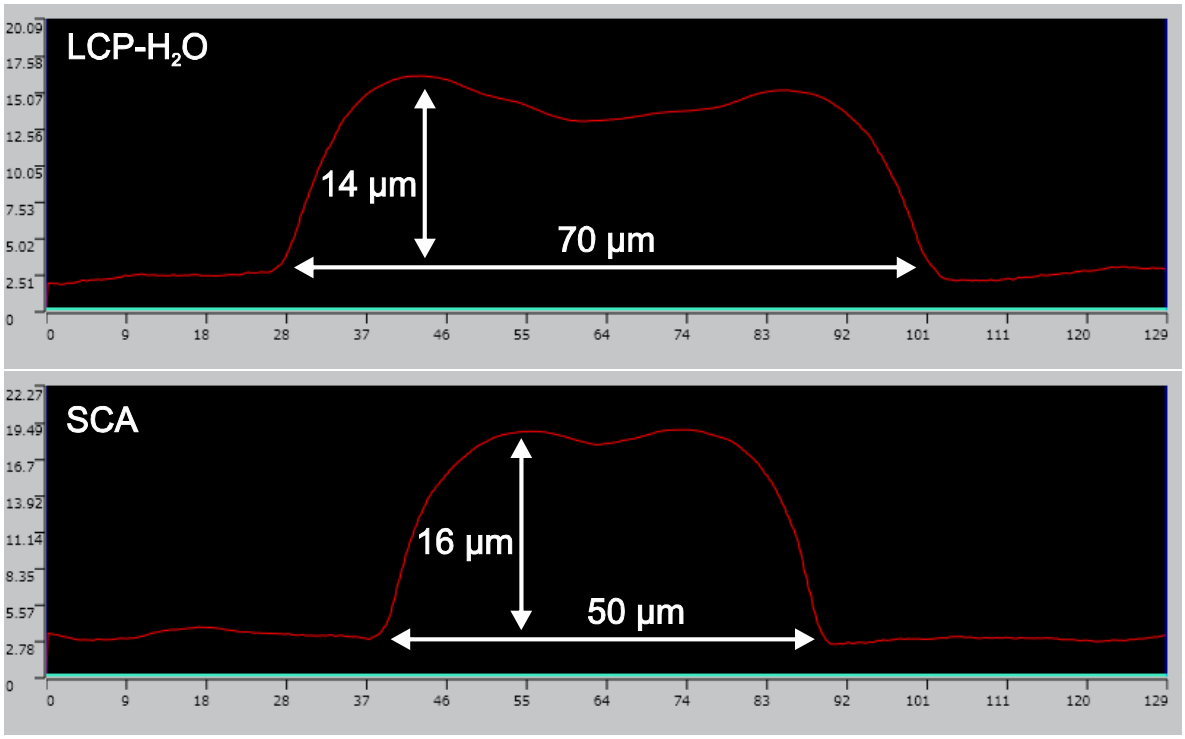

Figure 5.25. Best LCP-H_2O and SCA finger cross-section profiles, with height and width values estimated by confocal laser scanning microscopy.

Cross-section profiles of the metal fingers of finished solar cells processed with LCP-H_2O had an estimated width and height of approximately 70 µm and 14 µm, respectively, whereas SCA samples had an estimated width and height of approximately 50 µm and 16 µm, respectively. These metal fingers have different effective heights and widths. The shading is usually a function of the aspect ratio of the metal contacts (i.e. height divided by width), corrected by the amount of radiation that reaches the sample after reflection on the metal grid. From Figure 5.25, it is clear that the metal finger of finished SCA solar cells has a superior aspect ratio and, therefore, results in less active area shading. Additionally, since SCA metal fingers are thinner than LCP-H_2O metal fingers, it is also possible to reduce electrical losses of the devices by improving the distribution of the metal grid on the front surface, minimizing series resistance.

5.4.3. Electrical Performance of Samples and Finished Solar Cells

The impact of the different ablation techniques and laser pulse energies on the electrical performance of devices was evaluated and compared by means of

Suns-Voc and J-V measurements. Suns-Voc results for pFF and V_{OC} after Ag plating are shown in Figure 5.26 and Figure 5.27, respectively.

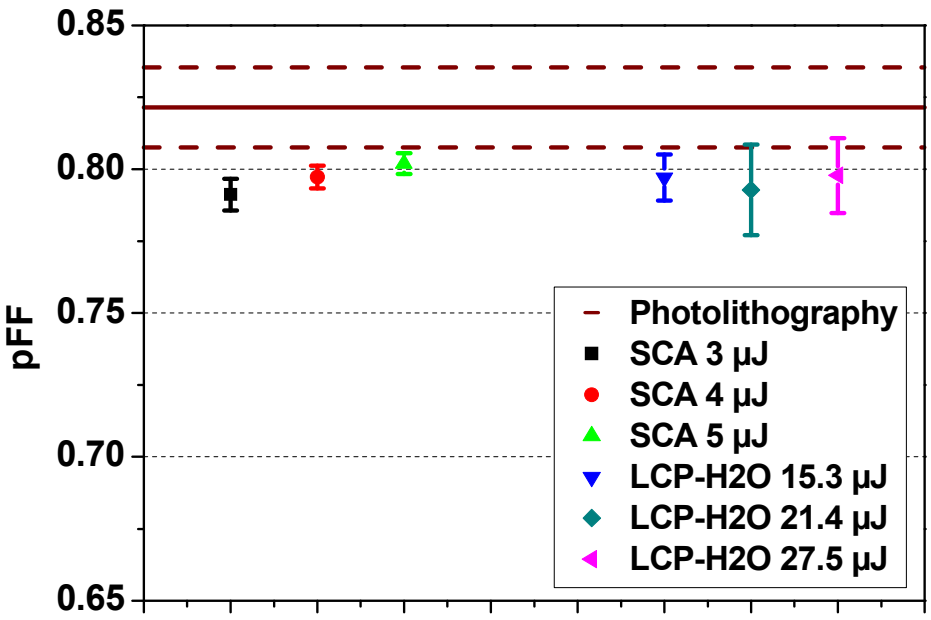

Figure 5.26. Suns-Voc results for the pFF of samples processed by different methods after Ag plating.

Analysis of Figure 5.26 indicates that, in general, pFF values were inferior for laser-ablated solar cells compared to photolithography processing. Since devices had equivalent rear surface structures, the cause can be isolated at the front surface of the solar cells. This type of reduction in pFF is generally attributed to shunting effects, which in this case may have been caused by laser-induced damage to the crystalline structure of the silicon substrate and possibly to the p-n junction itself, as the devices incorporated a shallow homogeneous phosphorus emitter. In terms of laser pulse energy values, there was no clear distinction between the laser processing parameters chosen for the LCP-H_2O technique, as all LCP-H_2O values were on the same range. For the SCA technique, the average pFF values showed a slight improvement with the use of higher laser pulse energies, with the best value found for 5.0 µJ. Nevertheless, when standard deviations are taken into consideration, a distinction between the performances of different laser pulse energies becomes challenging, as values intersect the same pFF range, with only minor variations between them. When directly comparing the LCP-H_2O and SCA

techniques, performances were found to be on the same range for all laser pulse energies tested.

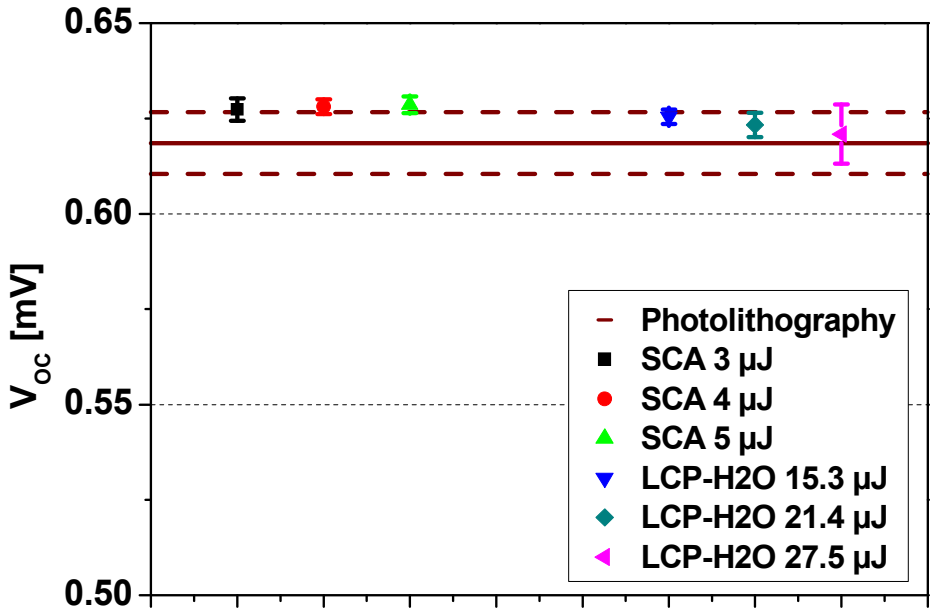

Figure 5.27. Suns-Voc results for the V_{OC} of samples processed by different methods after Ag plating.

Analysis of Figure 5.27 indicates that average V_{OC} values for laser-processed solar cells were superior to those obtained for photolithography. Additionally, standard deviation values of laser-processed samples were, in general, smaller than for photolithography. One possible cause for this phenomenon would be a difference in front surface area covered with the SiN_X passivation layer: on the one hand, photolithography samples had the whole SiN_X finger and busbar areas removed by chemical etching; on the other hand, laser-ablated solar cells may have parts of the finger regions that remained covered by SiN_X, such as pyramid sides. Therefore, a larger passivated front surface area for laser-processed solar cells could lead to higher V_{OC} values. For LCP-H_2O samples, a slightly decreasing trend for average V_{OC} values with higher laser pulse energy was observed. When taking into consideration standard deviations, a trend of increasing standard deviation for higher laser pulse energy is observed, indicating that excessive laser pulse energy results in a less homogeneous process, with higher spreading of sample performance to lower values. For SCA samples, no distinction between results was noted for the laser pulse energy interval tested.

After complete fabrication, the electrical performance of finished solar cells was evaluated by J-V measurements. Results are summarized in Table 5.4. Average values were calculated for at least 5 solar cells with identical processing. Fixed LCP-H_2O laser processing parameters were: 16.0 kHz q-switch frequency, 100 mm/s laser processing speed, and 6.25 µm pulse distance, 50 ns pulse duration, 80 µm nozzle diameter, 70 bar pump pressure. Fixed SCA laser processing parameters were: 130.0 kHz q-switch frequency, 813 mm/s laser processing speed, and 6.25 µm pulse distance, 50 ns pulse duration.

Table 5.4. Summary of the average values and best electrical parameters of solar cells with SiN_X laser ablation and Ni/Ag electrochemical metallization using LCP-H_2O and SCA techniques.

Process	P_E [µJ]	Solar Cell	V_{OC} [mV]	J_{SC} [mA/cm^2]	FF	η [%]
LCP-H_2O	15.3	Best	621.9	36.9	0.729	16.7
		Average	622.2 ± 2.1	36.4 ± 0.6	0.709 ± 0.015	16.1 ± 0.5
LCP-H_2O	21.4	Best	626.2	36.4	0.726	16.5
		Average	619.3 ± 5.1	36.0 ± 1.0	0.696 ± 0.031	15.5 ± 0.7
LCP-H_2O	27.5	Best	626.9	36.6	0.733	16.8
		Average	619.6 ± 8.5	35.5 ± 1.0	0.714 ± 0.022	15.7 ± 1.1
SCA	3.0	Best	628.1	35.9	0.734	16.6
		Average	624.6 ± 3.3	35.4 ± 0.4	0.727 ± 0.012	16.1 ± 0.4
SCA	4.0	Best	629.2	35.5	0.742	16.6
		Average	625.2 ± 2.5	35.3 ± 0.6	0.735 ± 0.005	16.2 ± 0.3
SCA	5.0	Best	628.4	35.8	0.737	16.6
		Average	625.7 ± 2.6	35.5 ± 0.3	0.735 ± 0.005	16.3 ± 0.2

For LCP-H_2O solar cells, when considering the best solar cells, no clear distinction between the three laser pulse energies tested in this work was observed. The best average performance for solar cells with LCP-H_2O processing was obtained using 15.3 µJ laser pulse energy, reaching an average of 622.2 mV V_{OC}, 36.4 mA/cm^2 J_{SC}, 0.709 FF, and an efficiency of 16.1 %. Nevertheless, the best solar cell produced with the LCP-H_2O technique was fabricated using 27.5 µJ laser pulse energy, reaching 626.9 mV V_{OC}, 36.6 mA/cm^2 J_{SC}, 0.733 FF, and an efficiency of 16.8 %.

Results for SCA solar cells indicate a slightly increasing trend in electrical performance for increasing laser pulse energy. The benefit of employing a higher laser pulse energy can be identified both for an increase on the average performance and a reduction on the standard deviation of the devices. The best average performance for solar cells with SCA processing was obtained using 5.0 µJ laser pulse energy, reaching an average of 625.7 mV V_{OC}, 35.5 mA/cm^2 J_{SC}, 0.735 FF, and an efficiency of 16.3 %. The best solar cell produced with the SCA technique using 5.0 µJ laser pulse energy, reaching 628.4 mV V_{OC}, 35.8 mA/cm^2 J_{SC}, 0.737 FF, and an efficiency of 16.6 %. Similar efficiencies for the best solar cells produced with the SCA technique using 3.0 µJ and 4.0 µJ laser pulse energies were obtained.

When comparing LCP-H_2O and SCA solar cells, the SCA technique appears to have performed slightly better than LCP-H_2O under the conditions investigated. It presented both a higher average performance and lower standard deviation values than the latter technique.

For both laser techniques, FF was identified as a limiting parameter of solar cell performance and all devices presented relatively low FF value. This can be attributed to a combination of localized shunts on the devices, as seen by Sun-Voc measurements of pFF, as well as high series resistances on the front contact metal grid. One possible approach to overcome these issues could be the incorporation of a selective emitter below the laser-ablated SiN_X openings, reducing the occurrence of local shunts.

5.5. Comparison of Solar Cells with Laser-Fired Contacts and SiN_X Laser Ablation

After developing, optimizing, and characterizing solar cells processed with LFC and SiN_X laser ablation, a comparison between devices produced with each of these methods was performed. This comparison focused on J-V measurements and covered the following topics: solar cell design and structure, processing sequences employed with each laser method, and electrical performance.

The J-V curves of the best solar cells produced with the LFC, LCP-H_2O, and SCA techniques are shown in Figure 5.28. The LFC solar cell presents a lower V_{OC} than both laser-ablated solar cells. This aspect may be attributed to an important solar cell design difference: the LFC sample employs a TiO_2 ARC layer, with possibly low surface passivation properties on the n-doped front surface, whereas both laser-ablated devices have a SiN_X front surface ARC layer, which performs quite well as passivation layer on the n-doped front surface. Additionally, it is important to note that solar cells were produced on different CZ-Si substrates, therefore some of the differences observed on the electrical performances of the devices may be attributed to substrate characteristics, such as: base resistivity, substrate quality and lifetime, amongst others.

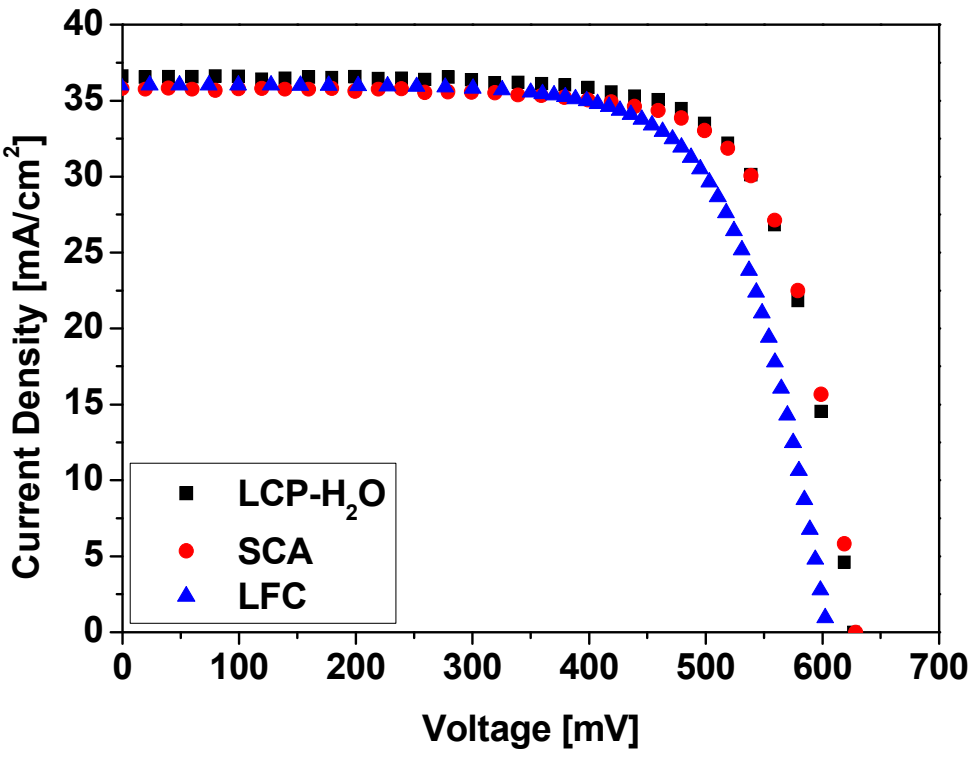

Figure 5.28. J-V curves of the best solar cells using SiN_X laser ablation, processed with LCP-H_2O and SCA, as well as the best LFC solar cell.

In terms of J_{SC}, the analysis is more complex, since both front and rear surfaces are playing distinct roles on each solar cell. On the one hand, LFC devices have the advantage of passivated rear surfaces and LBSFs, which can positively impact the J_{SC}. Nevertheless, they have screen-printed front contacts, with wider metal fingers and busbars on the front surface, resulting in more shading of the

active area of the device, which can negatively impact the J_{SC}. On the other hand, laser-ablated devices have screen-printed rear contacts, with a homogeneous Al-BSF, combined with narrower metal fingers and busbars on the front surface. Therefore, a direct comparison of both devices is not straightforward.

Finally, the three solar cells were limited by significantly low FF values. The causes of these losses are again distinct in each case. For the LFC solar cell, the limitation can be attributed to the rear structure of the device, with samples being affected by high series resistance losses, caused by a low-quality metal-semiconductor contact. For the SCA and LCP-H_2O solar cells, the limitation can be attributed to the front surface of the devices, with samples being affected by high series resistance losses and the formation of local shunts, originating from laser-induced damage.

6. CONCLUSIONS AND OUTLOOK

The outcomes of the research performed with the laser-fired contacts process were the following:

- A laser process for the fabrication of LFC silicon solar cells with SiO_2 rear surface passivation and evaporated aluminium layer was developed and optimized. The best laser processing parameters for the processing window investigated were: 33.0 A pumping lamp current, 20.0 kHz q-switch frequency, 13.0 W laser system average output power, and 0.50 mm rear contact distance.

- A thermal treatment process (annealing) for LFC solar cells was developed and optimized. The best annealing parameters for the processing window investigated were: 400 ºC annealing temperature and between 33 cm/min and 50 cm/min conveyor belt speed.

- P-type crystalline silicon solar cells with LFC and SiO_2 rear surface passivation were fabricated and characterized, reaching an average efficiency of 14.4 % after optimization of laser processing and annealing parameters. This result was higher than that obtained for industrial screen-printed solar cells with no Al-BSF produced under similar conditions, which reached an average efficiency of 13.3 %. Additionally, the result was comparable to that of industrial screen-printed solar cells with full-area Al-BSF produced under similar conditions, which reached an average efficiency of 14.5 %. The best LFC solar cell produced in this work had a V_{OC} of 604.4 mV, J_{SC} of 36.0 mA/cm^2, FF of 0.703, and efficiency of 15.3

%, matching the efficiency of the best industrial screen-printed solar cell with full-area Al-BSF.

- A fabrication sequence for LFC solar cells with only one thermal oxidation step was developed and evaluated. Results indicate that the same SiO_2 layer can be employed as diffusion barrier and passivation for the rear surface. Leaving the device rear surface exposed during PSG chemical etch resulted in solar cells with better electrical performance than protecting it from the etching solution. This benefit can be attributed to a reduction of the phosphorus content on the rear surface. Additionally, the passivation quality of the rear SiO_2 layer was not negatively affected by the etching solution.

The outcomes of the research performed with the silicon nitride laser ablation process were the following:

- A SiN_X laser ablation process using the LCP-H_2O method was developed and optimized. The best laser processing parameters for the processing window investigated were: 15.3 µJ laser pulse energy, 16.0 kHz laser pulse frequency, and 100 mm/s processing speed.

- A SiN_X laser ablation process using the SCA method was developed and optimized. The best laser processing parameters for the processing window investigated were: 5.0 µJ laser pulse energy, 130.0 kHz laser pulse frequency, and 813 mm/s processing speed.

- P-type crystalline silicon solar cells with SiN_X laser ablation and Ni/Ag front contact metallization by electrochemical deposition were fabricated and characterized. For solar cells produced by the LCP-H_2O technique, average efficiencies for the best laser processing parameters were 16.1 %. The best solar cell had a V_{OC} of 626.9 mV, J_{SC} of 36.6 mA/cm^2, FF of 0.733, and a resulting efficiency of 16.8 %. For solar cells produced by the SCA technique, average efficiencies for the best laser processing

parameters were 16.3 %. The best solar cell had a V_{OC} of 628.4 mV, J_{SC} of 35.8 mA/cm^2, FF of 0.737, and a resulting efficiency of 16.6 %.

This doctoral thesis may be considered as an important step forward to the development of crystalline silicon solar cells with laser processing methods in Brazil, as this was the first time that these devices were produced employing laser methods in the country. Based on the activities that were carried out during the thesis, different research topics and ideas can be suggested to complement and build upon the work that was developed, notably:

- Evaluate alternatives to improve the FF of LFC solar cells, such as: changing the substrate characteristics (i.e. base doping) and employing a better laser system to perform the LFC process.

- Improve front and rear surface passivation of p-type LFC solar cells. Front surface passivation may be improved by replacing the TiO_2 layer that was employed as ARC by a SiO_2 or SiN_X layer, that would simultaneously perform the roles of ARC and front surface passivation. The rear surface passivation may be improved by increasing the thickness of the SiO_2 layer or by introducing a high-temperature treatment step during the formation of the SiO_2 layer, with forming gas, in order to further reduce the rear surface recombination of devices.

- Develop and investigate a two-step processing method for the formation of a selective emitter on the SiN_X laser-ablated areas formed by the process developed in this work.

- Analyse the benefits of replacing the shallow emitter used in SiN_X samples by a deep emitter, to avoid nickel silicide shunting of the base and emitter regions during the thermal treatment performed to improve the adhesion of the front metal contacts to the solar cell.

- Evaluate a new solar cell design by combining the LFC and SiN_X laser ablation methods into the same device.

7. REFERENCES

[1] Intergovernmental Panel on Climate Change (IPCC), **Climate change 2007: synthesis report**. Contribution to the fourth assessment report on climate change, Cambridge University Press, Cambridge, United Kingdom, p. 26-73, 2007.

[2] GILLETT, N. P.; et al. Attribution of polar warming to human influence. **Nature Geoscience**, Vol. 1, p. 750-754, November 2008.

[3] ALLEN, M. R.; et al. Warming caused by cumulative carbon emissions towards the trillionth tonne. **Nature**, Vol. 458, p. 1163-1166, April 2009.

[4] TANS, P. Trends in carbon dioxide. National Oceanic and Atmospheric Administration – Earth System Research Laboratory. United States of America, 2011. Available at: <www.esrl.noaa.gov/gmd/ccgg/trends>. Retrieved in: 12th February 2011.

[5] STERN, N. **Stern review: the economics of climate change – Executive summary**, New Economics Foundation, 2006.

[6] International Energy Agency (IEA), **World energy outlook 2008**, Paris: OECD/IEA, 2008.

[7] USA, Official energy statistics from the U.S. government. World crude oil prices. Energy Information Administration, United States of America. Available at: <http://www.eia.doe.gov/dnav/pet/hist/LeafHandler.ashx?n=PET&s=WTOTWORLD&f=W>. Retrieved in: 12th February 2011.

[8] KREWITT, W.; et al. Environmental damage costs from fossil electricity generation in Germany and Europe, **Energy Policy**, Vol. 27, p. 173-183, 1999.

[9] United Nations Development Programme (UNDP), **World energy assessment: energy and the challenge of sustainability**, p. 61-110, New York, December 2000.

[10] European Commission, **ExternE – Externalities of energy**, EUR 21951 EN, ISBN 92-79-00423-9, Office for Official Publications of the European Communities, Luxembourg, 2005.

[11] MACHOL, B.; Rizk, S. Economic value of U.S. fossil fuel electricity health impacts, **Environment International**, Vol. 52, p. 75-80, 2013.

[12] TWIDELL, J.; Weir, A. **Renewable energy resources**, 2nd Edition, Taylor & Francis, New York, USA, p. 7/182-236, 2006.

[13] WENHAM, S. R.; et al. **Applied photovoltaics**, 2nd Edition, Earthscan, London, United Kingdom, p. 31-51, 2007.

[14] THEVENARD, D.; Pelland, S. Estimating the uncertainty in long-term photovoltaic yield predictions, **Solar Energy**, 2011 (in press: DOI: 10.1016/j.solener.2011.05.006).

[15] DENHOLM, P.; Margolis, R. M. Very large-scale deployment of grid-connected solar photovoltaics in the United States: challenges and opportunities. **Conference Paper Preprint for Solar 2006**, U.S. Department of Energy, National Renewable Energy Laboratory (NREL), 2006.

[16] DENHOLM, P.; Margolis, R. M. Evaluating the limits of solar photovoltaics (PV) in traditional electric power systems. **Energy Policy**, Vol. 35, Issue 5, p. 2852-2861, 2007.

[17] JARDIM, C. S.; et al. The strategic siting and the roofing area requirements of building-integrated photovoltaic solar energy generators in urban areas in Brazil. **Energy and Buildings**, Vol. 40, p. 365-370, 2008.

[18] BAZILIAN, M.; et al. Re-considering the economics of photovoltaic power. **Renewable Energy**, p. 329-338, 2013.

[19] BHANDARI, R.;Stadler, I. Grid parity analysis of solar photovoltaic systems in Germany using experience curves. **Solar Energy**, Vol. 83, p. 1634-1644, 2009.

[20] BREYER, C.; Gerlach, A. Global overview on grid-parity. **Progress in Photovoltaics: Research and Applications**, Vol. 21, p. 121-136, 2013.

[21] European Photovoltaic Industry Association (EPIA), **Global market outlook for photovoltaics until 2016**, Belgium, May 2012.

[22] NPD Solarbuzz, **Excerpts from marketbuzz and solarbuzz quarterly reports**, 2013.

[23] HERING, G. Year of the tiger. **Photon International**, p. 186-218, March 2011.

[24] GREEN, M. A. Estimates of Te and In prices from direct mining of known ores. **Progress in Photovoltaics: Research and Applications**, Vol. 17, p. 347-359, 2009.

[25] ZUSER, A.; Rechberger, H. Considerations of resource availability in technology development strategies: the case study of photovoltaics, **Resources Conservation and Recycling**, Vol. 56, p. 56-65, 2011.

[26] JAMES, A. M.; Lord, M. P. **Macmillan's chemical and physical data**, Macmillan, London, United Kingdom, 1992.

[27] POORTMANS, J.; et al. Where photovoltaics meets microelectronics, **Energy Procedia**, Vol. 15, p. 40-49, 2012.

[28] SWANSON, R. M. A Vision for crystalline silicon photovoltaics. **Progress in Photovoltaics: Research and Applications**, Vol. 14, p. 443-453, 2006.

[29] PARENTE, V.; Goldemberg, J.; Zilles, R. Comments on experience curves for PV modules. **Progress in Photovoltaics: Research and Applications**, Vol. 10, p. 571-574, 2002.

[30] SÖSEMANN, F. **EEG – The renewable energy sources act**, Federal Ministry of the Environment, Nature Conservation and Nuclear Safety (BMU), Germany, 2007.

[31] European Photovoltaic Industry Association (EPIA), **An argument for feed-in tariffs**, Belgium, January 2008.

[32] Renewable Energy Policy Network for the 21st Century (REN21), **Energy for development: the potential role of renewable energy in meeting the millennium development goals**, New York, USA, 2005.

[33] GOLDEMBERG, J.; Johansson, T. B. **Energy as an instrument for socio-economic development**, United Nations Development Programme (UNDP), New York, USA, 1995.

[34] Photovoltaic Power Systems Programme (PVPS), **Trends in photovoltaic applications 1992 to 2011**, International Energy Agency (IEA), August 2012.

[35] BRADFORD, T.; Flynn, H. **Polysilicon: supply, demand and implications for the PV industry**, Prometheus Institute for Sustainable Development, 2006.

[36] GREEN, M. A. Silicon photovoltaic modules: a brief history of the first 50 years. **Progress in Photovoltaics: Research and Applications**, Vol. 13, p. 447-455, 2005.

[37] BREYER, C.; et al. Research and development investments in PV – A limiting factor for a fast PV diffusion?, **25th European Photovoltaic Solar Energy Conference (EUPVSEC)**, Valencia, Spain, September 2010.

[38] GREEN, M. A.; et al. Solar cell efficiency tables (Version 41), **Progress in Photovoltaics: Research and Applications**, Vol. 21, p. 1-11, 2013.

[39] European Photovoltaic Industry Association (EPIA), **Unlocking the sunbelt potential of photovoltaics**, 2nd Edition, October 2010.

[40] ROSELL, A. D.; Hering, G. Land of the future? **Photon International**, p.14, January 2011.

[41] KRULEWITZ, A.; Litvak, N., **Solar in latin america and the caribbean 2013: markets, outlook, and competitive positioning**, 2013.

[42] PEREIRA, E. B.; et al. **Atlas brasileiro de energia solar (Brazilian atlas of solar energy)**. SWERA Project – UNEP, Instituto Nacional de Pesquisas Espaciais (INPE), São José dos Campos, São Paulo, Brazil, 2006.

[43] U. S. Geological Survey (USGS), **Mineral commodity summaries – Silicon**, January 2011.

[44] Empresa de Pesquisa Energética (EPE), **Balanço energético nacional 2011 – Ano base 2010: resultados preliminares**, Rio de Janeiro, 2011.

[45] Instituto Brasileiro de Geografia e Estatística (IBGE), **sinopse do censo demográfico 2010**, Rio de Janeiro, 2011.

[46] Agência Nacional de Energia Elétrica (ANEEL), **Resolução normativa Nº 482**, Brasília, Abril 2012.

[47] Agência Nacional de Energia Elétrica (ANEEL), **Resolução normativa Nº 517**, Brasília, Dezembro 2012.

[48] Agência Nacional de Energia Elétrica (ANEEL), **Resolução normativa Nº 481**, Brasília, Abril 2012.

[49] IHS Emerging Energy Research, **Emerging solar PV markets and strategies: 2012-2035**, November 2012.

[50] ZENZEN, E. A.; Zanesco, I.; Moehlecke, A.; Santos Júnior, S. L. R. *Formação de emissores seletivos em células solares por radiação laser*, ***II Congresso Brasileiro de Energia Solar e III Conferência Latino-Americana da ISES***, Florianópolis, Brazil, November 2008.

[51] BECQUEREL, A. E. Mémoire sur les effets électriques produits sous l'influence des rayons solaires. **Comptes Rendus Hebdomadaires des Séances de l'Académie des Sciences**, Vol. 9, p. 561-567, Académie des Sciences, France, 1839.

[52] CHAPIN, D. M.; Fuller, C. S.; Pearson, G. L. A new silicon p-n junction photocell for converting solar radiation into electrical power, **Journal of Applied Physics**, Vol. 25, p. 676-677, 1954.

[53] GOSWAMI, D. Y.; Kreith, F. **Energy conversion**, CRC Press, Taylor and Francis Group, 936p., 2007.

[54] LUQUE, A.; Hegedus, S. (editors). **Handbook of photovoltaic science and engineering**, John Wiley & Sons, United Kingdom, 1168p., 2003.

[55] GOETZBERGER, A.; Knobloch, J.; Voss, B. **Crystalline silicon solar cells**, John Wiley and Sons, 254p. 1998.

[56] GREEN, M. A. **Silicon solar cells – Operating principles, technology and system applications**, University of New South Wales, Australia, 274p., 1982.

[57] SZE, S. M. **Physics of semiconductor devices**, 2nd Edition, John Wiley & Sons, 880p., 1981.

[58] SHOCKLEY, W.; Queisser, H. J. Detailed balance limit of efficiency of pn junction solar cells, **Journal of Applied Physics**, Vol. 32, p. 510-519, 1961.

[59] TIEDJE, T.; et al. Limiting efficiency of silicon solar cells, **IEEE Transactions on Electron Devices**, Vol. 31, p. 711-716, 1984.

[60] KEN, M. J.; Campbet, P.; Cuevas, A. Lifetime and efficiency limits of crystalline silicon solar cells, **29th IEEE Photovoltaic Specialists Conference (PVSC)**, p. 438-441, New Orleans, Louisiana, USA, May 2002.

[61] American Society for Testing and Materials (ASTM) International, **Standard test method for measuring resistivity of silicon wafers with an in-line four-point probe**, ASTM Standard Code F84-99, USA, 1999.

[62] CORICA, D. **Deposition of indium sulfide films by ultrasonic spray pyrolysis and their application in cigs thin film solar cells**, Master Thesis, Thin Film Physics Group, ETH Zürich, Switzerland, December 2007.

[63] SINTON, R. A.; Cuevas, A. A quasi-steady-state open-circuit voltage method for solar cell characterization, **16th European Photovoltaic Solar Energy Conference (EUPVSEC)**, p. 1152-1155, Glasgow, United Kingdom, 2000.

[64] SEMI PV Group, **International technology roadmap for photovoltaic (ITRPV) - Results 2012**, March 2013.

[65] NEMET, G. F. Beyond the learning curve: factors influencing cost reductions in photovoltaics. **Energy Policy**, Vol. 34, p. 3218–3232, 2006.

[66] SCHULTZ, O.; et al. Silicon solar cells with screen-printed front side metallization exceeding 19 % efficiency. **22nd European Photovoltaic Solar Energy Conference (EUPVSEC)**, p. 980-983, Milan, Italy, September 2007.

[67] BLAKERS, A. W.; et al. 22.8 % efficient silicon solar cell. **Applied Physics Letters**, Vol. 55, Issue 13, p. 1363, 1989.

[68] GLUNZ, S. W.; et al. New simplified methods for patterning the rear contact of RP-PERC high-efficiency solar cells. **28th IEEE Photovoltaic Specialists Conference (PVSC)**, p. 168-171, Anchorage, Alaska, USA, 2000.

[69] ZHAO, J.; Wang, A.; Green, M. A. 24.5% efficiency PERT silicon solar cells on SEH MCZ substrates and cell performance on other SEH CZ and FZ substrates. **Solar Energy Materials & Solar Cells**, Vol. 66, p. 27-36, 2001.

[70] KOECHNER, W.; Bass, M. **Solid state lasers: a graduate text**, Springer-Verlag, New York, USA, 409p., 2003.

[71] SUHARA, T. **Semiconductor laser fundamentals**, Marcel Dekker Inc., New York, USA, 308p., 2004.

[72] GREEN, M. A.; et al. Very high efficiency silicon solar cells – Science and technology. **IEEE Transactions on Electron Devices**, Vol. 46, No. 10, p. 1940-1947, October 1999.

[73] CORDIS, **European commission seventh framework programme (FP7)**, Official website, 2008. Available at: <http://cordis.europa.eu/fetch?CALLER=FP7_PROJ_EN&ACTION=D&DOC=1&CAT=PROJ&RCN=90332>. Retrieved in: October 2011.

[74] Next generation solar cell and module laser processing systems, **Solasys Project**, Official website, 2008. Available at: <http://www.solasys.eu/>. Retrieved in: October 2011.

[75] EUROPEAN COMISSION, **Photovoltaic solar energy – development and current research**, Office for Official Publications of the European Union, Luxembourg, 76p., 2009.

[76] HAUSER, A.; et al., Comparison of different techniques for edge isolation. **17th European Photovoltaic Solar Energy Conference (EUPVSEC)**, p. 1739-1742, Munich, Germany, October 2001.

[77] SCHNEIDERLÖCHNER, E.; et al. Laser-fired rear contacts for crystalline silicon solar cells. **Progress in Photovoltaics: Research and Applications**, Vol. 10, p. 29-34, 2002.

[78] KRAY, D.; et al. Laser-doped silicon solar cells by laser chemical processing (LCP) exceeding 20% efficiency. **33rd IEEE Photovoltaic Specialist Conference (PVSC)**, p. 1-3, San Diego, California, USA, May 2008.

[79] DURAN, C.; et al. Bifacial solar cells with selective B-BSF by laser doping. **24th European Photovoltaic Solar Energy Conference (EUPVSEC)**, p. 1775-1778, Hamburg, Germany, September 2009.

[80] BESI-VETRELLA, U.; Pirozzi, L.; Salza, E. Large area, screen printed silicon solar cells with selective emitter made by laser overdoping and RTA spin-on glasses. **26th IEEE Photovoltaic Specialists Conference (PVSC),** p. 135-138, Anaheim, California, USA, 1997.

[81] KNORZ, A.; et al. Selective laser ablation of SiN_X layers on textured surfaces for low temperature front side metallizations. **Progress in Photovoltaics: Research and Applications**, Vol. 17, p. 127-136, 2009.

[82] MINGIRULLI, N.; et al. Screen-printed emitter-wrap-through solar cell with single step side selective emitter with 18.8% efficiency. **Progress in Photovoltaics: Research and Applications**, Vol. 19, p. 366-374, 2011.

[83] DOESWIJK, L. M. Passivating TiO_2 coatings for silicon solar cells by pulsed laser deposition. **Applied Physics A: Materials Science & Processing**, Vol. 69, p. S409-S411, 1999.

[84] KRIEG, A.; et al. Wafer identification using laser marked data matrix codes. **25th European Photovoltaic Solar Energy Conference and Exhibition (EUPVSEC)**, p.1337-1341, Valencia, Spain, September 2010.

[85] ABBOTT, M.; Cotter, J. Optical and electrical properties of laser texturing for high-efficiency solar cells. **Progress in Photovoltaics: Research and Applications**, Vol. 14, p. 225-235, 2006.

[86] GAST, M.; Köntges, M.; Brendel, R. Lead-free on-laminate laser soldering: a new module assembling concept. **Progress in Photovoltaics: Research and Applications**, Vol. 16, p. 151-157, 2008.

[87] SCHNEIDERLÖCHNER, E.; et al. Laser-fired contacts (LFC). **17th European Photovoltaic Solar Energy Conference (EUPVSEC)**, Munich, Germany, 2001.

[88] SCHNEIDERLÖCHNER, E.; et al. Silicon solar cells with screen printed-front contact and dielectrically passivated laser-fired rear electrode. **19th European Photovoltaic Solar Energy Conference (EUPVSEC)**, p. 447-450, Paris, France, June 2004.

[89] SCHNEIDERLÖCHNER, E.; et al. Investigation on laser-fired contacts for passivated rear solar cells. **29th IEEE Photovoltaic Specialists Conference (PVSC)**, p. 300-303, New Orleans, Louisiana, USA, 2002.

[90] GLUNZ, S. W.; New concepts for high-efficiency silicon solar cells. **Solar Energy Materials & Solar Cells**, Vol. 90, p. 3276-3284, 2006.

[91] PREU, R.; et al. Laser-fired contacts - transfer of a simple high efficiency process scheme to industrial production. **29th IEEE Photovoltaic Specialists Conference (PVSC)**, p. 130-133, New Orleans, Louisiana, USA, 2002.

[92] GROHE, A.; et al. Progress in the characterisation of laser-fired contacts. **20th European Photovoltaic Solar Energy Conference (EUPVSEC)**, p. 1158-1161, Barcelona, Spain, June 2005.

[93] ZASTROW, U.; et al. Characterization of laser-fired contacts in PERC solar cells: SIMS and TEM analysis applying advanced preparation techniques. **Applied Surface Science**, Vol. 252, p. 7082-7085, 2006.

[94] GROHE, A.; et al. Characterization of laser-fired contacts processed on wafers with different resistivity. **IEEE 3rd World Conference on Photovoltaic Energy Conversion**, p. 1032-1035, Osaka, Japan, May 2003.

[95] NAUMANN, V.; et al. Local electronic properties and microstructure of individual laser-fired contacts. **24th European Photovoltaic Solar Energy Conference (EUPVSEC)**, p. 2180-2184, Hamburg, Germany, September 2009.

[96] SCHNEIDERLÖCHNER, E. ***Laserstrahlverfahren zur Fertigung Kristalliner Silizium-Solarzellen***. Freiburg im Breisgau. 189p. Doctoral Thesis. *Fakultät für Angewandte Wissenschaften*, *Albert-Ludwigs-Universität*, Freiburg im Breisgau, July 2004.

[97] KRAY, D. ***Hocheffiziente Solarzellenstrukturen für kristallines Silicium-Material industrieller Qualität***. Konstanz. 158p. Doctoral Thesis. *Fakultät für Physik*, *Universität Konstanz*, Konstanz, December 2004.

[98] GLUNZ, S. W.; et al. Analysis of laser-fired local back surface fields using n^+np^+ cell structures. **IEEE 3rd World Conference on Photovoltaic Energy Conversion**, p. 1332-1335, Osaka, Japan, May 2003.

[99] HERMLE, M.; et al. Comprehensive comparison of different rear side contacting methods for high-efficiency solar cells. **20th European Photovoltaic Solar Energy Conference (EUPVSEC)**, p. 810-813, Barcelona, Spain, June 2005.

[100] BRENDLE, W.; et al. 20.5% Efficient silicon solar cell with a low temperature rear side process using laser-fired contacts. **Progress in Photovoltaics: Research and Applications**, Vol. 14, p. 653-662, 2006.

[101] HOFMANN, M.; et al. Industrial type Cz silicon solar cells with screen-printed fine line front contacts and passivated rear contacted by laser firing. **23rd European**

Photovoltaic Solar Energy Conference (EUPVSEC), p. 1704-1707, Valencia, Spain, September 2008.

[102] HÖRTEIS, M.; et al. Fundamental studies on the front contact formation resulting in a 21% efficiency silicon solar cell with printed rear and front contacts. **35th IEEE Photovoltaic Specialist Conference (PVSC)**, p. 672-677, Honolulu, Hawaii, USA, June 2010.

[103] HOFMANN, M.; et al. Overview on crystalline silicon solar cells using PECVD rear passivation and laser-fired contacts. **24th European Photovoltaic Solar Energy Conference (EUPVSEC)**, p. 1517-1522, Hamburg, Germany, September 2009.

[104] HOFMANN, M.; et al. 21%-efficient silicon solar cells using amorphous silicon rear side passivation. **21st European Photovoltaic Solar Energy Conference (EUPVSEC)**, p. 609-612, Dresden, Germany, September 2006.

[105] GLUNZ, S. W.; et al. Comparison of different dielectric passivation layers for application in industrially feasible high-efficiency crystalline silicon solar cells. **20th European Photovoltaic Solar Energy Conference (EUPVSEC)**, p. 572-577, Barcelona, Spain, June 2005.

[106] SAINT-CAST, P.; et al. High-efficiency c-Si solar cells passivated with ALD and PECVD aluminum oxide. **IEEE Electron Device Letters**, Vol. 31, No. 7, p. 695-697, July 2010.

[107] NEKARDA, J.; Grohe, A.; Schultz, O.; Preu, R. Aluminum foil as back side metallization for LFC cells. **22nd European Photovoltaic Solar Energy Conference and Exhibition (EUPVSEC)**, p. 1499-1501, Milan, Italy, September 2007.

[108] GROHE, A.; et al. Boundary conditions for the industrial production of LFC cells results from the joint project INKA. **21st European Photovoltaic Solar Energy Conference (EUPVSEC)**, p. 1101-1104, Dresden, Germany, September 2006.

[109] NEKARDA, J.; et al. Industrial PVD metallization for high efficiency crystalline silicon solar cells. **34th IEEE Photovoltaic Specialists Conference (PVSC)**, p. 892-896, Philadelphia, Pennsylvania, USA, 2009.

[110] NEKARDA, J.; et al. LFC on screen printed aluminium rear side metallization. **24th European Photovoltaic Solar Energy Conference (EUPVSEC)**, p. 1441-1445, Hamburg, Germany, September 2009.

[111] GROHE, A.; et al. Boundary conditions for the industrial production of LFC cells. **IEEE 4th World Conference on Photovoltaic Energy Conversion**, p. 1032-1035, Waikoloa, Hawaii, USA, May 2006.

[112] REINWAND, D.; et al. 21.1% Efficient PERC silicon solar cells on large scale by using inline sputtering for metallization. **35th IEEE Photovoltaic Specialists Conference (PVSC)**, p. 3582-3586, Honolulu, Hawaii, USA, June 2010.

[113] GAUTERO, L.; et al. All-screen-printed 120-µm-thin large-area silicon solar cells applying dielectric rear passivation and laser-fired contacts reaching 18% efficiency. **24th European Photovoltaic Solar Energy Conference (EUPVSEC)**, p. 1151-1157, Hamburg, Germany, September 2009.

[114] Pavlović, R.; et al. Large area solar cells with screen printed front side metallization and dielectric rear side passivation. **24th European Photovoltaic Solar Energy Conference (EUPVSEC)**, p. 2185-2189, Hamburg, Germany, September 2009.

[115] KONTERMANN, S.; et al. Optimizing annealing steps for crystalline silicon solar cells with screen printed front side metallization and an oxide-passivated rear surface with local contacts. **Progress in Photovoltaics: Research and Applications**, Vol. 17, p. 554-566, 2009.

[116] KRAY, D.; McIntosh, K. R. Analysis of ultrathin high-efficiency silicon solar cells. **Physica Status Solidi A**, Vol. 206, No. 7, p. 1647-1654, 2009.

[117] KRAY, D.; et al. Comprehensive experimental study on the performance of very thin laser-fired high-efficiency solar cells. **19th European Photovoltaic Solar Energy Conference (EUPVSEC)**, p. 608-611, Paris, France, June 2004.

[118] GLUNZ, S. W.; et al. Laser-fired contact silicon solar cells on p- and n-substrates. **19th European Photovoltaic Solar Energy Conference (EUPVSEC)**, p. 408-411, Paris, France, June 2004.

[119] SCHULTZ, O.; Glunz, S. W.; Willeke, G. P. Multicrystalline silicon solar cells exceeding 20 % efficiency. **Progress in Photovoltaics: Research and Applications**, Vol. 12, p. 553-558, 2004.

[120] GREEN, M. A.; et al. Solar cell efficiency tables (Version 38). **Progress in Photovoltaics: Research and Applications**, Vol. 19, p. 565-572, 2011.

[121] SCHNEIDERLÖCHNER, E.; et al. Scanning Nd-YAG laser system for industrially applicable processing in silicon solar cell manufacturing. **IEEE 3rd World Conference on Photovoltaic Energy Conversion**, p. 1364-1367, Osaka, Japan, May 2003.

[122] JENOPTIK Laser GmbH, **Laser fired contacts (LFC) for new solar cell concepts**, Application Notes, Germany, March 2011.

[123] ENGELHART, P.; et al. Q.ANTUM – Q-Cells next generation high-power silicon cell & module concept. **26th European Photovoltaic Solar Energy Conference (EUPVSEC)**, p. 821-826, Hamburg, Germany, September 2011.

[124] HAHN, G. Status of selective emitter technology. **25th European Photovoltaic Solar Energy Conference (EUPVSEC)**, p. 1091-1096, Valencia, Spain, September 2010.

[125] KRAY, D.; et al. Laser chemical processing (LCP) - A versatile tool for microstructuring applications. **Applied Physics A: Materials Science & Processing**, Vol. 93, p. 99-103, 2008.

[126] GRANEK, F.; et al. Screen-printed silicon solar cells with LCP selective emitters. **25th European Photovoltaic Solar Energy Conference (EUPVSEC)**, p. 2573-2577, Valencia, Spain, September 2010.

[127] KRAY, D.; et al. LCP Selective emitter solar cells with plated contacts. **35th IEEE Photovoltaic Specialists Conference (PVSC)**, p. 667-671, Honolulu, Hawaii, USA, June 2010.

[128] DREW, K.; et al. Combining laser chemical processing and aerosol jet printing - A laboratory scale feasibility study. **Progress in Photovoltaics: Research and Applications**, Vol. 19, p. 253-259, 2011.

[129] KLUSKA, S.; et al. Analysis of local boron dopings formed with LCP. **25th European Photovoltaic Solar Energy Conference (EUPVSEC)**, p. 1405-1409, Valencia, Spain, 2010.

[130] KLUSKA, S.; Granek, F. High-efficiency silicon solar cells with boron local back surface fields formed by laser chemical processing. **IEEE Electron Device Letters**, Vol. 32, No. 9, p. 1257-1259, September 2011.

[131] ENGELHART, P. Laser processing for high efficiency silicon solar cells, **Proceedings of SPIE**, Vol. 7202, 72020S, International Society for Optics and Photonics, 2009.

[132] HAASE, F.; et al. Layer selective laser ablation for local contacts to thin emitters, **Energy Procedia**, Vol. 8, p. 577-580, 2011.

[133] HERMANN, S.; et al. Picosecond laser ablation of SiO_2 layers on silicon substrates, **Applied Physics A**, Vol. 99, p. 151-158, 2010.

[134] ABBOTT, M. D.; et al. Laser-induced defects in crystalline silicon solar cells, **31st IEEE Photovoltaic Specialists Conference (PVSC)**, p. 1241-1244, Florida, USA, January 2005.

[135] MARKVART, T.; Castañer, L. **Solar cells: materials, manufacture and operation**, Elsevier, Oxford, United Kingdom, 555p. 2005.

[136] SAENGER, K. L. Mechanisms of lifetime degradation in Si/ARC samples patterned by laser lift-off, **Proceedings of SPIE**, Vol. 8473, 84730S, International Society for Optics and Photonics, 2012.

[137] HEINRICH, G.; et al. Investigation of ablation mechanisms for selective laser ablation of silicon nitride layers, **Energy Procedia**, Vol. 8, p. 592-597, 2011.

[138] GROHE, A.; et al., Selective laser ablation of anti-reflection coatings for novel metallization techniques, **4th IEEE World Conference on Photovoltaic Energy Conversion (WCPEC)**, p. 1399-1402, Hawaii, USA, May 2006.

[139] GLUNZ, S. W.; Preu, R.; Biro, D. Crystalline silicon solar cells: state-of-the-art and future developments, **Comprehensive Renewable Energy**, Vol 1, p. 353–387, Elsevier, Oxford, United Kingdom, 2012.

[140] ALEMAN, M.; et al. Advances in electroless nickel plating for the metallization of silicon solar cells using different structuring techniques for the ARC, **24th European Photovoltaic Solar Energy Conference (EUPVSEC)**, p. 1414-1418, Hamburg, Germany, 2009.

[141] BARTSCH, J. M. **Advanced front side metallization for crystalline silicon solar cells with electrochemical techniques**. Freiburg im Breisgau. 279p. Doctoral Thesis. *Fakultät für Angewandte Wissenschaften*, *Albert-Ludwigs-Universität*, Freiburg im Breisgau, Germany, 2011.

[142] DAS, J.; et al. Laser ablation: towards advanced industrial solar cell metallization processes, **26th European Photovoltaic Solar Energy Conference (EUPVSEC)**, p. 1691-1693, Hamburg, Germany, September 2011.

[143] HERNÁNDEZ, J. L.; et al. Application of CMOS metal barriers to copper plated silicon solar cells, **25th European Photovoltaic Solar Energy Conference and Exhibition (EUPVSEC)**, p. 1479-1483, Valencia, Spain, September 2010.

[144] KNORZ, A.; et al. Laser ablation of antireflection coatings for plated contacts yielding solar cell efficiencies above 20 %, **24th European Photovoltaic Solar Energy Conference (EUPVSEC)**, p. 1002-1005, Hamburg, Germany, September 2009.

[145] LEE, D. B. Anisotropic etching of silicon. **Journal of Applied Physics**, Vol. 40, No. 1, p. 4569-4574, October 1969.

[146] SEIDEL, H., et al. Anisotropic etching of crystalline silicon in alkaline solutions - Orientation dependence and behavior of passivation layers. **Journal of the Electrochemical Society**, Vol. 137, No. 11, November 1990.

[147] GREEN, M. A. **Silicon solar cells – Advanced principles and practice**, University of New South Wales (UNSW), Sydney, 366p., March 1995.

[148] ZHAO, J.; Green, M. A. Optimized antireflection coatings for high-efficiency silicon solar cells. **IEEE Transactions on Electron Devices**, Vol. 38, No. 8, p. 1952-1933, August 1991.

[149] LY, M.; et al. Influência da espessura do filme antirreflexo de TiO_2 nos parâmetros elétricos de células solares com Base N. **IV Congresso Brasileiro de Energia Solar e V Conferência Latino-Americana da ISES**, São Paulo, Brazil, September 2012.

[150] ZIMMER, M.; Birmann, K.; Rentsch, J. Online process control of alkaline texturing baths with near-infrared spectroscopy, **Vibrational Spectroscopy**, Vol. 53, p. 269-273, 2010.

[151] VAZSONYI, E.; et al. Improved anisotropic etching process for industrial texturing of silicon solar cells, **Solar Energy Materials & Solar Cells**, Vol. 57, p. 179-188, 1999.

[152] KING, D. L.; Buck, M. E. Experimental optimization of an anisotropic etching process for random texturization of silicon solar cells, **22nd IEEE Photovoltaic Specialists Conference (PVSC)**, p. 303-308, Las Vegas, USA, 1991.

[153] LI, H.; et al. Metal grids-based texturization of monocrystalline silicon wafers for solar cells, **Solar Energy Materials & Solar Cells**, Vol. 94, p. 942-945, 2010.

[154] DAVIS, J. R.; et al. Impurities in silicon solar cells. **IEEE Transactions on Electron Devices**, Vol. 27, No. 4, p. 677-687, April 1980.

[155] KERN, W. **Handbook of semiconductor wafer cleaning technology**, Noyes Publications, USA, p. 111-151, 1993.

[156] ABERLE, G. A. **Crystalline silicon solar cells – Advanced surface passivation and analysis**, University of New South Wales, Sydney, Australia, 335p., 2004.

[157] THOMSON, A. F.; McIntosh, K. R. Light-enhanced surface passivation of TiO_2-coated silicon, **Progress in Photovoltaics: Research and Applications**, Vol. 20, p. 343-349, 2012.

[158] MOEHLECKE, A.; Zanesco, I. ***Desenvolvimento de células solares eficientes em lâminas de silício tipo n***. Porto Alegre, 2012. (Technical Report, FINEP/2010)

[159] U.S. LASER CORPORATION. **Equipament manual: Nd:YAG laser micro-machining system model 4024**. Wyckoff, USA, 2005. 89p.

[160] EBERHARDT, D. **Desenvolvimento de um sistema completo para caracterização de células solares**. Porto Alegre. 104p. Master Thesis (Mestrado em Engenharia e Tecnologia de Materiais). Programa de Pós-Graduação em Engenharia e Tecnologia de Materiais, Pontifícia Universidade Católica do Rio Grande do Sul, Porto Alegre, Brasil, 2005.

[161] ZANESCO, I.; Moehlecke, A. **Implementação de duas unidades geradoras de energia elétrica com módulos fotovoltaicos eficientes**. Porto Alegre, 2010. 387 p. (Technical Report, MME 008/2005)

[162] PREU, R.; et al. The status of silicon solar cell production technology development at Fraunhofer ISE. **IEEE 4th World Conference on Photovoltaic Energy Conversion**, p. 1040-1043, Waikoloa, Hawaii, USA, 2006.

[163] SCHNEIDER, A.; et al. Bow reducing factors for thin screen-printed mc-Si solar cells with Al BSF, **29th IEEE Photovoltaic Specialists Conference (PVSC)**, p. 336-339, New Orleans, Louisiana, USA, May 2002.

[164] BÄHR, M.; et al. Comparison of bow-avoiding Al pastes for thin, large-area crystalline silicon solar cells, **20th European Photovoltaic Solar Energy Conference (EUPVSEC)**, p. 926-929, Barcelona, Spain, June 2005.

[165] HILALI, M. M.; Gee, J. M.; Hacke, P. Bow in screen-printed back-contact industrial silicon solar cells, **Solar Energy Materials & Solar Cells**, Vol. 91, p. 1228-1233, 2007.

[166] BISERNI, E. **Grooving and doping by laser chemical processing (LCP) for silicon photovoltaics**. Milan. 90p. Master Thesis. *Facoltà di Ingegneria dei Processi Industriali Politecnico di Milano*, Milan, Italy, 2010.

[167] MAYER, K. ***Chemische Ansätze zur Neuordnung des Solarzellenprozesses ausgehend vom Wafering bis hin zur Emitterdiffusion***. Frankfurt am Main. 349p. Doctoral Thesis. *Johann Wolfgang Goethe-Universität*, Frankfurt am Main, Germany, 2009.

[168] CARR, K. F. Optical materials: silicon carbide mirrors benefit high-speed laser scanning, **Laser Focus World**, Volume 44, Issue 4, April 2008.

[169] BARTSCH, J.; et al. Progress with multi-step metallization processes featuring copper as conducting layer at Fraunhofer ISE, **27th European Photovoltaic Solar Energy Conference (EUPVESC)**, p. 604-607, Frankfurt, Germany, September 2012.

[170] LETIZE, A.; et al. Light induced electroless plating of silver for efficiency improvement and cost reduction of silicon solar cells, **27th European Photovoltaic Solar Energy Conference (EUPVSEC)**, p. 1769-1772, Frankfurt, Germany, September 2012.

[171] FELL, A. **Modelling and simulation of laser chemical processing (LCP) for the manufacturing of silicon solar cells**, Freiburg im Breisgau. 167p. Doctoral Thesis. *Universität Konstanz*, Germany, 2010.

[172] KNORZ, A.; et al. Selective laser ablation of SiN_x layers on textured surfaces for low temperature front side metallizations. **Progress in Photovoltaics: Research and Applications**, Vol. 17, p. 127-136, 2009.